



Universidad de Cantabria



CSIC - Universidad de Cantabria

Instituto de Física de Cantabria

Espectros promedio en rayos X de Núcleos Galácticos Activos de muestreos profundos en rayos X

Memoria presentada por la Licenciada

Serena Falocco

para optar al título de Doctora por la Universidad de Cantabria, Doctorado en Ciencias,
Tecnología y Computación

2012

Declaración de Autoría

Francisco Jesús Carrera Troyano, Doctor en Ciencias Físicas y Profesor Titular de la Universidad de Cantabria,

y

Xavier Barcons Jáuregui, Doctor en Ciencias Físicas y Profesor de Investigación del Consejo Superior de Investigaciones Científicas,

CERTIFICAN que la presente memoria

Espectros promedio en rayos X de Núcleos Galácticos Activos de muestreos profundos en rayos X

ha sido realizada por **Serena Falocco** bajo nuestra dirección.

Consideramos que esta memoria contiene aportaciones suficientes para construir la tesis Doctoral del interesado.

En Santander, a 23 de Julio de 2012

Francisco Jesús Carrera Troyano

Xavier Barcons Jáuregui

a Luis...
alla mia famiglia...
alle mie amiche...

Agradecimientos

Al final de estos años de doctorado quería expresar mi gratitud a todas las personas que han contribuido al desarrollo de mi tesis y que han estado a mi lado.

Primero, Francisco: me ha enseñado mucho más de lo que me esperaba. Lo agradezco por todas las veces que me has ayudado y con mucha paciencia me ha dedicado todo el tiempo que podía dedicarme. Me ha enseñado una manera de trabajar que seguramente me será útil en el futuro y ha sabido transmitirme un interés por todos los detalles que hemos ido encontrando en el camino.

Xavier, gracias por todas las veces que me ha aclarado los temas más complicados con las explicaciones más sencillas.

Lucia: grazie per l'aiuto che mi hai dato fin dall'inizio. Ogni volta che mi hai aiutato, chiarito, spiegato, ho fatto un passo avanti per arrivare fino qui. Grazie anche a Valentina per l'aiuto, la collaborazione, la disponibilità quando sono stata a Leicester.

Un gracias particular a Silvia, porque su ayuda ha sido determinante desde el primer año de doctorado, no obstante haya llegado a IFCA más tarde y también a Maite por el soporte y la disponibilidad desde el principio.

Agradezco a las personas que trabajan en Altamira, por la disponibilidad y por haberme dado la posibilidad de utilizar su supercomputador. En particular gracias a Luis que siempre me lo ha explicado todo. Siempre disponible con los usuarios, me ha aclarado todas las dudas y me ha soportado todas las veces que no me funcionaban los trabajos. Además, al principio, me ha enseñado el lenguaje de programación Python, que no conocía: nunca habría sido capaz yo sola leyéndome el manual!

Agradezco a Amalia por su ayuda desde el principio en la utilización de la técnica de análisis. Gracias también a Angel por haberme hechado una mano con latex, para escribir la tesis.

Thanks to all the people I met during my short stays that have been fundamental for my thesis. I acknowledge the Astronomy group of Imperial College, in particular Elise for her help and availability.

Ringrazio il gruppo di Astronomia X dell'Osservatorio Astronomico di Bologna per avermi dato l'opportunità di lavorare nel progetto del CDFS. Grazie anche per l'ospitalità straordinaria con cui sono stata accolta. Nei tre mesi che sono stata lì ho conosciuto una città piena di persone meravigliose nell'osservatorio, nell'università, e fuori.

Alle persone dell'Università Roma 3, in particolare, ai dottorandi di Astrofisica: grazie per avermi fatto appoggiare nell'aula 81 nei giorni in cui sono stata a Roma.

Doy gracias particularmente a Luis por haberme ayudado siempre y darme la seguridad de que llegaría hasta el final, que lograría terminar todo esto algún día, aunque la verdad es que todavía no me lo creo.

Y muchas gracias a Azucena por haberme hecho conocer Santander, ya que ahora soy casi santandereña.

Grazie alle mie amiche, in particolare: a Elena per essere sempre stata d'accordo con i miei progetti; a Shamin, spero tanto che il mio sogno e le tue previsioni si avverino.

Tutto questo non sarebbe stato uguale senza il supporto della famiglia. I miei genitori sempre hanno capito e hanno appoggiato la mia scelta, nonostante tutte le difficoltà e tutte le volte che le cose non andavano esattamente come io volevo. A mia sorella, Anna, sempre presente e attenta, che ora trasmette più positività e ne abbiamo bisogno; a cugini e zii per avermi sempre accompagnato ed essere stati presenti. Ed infine grazie in particolare al più grande e al più piccolo della famiglia: a mio nonno per la sua saggezza e al piccolo Valentino...un sorriso che infonde ottimismo!

Resumen de la tesis en castellano

En esta tesis presentamos el estudio de las propiedades espectrales promedio de los Núcleos Galácticos Activos (AGN), incluyendo los que son parte de los muestreos más profundos de rayos X observados de los satélites *XMM-Newton* y *Chandra*.

Los Núcleos Galácticos Activos son las fuentes estables más brillantes del Universo, y se cree que el motor de sus luminosidades es el acrecimiento de gas alrededor de un agujero negro supermasivo (a partir de las iniciales en inglés de Super Massive Black Hole, SMBH).

Por conservación del momento angular, el material en acrecimiento toma la forma de un disco. Las propiedades de estos sistemas no son conocidas todavía con mucho detalle, pero se sabe que su emisión se puede detectar en los rayos X. De hecho, el espectro en esta banda está producido por difusión Compton inversa de la radiación térmica primaria del disco por parte de un plasma caliente a su alrededor. Ese proceso produce el espectro X que detectamos. El espectro, gracias a las propiedades penetrantes de los fotones X, no interacciona mucho con el exterior. Por esta razón la análisis del espectro X de los AGN ha ofrecido la posibilidad de explorar las regiones más cercanas al agujero negro central, dando los resultados más exitosos de las últimas décadas.

La espectroscopía en los rayos X de estas fuentes es un instrumento extremadamente útil para medir los efectos relativistas del campo gravitatorio del agujero negro central, y por tanto obtener algunas de sus propiedades como la rotación, la distribución de la emisión en el disco, y sus radios interno y externo. Además, ofrece una prueba directa de la presencia de los agujeros negros en el centro dinámico de estos objetos.

La característica espectral más prominente en los rayos X es la línea de emisión K_{α} del hierro. La fluorescencia puede ocurrir en regiones relativamente lejanas de la fuente central (una estructura con forma de toro) o en regiones cercanas a ella, en el disco. Si ocurre en el disco, los efectos del campo gravitatorio del agujero negro (BH) pueden producir diversos efectos de ensanchamiento y deformación, produciendo principalmente un perfil ancho con una ala pronunciada en el lado rojo de la línea. La detección y el estudio en detalle de estos efectos representa una de las pruebas más convincentes del paradigma de los agujeros negros.

Las líneas del hierro anchas han sido detectadas con significancia estadística muy elevada en objetos con alta calidad espectral, siendo MCG 6-30-15 el ejemplo más estudiado. Una cuestión muy urgente es saber si estas propiedades son comunes a la población completa de los AGN, o si caracterizan solo una clase de ellos, dependiendo del tiempo cósmico o de sus propiedades intrínsecas como la luminosidad.

La detección de estas líneas anchas necesita muy alta cociente señal-ruido (SNR de las iniciales en inglés Signal-to-Noise-Ratio), que con los observatorios de hoy ha sido conseguido solo en un número muy limitado de objetos.

Objetivos

La análisis de las propiedades espectrales de los AGN, en particular de la línea del hierro, constituye el objetivo principal del presente trabajo. Hemos adoptado la estrategia de compilar tantos espectros de rayos X como fuera posible y de calcular los espectros promedio. De estos, extraemos las características en banda X de los AGN.

Resultados anteriores al presente trabajo (Corral et al. 2008) han enseñado que la línea del hierro es una característica siempre presente en los espectros de *XMM-Newton* de los AGN, detectando un perfil estrecho. Considerando este resultado, lo queremos comprobar con muestras intrínsecamente distintas y observadas no solo de *XMM-Newton*, sino también de *Chandra*.

Nuestro fin es también averiguar si la línea del hierro posee una componente ancha en todos los AGN o solo en una clase de ellos.

Las condiciones físicas del AGN afectan la detección de la línea ancha. El estudio de cómo tales condiciones influyen en la detección de la línea emitida de parte del disco de acrecimiento ofrece informaciones interesantes sobre la física de estos objetos exóticos.

A la vista de los trabajos de de la Calle Pérez et al. (2010), es muy difícil detectar la línea ancha y sólo se ha hecho en unas cuantas observaciones particularmente profundas de fuentes brillantes, mientras la línea estrecha se ha detectado en muchas fuentes, más lejanas y débiles.

En nuestro trabajo, queremos entender si la detección de la línea ancha depende de las características de las observaciones, como el SNR y / o el número de cuentas totales acumuladas en los muestreos. En trabajos anteriores al nuestro como Guainazzi et al. (2006), Nandra et al. (2007) y Guainazzi et al. (2011), se ha demostrado que el SNR es una característica determinante para detectar tales líneas. Queremos estudiar muestreos distintos en número de cuentas acumuladas, en número de fuentes, en SNR, en distribución en el espacio luminosidad-redshift, para determinar cuales son las condiciones preferenciales de los muestreos de rayos X para un estudio detallado de las líneas anchas relativistas.

Hemos empezado compilando fuentes de los muestreos más profundos del satélite *Chandra*. Seguidamente, hemos procedido estudiando el muestreo más profundo del observatorio de *XMM-Newton*, de

cuya mayor sensibilidad y mayor número de fuentes esperábamos poder mejorar estos resultados, consiguiendo efectivamente detectar una componente ancha, pero sin obtener todavía un resultado claro sobre su dependencia con el redshift o la luminosidad. Finalmente, hemos extendido nuestro campo de análisis en objetos cercanos combinando el muestreo más grande de cuasares (Véron-Cetty & Véron que también llamamos VCV) con el mayor catálogo existente de fuentes de rayos X: el catálogo 2XMM para estudiar con algo más de detalle el perfil de la línea.

Para que nuestros resultados no sean afectados de posibles efectos metodológicos, que pueden ensanchar líneas estrechas, queremos desarrollar una nueva técnica de estimar la resolución intrínseca de nuestro método en la banda de energía que analizamos. En el caso que detectamos una línea ancha, queremos ajustarla con los modelos disponibles en la literatura.

En trabajos anteriores donde ha sido detectada la línea ancha (Streblyanska et al. 2005), se ha visto que las anchuras equivalentes (EW, de las iniciales en inglés de equivalent width) eran superiores a los valores encontrados en espectros individuales, probablemente por un efecto del método utilizado. Por esta razón, queremos desarrollar una manera nueva para calcular las anchuras equivalentes de las líneas, en manera independiente del modelo usado en los ajustes.

Queremos averiguar si las anchuras equivalentes de las líneas anchas (estimadas utilizando nuestro nuevo método y con los ajustes de los espectros promedio) son compatibles con los valores de los espectros individuales en la literatura para entender si los espectros con líneas anchas son de verdad muy comunes o si constituyen solo un pequeño porcentaje de los AGN.

En trabajos anteriores se ha visto que la EW de la línea estrecha cambia con el redshift, con la absorción y con la luminosidad.

La correlación más comprobada es el efecto Iwasawa-Taniguchi, que toma el nombre de sus descubridores (Iwasawa and Taniguchi 1993), que consiste en una disminución de la línea del hierro (de su EW) con el aumento de la luminosidad del continuo X de las fuentes. El uso de grandes surveys, con AGN que poseen luminosidades muy distintas, puede ayudar potencialmente a entender esta correlación.

Se espera que la EW de la línea estrecha sea más alta en fuentes absorbidas porque la absorción afecta al continuo (y a la componente ancha) pero no a la componente estrecha, aumentando así su EW. El estudio de grandes muestras de fuentes absorbidas en rayos X puede confirmar este modelo teórico y por esto queremos averiguar la correlación entre las propiedades de la línea y la densidad de columna del absorbente de rayos X en muestreos profundos caracterizados por un grande número de fuentes absorbidas.

Metodología

El estudio de características discretas en la espectroscopia X de los AGN es una clave única para averiguar los modelos teóricos de los AGN. Para poder efectuar una análisis eficiente, es necesario

tener datos de buena calidad espectral (Guainazzi et al. 2006) o, en ausencia de estos, hay que aplicar métodos de promediar o sumar los espectros. Estos maximizan el SNR.

Hemos aplicado el método elaborado de nuestro grupo de investigación (Corral et al. 2008) y hemos introducido en esta tesis unas novedades significativas.

La primera muestra que hemos utilizado en esta tesis está compuesta de las observaciones más profundas de *Chandra*: el *Chandra* deep Field North (Alexander et al. 2003), *Chandra* deep Field South (Luo et al. 2008) y la muestra AEGIS (Laird et al. 2009). Se trata de muestreos que contienen un número muy alto de fuentes detectadas y con informaciones disponibles de la espectroscopía óptica (los 'redshift'). Nos hemos centrado en las 123 fuentes distintas con más cuentas en la banda X.

La segunda muestra utilizada en este trabajo es la observación más profunda del satélite *XMM-Newton* en la dirección del *Chandra* deep Field South, que desde ahora llamamos XMM CDFS (Comastri et al. 2011). Gracias a la superior área eficaz de este satélite en la región espectral de la línea del hierro, XMM CDFS permite de acumular más cuentas de la anterior observación de parte de *Chandra*. Nos hemos centrado en las 51 fuentes que tienen información espectroscópica y con los mejores espectros de rayos X.

La última muestra que hemos analizado fue definida cruzando la información del catálogo Véron-Cetty&Véron (Véron-Cetty and Véron 2010) y la del catálogo 2XMM (Watson et al. 2008) de *XMM-Newton* (VCV). Hemos seleccionado los espectros con la mejor calidad, con un total de 340 fuentes distintas.

Las muestras analizadas han sido divididas en submuestras de luminosidad y de redshift con el mismo número de cuentas en cada una. Estas subdivisiones se han realizado para investigar la dependencia de las propiedades de la línea con estos parámetros en observaciones con igual calidad estadística.

Además, las hemos dividido en AGN absorbidos y no absorbidos considerando un corte en densidad de columna del absorbente a $\log(N_{\text{H}}/\text{cm}^2) = 21.5$. Con valores mayores de densidad de columna, de hecho, es posible detectar en los espectros de los AGN unas características de absorción en la banda de energía que estudiamos ($E > 1$ keV).

Aportaciones originales

Este trabajo de doctorado contribuye significativamente al estudio de los Núcleos Galácticos Activos en los rayos X. Varias novedades, con respecto a las muestras utilizadas y al método de análisis desarrollado, han sido introducidas en este trabajo.

Primero de todo, los espectros promedio de las muestras estudiadas en esta tesis nunca han sido publicado en anteriores artículos. Parte de las muestras profundas de *Chandra* ha sido estudiado en el trabajo de Brusa et al. (2005), pero nosotros hemos utilizado una muestra de CDFS más reciente y más profunda. Además, hemos añadido el campo de AEGIS que nunca ha sido estudiado antes.

La segunda muestra de la presente tesis es la de CDFS observado de *XMM-Newton*, que nunca ha sido analizado con técnicas parecidas antes. La última muestra, la del VCV, tal cual fue definida y analizada en nuestro grupo, así como la selección y la extracción de los espectros, han sido hechas solo en el trabajo presente, aunque algunas fuentes son probablemente en común con Chaudhary et al. (2010) y Corral et al. (2008).

Hemos introducido distintas novedades no solo con respecto a las muestras empleadas sino también con respecto a la metodología aplicada en nuestra análisis.

De hecho, hemos aplicado por primera vez un método de estimación de la significancia estadística de la línea del hierro y también de su anchura equivalente (EW). En la espectroscopía X, el calculo de estas cantidades puede ser afectado seriamente de una no correcta modelización del continuo debajo de la línea. Por esta razón, hemos trabajado en un método innovador independiente del modelo usado para estimarla: hemos comparado los espectros promedio simulados (mas de 100) con los espectros promedio observados para poder detectar cualquier diferencia y chequear si son significativos.

La resolución espectral limitada y dependiente de la energía de los detectores X, y el conjunto de fuentes con desplazamientos al rojo muy distintos, lleva inevitablemente a la necesidad de tener en cuenta la variación de la resolución espectral con la energía cuando se estudian las líneas anchas. Si no se tiene en cuenta este efecto, de hecho, es posible sobreestimar sus anchuras. Para poder medir esta tendencia hemos simulado líneas de emisión no resueltas centradas en distintas energías entre 1 y 10 keV. Luego hemos estudiado la variación de sus anchuras con la energía del centro de las líneas y lo hemos tenido en cuenta cuando hemos ajustado los espectros.

Nuestros resultados se han presentado en distintas reuniones y conferencias. Los resultados sobre la muestra de *Chandra* se han publicado en el artículo Falocco et al. (2012). La segunda muestra, el XMM CDFS, será enviada en un par de semanas a la revista A&A por publicación, mientras el VCV necesitará más tiempo.

Resultados y conclusiones

En nuestra análisis espectral nos hemos centrado principalmente en la línea del Hierro porque su estudio es muy prometedor para poder investigar tanto las zonas centrales del disco de acrecimiento como la distribución de material a grandes distancias del centro.

En nuestra muestra profunda de *Chandra*, con un total aproximado de 70000 cuentas, hemos encontrado que una línea del hierro estrecha caracteriza los espectros de los AGN de toda la muestra y de sus submuestras. La línea que se detecta es estrecha en la mayoría de las submuestras. Hemos investigado el perfil de la línea considerando la resolución instrumental de nuestro método que es de 120 eV en 6.4 keV, como hemos visto en nuestras simulaciones. Una línea más ancha de la resolución instrumental está detectada en la muestra de baja luminosidad y de bajo redshift pero su forma no es relativista. Este perfil aparentemente simétrico proviene probablemente de la contribución de líneas relativistas,

líneas ionizadas estrechas (centradas en distintas energías), y líneas estrechas provenientes de material neutro.

Hemos encontrado una indicación de que la intensidad de la línea estrecha disminuye al crecer de la luminosidad, pero con baja significación estadística.

En la muestra de XMM CDFS, que tiene un total de 200000 cuentas, hemos encontrado que la línea es significativa a más de 4 sigma. Hemos estudiado su forma teniendo en cuenta como varía la resolución espectral con la energía en la banda considerada.

La línea es más ancha de nuestra resolución (que en 6.4 keV es de 110 eV) y su perfil puede modelarse tanto con una ley gaussiana como con un modelo físico más apropiado para describir las líneas de disco de acrecimiento (el modelo `Diskline` de `Xspec`). No podemos concluir si un modelo ajusta mejor que el otro porque nuestra línea es aproximadamente simétrica. Probablemente, tenemos una estadística de cuentas insuficiente para detectar las asimetrías debidas a los efectos relativistas. Además, hemos visto que la anchura equivalente de la línea ancha es más alta de la que se encuentra en los espectros individuales en la literatura, mientras la de la línea estrecha es menor.

Como esto está en desacuerdo con los modelos teóricos, hemos considerado un distinto modelo para tener en cuenta las líneas emitidas por fluorescencia en material neutral lejano de la fuente central (Matt 2002). Con estos ajustes, no hemos conseguido modelar la estructura ancha presente en la línea y hemos tenido que añadir la componente `diskline`. Añadir esta componente es más significativo de 3 sigma y su anchura equivalente en la muestra total es de 164 eV, compatible con los valores de espectros individuales en la literatura.

En la última muestra analizada (VCV), en la que hemos acumulado 700000 cuentas, hemos observado un claro perfil ancho asimétrico bajo una línea estrecha a 6.4 keV. Ajustando la compleja línea detectada, hemos visto que añadir la componente relativista es significativo a más de 4σ y que esta componente tiene EW de 219 eV. La EW medida en la línea estrecha es de 95 eV.

Resumiendo, en este trabajo confirmamos que la línea del hierro es una característica prominente y común en los espectros de rayos X de los AGN, no obstante la dificultad de detectarla en observaciones de baja relación señal ruido.

Sobre la componente ancha de la línea, interesante prueba de los efectos relativistas del agujero negro, la respuesta es más compleja. A este propósito, volvemos a la pregunta fundamental de ese trabajo: ¿es posible generalizar la presencia de la línea ancha a todos los AGN, o al menos a una clase de ellos? Con nuestro trabajo, una vez más, después de Nandra et al. (2007) y de Guainazzi et al. (2006), se ha encontrado que su detección es más importante estadísticamente en muestras que tienen un más alto número de cuentas.

La componente ancha de la línea puede ser ajustada con los modelos relativistas de disco de acrecimiento disponibles en la literatura en muestras de muy alta calidad espectral (el VCV). Una línea

gaussiana ancha, el revés, ajusta los espectros tan bien como la línea relativista en muestreos con menor número de cuentas (XMM CDFS).

Además de la componente ancha, es también posible separar la componente estrecha de la ancha, por lo menos en muestras con bastante número de cuentas (en el VCV) y de manera más débil en muestras de calidad mediana, como algunas submuestras del CDFS.

En general, la anchura equivalente medida es compatible con la que se encuentra en fuentes individuales: esto indica que la línea ancha tiene que estar emitida por un porcentaje grande de fuentes. De hecho, al revés, si emitida por un porcentaje más bajo, las fuentes individuales tendrían que tener EW muchos más altas de las que se encuentran en la literatura, para compensar a la fracción de fuentes no contribuyentes. La diferencia de EW medidas en nuestro trabajo y en el de Streblyanska et al. (2005) que obtienen una EW superior es probablemente debida a los efectos de los distintos métodos utilizados (agrupar los espectros antes de promediarlos puede llevar a sobreestimar la línea).

Nuestro análisis de submuestras en luminosidad y en redshift en los campos profundos analizados nos ha indicado que son necesarias más cuentas para detectar una tendencia de la línea con estos parámetros.

Futura investigación

En este trabajo hemos determinado con un método innovador las propiedades de las líneas del hierro en los AGN hasta desplazamientos al rojos muy elevados. Hemos encontrado resultados que merece la pena analizar mejor:

- **VCV:** el análisis de la muestra de VCV se tiene que completar haciendo los ajustes de la muestra total y de las submuestras y utilizando modelos complejos de fluorescencia de parte de material lejano neutral y ionizado, con también la línea relativista
- *Variación de la anchura equivalente con luminosidad y con redshift:* en nuestros muestreos profundos, hemos encontrado una indicación de la dependencia de la línea del hierro de redshift y luminosidad, pero no es bastante significativa considerando los errores. Una dificultad común en las muestras profundas es la fuerte correlación entre redshift y luminosidad. Por esta razón, sería útil poder rellenar la zona de bajo redshift en el espacio de los parámetros, para construir bins en luminosidades en el Universo local. Para esto, la utilización del VCV es particularmente adecuada, por su alta estadística de cuentas
- *Detección de líneas anchas en muestras de AGN oscurecidos:* aunque no está esperado en la teoría, hemos detectado líneas anchas en AGN oscurecidos. Antes de intentar explicar esta evidencia, un análisis más profundo de estas fuentes es necesaria. Un método prometedor sería seleccionar fuentes de rayos X a $E > 5\text{keV}$, puesto a esas energías se espera tener un sesgo menor contra fuentes moderadamente absorbidas.

- *Estudio de las propiedades de la línea del hierro en función de las características del 'motor central'* El estudio de la dependencia de la línea de las características del motor central (como la masa del agujero negro y la velocidad de acrecimiento) nos daría una información de fundamental importancia sobre las propiedades físicas y la geometría de las regiones más internas del AGN.

Los actuales satélites de rayos X todavía tienen una cantidad de datos muy grande no explorada para conocer más profundamente los AGN, mientras esperamos que nuevos instrumentos serán introducidos y cumplirán con sus expectativas.



Universidad de Cantabria



CSIC - Universidad de Cantabria
Instituto de Física de Cantabria

Average X-ray spectra of Active Galactic Nuclei from deep X-ray surveys

A dissertation submitted in partial fulfillment of the requirements
for the degree of Doctor of Philosophy in Physics

by

Serena Falocco

2012

'No light, but rather darkness visible'

John Milton (Paradise Lost)

Summary

In this thesis we study the average X-ray spectral properties of distant and nearby Active Galactic Nuclei (AGN), including those belonging to the deepest X-ray surveys observed by *XMM-Newton* and *Chandra*.

AGN are the most luminous persistent sources in the Universe, and it is believed that the origin of their extraordinary luminosities is accretion of matter onto a Super Massive Black Hole (SMBH). By conservation of angular momentum, this material forms an optically thick, geometrically thin structure in the shape of a disk. Detailed properties of these systems are not well known yet. Inverse Compton scattering of the primary thermal radiation from the disk by a hot plasma close to the disk produces the detected X-ray continuum. X-ray radiation, thanks to its penetrating characteristics, does not strongly interact with the outer material. For this reason, the analysis of such spectra to study the properties of the innermost regions of the AGN has offered very exciting results in the study of AGN in these last decades.

X-ray spectroscopy of these sources is an extremely useful instrument to detect relativistic effects of the gravitational field near the central Black Hole, and to measure some properties related to it, such as the spin, the emissivity and its extension. Moreover, it offers a direct proof of the presence of a SMBH in the dynamical centre of such objects. The most prominent emission feature in the X-ray spectra of these objects is the iron K_{α} line. Fluorescence can occur in regions both far from the central source (i.e. a doughnut-shaped structure called torus) and close to it, such as the accretion disk. If it occurs in the disk, the effects of the BH gravitational field can produce line deformation and broadening, resulting in a broad line profile with a red wing. The detection and the study of such phenomena represents the most compelling probe of the BH paradigm.

Broad iron lines have been detected with extraordinary significance in many sources observed with high spectral quality, MGC 6-30-15 being the best-studied example. A pressing question is now whether such features are a general characteristic of the full AGN population, and whether their intensity depend on cosmic time or on intrinsic source properties, such as their luminosity.

Unfortunately, the detection and characterisation of such broad features in X-ray spectra requires very high signal-to-noise-ratios (SNR), which with current facilities can only be achieved in a very limited number of nearby objects.

Goals

The study the X-ray spectral properties of AGN, in particular of the iron line, is the main purpose of this work. We adopt the strategy of compiling as many spectra as possible and computing their average; from the average spectrum, we extract the X-ray properties of AGN.

Previous results with similar methods (Corral et al. 2008; Chaudhary et al. 2010) showed that the iron line is an ubiquitous characteristic of the *XMM-Newton* spectra of AGN, and that its profile is narrow. In our work, taking these results into account, we aim at checking the ubiquity of the line in intrinsically different surveys. Our main purpose is to check if the iron line display a broad component in all the AGN or just in a class of them, and to investigate if its presence depends on luminosity, redshift, column density of the intrinsic absorption. The study of how these parameters affect our detection of the broad iron line emitted from the accretion disk offer an interesting information on the physics of such exotic objects.

Considering previous works, the detection of the broad line has been possible in only few, very deep observations of nearby and very luminous sources.

Here, we aim at understanding whether the broad line detection depends on the characteristics of the observations, such as the spectral SNR and/or the number of counts accumulated in the surveys. In previous works as in Guainazzi et al. (2006), Nandra et al. (2007) and Guainazzi et al. (2011), it has been demonstrated that the SNR is a key parameter to detect such features. We aim at checking this issue employing surveys with different SNR, different number of counts and of spectra, different distribution of the sources in the parameter space, observed with different instrumentation, to determine whether any preferential conditions exist to study such features in detail.

We started compiling sources from the deepest surveys performed with the *Chandra* observatory to study the distant Universe. We then proceeded to study the deepest survey undertaken to this date with the most sensitive X-ray observatory, the observation of the CDFS by *XMM-Newton* (Comastri et al. 2011), to place further constraints in the spectral properties at high redshift. Finally, we extended the baseline of our work to nearby objects by combining the largest compilation of nearby and distant AGN (Véron-Cetty & Véron -VCV-) with the largest catalogue of X-ray sources: the 2XMM catalogue (Watson et al. 2008).

To study the relativistic line profile using stacking methods, it is necessary to estimate the instrumental resolution and to take this into account during the spectral fitting. Our purpose here is to develop a new methodology to estimate it. Whether a line broader than the instrumental resolution of our method is

detected in our work, we will fit it using the models available in the literature to check their suitability to fit the average spectra.

In the previous work where the detection of the relativistic line was significant (Streblyanska et al. 2005), the values of the EW of the relativistic components were higher than those of the single spectra in the literature. They were probably overestimated due to an effect of the method: for this reason, we want to develop a new model-independent method to calculate the EW and the significance of the relativistic line (and of the narrow core). We then will compare the EW of the relativistic components with those of the single spectra in the literature. If similar values are found, it would indicate that the broad iron lines are really common in the AGN. Instead, if lower values are found, they cannot be considered as a common feature in AGN.

In previous works, it has been found that the EW of the narrow line is correlated with the luminosity and with the intrinsic absorption. The Iwasawa-Taniguchi effect, from Iwasawa and Taniguchi (1993), consists in a decrease of the iron line equivalent width (EW) with the continuum luminosity of the sources. The use of large surveys encompassing a broad span of luminosities can be useful to investigate such correlation.

The narrow iron line is expected to be related with the column density of the intrinsic absorption because, for growing density, the solid angle subtended from the primary emission to the reflection is larger, and consequently also the line EW is higher. In the X-ray absorbed sources, it is expected to detect most intense narrow lines and faint broad lines (the broad lines, contrarily to the narrow lines, are absorbed). The study of large samples of absorbed sources or of deep X-ray fields (which have a large number of absorbed sources) can help potentially to check this trend.

Methodology

The study of discrete characteristics in X-ray spectroscopy is a unique key to check the theoretical models describing the AGN. To make a proficient analysis, it is necessary to have good quality data (Guainazzi et al. 2006) or, in their absence, it is possible to apply methods to average or sum the spectra, that maximise the SNR. We applied a method developed by our research group, and we introduced in this thesis significant novelties.

The first sample we analysed is composed by the deepest observations from *Chandra*: *Chandra* deep Field North (Alexander et al. 2003), *Chandra* deep Field South (Luo et al. 2008), and AEGIS (Laird et al. 2009). These samples have a very large number (~ 700) of sources detected with spectroscopic redshifts. We focused on the 123 distinct sources with more counts in X rays.

The second deep sample is an observation from *XMM-Newton* in the direction of *Chandra* deep Field South, hereafter XMM CDFS (Comastri et al. 2011). Thanks to its higher effective area in the spectral region of the iron line, XMM CDFS allows to accumulate more counts than the previous *Chandra*

observation. We focused on the 51 unique sources with spectroscopic information and the best quality spectra.

The last sample analysed in this work is a shallow survey. It was defined cross-correlating the information of the Véron-Cetty & Véron (Véron-Cetty and Véron 2006) and the 2XMM (Watson et al. 2008) catalogues (VCV). We selected the sources with the best spectral quality, including a total of 340 AGN.

In the three samples studied here, we investigated subsets in luminosity and redshift with the same number of counts in each one. Doing it, we aimed to check whether the line properties change with luminosity and redshift in observations with the same statistical quality. Moreover, we defined absorbed and unabsorbed AGN considering a threshold in columns density at $\log(N_{\text{H}}/\text{cm}^2) = 21.5$. We chose this threshold because with this value of N_{H} the spectra are absorbed for $E < 1$ keV and non-absorbed above. For higher N_{H} , the energy of transition between transparent and opaque regime is higher, allowing to detect absorption features at higher energies.

Novelties of our work

Several novelties have been introduced in this work, especially in the samples used and in the new methodologies developed. First of all, the average spectra of the surveys employed have never been studied previously. Part of the Chandra deep Fields was studied in the previous work of Brusa et al. (2005), but we have used here a later, longer observation. Moreover, we added the AEGIS field that was never studied before. The second deep survey under analysis, the *XMM-Newton* observation in the CDFS, has never been analysed before with similar techniques. Finally, the VCV, as was defined and analysed by our group at IFCA, and the selection and extraction of X-ray spectra have been done only for the present work, although some sources are probably common with other studies such as the one of Chaudhary et al. (2010) and of Corral et al. (2008).

We introduced several novelties not only in the data employed, but also in the methodology applied in the analysis. We developed a new method to estimate the line significance and its EW. In X-ray spectroscopy of AGN, the measurement of these quantities can be seriously affected by an incorrect interpretation of the continuum under the line. For this reason, we have worked out a model-independent method to estimate it: we have compared the average simulated spectra (about 100) with the average observed spectra in order to detect any deviations and check whether they are significant.

The limited and energy-dependent spectral resolution of X-ray detectors, together with the combination of spectra of sources at very different redshifts, inevitably leads to an energy-dependent spectral resolution in the average spectrum. This should be taken into account when the broad iron lines are studied, because it could bring to an overestimation of their width. In order to estimate this effect, we simulated unresolved emission lines centred from 1 to 10 keV. We then studied the trend of the resolution with the energy and took it into account when we fitted the spectra.

Our results have been presented in meetings and conferences. The results concerning the *Chandra* sample were published in the paper Falocco et al. (2012). The second sample, XMM CDFS, is going to be submitted in the next few weeks, while the VCV work will require some more time.

Results and conclusions

In the *Chandra* deep fields, we accumulated about 70000 spectral counts in the 2-12 keV rest-frame band. The detected line is narrow in the majority of the subsets. We investigated the line profile taking into account that the instrumental resolution of our method is about 120 eV from our simulations. A line significantly broader than the resolution is detected in the low luminosity - low redshift sample, but its shape is not relativistic. It is symmetrical: it is possible that the apparently symmetrical profile comes from both relativistic lines and narrow lines from ionized and neutral material. A second possibility is instead that we have accumulated an insufficient number of counts for the detection of the relativistic profile. We found a hint of a decrease of the narrow line EW with increasing luminosity, but the trend is not significant considering the error bars.

In the XMM CDFS survey, that accumulates 200000 counts, we found that the line is significant always at more than 4 sigma. We checked its shape after considering the trend of the method resolution with the spectral energy. The line is broader than our resolution (of about 110 eV) and it is fitted by simple broad gaussian as well as by a more suitable model in the literature (namely `diskline` in `Xspec`). The reason why we could not discriminate between the two models is that the line is basically symmetric: we probably did not have enough counts statistics to detect the difference. From the fits with a relativistic component added to a narrow core, the EW estimated for the broad component is higher than the values of the individual spectra in the literature; in the meantime, the EW of the narrow component is too low, in spite of the expectations (according to the Standard Model we expect to detect a significant narrow core in the line). When we took into account a complete set of fluorescent lines from material far away from the central source, with the prescriptions of Matt (2002), we found that a broad excess is still present in the line. The addition of the `diskline` brings to an improvement of the fits at more than 3σ .

In the last survey analysed, the VCV, we collected a very large number of spectral counts: 700000. With the high spectral quality we could detect a significant line. Moreover, the detected line is formed by a clear narrow core plus a broad component with a relativistic shape. The significance of the relativistic line is 4σ .

Summarising, in our work we confirmed that the iron line is a prominent feature in the average X-ray spectra of AGN, implying that it must be widespread in their individual spectra, despite the difficulty of its detection at low SNR.

About the presence/absence of any broad component, the answer is more complicated. In this respect, we come back to the main motivation for our work: is it possible to extrapolate the broad line presence to all the AGN, or only to a limited class of them? With our work, once again, after Guainazzi et al.

(2006) and Nandra et al. (2007), we found that its detection is more significant in surveys with a large number of counts. Such surveys in fact have a generally higher SNR, allowing a more detailed study of the line.

The possibility to eventually discriminate between several line models is offered only by surveys with high spectral quality (such as the VCV) because in such surveys the asymmetric lines can be detected. If such quality is not reached, a broad gaussian fits the line as well as the disk-line model because an approximately symmetric line will be detected (as happened in the XMM CDFS). It is also possible to disentangle the narrow core and the broad component, at least in surveys with enough counts (in the VCV) and perhaps in some subsamples of the XMM CDFS.

The EW in our average spectra are in general compatible with the ones found published spectra of individual bright sources: this means that the broad line must be present in a large percentage of sources. If emitted by a low fraction of sources, the ones presenting such lines should have EW much higher than the individual observed values, to compensate for the majority of non-emitting sources. The difference between the EW found in this work and the ones in the previous one from Streblyanska et al. (2005), is instead due to the different methods involved: Streblyanska et al. (2005) computed the sum of binned spectra, and such method can introduce an overestimation of the line EW.

Our analysis of subsamples of luminosities and redshifts did not show any significant dependence of the line on these parameters: we cannot tell whether this is an effect of the limited SNR in spectra of each subsample, or whether the line characteristics do not really depend on the luminosity or on cosmic time. We would need to employ surveys with more counts statistics to address this issue.

Future developments

In this work we have explored the iron line properties with an innovative method. Some further issues which could be investigated are:

- *Trend of the iron line with luminosity and redshift:* in our deep fields, we found a hint of a dependence of the iron line on redshift and luminosity, but it was not significant considering the error bars of the EW. A common difficulty in deep pencil-beam surveys is the strong correlation between redshift z and luminosity. For this reason, it would be useful to fill up the low redshift zone of the parameter space, in order to construct several bins in luminosity in AGN of the local Universe. For this purpose, the employment of our VCV sample is particularly suitable, given its high statistics
- *Broad line detection in obscured AGN:* although it is not expected by the theory, we detected broad iron lines in absorbed AGN. Before attempting any explanation for such result, a deeper analysis of such sources is necessary. A selection of sources at energies $>5\text{keV}$ would provide a selection of sources less biased against absorbed ones, since Compton-thin absorption would be less important at those energies.

- *Study of the iron line properties as a function of the properties of the 'central engine'*: The study of the dependence of the emission line characteristics with physical properties of the central engine (such as the BH mass or the accretion rate) would provide vital information as to the physical properties and geometry of the inner regions of AGN

Current facilities and their archives still have the potential to address some of the most fascinating questions in our current knowledge of AGN, while waiting for new facilities to be realised and fulfil their expectations.

Contents

Declaración de Autoría	iii
Agradecimientos	vii
Resumen en castellano	ix
Summary	xxi
List of Figures	xxxiii
List of Tables	xxxvii
1 Introduction	1
1.1 The Unified Model of the Active Galactic Nuclei	2
1.2 The X-ray emission of AGN	5
1.2.1 The primary X-ray emission of AGN	6
1.3 The X-ray reprocessing	6
1.3.1 Reflection by neutral material	7
1.3.2 Reflection by ionised material	10
1.4 X-ray obscuration in AGN	11
1.5 The iron emission line from the accretion disk	14
1.5.1 Expected shape of the iron line in accretion disks	14
1.5.2 The observed iron line profiles	17
1.5.3 The observed iron line profiles after statistical treatments in surveys	19
1.6 Our work	24
2 Our X-ray data	27
2.1 The <i>Chandra</i> surveys	27
2.1.1 The <i>Chandra</i> observatory	28
2.1.2 The parent <i>Chandra</i> surveys	29
2.1.3 The <i>Chandra</i> spectral extraction	30
2.2 The XMM surveys	30
2.2.1 <i>XMM-Newton</i> observatory	31
2.2.2 The <i>XMM-Newton</i> survey of the <i>Chandra</i> deep Field South	33

2.2.3	The 2XMM-Newton spectra of sources in the Véron-Cetty-Véron catalogue . . .	33
2.2.4	The spectral extraction and merging	34
3	Methodology	37
3.1	The X-ray spectral analysis	37
3.1.1	Spectral fits in Xspec	38
3.2	Selection of the samples	40
3.3	Our averaging method	40
3.4	Simulations of the continuum	41
3.5	Implementation of innovative methodologies to analyse the X-ray average spectra . . .	42
3.5.1	New model-independent estimation of the iron line significance	42
3.5.2	Model independent estimation of the EW	43
3.5.3	New method to estimate the effective resolution of our method	43
4	Stacking of the <i>Chandra</i> surveys	45
4.0.4	Properties of the <i>Chandra</i> samples	45
4.0.5	Subsample definition	48
4.1	The average <i>Chandra</i> spectrum of AGN in the total sample	50
4.2	Results	53
4.2.1	Results from our model-independent method	54
4.2.2	Results from our model dependent method (fits to the data)	55
4.2.3	Dependence on redshift and luminosity	60
4.2.4	Analysis of broad lines	60
4.3	Conclusions	61
5	Stacking of the CDFS from <i>XMM-Newton</i>	65
5.1	Sample definition and properties	65
5.1.1	Subsample definition	67
5.2	Results	69
5.2.1	Model-independent estimation of the significance and EW	73
5.2.2	Spectral fits on the full sample and subsamples	75
5.2.2.1	Partial covering absorption and Compton reflection	75
5.2.2.2	Iron line fitting with a gaussian model	76
5.2.3	Fits of the broad iron lines	81
5.2.4	Complex continuum models with a complete set of fluorescent lines	83
5.3	Discussion	86
5.4	Conclusions	95
6	Stacking of the VCV survey	97
6.1	Properties of the VCV sample	97
6.2	Results	99
6.3	Conclusions	101
7	Conclusions	105
7.1	Conclusions of this thesis	105
7.1.1	Average Fe line emission from <i>Chandra</i> deep fields	106
7.1.2	Average Fe line emission from the XMM CDFS deep field	106
7.1.3	Average Fe line emission from XMM VCV wide field	107

7.1.4 Overall conclusions	107
7.2 Pending issues	108
A Different selections of the Chandra sample	111
B The XMM CDFS background	117
C Tests of the method	121
References	125

List of Figures

1.1	Type 1 AGN NGC5548 (Ho et al. 1995)	3
1.2	Type 2 AGN NGC1667 (Ho et al. 1995)	3
1.3	Unified model of the AGN	5
1.4	Typical X-ray spectrum (thick black line) and its main components (coloured lines) of a type 1 AGN (Risaliti and Elvis 2004).	6
1.5	Coronal models. Several geometries for the configuration of the plasma	7
1.6	Simulated reflection spectrum of and incident powerlaw in the cold reflection regime (Reynolds et al. 1995)	8
1.7	Expected profile of the iron line considering the effect of the Compton Shoulder (Matt 2002)	9
1.8	Ionised reflection spectra for different ionisation parameters, from the theoretical prediction of Ballantyne et al. (2001) using constant density models.	10
1.9	Spectrum of NGC1068 (Matt et al. 2004)	11
1.10	Transition energies of a material (as a function of its column density N_H) between the transparent and the opaque regime considering photoelectric (dashed line) and the Compton scattering (continuous line)	12
1.11	Absorption in X-rays (Gilli et al. 2007)	13
1.12	Iron lines from the innermost regions of the accretion disks (Fabian et al. 2000)	15
1.13	Iron lines from accretion disks with different inclination angles (from the higher to the lower line: $i=20$; $i=50$; $i=87$) (Matt et al. 1992)	16
1.14	Iron lines from accretion disks with BH spins $a=0$ (double peaked profile) and $a=1$ (broader profile) (Fabian et al. 2000)	16
1.15	Iron line in MGC-6-30-15 (Fabian et al. 2002)	18
1.16	Iron lines in the stacked spectra of Streblyanska et al. (2005) in type 1 and type II AGN	21
1.17	Iron lines from the average spectra of XMS+XWAS sample in (Corral et al. 2008)	22
2.1	Artistic view of <i>Chandra</i> satellite in flight showing its main characteristics and the instruments on board (see text for details)	29
2.2	Schematic design of the main body of the <i>XMM-Newton</i> spacecraft showing its main characteristics and the disposition of the mirrors and the instruments (see text for details). Copyright 2009©European Space Agency.	32
2.3	<i>Chandra</i> and <i>XMM</i> efficiency as a function of the spectral energy.	32
3.1	Instrumental resolution of our method as a function of $E/6$ with E spectral energy in keV.	44
4.1	Distribution of the net counts between 2 and 12 keV (rest-frame). Filled histogram: CDF-S; histogram with horizontal stripes: AEGIS; histogram with vertical stripes: CDF-N.	46

4.2	Redshift distribution. Blue histogram: CDF-S; red histogram: AEGIS; green histogram: CDF-N.	47
4.3	Distribution of intrinsic column density in units of cm^{-2} . Blue histogram: CDF-S; red histogram: AEGIS; green histogram: CDF-N. We grouped the spectra with $\log(N_{\text{H}}) < 10^{20} \text{cm}^{-2}$ with the spectra having $\log(N_{\text{H}}) = 10^{20} \text{cm}^{-2}$	47
4.4	Distribution of rest-frame 2-10 keV luminosities in units of erg s^{-1} . Blue histogram: CDF-S; red histogram: AEGIS; green histogram: CDF-N.	48
4.5	Comparison of our full sample (black stars) with the deep <i>XMM-Newton</i> sample of Streblyanska et al. (2005) (LH, red triangles), in the luminosity-redshift plane.	49
4.6	Comparison of our full sample (black stars) with the medium <i>XMM-Newton</i> sample of Corral et al. (2008) (XMS+XWAS, red triangles), in the luminosity-redshift plane. For clarity, we omitted one XMS+XWAS source at $z = 2.34$, $L = 1.28 \times 10^{47} \text{erg s}^{-1}$	49
4.7	Distribution of the unabsorbed (red triangles) and absorbed (black diamonds) subsamples (see Sect. 2.3) in the luminosity-redshift plane.	49
4.8	Distribution of the $L - z$ subsamples (see text) in the luminosity-redshift plane. The dividing point is $z = 0.76$, $L = 1.435 \times 10^{44} \text{erg s}^{-1}$ (marked by the horizontal and vertical solid lines). The three blue stars mark the sources that allow defining distinct $L - z$ subsamples (see text).	50
4.9	Average observed spectrum of the full sample fitted with a powerlaw between 2 and 5 keV.	51
4.10	Average observed spectrum of the full sample (data points) with the average simulated continuum (continuous line) and the one-sigma confidence limits (dashed lines).	51
4.11	Average observed spectra (data points) of the absorbed (left) and unabsorbed (right) subsample with their average simulated continua (continuous line) and the one-sigma confidence limits (dashed lines).	52
4.12	Average observed spectra (data points) of the high- z (left) and low- z (right) subsamples with their average simulated continua (continuous line) and the one-sigma confidence limits (dashed lines).	52
4.13	Average observed spectra (data points) of the high- L (right) and low- L (left) subsamples with their average simulated continua (continuous line) and the one-sigma confidence limits (dashed lines).	52
4.14	Average observed spectra (data points) of the $L - z$ subsamples with their average simulated continua (continuous line) and the one-sigma confidence limits (dashed lines). For comparison, in the bottom-left panel we represent with a dotted line the result of adding to the simulated continuum a Gaussian centred at 6.4 keV, with $\sigma=120 \text{eV}$, as obtained from the simulations of the Fe line (Sect. 3.3).	53
4.15	Fit of the average spectrum of the full sample using the simulated continuum model + Gaussian (with free σ and free centroid energy)	58
4.16	Fit of the average spectrum of the absorbed (left) and unabsorbed (right) subsamples using the simulated continuum model + Gaussian (with free σ and free centroid energy)	58
4.17	Fit of the average spectrum of the low-luminosity (left) and high-luminosity (right) subsamples using the simulated continuum model + Gaussian (with free σ and free centroid energy)	58
4.18	Fit of the average spectrum of the low-redshift (left) and high-redshift (right) subsamples using the simulated continuum model + Gaussian (with free σ and free centroid energy)	59

4.19	Fit of the average spectrum of the $L - z$ subsamples (low L -low z subsamples in the left panels, low L - high z subsamples in the right bottom panel, high L -high z subsample in the right top panel) using the simulated continuum model + Gaussian (with free σ and free centroid energy)	59
4.20	Dependence of unresolved 6.4 keV Fe line equivalent width on the average luminosity (left) and the average redshift (right) of the subsamples (first row of 4.3). Squares: $L - z$ subsamples; circles: redshift subsamples; triangles: luminosity subsamples. We represent upper limits by a down-pointing arrow. Each set of points with the same symbol are statistically independent, but not between the symbols.	60
5.1	Spectral SNR between 2-12 keV of the full sample	66
5.2	Redshift distribution of the full sample	66
5.3	Distribution in Luminosity-redshift our full sample (red circles) and of the <i>Chandra</i> Deep Field South spectra (crosses) by Falocco et al. (2012)	66
5.4	Distribution in Luminosity-redshift of our absorbed (crosses) and unabsorbed (full circles) sub-samples	69
5.5	Average observed spectrum with its simulated continuum and the one sigma confidence line. Full sample (top panel), absorbed subsample (middle panel), unabsorbed subsample (bottom panel).	70
5.6	Average observed spectrum with its simulated continuum and the one sigma confidence line. From top to bottom: low- z subsample (top panel), middle- z subsample (middle panel), high- z subsample (bottom panel).	71
5.7	Average observed spectrum with its simulated continuum and the one sigma confidence line. Low- L subsample (top panel), middle- L subsample (middle panel), high- L subsample (bottom panel).	72
5.8	Unresolved line simulated at 6.4 keV for the full sample.	73
5.9	Fits results with the basic continuum and with 'free-free'. Full sample (top panel), absorbed (middle panel) and unabsorbed sample (bottom panel)	77
5.10	Fits results with the basic continuum and with 'free-free': low- z subsample (top panel), middle- z subsample (middle panel). The fit using 'fix-fix' is represented for the high- z subsample (bottom panel).	78
5.11	Fits results with the basic continuum and with 'free-free': low- L subsample (top panel), middle- L subsample (middle panel), high- L subsample (bottom panel).	79
5.12	Fits results with the complex model (top panel), with the <code>diskline</code> (fixed in the middle panel, free in the bottom panel). Full sample	84
5.13	Complex models with <code>diskline</code> : model with fixed <code>diskline</code> parameters (left panel); model obtained with free <code>diskline</code> parameters (right panel). Full sample	86
5.14	Fits with the complex model plus <code>diskline</code> with fixed parameters (top panel), with the complex model plus <code>diskline</code> with free parameters (middle-panel) and model found in this second case (bottom panel). Abs sample	87
5.15	Fits with the complex model plus <code>diskline</code> with fixed parameters (top panel), with the complex model plus <code>diskline</code> with free parameters (middle-panel) and model found in this second case (bottom panel). Unabs sample	88
5.16	Fits with the complex model plus <code>diskline</code> with fixed parameters (top panel), with the complex model plus <code>diskline</code> with free parameters (middle-panel) and model found in this second case (bottom panel). Low- L sample	89
5.17	Fits with the complex model plus <code>diskline</code> with fixed parameters (top panel), with the complex model plus <code>diskline</code> with free parameters (middle-panel) and model found in this second case (bottom panel). Mid- L sample	90

5.18	Fits with the complex model plus diskline with fixed parameters (top panel), with the complex model plus diskline with free parameters (middle-panel) and model found in this second case (bottom panel). High-L sample	91
5.19	Fits with the complex model plus diskline with fixed parameters (top panel), with the complex model plus diskline with free parameters (middle-panel) and model found in this second case (bottom panel). Low-z sample	92
5.20	Fits with the complex model plus diskline with fixed parameters (top panel), with the complex model plus diskline with free parameters (middle-panel) and model found in this second case (bottom panel). Mid-z sample	93
5.21	Fits with the complex model plus diskline with fixed parameters (top panel), with the complex model plus diskline with free parameters (middle-panel) and model found in this second case (bottom panel). High-z sample	94
6.1	Distribution of VCV sample (blue crosses) and XMM CDFS sample (red circles) in the parameter space	98
6.2	Fraction of sources with a given intrinsic N_{H} in 10^{22}cm^{-2} in the VCV catalogue (red hystogram) and in the CDFS catalogue (blue hystogram)	98
6.3	Average spectrum of the VCV full (top panel), absorbed (middle panel), unabsorbed sample (bottom panel) with their simulated continua	100
6.4	Average spectrum of the VCV unabsorbed sample fitted with the complex model (top panel), the complex model with the fixed diskline (middle panel), the complex model with the free diskline (bottom panel)	102
6.5	Complex model with the fixed diskline (top panel), complex model with the free diskline (bottom panel)	103
B.1	Average observed spectra of the background in rest-frame	118
B.2	Average observed spectra of the background in rest-frame	118
B.3	Average observed spectra of the background in rest-frame	119
B.4	Average observed spectra of in observed-frame	119
B.5	Average observed spectra in observed-frame	120
B.6	Average observed spectra in observed-frame	120
C.1	Comparison, for a simulated ‘‘average’’ source, between the input model (dashed blue line) and the unfolded spectra using the best fit (green circles), using $\Gamma = 2$ (red plus), using $\Gamma = 0$ (continuous black line).	122
C.2	Comparison, for a simulated absorbed source, between: the input model (dashed blue line) and the spectra using the best fit (green circles), using $\Gamma = 2$ (red plus), using $\Gamma = 0$ (continuous black line)	122
C.3	Comparison between the average spectra after having corrected for the detector response using: the best fit (average observed spectrum represented by red full circles, simulated continuum by a dashed line) and with the powerlaw with $\Gamma = 2$ (average observed spectrum represented by black stars, simulated continuum by a black continuous line). Sample with the sources with more than 200 net counts.	123

List of Tables

4.1	Properties of the <i>Chandra</i> full sample and the subsamples. Columns: (1) (Sub)Sample; (2) Number of sources; (3) number of net counts in 2-12 keV rest-frame; (4) number of net counts in 5-8 keV rest frame; (5) average redshift; (6) average rest-frame 2-10 keV luminosity in units of 10^{43} erg s^{-1} , from the fits to the single spectra, corrected for Galactic and intrinsic absorption; (7) average intrinsic column density in 10^{22} cm^{-2} *; (8) gamma from the fit of the average observed spectrum with a powerlaw between 2 and 5 keV (rest-frame); (9) χ^2/dof of the fit of the average observed spectrum with a powerlaw between 2 and 5 keV (rest-frame); (10) slope of the powerlaw of the average spectrum obtained with the simulations of the Fe line fitted with <code>pow+gauss</code> ; the errors estimated are always ~ 0.001 ; (11) width obtained in those line simulations; (12) line EW obtained from those simulations.	46
4.2	Significance of the Fe line estimated from the fraction of simulations that have fluxes in the corresponding bands higher than the average spectra of the full sample and the subsamples.	54
4.3	Results of fits of the average spectrum of the full sample and its subsamples. L_{43} : luminosity in units of 10^{43} erg s^{-1} . Columns: (1) sample; (2) χ^2/dof of the fit with simulated continuum model; (3) χ^2/dof of the fit with the same continuum and the Gaussian; (4) probability $P(\Delta\chi^2, \Delta\nu)s, g$ (of adding the Gaussian to the model, see text); (5) probability $P(\Delta\chi^2, \Delta\nu)g, g_0$ (of leaving the parameter of the Gaussian free, see text); (6) central energy of the Gaussian; (7) σ after subtracting resolution obtained in the simulations of the Fe line; (8) EW of the Gaussian; (9) average redshift of the sample; (10) average luminosity of the sample in (10^{43}) erg s^{-1} ; (11) average column density of the sample in $10^{22}cm^{-2}$	64
5.1	Properties of the full sample with $SNR > 15$ and its sub-samples. Columns: (1) (Sub)Sample; (2) Number of sources; (3) number of net counts in 2-12 keV rest-frame; (4) number of net counts in 5-8 keV rest frame; (5) average redshift; (6) Average of the logarithm of the rest-frame 2-10 keV luminosity in units of 10^{43} erg s^{-1} , from the fits to each spectrum (see text), corrected for Galactic and intrinsic absorption; (7) average intrinsic column density from the fits to each spectrum (see text); (8) average SNR of the (sub)sample between 2-12 keV rest-frame; (9) slope of the dependence $\sigma \propto E^{-\alpha}$ of the effective energy resolution of our method (see Chapter 3); (10) sigma at 6 keV of the effective energy resolution of our method at 6 keV (see Sect. 3.3)	67
5.2	Model independent significance of the iron line estimated in several bandwidths using the simulations (as the fraction of simulations with a lower flux than the flux of the average observed spectrum, see text). The bandwidths are expressed in keV.	74
5.3	Median of the EW calculated in different energy ranges using the simulations. The symmetrical errors are calculated using the error propagation, the non-symmetrical errors correspond to the 1 sigma percentils of the simulations. The range is expressed in keV and the EW in eV.	74

- 5.4 Results of fits of the average spectrum of the full sample and its subsamples with the basic continuum and the gaussian centered at 6.4 keV: `gsmooth*(pha*pow+gauss)`. L : luminosity in erg s^{-1} . Columns: (1) sample; (2) χ^2/dof of the fit with the basic continuum model; (3) χ^2/dof of the fit with the same continuum and the Gaussian; (4) probability $P(\Delta\chi^2, \Delta\nu)$, s , g (of adding the Gaussian to the continuum model and of leaving the parameter free to vary, see text); (5) intrinsic column density estimated in the fits; (6) slope of the powerlaw; (7) central energy of the Gaussian; (8) σ of the gaussian; (9) EW of the Gaussian; (10) average redshift of the sample; (11) average of the logarithmic luminosities in erg s^{-1} from the fits of the single sources after the correction for Galactic and intrinsic absorption (see text); (12) average of the column densities from the fits to the single sources in 10^{22}cm^{-2} 80
- 5.5 Results of fits of the average spectrum of the full sample and its subsamples using `gsmo*(pha*pow+diskline)` and `gsmo*(pha*pow+diskline+gauss)`. Columns: (1) sample; (2) χ^2/dof of the fit with disk-fix in the first line of each sample, disk-free in the second one, disk-fix-na in the third one, disk-free-na in the fourth one. (3) Probability of each fit with respect to the fit with the basic continuum. (4) Probability between disk-free and disk-fix (second line), between disk-fix-na and disk-fix (third line), between disk-free-na and disk-free (fourth line). (5) intrinsic column density given by the fits to the average spectra. (6) powerlaw slope. (7) inner radius. (8) emissivity index. (9) inclination angle. (10) diskline EW. (11) central energy of the narrow component. (12) EW of the narrow component 82
- 5.6 Results of fits of the average spectrum of the full sample and its subsamples using the complex model: `gsmo*absori[pha*pow+sum_gauss]` in the first line of each sample; the complex model plus the `diskline` with fixed parameters: `gsmo*absori[pha*(pow+diskline)+sum_gaus]` in the second line; the complex model plus the `diskline` with free parameters in the third line. Columns: (1) sample; (2) χ^2/dof of the fit with the complex model with narrow lines only in the first line of each sample; with the addition of fix `diskline` in the second one, addition of both fix `diskline` and ionised line in the third one, with free `diskline` in the fourth one. (3) Significance of the addition of the `diskline`, in the first line, and significance of leaving its parameters free to vary in the second line. (4)intrinsic column density given by the fits. (5) powerlaw slope. (6) inner radius. (7) emissivity index. (8) inclination angle. (9) `diskline` EW. (10) EW of the narrow gaussian line at 6.4 keV 85
- 6.1 Properties of the VCV full sample and the subsamples. Columns: (1) (Sub)Sample; (2) Number of sources; (3) number of net counts in 2-12 keV rest-frame; (4) number of net counts in 5-8 keV rest frame; (5) average redshift; (6) average rest-frame 2-10 keV luminosity; (7) average intrinsic column density in 10^{22}cm^{-2} * 97

- 6.2 Results of fits of the average spectrum of the full sample and its subsamples using the complex model ($\text{gsmo*absori}(\text{pha*pow}+\sum\text{gaus})$) in the first line of each sample; the complex model plus the `diskline` with fix parameters $\text{gsmo*absori}[\text{pha}*(\text{pow}+\text{diskline})+\sum\text{gaus}]$ in the second line; the complex model plus the `diskline` with free parameters in the third line. Columns: (1) sample; (2) χ^2/dof of the fit with the complex model with narrow lines only in the first line of each sample; with the addition of fix `diskline` in the second one, addition of both fix `diskline` and ionized line in the third one, with free `diskline` in the fourth one. (3) Significance of the addition of the `diskline`, in the first line, and significance of leaving its parameters free to vary in the second line. (4)intrinsic column density given by the fits. (5) powerlaw slope. (6) inner radius. (7) emissivity index. (8) inclination angle. (9) `diskline` EW. (10) Narrow gaussian line at 6.4 keV EW.(11) central energy of the ionized component. (12) EW of the ionized component 104
- A.1 Properties of the sample composed of all the sources with more than 50 counts. L_{43} : luminosity in units of $10^{43} \text{ erg s}^{-1}$. Columns: (1) (Sub)Sample; (2) Number of sources; (3) Number of counts in 2 -12 keV; (4) Number of counts in 5-8 keV; (5) average redshift; (6) average luminosity in $10^{43} \text{ erg s}^{-1}$; (7) average column density of the local absorber in 10^{22} cm^{-2} ; (8) model-independent significance of the Fe line (calculation made between between 6.2 and 6.6 keV). 112
- A.2 Comparison between fluxes of real and simulated spectra in the total sample with more than 50 counts in each spectrum. F_{simu} : flux of the average simulated spectrum (units of normalized flux per keV); F_{real} : flux of the average observed spectrum; $\frac{N_{<\text{real}}}{N_{\text{simu}}}$ is the percentage of simulations having lower flux than the observed spectrum. Calculation is performed between 6.3 and 6.5 (1); 6.2 and 6.6 keV (2); between 6.0 and 6.8 keV (3) 112
- A.3 Properties of the sample composed of all the sources with more than 100 counts. L_{43} : luminosity in units of $10^{43} \text{ erg s}^{-1}$. Columns: (1) (Sub)Sample; (2) Number of sources; (3) Number of counts in 2 -12 keV; (4) Number of counts in 5-8 keV; (5) average redshift; (6) average luminosity in $10^{43} \text{ erg s}^{-1}$; (7) average column density of the local absorber in 10^{22} cm^{-2} ; (8) significance of the Fe line calculated as the number of average simulated spectra with a lower flux than the flux of the average observed spectrum (calculation between 6.2 and 6.6 keV). 113
- A.4 Comparison between fluxes of real and simulated spectra in the total sample with more than 100 counts in each spectrum 113
- A.5 Sample composed by all the sources with more than **50** net counts in 2 - 12 keV. (1) sample; (2) photon index of the powerlaw; (3) χ^2 of the fitting with the powerlaw; (4) χ^2 of the fitting with table model; (5) χ^2 of the fitting with table model plus gaussian; (6) significance of adding the gaussian to the table model; (7) gaussian centroid; (8) gaussian width; (9) EW of the gaussian; (10) average redshift; (11) average luminosity; (12) average column density of the absorber; *: indicates that it was not possible to calculate errors because `Xspec` gives un-physical values and `steppar` gives a constant $\Delta\chi^2 < 2.71$ for high sigma ($> 1\text{keV}$) 114
- A.6 Sample composed by all the sources with more than **100** net counts in 2-12 keV. (1) sample; (2) photon index of the powerlaw; (3) χ^2 of the fitting with the powerlaw; (4) χ^2 of the fitting with table model; (5) χ^2 of the fitting with table model plus gaussian; (6) significance of adding the gaussian to the table model; (7) gaussian centroid; (8) gaussian width; (9) EW of the gaussian; (10) average redshift; (11) average luminosity; (12) average column density of the absorber; * impossible to calculate the error; with `steppar` we get a $\Delta\chi^2$ lower than 2.7 115

Chapter 1

Introduction

Active Galactic Nuclei (AGN) are the most luminous persistent objects in the Universe.

The variability of the sources have been studied to probe that the emission comes from extremely compact regions, where huge masses are involved, in the AGN, ranging from 10^5 to 10^9 solar masses (Kaspi et al. 2000; Peterson and Horne 2004).

It is now broadly accepted by the scientific community that the central mechanism producing such huge luminosities (above 10^{42} erg/s) is accretion around a Super Massive Black Hole (SMBH). In fact, the luminosity emitted during accretion is:

$$L = \mu \dot{M} c^2$$

where \dot{M} is the accretion rate and μ is the efficiency of extraction of gravitational energy from material which accretes around a gravitating body, and it is formally defined as:

$$\mu = \frac{R_g}{R}$$

where R_g is the Gravitational radius ($R_g = \frac{GM}{c^2}$). To produce the huge AGN luminosities, efficiency should range from about 0.1 to 0.4. Just for comparison, if thermonuclear processes of conversion of Hydrogen into Helium are considered, the ones powering the stars in the main sequence, the efficiencies are 0.007, only about one twentieth of the huge power emitted by the AGN.

Accretion is the only mechanism which can yield sufficient emissivity. For example, values for μ for accretion around a neutron star are around 0.1. The main difference between accretion around a neutron star and around a black hole (BH) is that BH have no impact surface. In neutron stars, this is where where the conversion of gravitational potential energy in luminosity occurs.

In BH, the 'surface' is made by a centrifugal barrier, given by the fact that the kinetic energy (that changes as r^{-2}) grows more rapidly with decreasing radii than the gravitational energy (r^{-1}). Accreting matter is not allowed to arrive to $r=0$, but can collapse in direction of its angular momentum, forming an accretion disk. In the accretion disk, viscosity is a key parameter to understand the emission in the AGN. In fact, while allowing the transfer of angular momentum outward, it dissipates energy, converting gravitational potential in radiation. The disk persists down to the last stable orbit (from $6R_g$ to $1.23R_g$ depending on the BH spin, as we will see below). When matter arrives to the radius corresponding to this orbit, inside it the emission processes are no longer efficient, and the exact physical processes at work are not well known.

1.1 The Unified Model of the Active Galactic Nuclei

Observationally, AGN are defined as galactic nuclei which display strong bolometric luminosities ($L > 10^{42}$ erg/s). Moreover, they are characterised by a multi-wavelength emission, which probes the morphology of the central engine. Using the multiwavelength emission of AGN and the analysis of their spectral energy distribution (SED), a unified model of AGN, able to describe the morphology of their central engine, has been developed. Such model connects different classes, defined on an observational basis, by proposing that they are instead a single type of objects observed under different conditions. The main properties of the AGN SEDs can be summarised as follows:

- **The radio emission:** The majority (80-90 %) of AGN are radio quiet, and do not possess radio powerful components.

The radio emission of AGN represents a low percentage of their bolometric emission. It assumes the shape of an extremely flat powerlaw, and it has a high degree of polarisation. These characteristics are typical of a synchrotron emission that, according to the current interpretation, comes from compact jets.

There seems to be a dichotomy, on the basis of the radio luminosity, between radio loud sources and radio quiet AGN. Radio loud AGN possess opposite-side jets of plasma, that are produced close to the central SMBH and propagate outward at relativistic velocities, up to distances of about $10^5 - 10^6$ pc. The primary processes at the bases of the jet emission are not fully understood yet, but it seems that they are emitted by the inner accretion disk and they are accelerated and collimated by magneto hydrodynamic processes.

In some cases, one of the jets is directed in our direction: in these sources, called blazars, relativistic beaming enhances the jet emission, making it difficult to observe any other emission from the AGN. Such sources are more commonly found in the nearby Universe.

- **The IR:** The Spectral Energy Distributions (SED) of AGN are characterised by a maximum in IR wavelengths, and a minimum around $1 \mu\text{m}$. The interpretation of these properties is that AGN

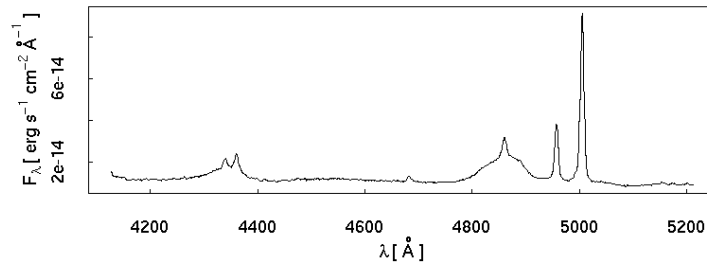


FIGURE 1.1: Type 1 AGN NGC5548 (Ho et al. 1995)

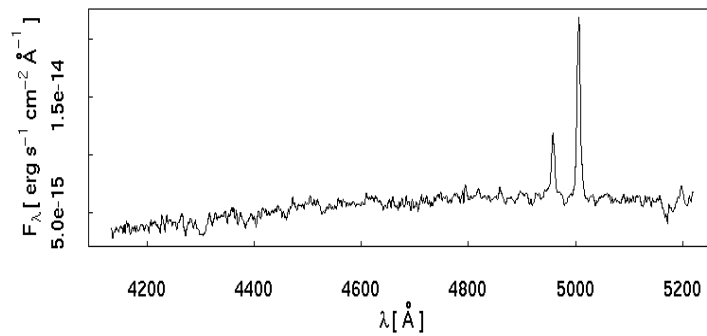


FIGURE 1.2: Type 2 AGN NGC1667 (Ho et al. 1995)

display a thermal emission in this band, coming from heated dust. In this scenario, the primary radiation coming from the nuclear region illuminates dusty material with axial symmetry, with high opacity. This material heats up and emits the detected thermal radiation

- **The optical-UV continuum emission:** In the SED of AGN it is often possible to observe a peak in the optical-UV, corresponding to temperatures of 10000 K. To understand the origin of this feature, it is necessary to invoke the commonly accepted model of accretion disk (N. I. Shakura and R. A. Sunyaev 1974). According to the model, matter spirals around the SMBH forming a geometrically thin, optically thick accretion disk (N. I. Shakura and R. A. Sunyaev 1974). In this scenario, accretion is the main process of emission of the high luminosities detected in the AGN. Each annulus of the accretion disk emits as a black body, its temperatures depending on the distance from the SMBH: the convolution of the emission at each annulus assumes the shape of the bump often observed in the AGN spectra at around 10000 K.

Optical spectroscopy of AGN suggests a classification in two broad categories. AGN spectra show commonly, forbidden narrow (~ 100 km/s) lines. The permitted lines, instead, can have two components: the broad (~ 10000 km/s) one and the narrow (~ 100 km/s) one. Objects showing only broad components or both are called type 1 AGN. We can see in Fig. 1.1 an example of such kind of spectra: the optical spectrum of NGC 5548 (Ho et al. 1995). Those showing only narrow components to their permitted lines are called type 2 AGN. An example is NGC 1667, in Fig. 1.2.

Depending on the relative emission of the narrow and broad components, intermediate types are also defined (Osterbrock 1978).

The different shapes of the emission lines can be interpreted considering the line width as an effect of the movement of the emitting clouds. In this scenario, the broad lines are emitted in a region close to the central nucleus, called Broad Line Region ; the narrow lines are instead produced in an outer region, called Narrow Line Region.

The studies of the broad optical lines in type 1 AGN have permitted so far to obtain the estimation of the BH masses, using reverberation mapping. This method allows the measurement of the size of the BLR through monitoring the light-travel time delayed response of the emission lines to continuum variations (Blandford and McKee 1982). The mass is derived by the virial theorem as $M = \frac{r\sigma^2}{G}$ where σ is measured from the width of the broad lines (generally from the H_β line).

Although spectroscopy seems to suggest a dichotomy, the lack of broad lines in the type 2 AGN has been proved to be just an orientation effect: in type 2 AGN, the torus does not allow to detect the BLR, that is instead detected in type 1 AGN. This model, presented for the first time by Osterbrock (1978), still needs an additional component to explain the full suppression of broad lines, and the only partial suppression of the optical continuum. An additional component, composed by diffusion material, likely free electrons located above and below the torus, has been introduced, after having been confirmed by spectropolarimetric studies of obscured AGN in the local Universe (Antonucci and Miller 1985). In these studies, analysing in particular the obscured AGN NGC1068, a high polarisation level was found in the continuum. Moreover, the optical polarised spectrum of NGC1068 showed the presence of broad lines, similar to the ones observed in the type 1 AGN. We can see in the Fig. 1.3 a schematic picture of the morphology of the AGN: a toroidal structure that extends from 1 to 100 pc, obscures the BLR emission for high inclination angles. This structure contains dust and cold gas, and is likely not homogeneous (Antonucci and Miller 1985).

In the Fig. 1.3, we can see the BLR, where the broad (10000-30000 km/s) permitted lines come from: the absence of forbidden lines in these regions allows to predict their density, higher than 10^8cm^{-3} . The extension is constrained by reverberation mapping studies, and it is between 0.01 and 0.1 pc.

The figure shows, outside the torus, the NLR, the place where narrow (<1500 km/s) lines come from, the forbidden line emission have place in low density gas (between 10^3 and 10^6cm^{-3}). It is extended at distances higher that 100 pc from the central nucleus.

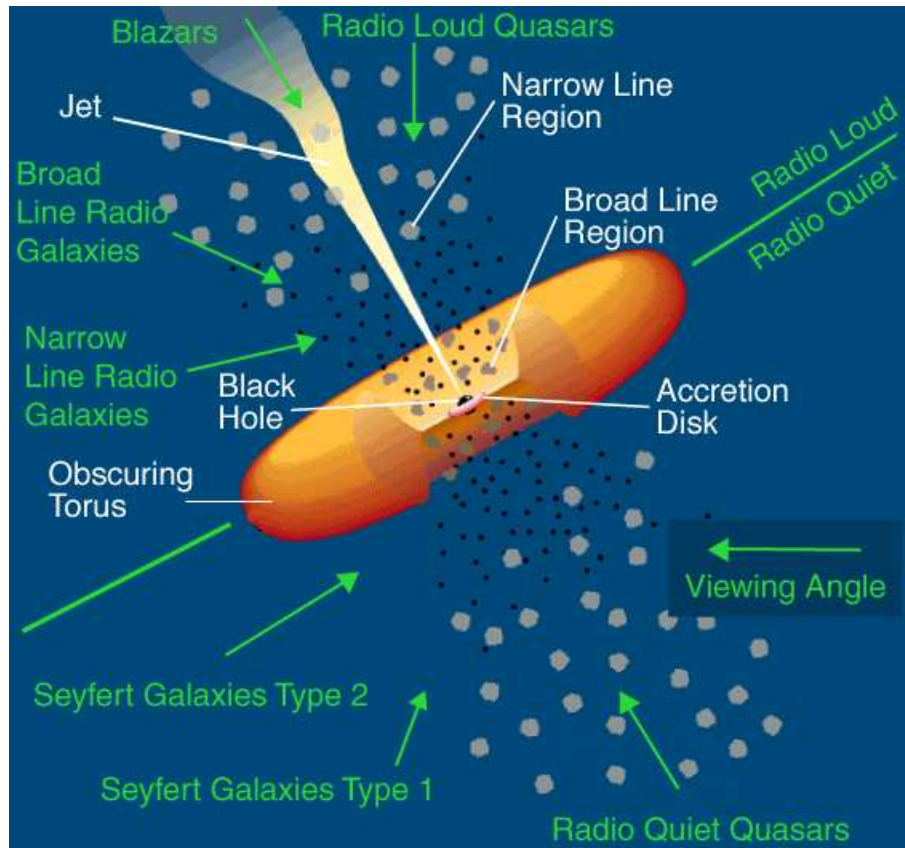


FIGURE 1.3: Unified model of the AGN

In some cases, we can see, in direction perpendicular to the plane of the torus, a jet emission, the responsible of the radio emission in Radio Loud AGN and of acceleration of particles along the poles of the disk.

The unified model works perfectly in the majority of the cases but recently, some counterexamples have been found: Corral et al. (2005), Bianchi et al. (2008), Panessa et al. (2009). Such cases suggest that the inclination might not be the only parameter to describe such systems.

1.2 The X-ray emission of AGN

The X-ray emission of the AGN probes the innermost regions of the central engine, as it does not strongly interact with the outer: X-rays, due to their small wavelength, are relatively penetrating.

In this section, the X-ray properties of AGN are discussed in detail, considering the main X-ray spectral components of AGN shown in Fig. 1.4.

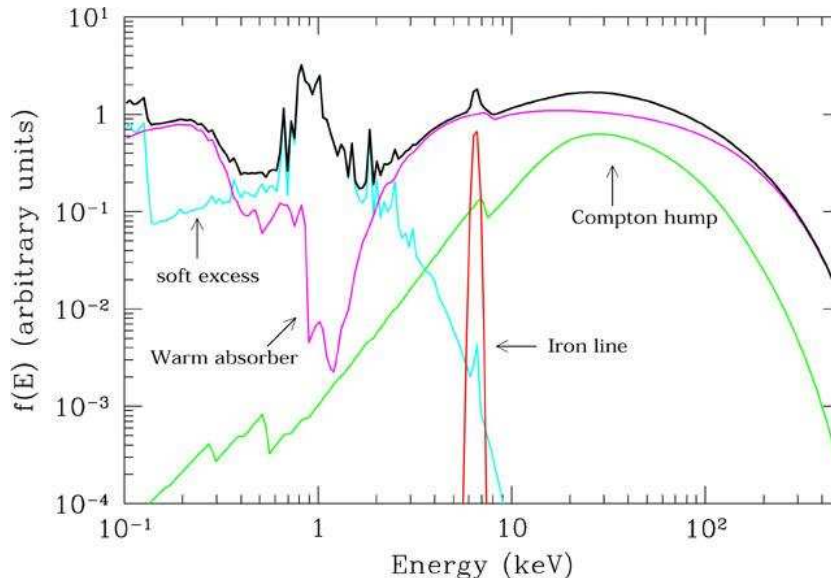


FIGURE 1.4: Typical X-ray spectrum (thick black line) and its main components (coloured lines) of a type 1 AGN (Risaliti and Elvis 2004).

1.2.1 The primary X-ray emission of AGN

Accreting black hole systems often exhibit power law components to their spectra which extend to hard X-ray energies. The broad band continuum cannot be interpreted as directly emitted from the accretion disk, because, according to the standard model, the disk produces a relatively soft, thermal spectrum (dominated by optical-UV radiation in AGN). A likely mechanism producing the powerlaw is instead inverse Compton scattering of the primary photons of the disk (Haardt and Maraschi 1991).

The process is thought to have place in a hot plasma, the so-called 'X-ray corona', that is likely bound by the magnetic fields very close to the central BH. While the presence of this corona is broadly accepted to interpret the X-ray continuum, there are still some uncertainties in applying the coronal models to black hole systems. In fact, the heating mechanism is still unknown: several models have been proposed to describe its geometry but none of them is fully satisfactory. Anyway, the second and third geometries shown in Fig. 1.5 seem to be the most commonly invoked.

1.3 The X-ray reprocessing

The primary X-ray powerlaw can be reprocessed through several mechanisms, depending on the physical state of the material (density, ionisation, etc.) and on the photon energy. The mechanisms of interaction between the primary continuum are generally called reprocessing and include scattering and fluorescence.

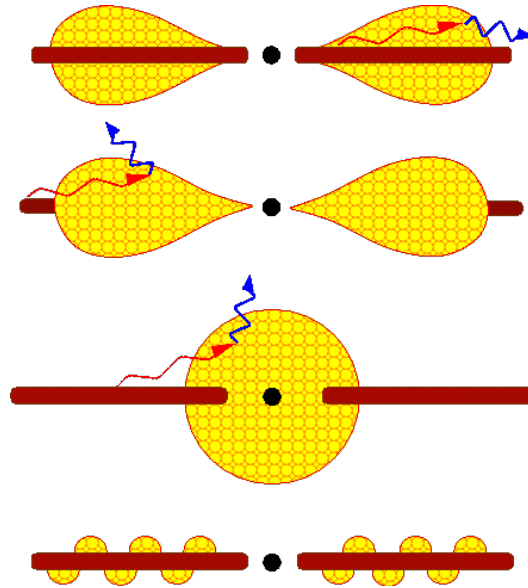


FIGURE 1.5: Coronal models. Several geometries for the configuration of the plasma

Fluorescence on the accretion disk can imprint unique features on the X-ray spectra of AGN, like emission lines. For this reason, X-ray spectroscopy of AGN has represented so far the most direct probe of their innermost regions. To understand the origin of such features it is worth to consider both reflection from a neutral material (called 'cold reflection') and from an ionised material (called 'warm reflection').

1.3.1 Reflection by neutral material

The simplest reflection model is composed by a semi-infinite slab of gas with uniform density, irradiated from above by a continuum X-ray spectrum (produced in the corona by inverse Compton scattering). Moreover, we can assume that metals are all neutral, while hydrogen and helium are fully ionised. We call this configuration a 'cold' reflection.

There are two possible interactions between an incoming photon and the matter inside the disk. In the first possibility, the incoming photon can be Compton scattered in the disk, due to the presence of electrons associated to the ionised hydrogen and helium, or to the outer shell of the other elements. Secondly, the photon can be photoelectrically absorbed by the metals. This process can happen just if the photon possesses a energy higher than the threshold energy for the particular photoelectric transition. The relative probabilities of Compton scattering and photoelectric absorption are given by the cross sections of the processes. At low energies, the photoelectric absorption, due to its higher cross sections, is dominant.

The most probable photoelectric transitions, with the largest cross-sections, are associated with the photo-ejection of a K-shell electron. After the K-shell photoionisation, the ion stays in an excited

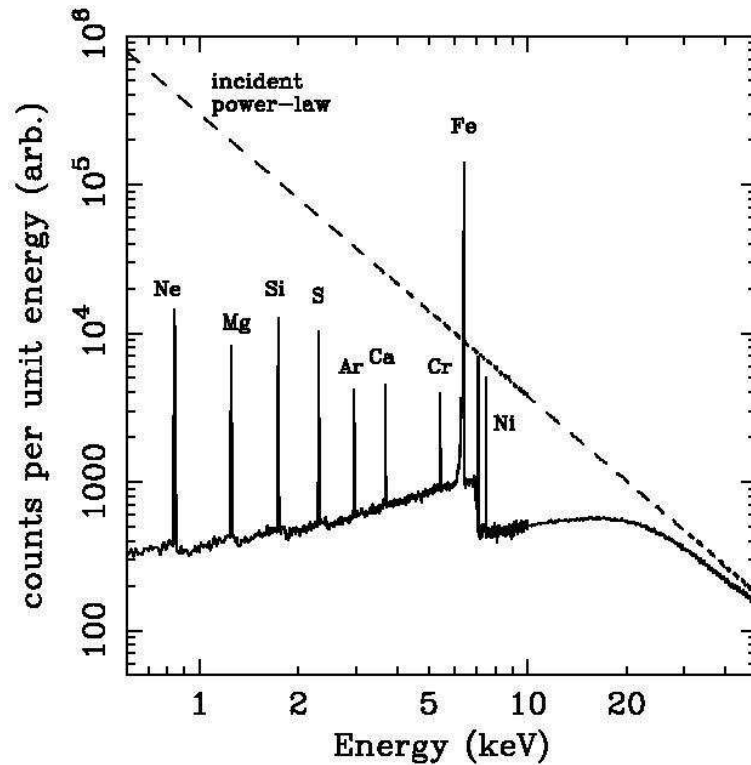


FIGURE 1.6: Simulated reflection spectrum of an incident power-law in the cold reflection regime (Reynolds et al. 1995)

energy level, and the L-shell electron drops into the K-shell. After this process, the de-excitation can occur in two ways. The first one is fluorescence: the excess energy is radiated emitting a K_{α} photon. Actually, the K_{α} is a doublet, composed by $K_{\alpha 1}$ and $K_{\alpha 2}$, but the energy difference between the two centroid energies is a few eV, lower than the spectral resolution of the current X-ray detectors. For this reason, we will call this K_{α} , as a single line, ignoring its inner structure.

An alternative way to emit the excess of energy is the ejection of an L-shell electron, called Auger effect.

We can see in Fig. 1.6 the results of a Monte Carlo simulation of the reflection of an incident power law X-ray spectrum by a cold accretion disk (Reynolds et al. 1995). In this calculation, cosmic abundances were assumed. At low energies, photoionisation is the dominant process because its cross section is large. On the contrary, at high energies, the majority of the incoming X-ray photons are Compton-scattered, producing the '*Compton reflection Hump*' peaking at about 30 keV: this happens because the photoelectric cross section falls to small values and the dominant process is the Compton scattering.

An useful quantity that indicates the intensity of an emission line is its equivalent width: it is defined as the energy interval over which the continuum radiation contains a flux equal to the flux emitted in the line:

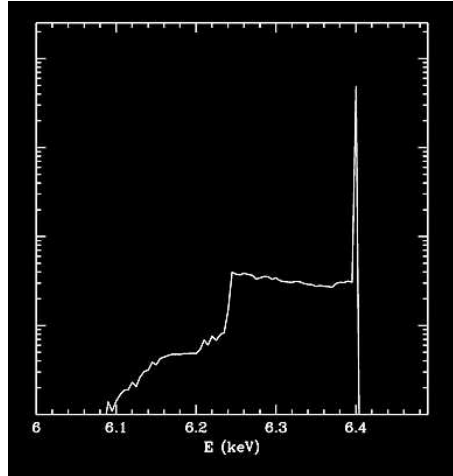


FIGURE 1.7: Expected profile of the iron line considering the effect of the Compton Shoulder (Matt 2002)

$$EW = \int_{E-\Delta}^{E+\Delta} 2dE \frac{T(E) - C(E)}{C(E)} \quad (1.1)$$

where $T(E)$ is the total spectrum (continuum plus line), the $C(E)$ refers to the continuum, the integral is performed in the region where the iron line is found and Δ is a quantity broader than the line σ .

There are several emission lines in the photoelectric absorption dominated regime. Their intensities are determined by the probability of the elements to de-excite via fluorescence rather than Auger effect: this probability is called fluorescent yield.

Due to its fluorescence yield and to its large cosmic abundance, iron emits the most prominent line: the K_{α} line at 6.4 keV. The dependence of the iron line EW on the abundance of the iron has been studied by Matt et al. (1997), and it depends on the abundance of iron and on the inclination angle of the reflecting material.

The bulk of the iron lines emitted in neutral matter consists of a narrow core, corresponding to the line photons that emerge, without being scattered, from the emitting region. The scattering of the line photons can produce a feature called Compton Shoulder (fig 1.7). This feature corresponds to the line photons emerging after one or more scatterings. Thanks to the improved sensitivity and instrumental resolution of the current X-ray detectors such as *Chandra* and *XMM-Newton*, it is possible to detect at least the first order Compton Shoulder (Matt 2002).

In high quality spectra, (Matt et al. 2004), several fluorescent lines have been observed, such as the Fe K_{α} , Fe K_{β} , Ni K_{α} and Ni K_{β} . The detection of such set of lines has been possible in absorbed sources because the suppression of the continuum makes the line emerge above it.

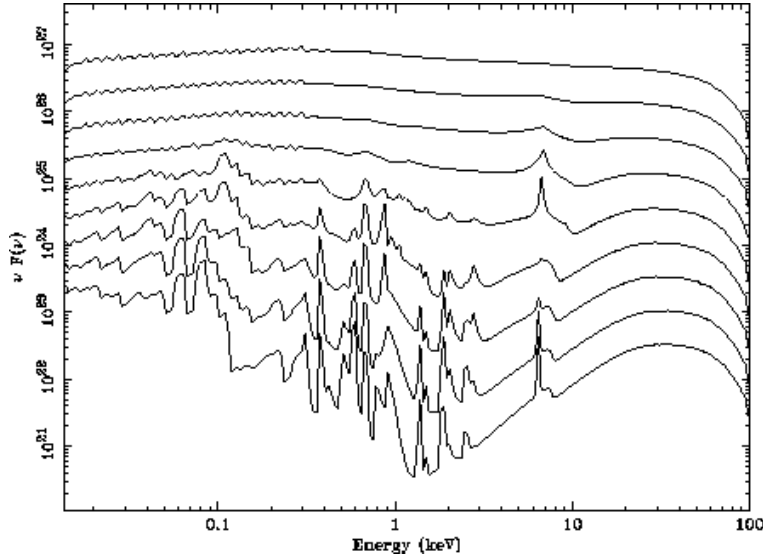


FIGURE 1.8: Ionised reflection spectra for different ionisation parameters, from the theoretical prediction of Ballantyne et al. (2001) using constant density models.

1.3.2 Reflection by ionised material

In a real physical situation, the reflection is more complex than in the theoretical 'cold' reflection model. A useful quantity in the discussion of this model is the ionisation parameter, that measures the fraction between the photoionisation rate (proportional to $n(r)$) and the recombination rate (proportional to $n^2(r)$). It is defined as:

$$\psi(r) = \frac{4\pi \cdot F_x(r)}{n(r)}$$

where $F_x(r)$ is the flux received of the disk at each radius, $n(r)$ the electron density as a function of the radius.

The warm reflector introduces lines from ionised atoms to the complex set of fluorescent features that we have discussed in the previous section. The spectral features, according to theoretical predictions using constant density models (Ballantyne et al. 2001), are determined by the values of the parameter ψ (see fig. 1.8).

According to the different values assumed by this parameter, we can define four regimes of behaviour:

- $\psi < 100 \text{ erg cm s}^{-1}$: this is the 'cold' or 'neutral' reflection regime, shown in the previous section.
- $100 < \psi < 500 \text{ erg cm s}^{-1}$: in this 'intermediate ionisation' regime, the iron is found as Fe XVII- Fe XXII and has a vacancy in the L-shell. In this situation, the ion can resonantly absorb

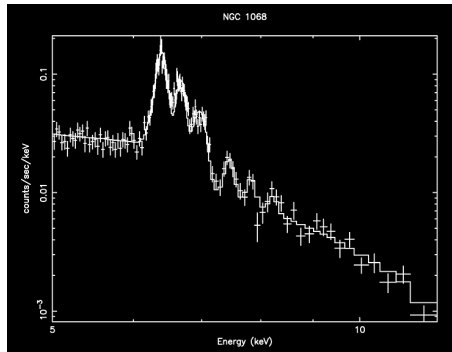


FIGURE 1.9: Spectrum of NGC1068 (Matt et al. 2004)

the K_α photons, that can be again absorbed to produce fluorescence or an Auger electron. This mechanism, called resonant scattering, is repeated until it is terminated by a Auger event. Few line photons can escape from the material, producing a very faint line.

- $500 < \psi < 5000 \text{ erg cm s}^{-1}$: in this 'high ionisation' regime, the ions are too highly ionised to permit the Auger effect. The resonant scattering, for this reason, produces emission lines. The resulting line is the emission of Fe XXV at 6.67 keV and Fe XXVI at 6.97 keV.
- $\psi > 5000 \text{ erg cm s}^{-1}$: in this 'fully ionised regime' there cannot be any atomic signatures, consequently no iron line can be emitted.

The emission lines from iron in different ionisation states have been observed in several spectra (Matt et al. 2004). We can see in Fig. 1.9 the spectrum of the type 2 AGN NGC1068, with the complete set of fluorescent lines, including from ionised material. In such observation the presence of the warm reflector, besides the cold one, was clearly required.

1.4 X-ray obscuration in AGN

X-ray spectra can display absorption features due to absorbing material in the line of sight (see in Fig. 1.11). Such features are due to the presence of absorbing material, such as the torus.

The presence of an obscuring torus around the nucleus can strongly modify the X-ray spectra of both type 1 and type 2 AGN, although its effect can introduce the strongest features mostly in type 2 AGN. The primary continuum will be absorbed by material in the line of sight through photoelectric absorption and/or Compton scattering. For a photon of energy E , the probability of being photoelectrically absorbed by a neutral atom is:

$$P(E) = 1 - e^{-\sigma(E)N_H}$$

where $\sigma(E)$ is the cross section. The spectrum coming out from a primary powerlaw absorbed by neutral material will contain different edges corresponding to the different ionisation potential for each

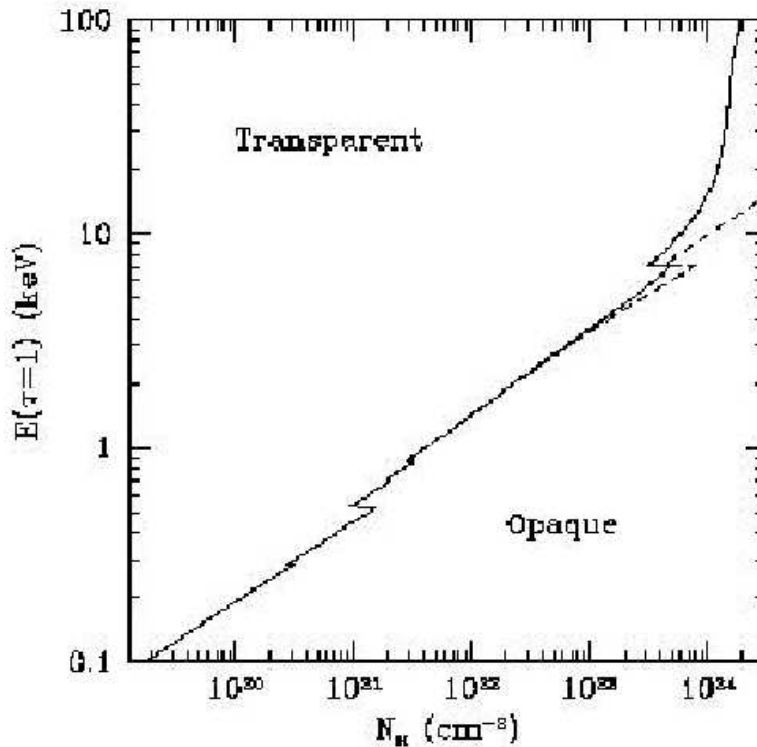


FIGURE 1.10: Transition energies of a material (as a function of its column density N_H) between the transparent and the opaque regime considering photoelectric (dashed line) and the Compton scattering (continuous line)

species in the absorbing material. The cross section depends on the abundance of the elements. In Fig. 1.10 we represent the energy at which the transition between transparent and opaque regimes occurs ($\tau \geq 1$), as a function of the column density (N_H) of the intrinsic absorber. The dashed line in the Fig. 1.10 refers to photo-absorption only, the solid line refers instead to Compton scattering. The two lines coincide for column densities below about 10^{24}cm^{-2} .

The transition between the transparent and the opaque regime considering these two phenomena occurs when the optical depth becomes higher than one. The energy where this transition occurs grows with growing column density of the absorbers, as shown in Fig. 1.10. For logarithmic column densities of 21.5 the spectra are absorbed for $E < 1 \text{ keV}$ and non-absorbed above. The spectral energy from which the absorption features begin to be detected grows for growing column densities.

The Compton scattering cross section differs sensitively from the photo-absorption one for higher $N_H > 10^{24} \text{cm}^{-2}$ values. Sources with such absorbing column densities ($\geq 10^{24.5} \text{cm}^{-2}$) are commonly called Compton Thick. They are strongly absorbed for Compton effect below 10 keV. In such sources, being observed at very high inclination angles, the observed continuum spectra are the result of the

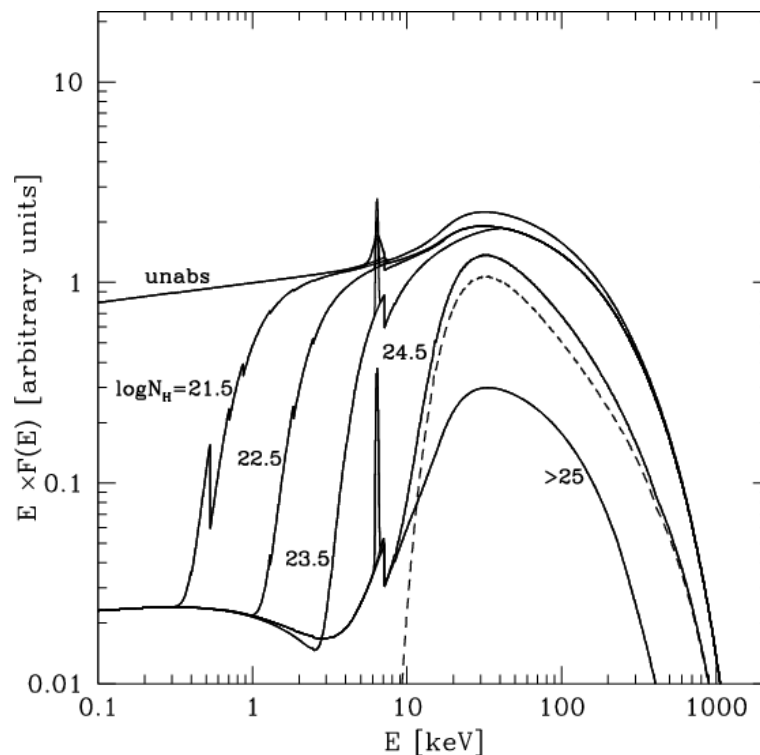


FIGURE 1.11: Absorption in X-rays (Gilli et al. 2007)

reflection in the inner walls of the torus. The narrow fluorescent lines are instead higher, and the resulting iron line EW can be very intense, up to 1 keV.

We can see in Fig. 1.11 the resulting spectra (Gilli et al. 2007) for different column densities. For unabsorbed sources with $N_{\text{H}} \ll 10^{24} \text{cm}^{-2}$, the radiation passing through the torus either escapes or it is absorbed, the scattering is negligible ($\tau \ll 1$), therefore the torus does not contribute significantly to the spectrum. Below 10 keV, spectra are the sum of two components: the radiation transmitted through the torus and the radiation reflected by that part of the torus inner surface that is directly visible to the observer. For $N_{\text{H}} < 10^{24} \text{cm}^{-2}$ the transmitted component dominates, as indicated by the exponential shape of the spectrum.

For $N_{\text{H}} > 10^{24} \text{cm}^{-2}$, when the scattering optical depth is of the order of unity or greater, an important fraction of hard X-rays is Compton-scattered and reflected by the funnel of the torus, while softer photons are photo-absorbed (the Compton scattering and photo-absorption cross-sections are equal at about 10 keV for neutral matter). For intermediate values of N_{H} , the reflected component dominates at energies up to a few keV, while the transmitted part dominates at higher energies, the ratio between the reflected and transmitted spectra depends on the inclination angle.

For $N_{\text{H}} > 10^{26} \text{cm}^{-2}$, when the torus is optically thick to both photo-absorption and scattering, the reflected component, with a power-law spectrum, dominates.

The intensity of the iron line emitted for reflection in the torus is higher for growing column densities (see Fig. 1.11).

It has been proved that the EW is expected to decrease with the decreasing inclination angle (subtended from the perpendicular to the surface of the absorber and the line of sight) of the absorber (Ghisellini et al. 1994).

The expectations were confirmed by Gilli et al. (1999), where an increasing EW with increasing N_{H} was found in an AGN sample observed by *Ginga* and *ASCA*. In that sample, the EWs of type I AGN were lower than those of type II AGN.

If the absorbing material is partially ionised, the absorber pattern depends not only on the abundances of the elements in the obscuring material, but also on its ionisation degree. Such material is commonly called *warm absorber* and is normally partially ionised. Given the energy-dependent cross section, the absorption would preferentially occur at certain energies. For this reason the warm absorber can introduce curved spectra at determined energies, as we can see in Fig. 1.4. When the material is highly ionised (i.e. $\psi \sim 5000$), the feature cannot be detected.

1.5 The iron emission line from the accretion disk

The iron emission line at 6.4 keV, when emitted in the accretion disk, represents an important indicator of accretion around SMBH. At the same time, it is the strongest spectral line and it can be found in the spectra of all types of accreting systems, from binary black holes to neutron star systems and AGN. The iron line has been used so far to probe the innermost regions of the AGN, as well as in binary systems: when they are emitted close to the central SMBH, the observer will detect the effects of relativistic physics in strong gravitational fields.

1.5.1 Expected shape of the iron line in accretion disks

Assuming a geometrically thin, optically thick, keplerian accretion disk, we can parametrise its emissivity as:

$$I(r) = f \cdot r^{-\beta}$$

where f is a constant parameter in the optically thick regime.

The line emission is assumed to be emitted from the radius of marginal stability up to an outer radius within which the disk persists. The outer radius plays an important role for $\beta \ll 2$, because in this case the bulk of the emission comes from the outer regions. On the contrary, the location of the outer radius

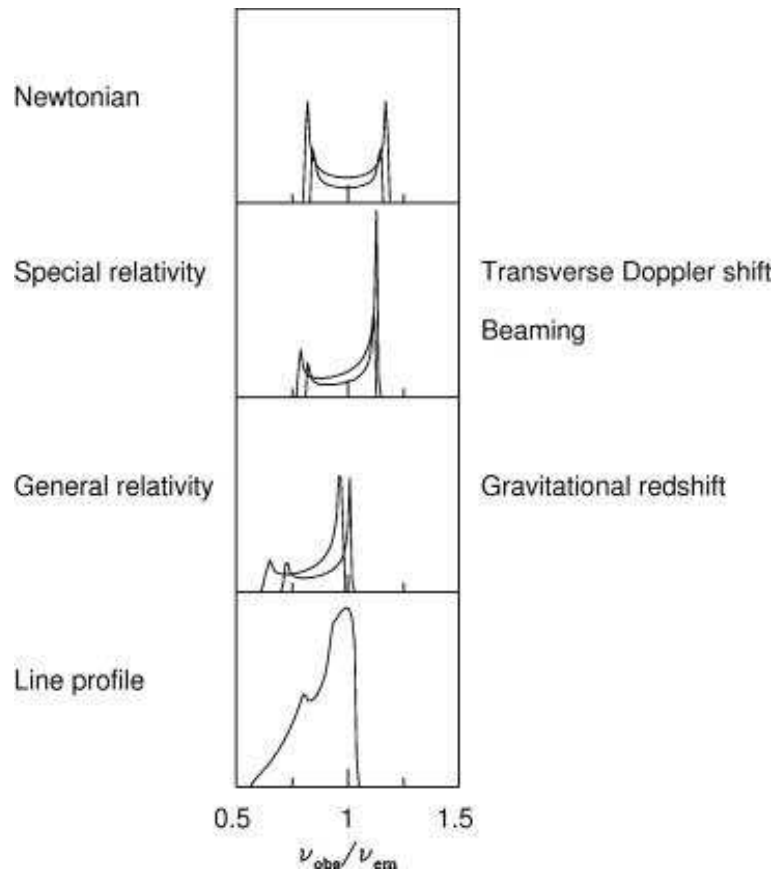


FIGURE 1.12: Iron lines from the innermost regions of the accretion disks (Fabian et al. 2000)

is irrelevant if $\beta \gg 2$, because the majority of the line emission comes from the innermost annuli of the accretion disk.

The line emitted from the accretion disk can be deformed by the effect of its Newtonian rotation and the relativistic physics in the strong gravitational field of the BH. We can see in the first panel of Fig. 1.12 the expected line profile. The double-horned profile is due to the Doppler effect introduced by the keplerian movement of the gas in the accretion disk. The separation of the horns depends on the inclination angle between the observer line of sight and normal to the disk plane. The blue peak is produced from the approaching part of the disk, while the red peak form the receding part.

In addition to the double horn, the effects of relativistic physics are in principle expected. The first of such effects is the relativistic aberration (relativistic beaming in the direction of the motion), that enhances the blue peak of the line, coming from the approaching part of the disk. We can see this effect clearly in the second panel of Fig. 1.12.

Besides the relativistic aberration effect, the line can be redshifted because of the gravitational redshift and the transverse Doppler effect (third panel in Fig. 1.12).

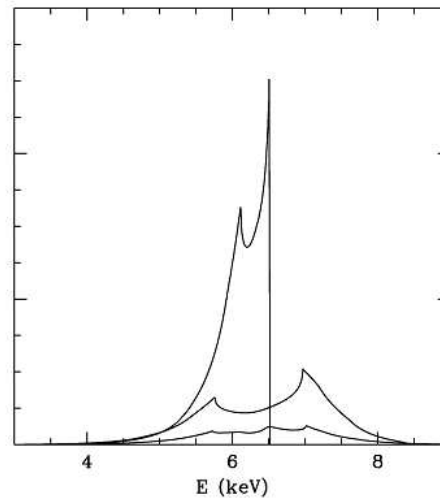


FIGURE 1.13: Iron lines from accretion disks with different inclination angles (from the higher to the lower line: $i=20$; $i=50$; $i=87$) (Matt et al. 1992)

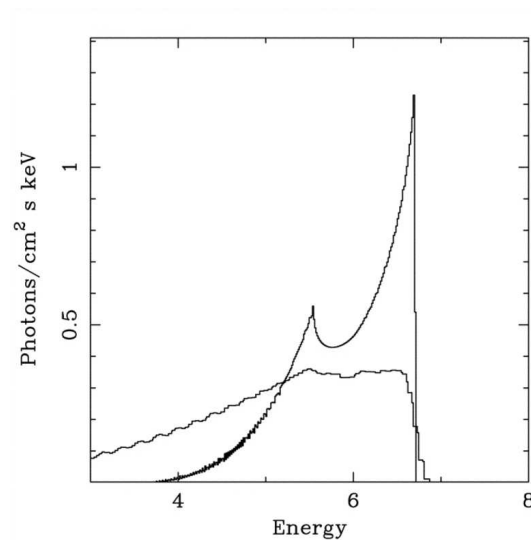


FIGURE 1.14: Iron lines from accretion disks with BH spins $a=0$ (double peaked profile) and $a=1$ (broader profile) (Fabian et al. 2000)

These effects depend on the inclination angle, increasing with increasing angle. In Fig. 1.13 we can see how the separation between the two horns grows with growing angles, while the red tail becomes more extended and the blue horn grows in intensity. In the relativistic regime, we expect a broad profile also for face-on disks, unlike the Newtonian regime, in which we expect a narrow line from face-on disks. We can see this effect in Fig 1.13 where the line seen from different angles of view is shown.

The inner radius of an accretion disk around a non-rotating black hole, is $6 R_g$, while it is of $1.23 R_g$ if around a maximally rotating BH (Bardeen et al. 1972).

If the inner radius of the emitting disk coincides with the marginal stability radius, the strong dependence existing between the radius and the spin of the BH corresponds to a strong dependence of the line profile on the BH spin. If the BH is rapidly rotating, in fact, the red wing of the line can extend to much lower energies, than in the case of a non-rotating BH. The results of the computed iron line for different spins is shown in Fig. 1.14. The red tails of the iron lines are more extended in cases where spin is higher, of course because in such case the inner radius is lower. Thanks to this effect, the iron lines have been used to measure the BH spins.

1.5.2 The observed iron line profiles

The clearest examples of relativistic Iron lines have been observed in AGN. In fact, their continuum is often found almost featureless, being well modeled by a powerlaw between 2-12 keV, at least in unabsorbed AGN. The continuum shape can become more complicated in AGN with strong X-ray absorption, where absorbing systems should be taken into account to model the deviations from the powerlaw.

Some X-ray observations of the AGN have become extremely useful to probe black hole and accretion physics. The first of such objects is MGC-6-30-15, a Seyfert Galaxy at $z=0.008$, whose X-ray observations have allowed to unveil the most interesting characteristics of accretion physics observed so far.

The first EXOSAT and Ginga observations probed the presence of a neutral, optically thick material around the SMBH irradiated by a powerlaw continuum (Nandra et al. 1989).

Following observations of ASCA confirmed that this optically thick material was indeed the accretion disk, representing consequently the first important probe of the accretion disk theory (Tanaka et al. 1995).

The ASCA observation, thanks to its higher resolution, allowed to detect the iron line and to unveil its properties: when modeled by a Gaussian, the line appears centred at 6.2 keV and significantly broadened ($\sigma = 0.7$ keV), see Tanaka et al. (1995), Fabian et al. (1994), Reynolds et al. (1995).

A much longer observation allowed to determine better the line profile, that was well fitted with a line emitted in a disk around a Schwarzschild black hole with a disk inclination of $\theta = 27^\circ$, the emissivity as r^{-3} , and the inner radius of the accretion disk $6R_g$.

(Iwasawa et al. 1999) studied the X-ray variability of this source, focusing on the changes of the line profile. He used two observations, the first on 1994, the second on 1997. During the first observation, corresponding to a minimum in the light curve of the source, a very broad line was detected. On the contrary, the second observation showed a line shifted to lower energies and there is no significant emission at 6.4 keV. The second observation corresponded to a flare in the light curve. The fact

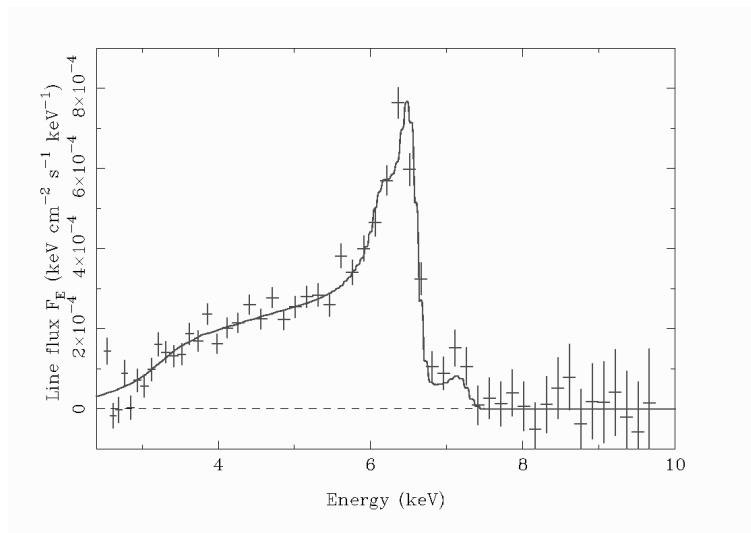


FIGURE 1.15: Iron line in MGC-6-30-15 (Fabian et al. 2002)

that the line appears redshifted below 6 keV suggested dominant emission from small radii in which gravitational effects are large. The very broad line detected in the first observation suggested the presence of a rotating black hole because the analysis of that line required an emission from within $6R_g$. Considering that there is no fluorescent emission from within the radius of marginal stability, the spectrum requires a rapidly spinning black hole.

The following observation from *XMM-Newton*, thanks to its higher sensitivity, allowed a much more detailed study of its iron line (Wilms et al. 2001). This study required a much more suitable modeling of the underlying continuum as the relativistic effects appeared to be detected not only in the line, but also in the reflection continuum. After the study of the line shape made assuming a Kerr metric, the inner radius of the accretion disk was constrained to $r_{in} < 2R_g$. The emissivity index was measured, giving a steep profile with $4.5 < \beta < 6$, meaning that the bulk of the emission was produced in the innermost radii of the disk, under the effects of the relativistic physics. The data interpretation made considering the Schwarzschild scenario required very extreme parameters, as the inner radius was $< 3R_g$, and the $\beta > 10$, that seemed physically unreasonable.

The following observation of *XMM-Newton*, 400 ks, by (Fabian et al. 2002), allowed to unveil the most beautiful line profile from an AGN detected at that time. This last observation showed a prominent blue horn, indicating the emission from larger radii in the disk. However, a broad red tail was detected, confirming the relativistic effects due to the emission from the disk innermost regions, requiring a very steep line emissivity. The red tail, as shown in Fig. 1.15, is extended down to ~ 3 -4 keV.

While a large effort has been employed to understand the characteristics of the complex of MGC-6-30-15 through several campaigns, following studies of other Seyfert galaxies further probed relativistic disks.

Deep ASCA observations of the Seyfert nuclei NGC3516 and NGC4151 unveiled broad, relativistic lines (Nandra et al. 1999; Ruszkowski and Fabian 2000; Yaqoob et al. 1995; Wang et al. 1999). The study of NGC3516 showed that the red wing tracks the variability of the continuum, in agreement with the theory. The blue horn, instead, appeared uncorrelated with the continuum, and it suggested more complex models of changes of fluorescence across the disk. An absorption feature at 5.9 keV was also found, suggesting the presence of a tenuous plasma above the disk with the energy shift due to fall of material or gravitational redshift (Nandra et al. 1999; Ruszkowski and Fabian 2000). More recent simultaneous observations from *Chandra* and *XMM-Newton* of the same source revealed narrow spikes at 5.6 keV and 6.2 keV, an probable indication of a transient non-axisymmetric illumination.

Another Seyfert Nucleus with an interesting relativistic line detected in an ASCA observation is NGC4151: this nucleus showed an interesting variability in its iron line, especially in its red wing, despite relatively small changes in its continuum. (Yaqoob et al. 1995; Wang et al. 1999).

Unambiguous broad lines were also found in more recent well-exposed *XMM-Newton* observations of AGN (Nandra et al. 2006; Braitto et al. 2007).

In comparison with the broad iron lines in these AGN, probing the relativistic disk theory, there are some interesting cases of high signal-to-noise-ratio (SNR) AGN spectra displaying narrow iron lines, representing their counterexamples. The first of such cases is NGC5548, a well known Seyfert with a rather narrow Fe line. The first ASCA data of this source unveiled a truncated disk with $R_i = 10R_g$ (Mushotzky et al. 1995; Chiang et al. 2001). However, we now know that this nucleus shows a composite iron line (Yaqoob et al. 2001). Its *Chandra* HETG spectrum has revealed a narrow core of the line, originating at quite large distances from the central BH. The narrow line EW, being quite large (~ 130 eV), suggests that the reflecting material subtends a significant part of the primary continuum. Once the narrow component was taken into account in the spectral analysis of this source, the broad component of the iron line was detected with high significance in its *Chandra* spectrum. However, later *XMM-Newton* observations of the source did not show the broad iron line (Pounds et al. 2003).

The case of NGC5548 showed that narrow iron line components can be blended with the relativistic line profiles, due to the spectral resolution of the X-ray detectors: this can produce systematic errors in the measurement of the BH spin, the inner radius of the accretion disk, the disk inclination and its emissivity profile. It is, for this reason, necessary to take in account this blending to make robust estimations of such disk parameters from the iron line shape.

1.5.3 The observed iron line profiles after statistical treatments in surveys

The study of large samples is often employed to study the properties of the iron line, such as their physical width and EW, and to understand if they depend on the physical properties of the AGN, such as luminosity and redshift.

For example, a dependence of the narrow iron line EW on the X-ray continuum luminosity has been found in AGN (Iwasawa and Taniguchi 1993): the decrease of the iron line EW with increasing continuum luminosity was explained arguing that the luminosity of the continuum in X-rays depends on the covering factor of the obscuring clouds. Given also that the EW depends on the covering factor of the fluorescence regions, the anti-correlation is clearly explained. This effect is known as the 'Iwasawa-Taniguchi effect' and it has been further assessed in following observations of *XMM-Newton* (Bianchi et al. 2007). It is also known as the X-ray Baldwin effect.

The study of large samples has been employed also to address fundamental questions about the relativistic iron lines: if its detection is common in the AGN and if the presence of broad lines depends on the physical properties of the AGN. When studies based on sizable samples of sources are considered, the average fraction of sources with relativistic broad lines is always less than 50% (Nandra et al. 1997; Jiménez-Bailón et al. 2005).

In particular, it has been proved by Guinazzi et al. (2006) that X-ray spectra with good statistical quality are needed to detect any broad Fe line component, which would otherwise be hidden under the level of noise. In that work, in fact, finding broad lines with relativistic profiles has been proved to not be very common, as analysing the AGN spectra observed with *XMM-Newton*. Guinazzi et al. (2006) found that 25% of their sample had relativistic lines. This percentage is 50% for a higher SNR, by selecting only spectra with large numbers of counts. Moreover, they found the strongest relativistic profiles in low- luminosity objects.

In this context, statistical methods to accumulate the X-ray spectra of AGN have been recently introduced to allow study of large AGN samples including lower-quality spectra that otherwise could not be analysed well individually. These methods, used in the study of large AGN surveys, include the computation of the average or the sum (commonly called *stacking*) of AGN spectra. The first of such works was that of Nandra et al. (1997): in order to obtain a reasonable SNR to detect a relativistic broad line, the limited collecting area of ASCA required extremely long observations. Before the coming of better data-sets, Nandra et al. (1997) studied the averaged spectrum of 26 AGN observed with ASCA. They showed that a relativistic line is present in this survey, proving in this way its statistical significance.

The second of such works is that of Streblyanska et al. (2005), who performed a stacking analysis on the *XMM-Newton* deep observation of the Lockmann Hole, finding a large line EW and broad line profile. A relativistic profile was found in the stacked spectra, with an evident red tail in particular in type 1 AGN, as shown in Fig. 1.16. The EWs of the broad relativistic lines range between 400-600 eV, higher than the values found in individual spectra, probably for an effect of the method (binning the spectra before stacking can bring to an overestimation of the broad component).

Civano et al. (2005) and Brusa et al. (2005) stacked the spectra of CDF-N (2 Ms exposure time) and CDF-S (1 Ms exposure time) surveys by the *Chandra* satellite. They computed the stacked spectra in bins of redshift aiming to characterise the Fe line emission of the sources in the X-ray background

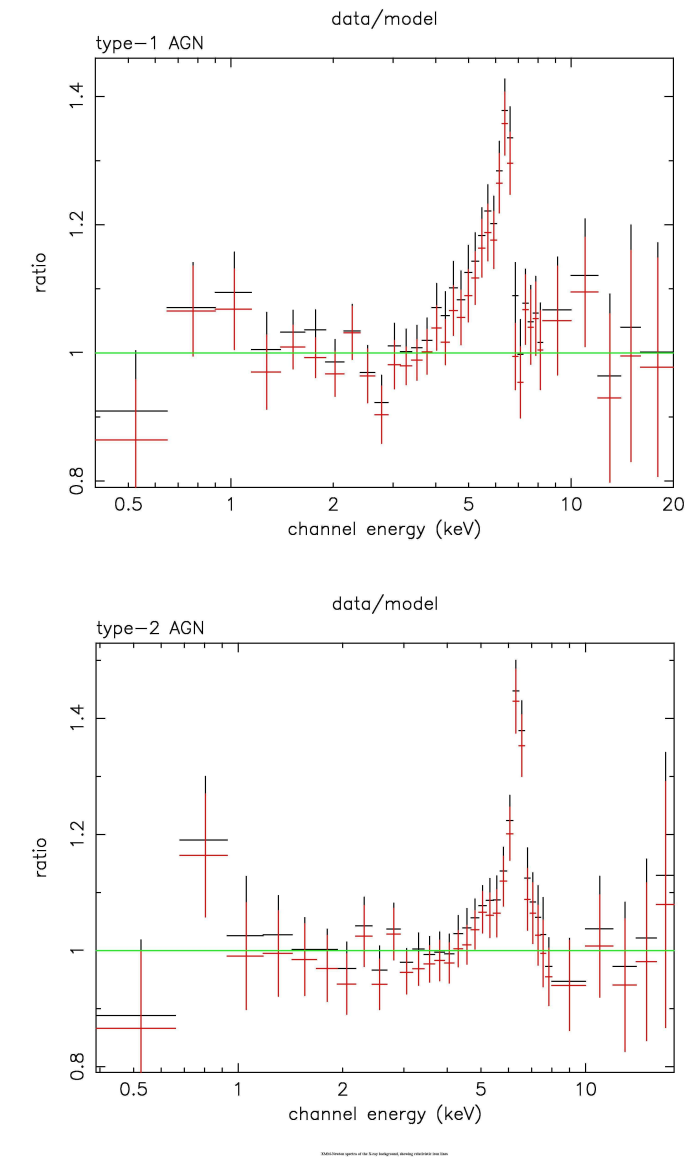


FIGURE 1.16: Iron lines in the stacked spectra of Streblyanska et al. (2005) in type 1 and type II AGN

(diffuse radiation that dominates the energy density of the X-ray sky) up to $z \sim 4$. An intense and apparently broad 6.4 keV Fe line was detected with an EW consistent with the results of Streblyanska et al. (2005). To explain the red component, they argue that it can strongly depend on the modelling of the underlying continuum and that a spurious red wing might be produced by the contribution of absorbed spectra at different redshifts. The line EW ranged from 100 to 230 eV in the different redshift intervals that were considered.

Corral et al. (2008) averaged about 600 *XMM-Newton* spectra of type 1 AGN belonging to the AXIS (Mateos et al. 2005) and XWAS (Mateos et al. 2008) samples, up to redshift ~ 3.5 .

The average observed spectrum together with the simulated continuum and its one and two sigma

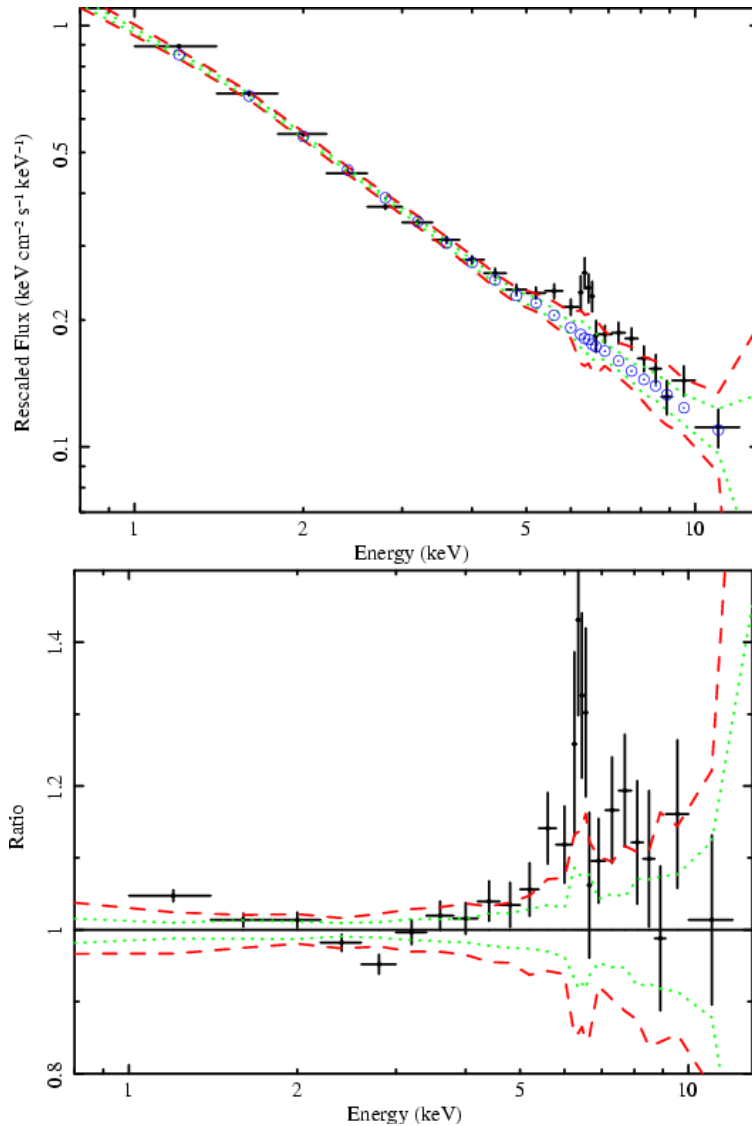


FIGURE 1.17: Iron lines from the average spectra of XMS+XWAS sample in (Corral et al. 2008)

confidence lines are shown in the top panel of Fig 1.17, while the ratios are shown in the bottom panel. The iron line is clearly narrow, emitted from material far away from the central continuum source. The detected unresolved Fe K_{α} emission line around 6.4 keV has an EW of 90 eV. While the significance of its detection was at 3σ , the relativistic line was detected only marginally, with an upper limit for the EW of any relativistic line of 400 eV at a 3σ confidence level.

The reason for the discrepancies between the broad lines and the high EWs detected in (Streblyanska et al. 2005) and the narrow lines of (Corral et al. 2008) can be explained by differences in the samples, where the Corral et al. (2008) sample has higher luminosities (and therefore lower predicted EWs of the narrow lines, following the Iwasawa-Taniguchi effect) and lower spectral counts, including more noisy sources. Another reason for the discrepancy can be found in the method, as already mentioned before. Corral et al. (2008) estimated the continuum shape using simulations, while in Streblyanska

et al. (2005) it was not constructed and subtracted in the same way, which could introduce some uncertainties. Moreover, Streblyanska et al. (2005) binned the spectra before stacking them, and Yaqoob et al. (2005) show that this procedure can mimic features like a broad red tail in an emission line.

A stacking analysis of a deep and complete sample of 507 AGN with $z < 4.5$ defined from the 2XMM catalogue was performed by Chaudhary et al. (2010). They were able to characterise the properties of the stacked spectrum of the AGN, such as the Fe line shape and the dependence of its intensity on X-ray continuum luminosity and the redshift. They detected a narrow neutral Fe line, and they confirmed the Iwasawa-Taniguchi effect in AGN over a broad range of redshift.

Recently, a stacking analysis of XMM-Newton X-ray spectra of the COSMOS sample has been performed (Iwasawa et al. 2012) finding an excess on the high-energy side of the Fe line, interpreted as the convolution of narrow lines from ionised Fe.

Concluding, while broad relativistic lines were detected in the ASCA observations, according to recent XMM-Newton results, they seem to be more difficult to detect due to the high SNR required (Nandra et al. 2007; de la Calle Pérez et al. 2010). Considering these results, one might be tempted to believe that the first ASCA studies of the iron lines have lead to an over-estimation of the presence of relativistic iron lines in Seyfert galaxies.

The paucity of relativistic lines is quite puzzling, since they are expected in the accretion disk scenario. The problem has been discussed in Bhayani and Nandra (2011), and in many other previous works. There are a number of possible solutions for this problem.

The first solution invokes the presence of ionised discs, as in Iwasawa et al. (2012); Matt et al. (1996). The ionisation was discovered to be a key parameter in the detection of the iron lines in the AGN spectra in Nandra et al. (1997), at least for high luminosity AGN. In that work, the average ASCA spectrum of a large sample of AGN was investigated as a function of the continuum luminosity. The sample spans several orders of magnitude of luminosities, from normal Seyfert luminosities to the bright ones characterising quasars. They found that a broad line becomes significantly weaker once we consider AGN with luminosities above 10^{44} - 10^{45} erg/s. The most reasonable explanation for this trend is that the high luminosity AGN possess more highly ionised accretion disks. A support for this picture came soon after with the XMM-Newton observation of Mrk205 and Mrk509, Seyfert nuclei with luminosities $\sim 10^{45}$ erg/s. In their spectra, significantly broad iron lines were found, with disk-line profiles, and centroid energies corresponding to ionised iron (Pounds et al. 2001).

The lack of broad lines can be explained also arguing the presence of quickly spinning BH (Iwasawa et al. 1996) and (Fabian et al. 2002). In this case the lines would be very broad and sometimes difficult to separate from the continuum.

The last explanation for the lack of broad lines postulates truncated discs, and the existence of different accretion states in the AGN activity, in analogy with the Galactic Black Hole Candidates (Zdziarski

et al. 1999). Evidences for this hypothesis were found in Mushotzky et al. (1995), Chiang et al. (2001) and, more recently, in Matt et al. (2005).

The large amount of data accumulated by *Chandra* and *XMM-Newton* has allowed a detailed investigation on the reflection features of the AGN in the nearby Universe. These observatories have provided also the first constraints on the environment immediately close to the accreting SMBH at very high redshift.

During the next decades, it is hoped that new observatories will be used to collect even more information in this field. In fact, they can make significant advances in AGN research, answering the most important open questions of today's X-ray Astronomy. The possibility of their employment to produce deep AGN fields with the highest quality spectra opens the prospect of being able to constrain the cosmic history of accretion.

1.6 Our work

The ultimate goal of our work is to study the iron line properties in AGN in cosmic times.

In previous studies of large *XMM-Newton* samples of AGN, as in Corral et al. (2008) and Chaudhary et al. (2010), it has been found that an iron line is present in all the average X-ray spectra of these sources. We aim in this work at checking its ubiquity in AGN over a broad range of redshift and luminosity, using data from the deepest and widest surveys performed both *Chandra* and *XMM-Newton*.

Recent results of the search of relativistic lines are not uniform, ruling in (Streblyanska et al. 2005) or ruling out (Corral et al. 2008) their presence. In this thesis, we want to check if the relativistic lines are common in all the AGN or just in a class of them, checking whether their detection depends on the characteristics of the AGN like luminosity, redshift or intrinsic absorption. For example, according to Guainazzi et al. (2006), broad iron lines look to be more common in low luminosity AGN than in high luminosity ones. Moreover, the broad components are expected to be suppressed in obscured AGN. The presence of relativistic iron lines has been proved in low redshift AGN (Nandra et al. 2006), but it has not been well assessed at high redshift, yet. In fact, given the instrumental limitations of today's observatories, far away sources have lower number of counts. Our averaging method, as we will see below, allows to extend such analysis to high redshift AGN: a similar analysis with our method has been made only for the *XMM-Newton* observations studied in Corral et al. (2008), but never for *Chandra* observations.

In our work we compile as many AGN as possible to map the iron lines properties in different kind of surveys. The detection of the broad iron lines is strongly affected by the observational conditions because high SNR is required. Such conditions, unfortunately, are fulfilled only in few observations, given the limited effective area of the current detectors. In absence of large datasets with such high

quality, we average a large number of spectra belonging to the most relevant surveys of today's facilities.

In a previous work, a relativistic line has been significantly detected with a stacking method (Streblyanska et al. 2005): in that work, the EW is higher than the ones found in the individual spectra in the literature, indicating that the relativistic contribution might have been overestimated, perhaps because of the methodology used. This and other results have highlighted that the estimation of the line EW and significance in the average spectra is a delicate issue in stacking: for this reason we aim at developing a new method of analysis to calculate them. Our purpose in this step is to estimate the line EW in a model-independent way to check the robustness of our stacking method. Once addressed this issue, we have the purpose to compare the EW of the relativistic component with the values of the single spectra in the literature. If lower values are found, this would indicate that the iron lines are not common because only a low percentage of sources must contribute to the average. On the contrary, obtaining similar values would be a relevant indication that the iron lines are really common between AGN.

A new technique to estimate the intrinsic resolution of our method is needed and will be developed in this work. To study the broad iron lines, in fact, the limited spectral resolution of the instruments used and any additional effects introduced by the method should be taken into account. Whether broad lines are detected, it is possible to fit the data with the relativistic models available in the literature, checking if they are suitable to fit the average spectra, and eventually constraining their parameters.

It has been seen that narrow iron lines depend on redshifts, luminosities, and intrinsic absorption. Until now, a significant trends of the line EW with the redshift has not been found. Investigating samples at different redshifts, it is possible to understand the evolution of the abundance of the Iron in cosmic timescales.

The further question is to check the trend of EW with the luminosity of the X-ray continuum. If the Iwasawa-Taniguchi effect is due to the presence of absorbing material around the central source of the primary continuum, both a dependence of the iron line EW on the primary continuum luminosity and the X-ray absorption is expected. To examine, confirm or reject this hypothesis, the study of samples covering a broad span of absorption and luminosities can be useful. With such multi-comprehensive samples, when enough counts statistics is reached, the investigation of subsets in luminosity and redshift can help to check such relations.

Using the deep *Chandra* fields, we aim at extending the iron line studies to high redshift AGN observed with *Chandra*. Using the *XMM-Newton* CDFS field (Comastri et al. 2011), instead, we are allowed to study better the iron line profile, due to the higher number of counts collected thanks to the higher effective area. However, the deep observations from *XMM-Newton* are affected by a strong background, and our ability to study the detailed characteristics of the detected features is still limited by the total number of counts collected, for this reason we have investigated the broad iron line in more detail

with a sample that allowed us to collect many more total counts. We have assembled such sample by cross-correlating the largest catalogue of X-ray sources, the 2XMM (Watson et al. 2008) and the largest quasar catalogue, the Véron-Cetty and Véron (2006) catalogue, hereafter called VCV: it makes sure to have good enough counts statistics for the detailed study of the relativistic line.

In Chapter 2, we describe the X-ray instrumentation involved. In Chapter 3, we describe our methodology of analysis. The Deep *Chandra* Fields are discussed in Chapter 4. Our work on the *Chandra* Deep Field South observed by *XMM-Newton* (called XMM CDFS) will be described instead in Chapter 5. In Chapter 6, we will show our analysis of Véron-Cetty & Véron catalogue. Finally, in Chapter 7, we will draw our overall conclusions and describe the possible future developments of our work.

Chapter 2

Our X-ray data

To explore the physics and evolution of the AGN, both "deep" and "wide" X-ray surveys are required; the trade-off between the two, of course, is between sensitivity limits and solid-angle coverage on the sky. The lowest sensitivity limits are achieved in 'pencil-beam' surveys, such as the high exposure Deep *Chandra* Fields that allow to reach the sensitivity limits of 2×10^{-17} erg s⁻¹ cm⁻². They allow to achieve scientific goals such as the study of low luminosity and high redshift AGN. The ultra-deep observation by *XMM-Newton* of the Chandra deep Field South has instead a sensitivity limit of 6.6×10^{-16} erg s⁻¹ cm⁻².

On the contrary, shallower surveys such as the 2XMM catalogue allow a wider coverage of the sky and allow to accumulate a high number of sources in the local Universe. Such surveys are often characterised by a higher number of X-ray spectral counts. The 2XMM catalogue has a sensitivity limit of 2.5×10^{-14} erg s⁻¹ cm⁻².

In this thesis, we studied pencil-beam surveys, observed by *Chandra*: the Chandra deep Field North of Alexander et al. (2003), Chandra deep Field South of Luo et al. (2008) and AEGIS fields of Laird et al. (2009). We then studied the ultra deep survey of *XMM-Newton* in the Chandra deep Field South (Comastri et al. 2011). We also studied the wide sample composed by the cross-correlation between the Véron-Cetty-Véron catalogue (Véron-Cetty and Véron 2006, 2010) and the 2XMM catalogue (Watson et al. 2008). This sample represents the local Universe counterpart of our research.

2.1 The *Chandra* surveys

The *Chandra* surveys studied in this work reach very low flux limits at which many scientific goals can be achieved: with these fields, it is possible to accumulate spectra of even moderate-luminosity AGN at very high redshift. With the employment of such sample we could characterise the X-ray spectra of the AGN in the distant Universe observed by the *Chandra* satellite.

2.1.1 The *Chandra* observatory

Chandra is part of a NASA project with four observatories that cover the Optical, Infrared, Gamma, X-rays: these observatories are the Hubble Space Telescope, Spitzer, Compton Gamma-Ray Observatory, and *Chandra*. The name of that project was chosen in honours of S. Chandrasekhar that studied the theory of gravitational collapse into Black Holes in 1931. The time to complete an orbit is 64 hours and 18 minutes and the spacecraft spends 85% of its orbit above the belts of charged particles that surround the Earth. Uninterrupted observations as long as 55 hours are possible and the overall percentage of useful observing time is much greater than for the low Earth orbit of a few hundred kilometres used by most satellites.

The *Chandra* telescope was designed to have considerable collecting area between 6 and 7 keV, the energy of iron lines emitted by many astrophysical sources. The whole telescope has a focal length of 10 m. The mirror consists of four pairs of nested reflecting surfaces, arranged in the usual Wolter type 1 geometry. The high energy response is achieved by use of relatively small reflection angles and by coating the mirrors with iridium. Improvements in mirror technology introduced by *Chandra* include significant advances in grinding, polishing, alignment, and testing.

Mirrors with a resolution of 0.5 arcsec on-axis have been achieved. The combination of high resolution, large collecting area, and sensitivity to higher energy X-rays makes it possible for *Chandra* to study extremely faint sources, sometimes strongly absorbed sources, in crowded fields.

On-board *Chandra* there are four instruments:

- ACIS (Advanced CCD Imaging Spectrometer): with two components. The first one is ACIS-I, with FI ('Front Illuminated') CCD; the second one is ACIS-S, with BI ('Back Illuminated') CCD. The response of BI is extended from 0.8 to 8 keV; the response of FI is extended from 0.8 to 10 keV. When operated in 'imaging' mode, the X-rays strike these CCDs directly, producing a high quality image in which the energy of each photon is tagged with moderate energy resolution ($E/\Delta E \sim 50$).
- HRC (High Resolution Camera): comprises two micro-channel plate imaging detectors, and offers the highest spatial (<0.5 arcsecond) and temporal (16 msec) resolutions. It has two components: HRC-I and HRC-S.
- HETG (High Energy Transmission Grating): together with ACIS-S, its forms the HETG spectrometer. In 'spectroscopy mode', one of a set of (transmission) diffraction gratings is placed in the X-ray beam, allowing high resolution spectra (up to $E/\Delta E \sim 1000$ at soft X-rays, $E/\Delta E \sim 200$ at 6 keV).

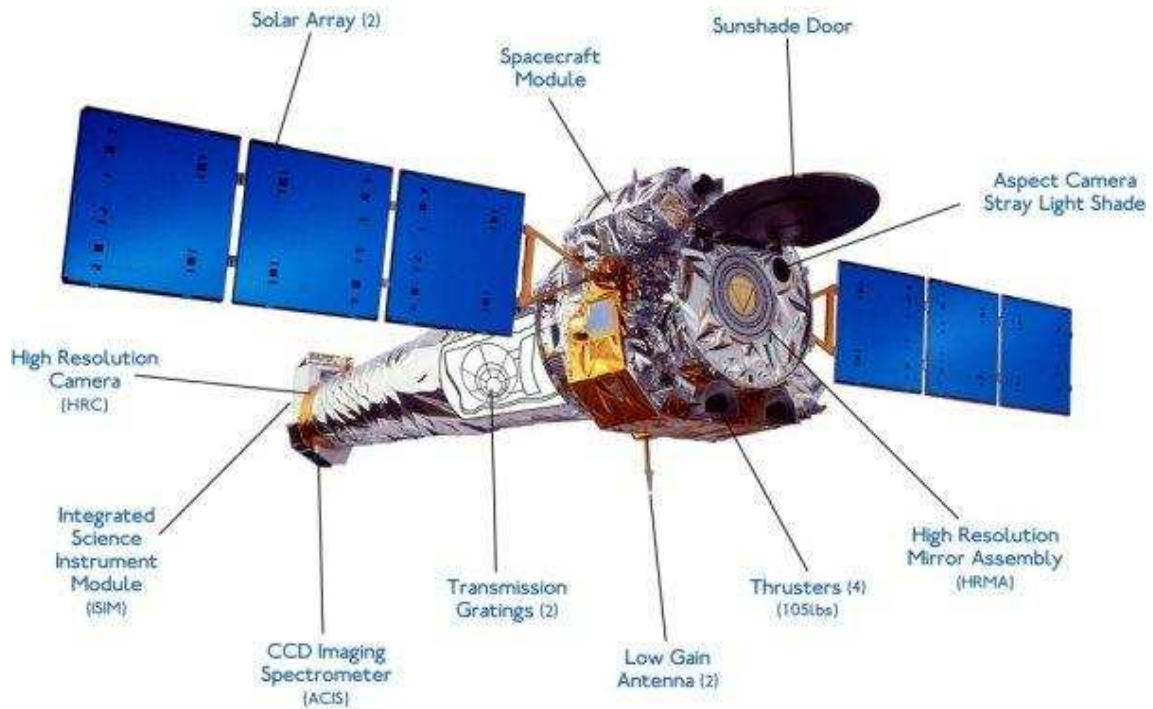


FIGURE 2.1: Artistic view of *Chandra* satellite in flight showing its main characteristics and the instruments on board (see text for details)

- LETG (Low Energy Transmission Grating): together with HRC-S, it forms the LETG spectrometer. Its resolution is $E/\Delta E \sim 1000$ in the 'soft' spectral region, between 0.08 and 0.2 keV. It also works by placing a transmission diffraction grating in the X-ray beam

The effective area of ACIS is shown in Fig. 2.3. A deep absorption feature is present at about 2 keV due to the absorption of the material coating the mirrors, then there is a secondary maximum between 3-4 keV and finally a steep decrease from about 5 keV.

2.1.2 The parent *Chandra* surveys

The AEGIS-X survey is a *Chandra* survey of the Extended Groth Strip (EGS) region, designed primarily for studying the co-evolution of black holes and their host galaxies. The data we used are the result of eight contiguous ACIS-I pointings, each with exposures of 200 ks, totalising 1.6 Ms. The survey covers a total area of approximately 2302 arcmin² in a strip with two degrees length. The total number of identified sources with spectroscopic redshifts is 409. The data reduction and point source detection algorithms used to analyse these data are described in Laird et al. (2009).

The *Chandra* Deep Field-North (CDF-N) survey is one of the deepest (2Ms with ACIS-I) 0.5-8.0 keV surveys ever made: nearly 600 X-ray sources were detected over 448 arcmin². The total number of

sources identified with spectroscopic redshifts is 307. Details of data reduction and the point source catalogue are described by Alexander et al. (2003).

The *Chandra* Deep Field South (CDF-S) is the deepest and most sensitive observation obtained with *Chandra*. We used the 2 Ms survey, covering an area of 436 arcmin². Several hundred X-ray point sources were detected. The number of sources identified with spectroscopic redshifts is 152. A detailed description of the survey can be found in Luo et al. (2008). It has recently been extended to 4 Ms, as described in Xue et al. (2011).

2.1.3 The *Chandra* spectral extraction

Source and background spectra, and their ancillary and response matrices, were extracted for each source by Digby-North (2011). For this purpose, the tool ACIS-EXTRACT, version 2008-03-04 (Broos et al. 2010) was used. The tool, written in IDL language¹, automates the the extraction and analysis of both point-like and diffuse sources; it relies on tools in the Chandra Interactive Analysis of Observations (CIAO)² package (Fruscione et al. 2006). The process of “extracting” a putative point source consists of several tasks: defining an appropriate aperture around the source position, defining an appropriate background region that is expected to be a good estimator for the background contaminating the source aperture, collecting the observed events within the aperture and background regions, and constructing a model for the response of the observatory that correctly calibrates the extraction so that intrinsic source properties can be derived.

Before the spectral fitting, in our work all the *Chandra* spectra were grouped with a minimum of five counts per bin, and we applied the modified Cash statistics described in Cash (1979) (and discussed in the Xspec pages³).

2.2 The XMM surveys

The *XMM-Newton* surveys studied in this work, the XMM CDFS and in the VCV catalogue, are substantially different. The XMM observation of the CDFS, given the higher sensitivity than *Chandra*, allows to collect a higher number of good quality spectra and a better counts statistics in the iron line region. For this reason, it has been employed for the detailed study of the iron lines in distant AGN.

The VCV catalogue, being a wide field that allows the accumulation of a superior number of counts and the collection of a high number of low-redshift sources, makes possible to study in better detail the relativistic iron line. Moreover, having a large number of high-redshift sources, it will make possible in the future to investigate the iron line properties in relation with the characteristics of the central engine.

¹<http://www.itvis.com/ProductServices/IDL.aspx>

²<http://cxc.harvard.edu/ciao/>

³ <http://heasarc.gsfc.nasa.gov/docs/xanadu/xspec/wstat.ps>

2.2.1 *XMM-Newton* observatory

Result of a project of ESA (European Space Agency), *XMM-Newton* is the X telescope with the highest sensitivity ever gone into orbit. The name XMM comes from X-Ray Multi-Mirror Satellite, 'Newton' refers to Sir I. Newton, the scientist of the XVII century that studied the Universal Gravitation and the three laws of the motion. The main purpose of the mission was to observe the compact objects, including the black holes, and phenomena related to strong gravitational fields in which they are engaged.

The focal length of the telescope as a whole is 7.5 m, and the on-axis angular resolution of 20 arcsec.

XMM-Newton has a highly eccentric orbit of 48 hours, inclination 40°, with 114000 km apogee and perigee at 7000 km, which allows 40 hours of continuous observation.

XMM-Newton is equipped of three telescopes.

Each of the three X-ray telescopes on board *XMM-Newton* consists of 58 Wolter I grazing-incidence mirrors, made of nickel coated with gold, which are nested in a coaxial and co-focal configuration. The design of the optics was driven by the requirement of obtaining the highest possible effective area over a wide range of energies, with particular emphasis in the region around 7 keV.

Aboard of *XMM-Newton* there are three main scientific instruments:

- The EPIC (European Photon Imaging Cameras): The detectors are CCD, located in the main focus of each of the three mirror modules: two EPIC-MOS (Metal Oxide Semiconductor) and EPIC PN (p-type / n-type semiconductor junction). The two EPIC-MOS have a good energy resolution in the portion of the spectrum in the X-ray soft (< 2 keV), but are less sensitive to hard X-photons (2-10 keV). The hard spectrum is better covered by EPIC-PN cameras. They cover the whole band 0.1-15 keV and have a field-of-view diameter of 30. The EPIC-PN can operate at a high temporal resolution, up to 0.03 ms.
- RGS (Reflection Grating Spectrometers): Gratings are mounted on two of the three mirror modules (the ones corresponding to the two EPIC MOS). They reflect about 50 percent of the radiation on a secondary camera which analyses the diffraction spectrum produced.
- OM (Optical/UV Monitor): a secondary optical telescope (which covers the spectral range 170-600 nm), aligned with the X-ray telescopes for simultaneous optical observations.

The main characteristics and the disposition of the mirrors and instruments are shown in the Fig. 2.2.

The collection area is very large on a wide band of energy, up to 10 keV. The effective area between 0.1 and 10 keV is shown in Fig. 2.3. It has a deep 'edge' of absorption at about 2 keV (the edge of Gold M absorption of the mirror coating).

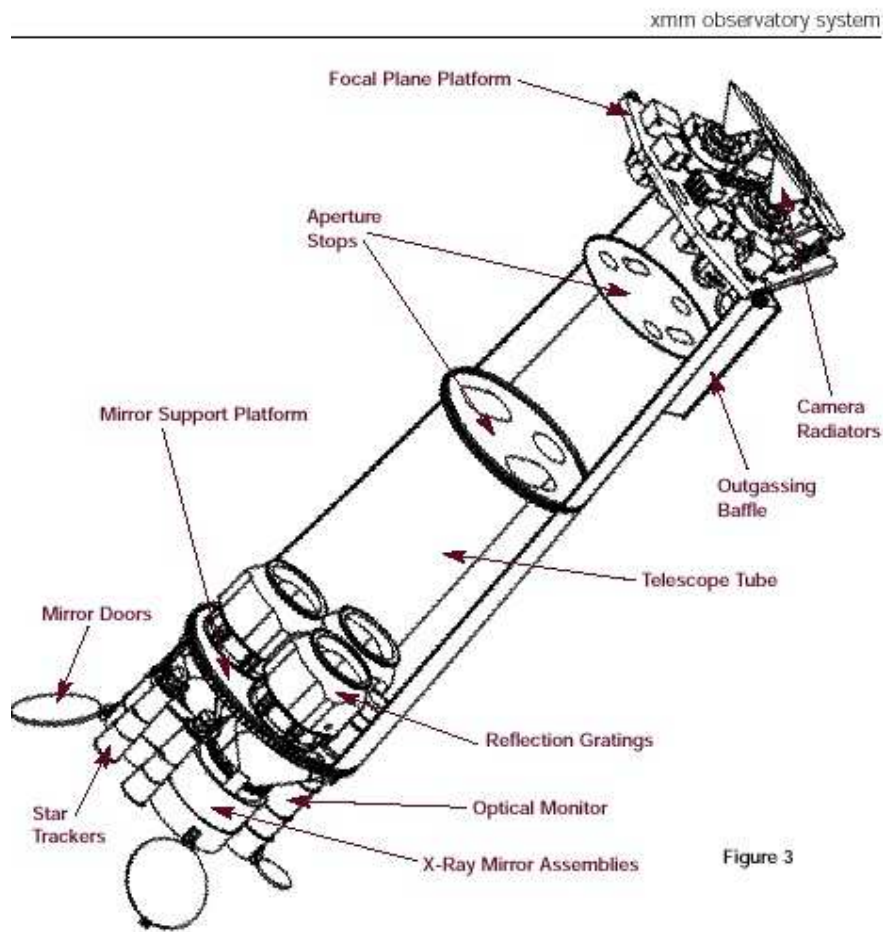


FIGURE 2.2: Schematic design of the main body of the *XMM-Newton* spacecraft showing its main characteristics and the disposition of the mirrors and the instruments (see text for details). Copyright 2009©European Space Agency.

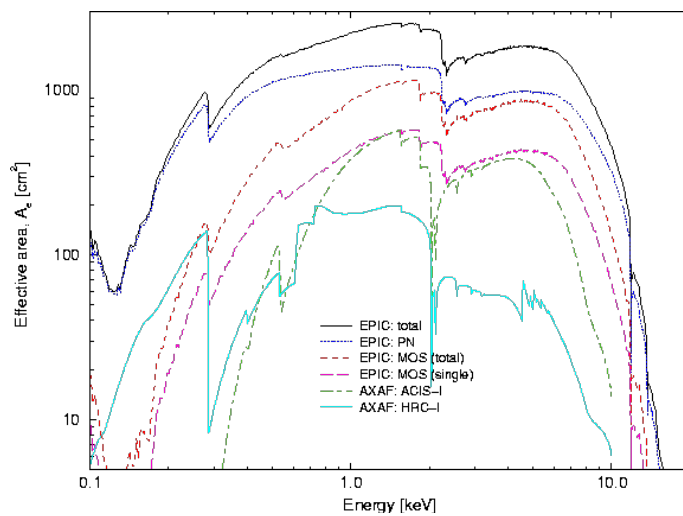


FIGURE 2.3: Chandra and XMM efficiency as a function of the spectral energy.

The efficiency has a peak at 2-5 keV, then decreasing with the energy for energies higher than 6 keV.

The background level in *XMM-Newton* is higher than the level of *Chandra* because *Chandra* has a superior angular resolution. The background, composed by particle and cosmic background, forms a continuum.

Besides the background, radiation excites the material in the detectors, and these processes give place to a radiation of secondary lines. The most prominent one in EPIC is the Al spike at 1.5 keV. Other prominent features are: at 5.5 keV Cr-K α , at 8 keV Ni-K α , Cu-K α , Zn-K α .

2.2.2 The *XMM-Newton* survey of the *Chandra* deep Field South

The *XMM-Newton* CDFS survey is a 3.3 Ms observation of *Chandra* Deep Field South. The bulk of the observations was made between July of 2008 and March of 2010, and has been combined with archival data taken between July 2001 and January 2002.

The main XMM CDFS catalogue is composed by the 337 sources detected with PWXDetect and EMLDetect. For the spectral extraction, a manual procedure has been performed. The background selection has been made requiring that it does not fall into gaps, that it falls in one chip only and possibly in the same chip of the source, to have enough good pixels, to stay as close as possible to the source.

The details on data reduction and analysis and the source detection will be presented in Ranalli et al. (2012) in preparation.

In this work, we used high quality X-ray spectra for sources detected with a significance of detection above 8, corresponding to a flux limit of $\sim 2 \times 10^{-15} \text{erg s}^{-1} \text{cm}^{-2}$.

We checked the presence of spectroscopic identifications of these sources in the literature making use of several spectroscopic campaigns: Balestra et al. (2010), Casey et al. (2011), Cooper et al. (2011), Kriek et al. (2008), Le Fèvre et al. (2005), Le Fèvre et al. (2004), Mignoli et al. (2005), Ravikumar et al. (2007), Szokoly et al. (2004), Taylor et al. (2009), Treister et al. (2009), van der Wel et al. (2005), Vanzella et al. (2008), Silverman et al. (2010). In this work, we used only sources with secure spectroscopic redshifts.

2.2.3 The 2XMM-Newton spectra of sources in the Véron-Cetty-Véron catalogue

We used the 2XMM catalogue presented by Watson et al. (2008). The 2XMM catalogue is the largest X-ray source catalogue ever produced, containing almost twice as many discrete sources as either the ROSAT survey or pointed catalogues. 2XMM complements deeper *Chandra* and *XMM-Newton*

small area surveys, probing a much larger sky area. The catalogue contains source detections drawn from 3491 *XMM-Newton* EPIC observations made between 2000 February 3 and 2007 March 31. It possesses 246897 X-ray source detections which relate to 191870 unique X-ray sources. The median flux in the total photon energy band (0.2 - 12 keV) of the catalogue detections is $2.5 \cdot 10^{-14}$ erg cm⁻² s⁻¹; in the soft energy band (0.2 - 2 keV) the median flux is $5.8 \cdot 10^{-15}$ erg cm⁻² s⁻¹, and in the hard band (2 - 12 keV) it is $1.4 \cdot 10^{-14}$ erg cm⁻² s⁻¹. About 20% of the sources have total fluxes below 10^{-14} erg cm⁻² s⁻¹.

We filtered the 2XMM catalogue selecting the sources with the best quality PN spectra (with PN in full frame mode), and not located in the Galactic equator (located at angles $b > 20^\circ$ from the Galactic equator, in absolute value). We cross-correlated the sources of the filtered 2XMM catalogue with the largest catalogue of quasars: the Véron-Cetty & Véron (Véron-Cetty and Véron 2006, 2010). A radius of cross-correlation of 5 arcsec was employed. If more than one source resulted in the cross-correlation, the nearest one was selected. We discarded all the sources classified as LINERs and BL-Lac in order to focus only on bona-fide AGN in which the main source of X-rays is not synchrotron radiation.

We then extracted the PN spectra with more than 50 counts in the entire band and the MOS1 and MOS2 spectra with summed counts higher than 50. The full sample (of ~2900) sources was extracted as explained in the following section.

2.2.4 The spectral extraction and merging

In this Section we review the main steps of the spectral extraction. The code I used for the spectral extraction of the VCV catalogue was developed in IDL language by S. Mateos (Mateos et al. 2005). Spectra were extracted for each detection and EPIC camera in circular regions centred at the source positions. The size of the source extraction regions was selected to optimise the SNR via the SAS task `eregionanalyse`. Background spectra were obtained in regions after masking out all the detected sources. The code performed an automatic choice of the background region after generating 16 background regions. The code then flags background regions as bad according with these criteria: if they fall into two gaps, if they include area in more than one chip, if they fall in a different chip than the source, if they do not have enough good pixels. It finally selects the region closest to the source. The radius of extraction of spectra varies from source to source, but typically was between 14 and 20 arcsec. Calibration matrices (`arf` and `rmf`) for each spectrum were obtained with the SAS tasks `arfgen` and `rmfgen`.

To maximise the SNR, we have combined the MOS1 and MOS2 spectra observed with the same filter and the corresponding response matrices. Merged source and background spectra were obtained by adding the individual spectra. 'Back-scale' values (size of the regions used to extract the spectra) and calibration matrices for the combined spectra were obtained weighting the input data with the exposure times. For the fields with more than one observation, we added all the MOS and PN data

(with difference of off-axis angles lower than 1 minute of arc) for each epoch. MOS and PN data were not merged because of their different responses.

Chapter 3

Methodology

Stacking methods are employed by several research groups to treat wide surveys in X-ray spectroscopy because they allow to improve the spectral SNR. With these methods, the sum (or average) spectrum is computed. Due to the limited spectral resolution, and the strong dependence on the energy of the response, a straight sum is not suitable, for this reason such methods are complex and need a previous basic fitting of the spectra.

In this work, we study the average properties of the X-ray spectra of AGN in deep fields from *Chandra* and *XMM-Newton*. To do that, we use a statistical method, employing our own stacking procedure. We also developed for the first time in X-ray stacking a new methodology to check the instrumental effects introduced by the averaging over a broad AGN sample. We also devised a model-independent method to estimate the EW and the significance of the iron line in average spectra.

3.1 The X-ray spectral analysis

The X-ray spectral analysis was performed using the Xspec software (Arnaud 1996).

X-ray data have a limited spectral resolution. For this reason we use the calibration files to convert the spectra in channels to spectra in physical units. In fact, the input spectrum is expressed in counts C per channel I and is the result of the incident spectrum $f(E)$ after being modified by the detector response $R(I, E)$:

$$C(I) = \int_{E_{min}}^{E_{max}} dE f(E) R(I, E)$$

These $R(I, E)$ response files model the detection response, which is proportional to the probability to detect a photon as a count in a determined channel I . This discrete function is obtained by the product of the Redistribution Matrix File (RMF) and the Auxiliary Response File (ARF). The RMF is a matrix

employed to convert the photon energy in channels, while the ARF takes into account the effective area at each energy.

A minimum number of 20 source counts should be selected in order to use χ^2 statistics. For spectra with less counts it is necessary to use the Cash statistics, that does not provide a goodness of fit criterion, but only allows the estimate of the model's parameters.

The spectral fits we employed in our work make use of simple models that describe the radiative processes in the AGN. We describe these models below.

3.1.1 Spectral fits in Xspec

The models we used in our analysis are made by combinations of these simple models included in Xspec package.

- Primary emission
 - `powerlaw`: this model is commonly used to represent the AGN X-ray continuum. It is an additive model that corresponds to a powerlaw: $M(E) = KE^{-\Gamma}$ where K is the normalisation defined as the flux (in photons $\text{keV}^{-1} \text{cm}^{-2}\text{s}^{-1}$) at 1 keV and Γ is the photon index.
- Absorption models
 - `phabs`: the detected continuum is the above mentioned powerlaw after interacting with the absorber, for this reason absorber models are used. Phabs represents neutral photoelectric absorption:

$$M(E) = \exp(-N_H\sigma(E))$$

where $\sigma(E)$ is the photo-electric cross-section and the N_H is the equivalent hydrogen column density (in units of 10^{22} atoms cm^{-2}). The model called `zphabs` is its redshifted variant, that uses the formula:

$$M(E) = \exp(-N_H\sigma(E[1+z]))$$

- `pcfabs`: a partial covering fraction absorption. It is well known that the absorption suppress the spectral emission below a certain energy (See Chapter 1). The energy at which this feature can be detected grows with growing N_H . Pcfabs is a more flexible absorption model that takes into account not only the column density of the absorber, but also the covering fraction (f) of the absorbing clouds.

$$M(E) = f \cdot \exp[-N_H\sigma(E) + (1-f)]$$

where $\sigma(E)$ is the photo-electric cross-section. This model considers neutral absorption from a material of intrinsic column density N_H . The absorbed flux is only a fraction f of the primary emission. The remaining part $1 - f$ is instead transmitted.

- `absori`: an ionized absorber based on that of Done et al. (1992) and developed by Zdziarski et al. (1995). The parameters are powerlaw index (that we fix in this work to the photon index of the primary powerlaw), Hydrogen column in units of 10^{22}cm^{-2} , absorber temperature in K, absorber ionisation state, redshift and iron abundance relative to solar. The most important parameter is the Hydrogen column density in units of 10^{22}cm^{-2} and all the others are fixed to their default values in this work. In fact, we have seen that they do not vary much during fitting.

- Line models

- `gaussian`: A simple Gaussian line profile.

$$A(E) = \frac{K}{\sigma \sqrt{2\pi}} e^{-\frac{(E-E_l)^2}{2\sigma^2}}$$

where: E_l = centroid energy of the line in keV; σ = line width in keV; K = line flux in photons in $\text{cm}^{-2}\text{s}^{-1}$.

- `diskline`: line emission from a relativistic accretion disk (Fabian et al. 1989) around a non rotating black hole. The emissivity scales as R^β . The parameters are: E =line energy in keV; β = powerlaw dependence of emissivity; R_i = inner radius in units of gravitational radii; R_o =outer radius in units of R_g ; θ = angle between the perpendicular to the disk and the observer; K =photons in the line (in $\text{cm}^{-2}\text{s}^{-1}$). Setting the emissivity β to 10 is the special case of the accretion disk emissivity law $\frac{1-\sqrt{\frac{6}{R}}}{R^3}$.
- `LaorA` line emission from a relativistic accretion disk (Fabian et al. 1989) around a maximally rotating black hole. It is a result of Laor's model that includes the effects of the BH spin on the line profile (Laor 1991). The parameters are the same as in the previous model.

- Reprocessing from cold material

- `pextrav`: exponentially cut off power law spectrum reflected from neutral material (Magdziarz and Zdziarski 1995). The output spectrum is the sum of the cut-off power law and the reflection component. The reflection component (whose reflection scaling factor is rel_{refl}) alone can be obtained for $\text{rel}_{refl} < 0$. The metal and iron abundance are variable with respect to those that can be defined by the command `abund`. The opacity can be set by the command `xsect`. As expected in AGNs, H and He are assumed to be fully ionised. The parameters are: the input power law photon index, $N_E = E^{-\Gamma}$; E_c =cutoff energy; cutoff energy; z =redshift; a =abundance of elements heavier than He relative to the solar abundances; a_i =iron abundance relative to that defined by `abund`; $\cos(\theta)$ =cosine of inclination

angle (defined as usual); K = photon flux (in the same units as above) of the cutoff broken power-law only (no reflection) in the observed frame. This model does not take into account the effects of the fluorescent lines, considering the Compton reflection only.

- Convolution model
 - `gsmooth` gaussian smoothing with a variable width $\Sigma(E)$, which varies as the α power of the energy: $\Sigma(E) = \sigma_6(\frac{E}{6})^\alpha$. The width at 6 keV is set with the parameter σ_6 and the slope with α . We have used this model to take into account the varying spectral resolution of the EPIC camera and the effects of our stacking method

$$dC(E) = \sqrt{2\pi\Sigma(E)} \exp\left(-\frac{1}{2}\left(\frac{(E-X)}{\Sigma(E)}\right)^2\right) A(E)dE$$

3.2 Selection of the samples

The sample selection is the first, important step of the analysis of surveys. It should represent a good compromise between the inclusion of a large number of sources, in order to accumulate a high number of counts, and the selection of good enough spectra in order to avoid the inclusion of too much noise. As it has been shown in Guainazzi et al. (2006), the spectral quality is a key parameter to detect the broad iron lines: if the spectra to analyse include low quality spectra, broad relativistic features would be hidden below the noise in the continuum and will not be detected. Taking into account these considerations, we made the selection of our *Chandra* sample discarding all the sources with less than 200 counts in the spectral range between 2 and 12 keV. We also considered different cuts in counts such as 50 and 100 spectral counts, that we will discuss in App. A.

In the two *XMM-Newton* samples, due to the higher level of the background, the number of net counts alone is not enough to ensure a selection of good quality spectra. In fact, the background can be dominant even in spectra with a relatively high number of counts. To avoid including spectra with a high background contribution, we estimated the SNR in the band between 2 and 12 keV and included the 100 spectra with the best SNR. This turned out to discard all the spectra with $\text{SNR} < 15$. We show in more detail the background problem in the high exposure XMM CDFS observation in App. B.

3.3 Our averaging method

Our averaging method was originally developed by Corral et al. (2008) for the *XMM-Newton* spectra of XMS-XWAS surveys. It was then also used for the study of the XBS sample by Corral et al. (2011). We adapted and tested it for the *Chandra* spectra and then we further developed it for *XMM-Newton* surveys, introducing significant novelties.

The first step is to convert each spectrum in counts to physical units, using its own particular response matrix. To do this, the spectra were grouped and fitted with simple continuum models formed by a powerlaw absorbed by a Galactic and an intrinsic absorber. This best fit model was then used to extract the unbinned background-subtracted spectra in physical units. The effect of the spectral method in this deconvolution is discussed in App. C.

Once we obtained all the spectra in physical units, the following step was to apply the corrections described in Corral et al. (2008) that we can summarise as follows:

1. Correction for Galactic absorption
2. Shift the spectra to a rest frame, using the spectroscopic redshifts known for each source
3. Re-normalise the spectra with respect to the integrated flux of the continuum in a given band in order to balance the contribution from all sources, making sure that the average spectrum is not dominated by a few high-flux sources

Once we obtained the de-absorbed and renormalised spectra at rest-frame, we rebinned each spectrum. This binning was constructed to have at least 1000 net counts in each bin of the co-added spectrum in rest-frame. In order to maximise our ability to detect a narrow Fe line, we always centered one bin at 6.4 keV.

We finally averaged the flux values in each bin using the unweighted arithmetic average. This process of de-convolving, shifting to rest-frame and re-binning, together with the limited and energy-dependent energy resolution of the EPIC cameras, results in an overall effective energy-dependent energy resolution in the average spectrum.

To quantify any possible effect of broadening introduced by the stacking method on the X-ray instrumentation, we performed extensive simulations of the continuum and of the Fe Line as described in Sects. 3.4 and 3.5.3. Once we obtained the average spectra, they were fitted with one or more of the spectral components mentioned in Section 3.1, taking into account the resolution of our method estimated through the simulations.

3.4 Simulations of the continuum

Previous works have shown that the stacking methods can distort the shape of the spectrum. Therefore, it is important to take this into account before drawing conclusions from the spectral analysis of the average spectrum.

To characterise the underlying continuum of our sample, we made more than 100 simulations of each source using the best-fit parameters of the continuum model (see Sect. 2.2).

To each of these 100 simulated samples we applied the same method as the one used for the observed sample (spectral fitting, correcting for response, correcting for Galactic absorption and z , rescaling and averaging). After this, we represented our continuum with the median of the 100 averaged simulated continua. We decided to use the median and not the arithmetic average because it is a more robust estimate of a central value, and in particular, it is less sensitive to extreme values. Hereafter, we call this the simulated continuum. Simulating ~ 100 sources, we could determine the confidence levels in the following way: we sorted the simulated flux values in each bin. The one sigma ranges are determined by the values that include 68 % of the simulated continua and the two sigma range by those that include 95 %.

In the simulations and their analysis, we made use of the super-computer Altamira. This is a cluster working in High Performance Computing belonging to the Spanish Supercomputing Network (RES)¹.

3.5 Implementation of innovative methodologies to analyse the X-ray average spectra

Several novelties in our stacking method have been developed in this thesis. In the iron line studies, the fitting of the continuum is a delicate issue because conclusions about its EW and profile can be strongly model-dependent: an underestimation of the continuum can bring to an overestimation of the EW and to an incorrect study of its profile. To avoid being affected by such methodological errors, we introduced a new method to provide a model-independent estimation of the iron line significance (Sect. 3.7.2) and EW (3.7.3). We also introduced a spectrum-wide modelling of the effective resolution of our method (Sect. 3.7.1).

3.5.1 New model-independent estimation of the iron line significance

Taking the average simulated spectrum as a measurement of the underlying continuum in absence of emission features, we calculated the significance of the iron line excess in the observed spectrum with respect to the simulated continuum (see Table 3). To do this, in both the Chandra and the XMM CDFS fields, we calculated the percentage of simulations with a flux in a given range higher than that of the observed spectrum. Several energy ranges were chosen to represent a neutral iron line with variable σ for the *Chandra* deep fields and the XMM CDFS: 6.2-6.6 keV, 6-6.8 keV. Visually, the iron line of the deep *Chandra* fields looked narrow, for this reason we considered also a narrower range: 6.3-6.5 keV. For the XMM CDFS, instead, the detected line looked broad, to check this qualitative impression, we considered a broader range: from 5.5 to 7 keV. In the XMM CDFS sample, we also found an excess at about 7 keV, indicating a probable presence of an ionised line that we checked considering a range from 6.8 to 7. keV.

¹<http://i.top500.org/site/49911>

3.5.2 Model independent estimation of the EW

We developed a model-independent methodology to estimate the line EW for our XMM CDFS sample.

The EW of the iron line was estimated using the simulated continua, using the same energy bands considered in the calculation of its significance. We calculated, for each simulated sample, the EW. Approximating the definition of the EW in the equation 1.1 (see Chap. 1), we use the formula:

$$EW \sim 2\Delta \sum_{E-\Delta}^{E+\Delta} \frac{T(E) - C(E)}{C(E)}$$

where $T(E)$ represents the average observed spectrum, $C(E)$ the average continuum and the sum is performed over the bins (of width 2Δ) that correspond to the feature under consideration.

We have estimated the uncertainties in these EW in two different ways. We have first calculated them propagating the errors on the fluxes of the average observed and simulated spectra. Secondly, we have estimated the dispersion of the value of the EW using the 1σ percentiles of the distribution of the EW among the 110 simulations. In general, the dispersions are compatible with the error bars, if somewhat wider.

3.5.3 New method to estimate the effective resolution of our method

To study how the spectral resolution of the X-ray detectors and the averaging process widen the narrow spectral features in X-ray spectra, we performed simulations of unresolved lines. We simulated high SNR spectra (one simulation for each spectrum, without Poisson's noise) using a powerlaw with Γ fixed at 1.9, with unit normalisations, and an unresolved Gaussian ($\sigma=0$). The input EW was 200 eV. Initially the energy was fixed at 6.4 keV rest-frame. We corrected the spectra for the response (using a powerlaw with Gamma fixed at 1.9) and finally computed the average spectrum with the same treatment as that applied to the real spectra.

The original method just described was devised by Corral et al. (2008), but we further developed it to estimate the resolution of our method in the full 1-12 keV rest-frame band. We repeated the simulations of unresolved features at different energies for the XMM CDFS sample, since broad emission features were detected in the average spectrum of that sample and its subsamples. Unresolved gaussians centred at energies from 1 and 10 keV, with steps of 1 keV were simulated excluding Poisson noise. In addition, we simulated lines centred at 6.4 keV and 6.9 keV.

Each of these simulated spectra was then fitted with a $\Gamma=1.9$ continuum and a Gaussian of width σ_0 . The dependence of σ_0 with the energy E was fitted with a powerlaw $\sigma_0 \propto E^\alpha$. The values obtained with this trend allowed us to use the convolution model `gsmooth` in `Xspec` (see Sect. 3.1.1) to take into account this effective energy resolution.

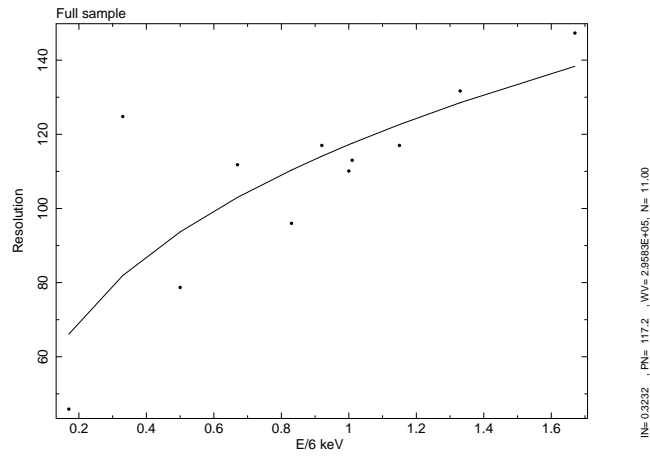


FIGURE 3.1: Instrumental resolution of our method as a function of $E/6$ with E spectral energy in keV.

The trend for the full XMM CDFS sample is shown in Fig. 3.1 where $\alpha \sim 0.3$.

Chapter 4

Stacking of the *Chandra* surveys

In this Chapter, we explore the AGN X-ray spectral properties from *Chandra* ultra-deep observations. The deep exposure of CDFS, AEGIS samples allows to survey a considerable population of high redshift AGN with good enough spectra to be analysed through stacking. The sample possesses a large number of absorbed sources; moreover, it encompasses a broad range of luminosities: for this reason the main tasks of this chapter are the study of the iron line properties in relationship with luminosity, redshift, and X-ray obscuration.

Chronologically, this was the first sample studied in our work and it has been published in Falocco et al. (2012).

4.0.4 Properties of the *Chandra* samples

The individual X-ray spectra of our sample have in average ~ 570 spectral counts in the 2-12 keV rest-frame band and do not allow detailed analysis of the individual spectra, except for a handful of sources. To increase the probability of detecting any broad component that would otherwise be hidden by the noise, we included in our analysis only those sources with more than 200 net (background-subtracted) counts in the band between 2 and 12 keV rest-frame. We discuss in App. A. the results corresponding to lower thresholds (50 and 100 counts). We further selected only sources with spectroscopic redshifts. Finally, we also excluded from our analysis two sources with more than 10000 counts individually: CDFS_056 (RA: 53.112, DEC: -27.685) and CDFN_141 (RA: 189.1, DEC: 62.383). These sources have such a strong signal in their spectra that they would dominate the average stacked spectrum.

Our full sample contains 123 sources with spectroscopic redshifts, with 70667 counts in total (see Table 4.1). The distribution of the net counts per source for this full sample is shown in Fig. 4.1. The redshift distribution of the sources is shown in Fig. 4.2, where we can see that our sample spans a broad range of redshifts from $z = 0$ up to $z = 3.5$.

TABLE 4.1: Properties of the *Chandra* full sample and the subsamples. Columns: (1) (Sub)Sample; (2) Number of sources; (3) number of net counts in 2-12 keV rest-frame; (4) number of net counts in 5-8 keV rest frame; (5) average redshift; (6) average rest-frame 2-10 keV luminosity in units of 10^{43} erg s^{-1} , from the fits to the single spectra, corrected for Galactic and intrinsic absorption; (7) average intrinsic column density in 10^{22} cm^{-2} *; (8) gamma from the fit of the average observed spectrum with a powerlaw between 2 and 5 keV (rest-frame); (9) χ^2/dof of the fit of the average observed spectrum with a powerlaw between 2 and 5 keV (rest-frame); (10) slope of the powerlaw of the average spectrum obtained with the simulations of the Fe line fitted with pow+gauss; the errors estimated are always ~ 0.001 ; (11) width obtained in those line simulations; (12) line EW obtained from those simulations.

Sample	N	N_{2-12}	N_{5-8}	$\langle z \rangle$	$\langle L_{43} \rangle$ 10^{43} erg/s	$\langle N_{H,22} \rangle$ 10^{22} cm^{-2}	Γ	χ^2/dof	Γ_{sim}	σ_{sim} eV	EW_{sim} eV
(1)	(2)	(3)	(4)	(5)	(6)	(7)	(8)	(9)	(10)	(11)	(12)
CDF-S	33	21561	5223	1.26	5.20	3.80	-	-	-	-	-
CDF-N	25	16134	3429	1.11	8.00	0.88	-	-	-	-	-
AEGIS	65	32971	6873	1.11	20.31	1.04	-	-	-	-	-
Total	123	70667	15526	1.15	13.82	1.75	1.24 ± 0.05	9.77/13	1.897	117 ± 1	182
$\log(N_H) > 21.5$	54	27888	7304	1.15	14.11	3.93	0.48 ± 0.07	8.94/13	1.898	129 ± 1	190
$\log(N_H) < 21.5$	69	42778	8222	1.14	13.55	0.05	1.78 ± 0.06	14.96/13	1.896	116 ± 1	181
$L_{43} < 8$	74	34620	7630	0.85	2.89	1.64	1.21 ± 0.06	10.42/13	1.893	111 ± 1	183
$L_{43} > 8$	49	36047	7896	1.60	30.20	1.91	1.31 ± 0.07	14.70/13	1.878	128 ± 1	174
$z < 1.005$	63	34843	7507	0.70	5.43	1.28	1.23 ± 0.06	10.57/13	1.896	105 ± 1	186
$z > 1.005$	60	35824	8019	1.62	22.50	2.24	1.24 ± 0.07	5.66/13	1.886	138 ± 1	180
$z < 0.76$	39	23713	5285	0.57	3.23	1.17	1.31 ± 0.07	11.68/13	-	-	-
$L_{43} < 14.3, z < 0.76$	36	19007	4446	0.57	2.00	1.25	1.29 ± 0.08	10.99/13	-	-	-
$L_{43} < 14.3, z > 0.76$	49	24286	4902	1.14	5.58	1.90	1.11 ± 0.08	7.27/13	-	-	-
$L_{43} > 14.3, z > 0.76$	35	22669	5339	1.80	37.05	2.19	1.34 ± 0.09	11.76/13	-	-	-

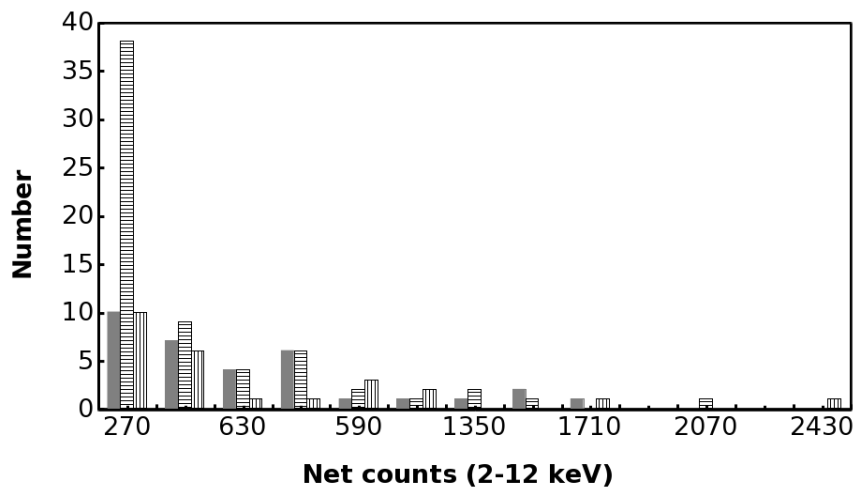


FIGURE 4.1: Distribution of the net counts between 2 and 12 keV (rest-frame). Filled histogram: CDF-S; histogram with horizontal stripes: AEGIS; histogram with vertical stripes: CDF-N.

Before spectral fitting, all the spectra were grouped with a minimum of five counts per bin, and we applied the modified Cash statistics discussed in the Xspec pages ¹ and described in Cash (1979).

This grouping was adopted because we used the same method for all the sources with more than 50 counts (see Appendix A), for which the more common χ^2 statistics would not be adequate.

¹ <http://heasarc.gsfc.nasa.gov/docs/xanadu/xspec/wstat.ps>

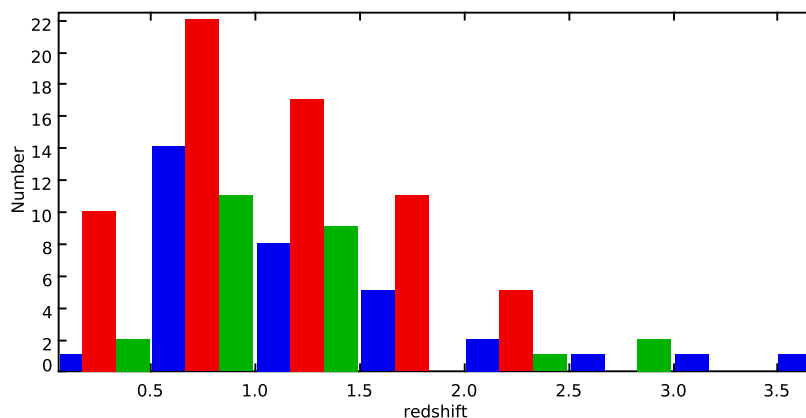


FIGURE 4.2: Redshift distribution. Blue histogram: CDF-S; red histogram: AEGIS; green histogram: CDF-N.

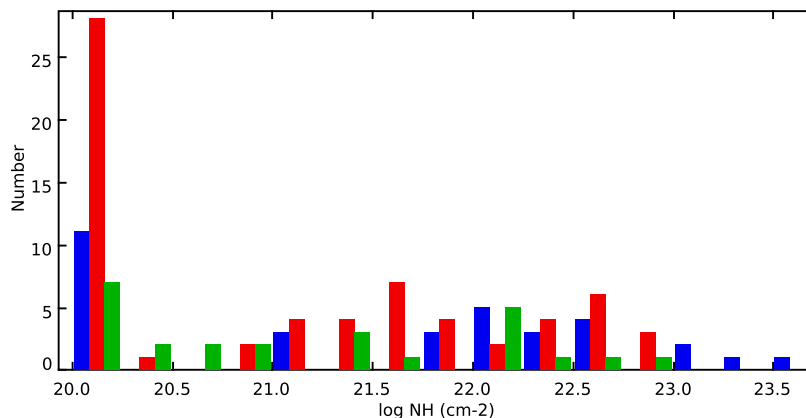


FIGURE 4.3: Distribution of intrinsic column density in units of cm^{-2} . Blue histogram: CDF-S; red histogram: AEGIS; green histogram: CDF-N. We grouped the spectra with $\log(N_{\text{H}}) < 10^{20}\text{cm}^{-2}$ with the spectra having $\log(N_{\text{H}}) = 10^{20}\text{cm}^{-2}$.

It should be noted that in this step we did not aim at making a detailed analysis of the individual spectra but rather only at obtaining a set of parameters that we used to unfold the spectra for all the instrumental effects (see Sect. 3). The model is a single powerlaw modified by Galactic absorption (with fixed column density values at $1.4 \times 10^{20}\text{cm}^{-2}$ for AEGIS, $0.772 \times 10^{20}\text{cm}^{-2}$ for CDF-S, $0.993 \times 10^{20}\text{cm}^{-2}$ for CDF-N) plus intrinsic absorption at the redshift of each source. We left the slope of the powerlaw, its normalisation and the intrinsic column density as free parameters. The fit was performed in the rest-frame energy range between 1 and 12 keV, minimising the contribution from any putative soft excess present in the sources. The resulting distribution of intrinsic column densities is shown in Fig. 4.3. Most of the absorbed sources ($\log(N_{\text{H}}/\text{cm}^2) > 21.5$) belong to CDF-S, as indicated by the higher average column density for that sample in Table 4.1.

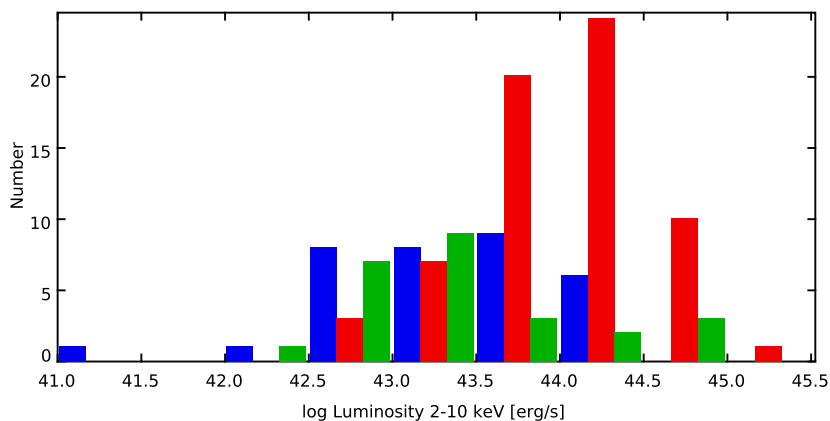


FIGURE 4.4: Distribution of rest-frame 2-10 keV luminosities in units of erg s^{-1} . Blue histogram: CDF-S; red histogram: AEGIS; green histogram: CDF-N.

4.0.5 Subsample definition

We show in Fig. 4.4 the distribution of the X-ray luminosities (between 2 and 10 keV rest-frame) of the sources corrected for Galactic and intrinsic absorption, calculated from the fit to the individual spectra. The average luminosity of the AEGIS sources is one order of magnitude higher than the average luminosity of CDF-N and CDF-S sources (Table 4.1).

We compared the distribution of our full sample in the luminosity-redshift plane with that of Streblyanska et al. (2005) in the Lockmann Hole (Fig. 4.5). We sampled that plane better at $z < 3$ for all luminosities. Compared to the Corral et al. (2008) sample (XMS-XWAS) (Fig. 4.6), we covered about one order of magnitude lower luminosities for $0.5 < z < 3$. Finally, with respect to Brusa et al. (2005), the addition of the AEGIS sample and the restriction to sources with high numbers of counts allowed us to span a broader range of luminosities at similar z . In summary, our sample, if compared with previous surveys studied with similar analysis, possesses a unique combination of deep coverage with high z sources, a broad span of luminosities, and good statistics.

One of the main aims of our work is to understand the dependence of the spectral properties of the AGN on luminosity, redshift, and intrinsic absorption. For this reason, we performed the analysis of the stacked spectra not only for the full sample, but also for subsamples defined in terms of column density (N_{H}), luminosity, and redshift. Except for N_{H} (see below), the bins have been designed to have a similar numbers of total counts. The characteristics of each subsample can be seen in Table 4.1.

- Intrinsic N_{H} : The threshold column density was set at $\log(N_{\text{H}}/\text{cm}^2) = 21.5$. because the absorption features of the X-ray spectra are detected in the AGN with $\log(N_{\text{H}}/\text{cm}^2) > 21.5$ (see Sect. 1.4). We show in Fig. 4.7 the distribution of the absorbed and unabsorbed subsamples just defined: the two subsamples have a similar distribution in the luminosity-redshift plane, so

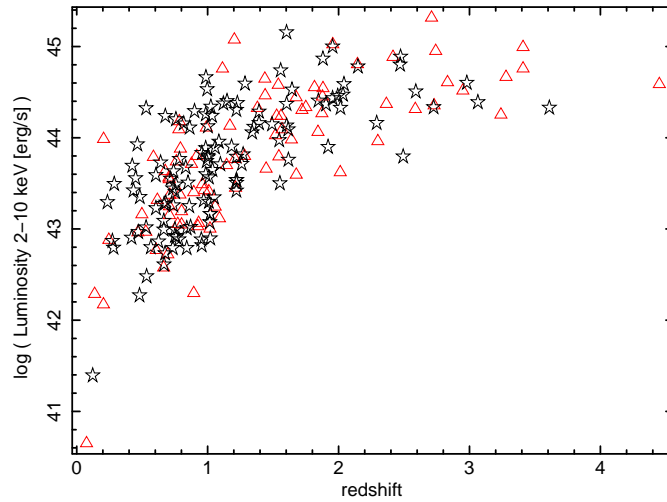


FIGURE 4.5: Comparison of our full sample (black stars) with the deep *XMM-Newton* sample of Streblyanska et al. (2005) (LH, red triangles), in the luminosity-redshift plane.

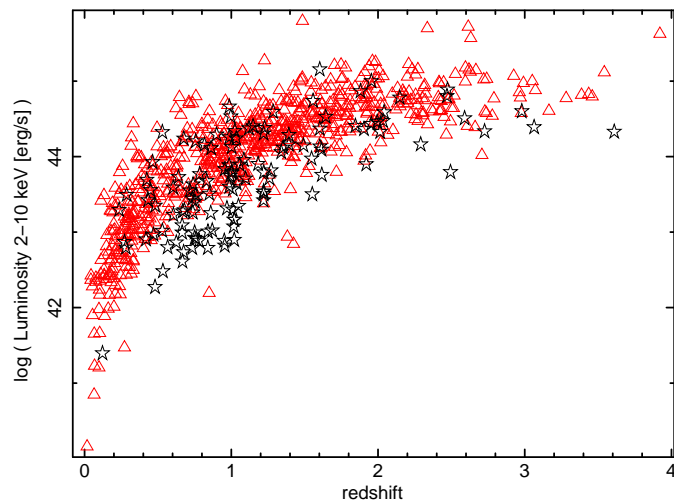


FIGURE 4.6: Comparison of our full sample (black stars) with the medium *XMM-Newton* sample of Corral et al. (2008) (XMS+XWAS, red triangles), in the luminosity-redshift plane. For clarity, we omitted one XMS+XWAS source at $z = 2.34$, $L = 1.28 \times 10^{47} \text{ erg s}^{-1}$.

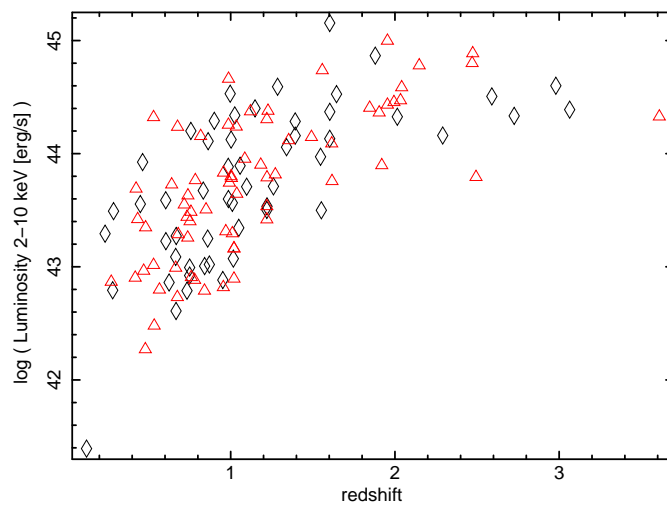


FIGURE 4.7: Distribution of the unabsorbed (red triangles) and absorbed (black diamonds) subsamples (see Sect. 2.3) in the luminosity-redshift plane.

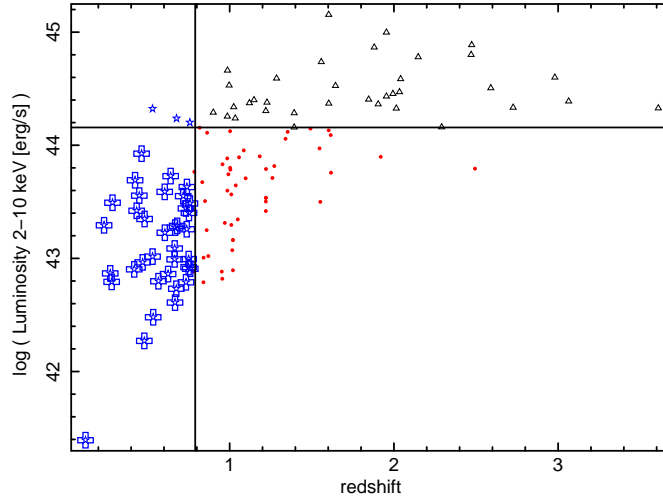


FIGURE 4.8: Distribution of the $L - z$ subsamples (see text) in the luminosity-redshift plane. The dividing point is $z = 0.76$, $L = 1.435 \times 10^{44} \text{ erg s}^{-1}$ (marked by the horizontal and vertical solid lines).

The three blue stars mark the sources that allow defining distinct $L - z$ subsamples (see text).

they are fair representations of the AGN with and without absorption, with no other parameters playing an important role (see also Table 4.1).

- **Luminosity:** We separated high and low luminosity sources using a threshold $L = 8 \times 10^{43} \text{ erg s}^{-1}$. The L is the luminosity between 2 and 10 keV.
- **z :** We built a low- z and a high- z subsample with a threshold $z = 1.005$.
- **$L - z$:** Initially we divided the full sample into three subsamples: (i) $z < 0.76$ (hereafter low z -low L) (ii) $z > 0.76$ and $L < 14.35 \times 10^{43} \text{ erg/s}$ (hereafter high z -low L) (iii) $z > 0.76$ and $L > 14.35 \times 10^{43} \text{ erg/s}$ (hereafter high z -high L). In the low z -low L subsample just defined there are only three sources above $L = 14.35 \times 10^{43} \text{ erg/s}$ (with ~ 4000 total counts), so we also used a second version of this subsample using only sources with $z < 0.76$, $L < 14.35 \times 10^{43} \text{ erg/s}$ so that this subsample and the two high z subsamples cover distinct z and L intervals. All results are very similar, and we used the latter definition of distinct areas as our default.

4.1 The average *Chandra* spectrum of AGN in the total sample

We show in Fig. 4.9 the average spectrum of the total *Chandra* sample. In the normalisation process the integral of the continuum flux per each source is performed in the band between 2 and 5 keV. In spite of the high number of absorbed sources, especially belonging to the CDFS survey, we did not include the band between 8 and 10 keV in the calculation of the continuum as we did for XMM CDFS (see Chap. 5). In fact, due to the low number of counts in this spectral range in the *Chandra* observations, this band has a much lower flux than the region in 2-5 keV.

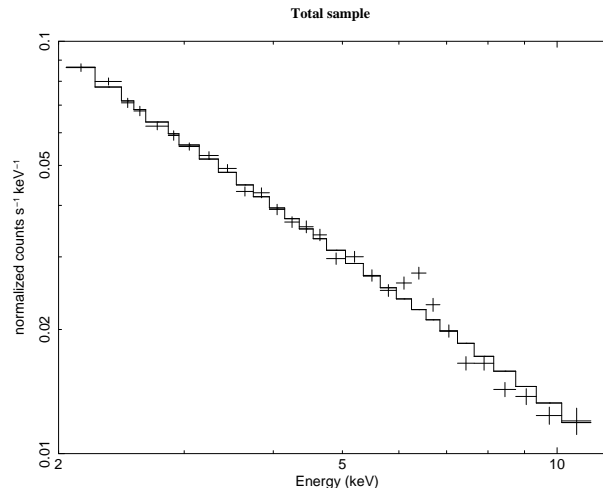


FIGURE 4.9: Average observed spectrum of the full sample fitted with a powerlaw between 2 and 5 keV.

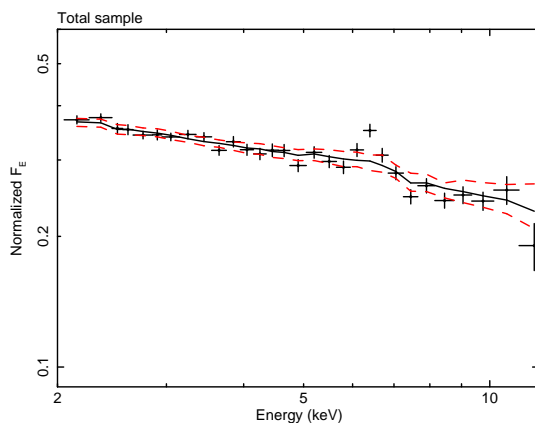


FIGURE 4.10: Average observed spectrum of the full sample (data points) with the average simulated continuum (continuous line) and the one-sigma confidence limits (dashed lines).

If we fit the 2-5 keV range with a powerlaw and extrapolate it to the full range, an excess can be clearly seen around the expected position of the Fe emission line. However, any features found in the average spectra must be carefully evaluated, as the averaging procedure itself may introduce some distortions. For this reason, we computed the continuum using simulations, as described below.

We represent in Figs. 4.10, 4.11, 4.12, 4.13, and 4.14 the average observed spectra of the full sample and all subsamples, along with the simulated continua, and the 1 sigma confidence limits. Features around the expected location of the Fe K line are conspicuous in all the subsamples.

Before attempting to draw any conclusions from those features, we characterised the effect of our averaging method on narrow lines using simulations, as described in Chapter 3.

We simulated a high SNR iron line using the procedure explained in detail in Chapter 3. $\Gamma_{simline}$, $\sigma_{simline}$, and EW of Table 4.1 are the results of fitting a powerlaw plus a Gaussian to these simulations for some of the samples. The EW and powerlaw slope are recovered very well. The width of the line has become $\sigma \sim 120$ eV. Therefore, our resulting “instrumental resolution” is around 120 eV; i.e., any

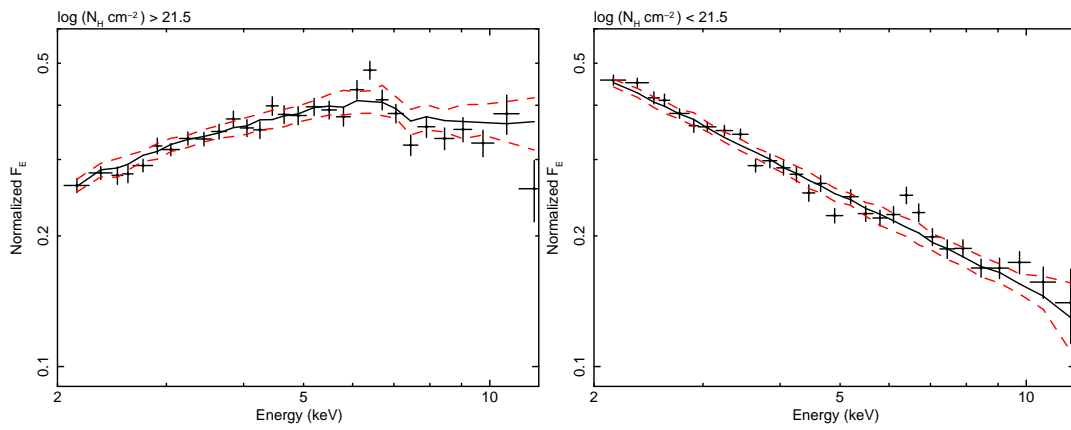


FIGURE 4.11: Average observed spectra (data points) of the absorbed (left) and unabsorbed (right) subsample with their average simulated continua (continuous line) and the one-sigma confidence limits (dashed lines).

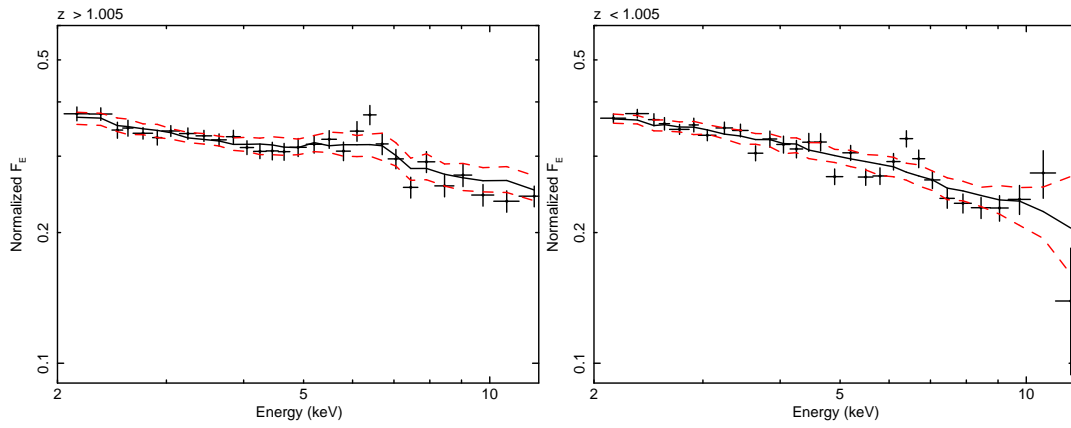


FIGURE 4.12: Average observed spectra (data points) of the high- z (left) and low- z (right) subsamples with their average simulated continua (continuous line) and the one-sigma confidence limits (dashed lines).

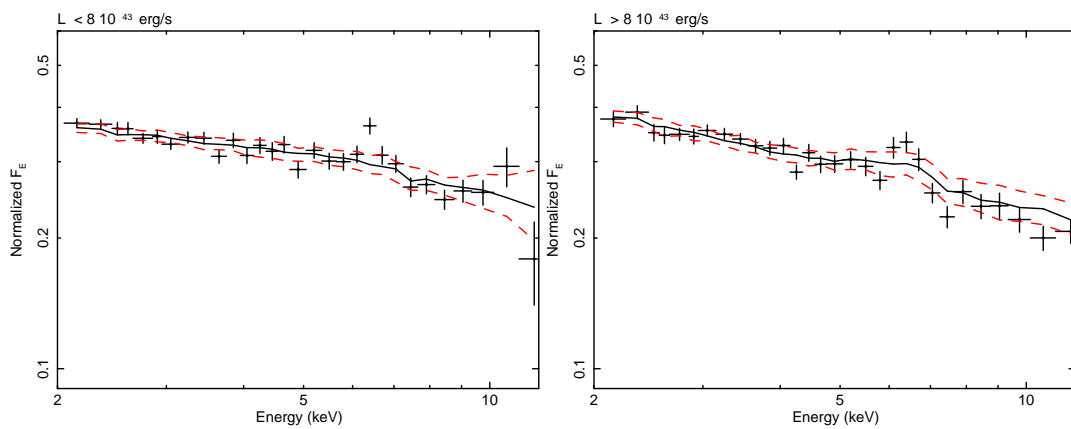


FIGURE 4.13: Average observed spectra (data points) of the high- L (right) and low- L (left) subsamples with their average simulated continua (continuous line) and the one-sigma confidence limits (dashed lines).

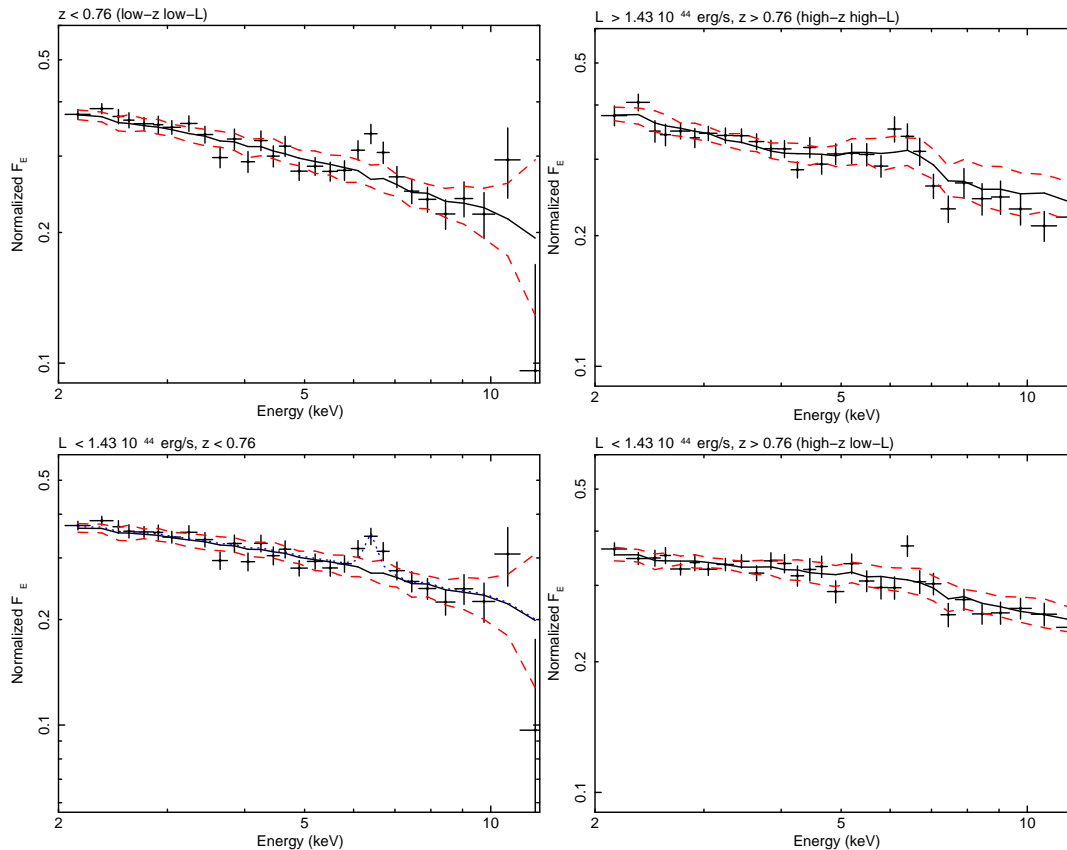


FIGURE 4.14: Average observed spectra (data points) of the $L - z$ subsamples with their average simulated continua (continuous line) and the one-sigma confidence limits (dashed lines). For comparison, in the bottom-left panel we represent with a dotted line the result of adding to the simulated continuum a Gaussian centred at 6.4 keV, with $\sigma=120$ eV, as obtained from the simulations of the Fe line (Sect. 3.3).

real detected feature around rest-frame 6.4 keV should be wider than this value, and its actual width will be the convolution of its intrinsic width with this value, roughly added in quadrature (see Eq. 1 below).

We show in the bottom-left corner of Fig. 4.14 the expected profile of an unresolved 6.4 keV line added to the simulated continuum for the corresponding subsample. In general, the features we observe around that energy appear to be compatible with such an unresolved line, except perhaps for the low z -low L , subsample. We quantify these qualitative impressions in Section 4.2.2.

4.2 Results

In this section we study the statistical significance of the Fe line and its properties in several steps. We first describe our results from our model-independent way to calculate the significance of the line detection, then we discuss its significance and characteristics again by fitting the average spectra using a

single Gaussian to fit the Fe line. Then, we study the dependence of the line on z and X-ray luminosity. Finally, we try complex line models with those subsamples that show significant broad line profiles.

4.2.1 Results from our model-independent method

To estimate the significance of the excess observed in the Fe K line region, we calculated the percentage of average simulated spectra (from the simulations of the continuum described in Sect. 3.4) having a flux in the Fe K region lower than the flux of the observed spectrum (as explained in Sect. 3.5). The Fe line flux was calculated in three regions centred at 6.4 keV, with half-widths of 0.1 keV, 0.2 keV, and 0.4 keV, respectively. The significances of the Fe line estimated in this way for the full sample and all subsamples are shown in Table 4.2.

The narrowest interval was chosen at the limit of the instrumental broadening, a significant excess found just in this range and not in the other two would in principle correspond to a detection of a narrow line. On the other hand, increasing the width includes more flux from a putative broad line, but it also increases the noise, hence a broad component would be more difficult to detect. We use the ± 0.2 keV wide option (column S_2 in Table 4.2) as our fiducial value, since it maximises the SNR for unresolved and moderately broad lines. We can see that the line is very significant ($> 98\%$) in the full sample and in almost all the subsamples, with the exception of the high z -high L one. In general, the significance is higher for low z and low L .

In all cases, the significance stays about the same or decreases when ΔE increases. This is either an effect of the expected lower SNR for wider intervals, or might indicate the presence of a wider profile in the cases where the significance does not decrease noticeably.

TABLE 4.2: Significance of the Fe line estimated from the fraction of simulations that have fluxes in the corresponding bands higher than the average spectra of the full sample and the subsamples.

Sample	6.3-6.5 keV	6.2-6.6 keV	6.0-6.8 keV
	(1)	(2)	(3)
Total	100	100	99
$\log(N_{\text{H}}/\text{cm}^2) > 21.5$	99	99	98
$\log(N_{\text{H}}/\text{cm}^2) < 21.5$	100	100	100
$L_{43} < 8$	100	100	100
$L_{43} > 8$	97	98	96
$z < 1.005$	100	100	100
$z > 1.005$	98	98	98
$L_{43} < 14.3, z < 0.76$	100	100	100
$z < 0.76$	100	100	100
$L_{43} < 14.3, z > 0.76$	99	98	91
$L_{43} > 14.3, z > 0.76$	88	88	86

4.2.2 Results from our model dependent method (fits to the data)

We performed the spectral analysis employing the simulated continuum as a `table` model in `Xspec` to represent the broad band continuum. During the fits described below, we have always left its normalisation free to vary, and its value returned in `Xspec` is always around one. We added the required components to the table model when we found residuals. We used the goodness of fit criterion and the confidence interval for a given parameter corresponding to a $\Delta\chi^2 = 2.71$ (90 % probability).

The fit results are shown in Table 4.3.

The σ we mention in the remainder of this work (including Table 4.3) refers to the intrinsic width of the line, taking the broadening introduced by our method into account.

$$\sigma^2 = \sigma_{obs}^2 - \sigma_{sim}^2$$

where σ_{obs} is the total width returned by Xspec, and σ_{sim} the instrumental width obtained from the simulations of an unresolved Fe K line (120 eV, see Sect. 4.3.). During the fits, we forced the width of the Gaussian line to satisfy the condition: $\sigma_{obs} \geq \sigma_{sim}$ (where we used the average value obtained as explained in Chapter 5, with σ_{sim} reported in Table 4.1 of ~ 120 eV).

We made the fits in several steps:

- Fixed $\sigma=0$ and fixed centroid energy at 6.4 keV: this allows us to estimate the significance of the narrow component of a neutral Fe K line (first line for each sample in Table 4.3)
- Fixed centroid energy at 6.4 keV and free σ : it studies the significance of a possible broad component and constrains its width (second line for each sample)
- Free centroid energy and fixed $\sigma=0$: it considers the presence of an ionised narrow Fe component and estimates its centroid energy (third line for each sample)
- Free centroid energy and free σ : this leaves all options open (fourth line for each sample)

We calculated the significance of the Gaussian with the $\Delta\chi^2$ corresponding to the fits with and without the line component, and we checked the corresponding probability using the incomplete β function (Press et al. 2007).

The significance of adding the gaussian is in Col. 3 in Table 4.3. In the same way, we estimated the significance of allowing the width and/or the centroid energy to vary with respect to the baseline narrow and neutral line.

We summarise here the results for our (sub)samples (see Table 4.3 and Figs. 4.15, 4.16, 4.17, 4.18, and 4.19):

- *Full sample:*

The spectrum of the full sample fitted with the table model and the Gaussian with free energy and free σ are shown in Fig. 4.15. We can see that the model fits the spectrum well in the Fe line region. The detected line is narrow. We do not observe any ionised Fe line component.

- *Absorbed and unabsorbed subsamples:*

The spectra and fitted models are shown in Fig. 4.16. The continuum of the unabsorbed sample is well fitted by a powerlaw with $\Gamma \sim 1.8$ (see table 4.1), a common value for the AGN, and is flatter in the absorbed sample, as expected. The line is characterised by having a narrow profile for both subsamples. Only in the unabsorbed sample might the centroid energy of the line suggest a contribution from mildly ionised Fe. However, the centroid energy is consistent with 6.4 keV within the 90 % confidence level, and the significance of $\sigma > 0$ from the $\Delta\chi^2$ is < 90 %.

- *High- and low-luminosity subsamples:*

The spectra and fitted models are shown in Fig. 4.17. The results of the fits suggest a more intense Fe line in the low- L subsample. We discuss the dependence of the EW on redshift and luminosity more in detail in the next Section. The detected line is narrow, and there is no significant ionised Fe contribution.

- *High and low redshift subsamples:*

The spectra and fitted models are shown in Fig. 4.18. The Fe line is more significant at low redshift than at high redshift, and this can reflect the same trend just found with the luminosity, since sources with higher L are usually found at higher z . The line profile is narrow in both cases. The fits with the centroid energy free shows a mildly ionised Fe contribution in the low redshift sample, but 6.4 keV is within the 90 % confidence interval.

- *L-z subsamples:*

The strongest line significance is found at low z and low L , then decreasing with both redshift and luminosity. The line profile is broad only in one case, in the low redshift- low luminosity sample (>95.4 % probability). The line profile looks symmetric (see Figs. 14 and 4.19, two left hand panels). Moreover, in the top-left hand panel there seems to be an excess in the narrow bin around 6.4 keV, which might come from an additional narrow component. We discuss in more detail the shape of this feature in Section 4.2.4. In the two other subsamples, the detected profile of the Fe line is narrow. We did not find any ionised Fe component.

At high energies (~ 10 keV), we observed an excess in some spectra that can be interpreted as part of the Compton reflection. The paucity of counts at these energies does not allow us to make a more accurate assessment of this continuum component. An absorption feature was also detected, to some extent, in some of our average spectra around 7-8 keV. This can be explained as the Fe edge commonly found along the Compton reflection component.

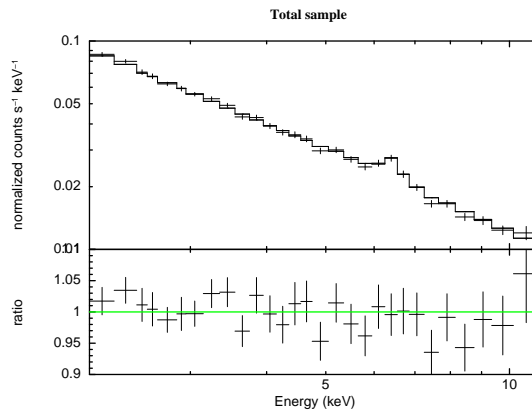


FIGURE 4.15: Fit of the average spectrum of the full sample using the simulated continuum model + Gaussian (with free σ and free centroid energy)

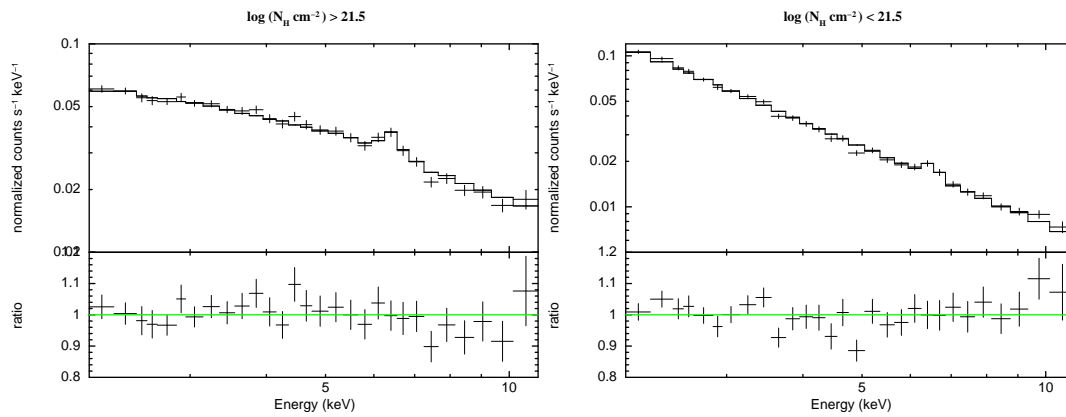


FIGURE 4.16: Fit of the average spectrum of the absorbed (left) and unabsorbed (right) subsamples using the simulated continuum model + Gaussian (with free σ and free centroid energy)

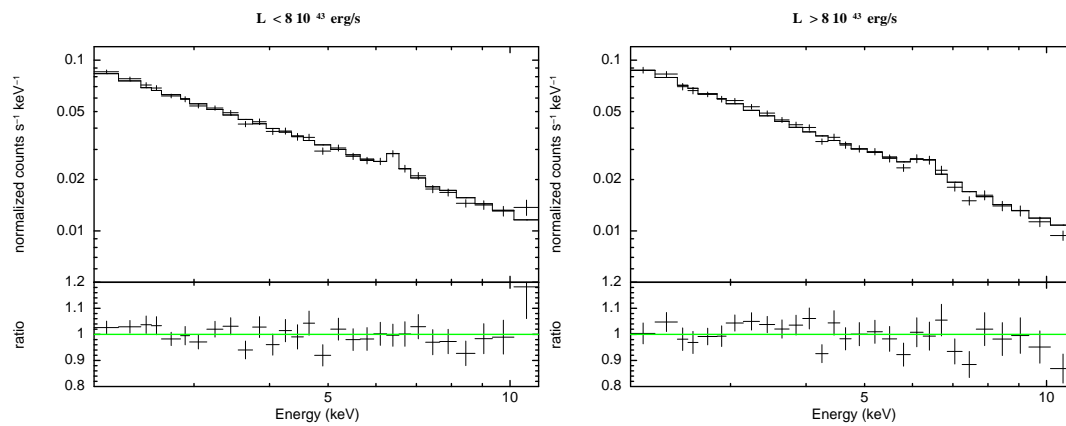


FIGURE 4.17: Fit of the average spectrum of the low-luminosity (left) and high-luminosity (right) subsamples using the simulated continuum model + Gaussian (with free σ and free centroid energy)

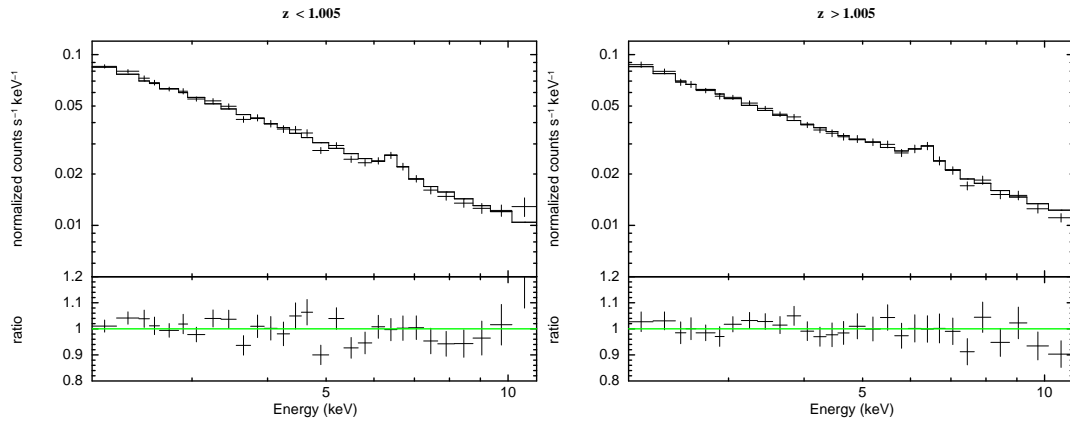


FIGURE 4.18: Fit of the average spectrum of the low-redshift (left) and high-redshift (right) subsamples using the simulated continuum model + Gaussian (with free σ and free centroid energy)

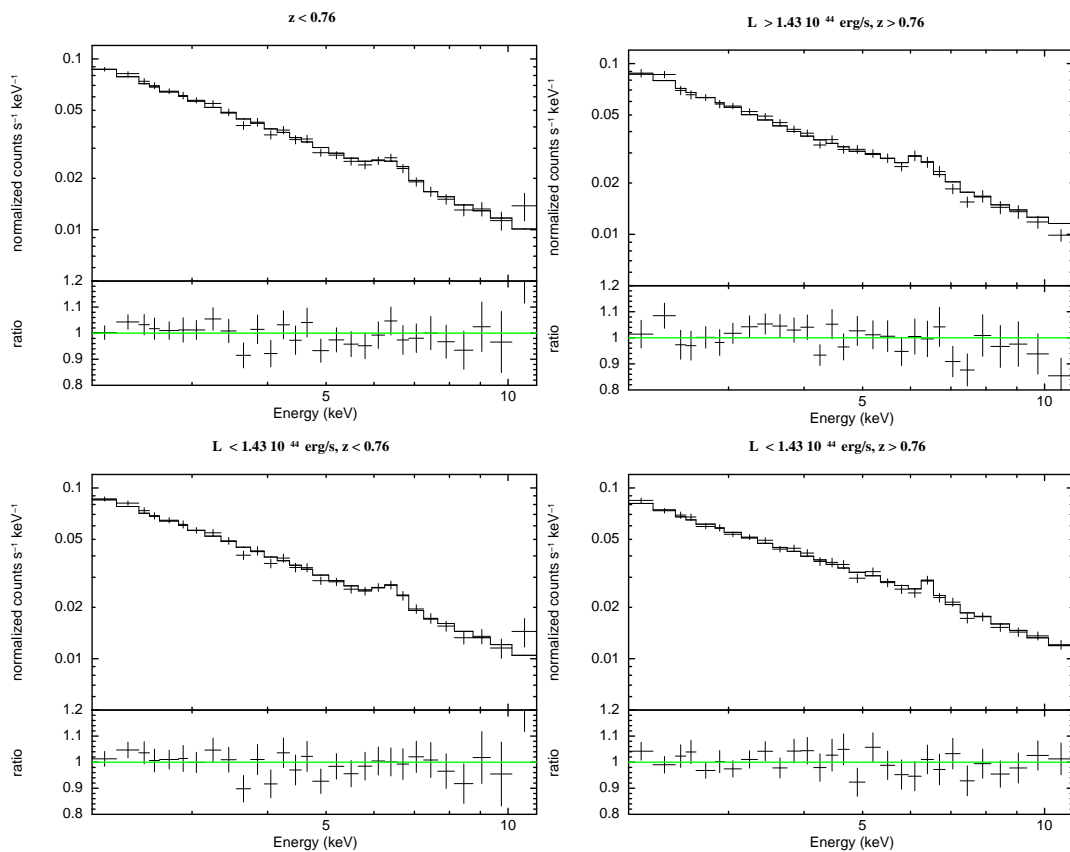


FIGURE 4.19: Fit of the average spectrum of the $L - z$ subsamples (low L -low z subsamples in the left panels, low L - high z subsamples in the right bottom panel, high L -high z subsample in the right top panel) using the simulated continuum model + Gaussian (with free σ and free centroid energy)

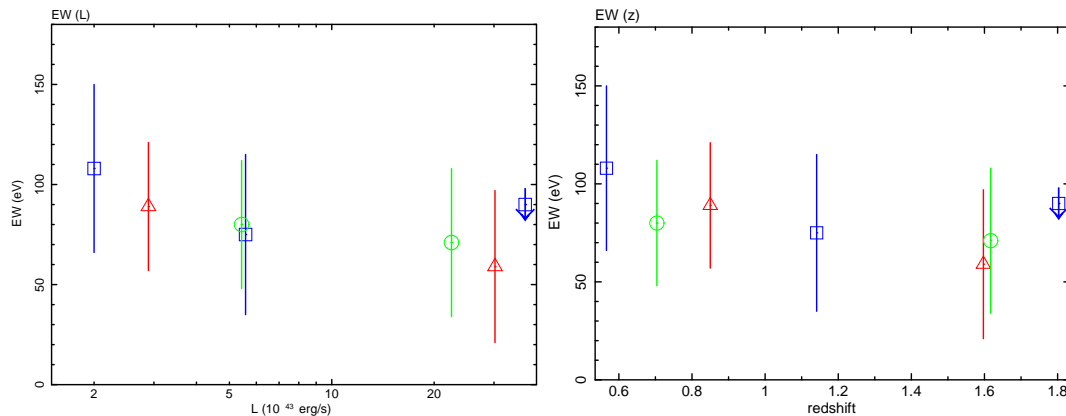


FIGURE 4.20: Dependence of unresolved 6.4 keV Fe line equivalent width on the average luminosity (left) and the average redshift (right) of the subsamples (first row of 4.3). Squares: $L - z$ subsamples; circles: redshift subsamples; triangles: luminosity subsamples. We represent upper limits by a down-pointing arrow. Each set of points with the same symbol are statistically independent, but not between the symbols.

4.2.3 Dependence on redshift and luminosity

As our results seem to suggest a dependence of the Fe line EW on redshift and on luminosity, for low- z and low-luminosity AGN, we checked this result in more detail to understand it better. The distribution of the line EW with the average z and the average luminosity of the subsamples are shown in Fig. 4.20. In those figures, the same symbols refer to statistically independent subsamples. In contrast, subsamples with different symbols are not statistically independent and there will be significant overlapping among the sources included in each subsample. We have used the fits corresponding to an unresolved line fixed at 6.4 keV (first line for each subsample in Table 4.3).

At first view the EW seems to decrease both with increasing z and X-ray luminosity. However, looking, for example, at the blue squares (corresponding to independent $L - z$ subsamples), it is clear that a constant EW is consistent with the data points within the error bars, so the trend, albeit suggestive, is not statistically significant.

4.2.4 Analysis of broad lines

We detected with strong significance narrow Fe K lines in all samples. Additionally, in the low L -low z subsample, the Fe line appears significantly broadened (with a significance above two sigma). We investigate here whether relativistic profiles are better fits than a simplistic broad Gaussian.

We added to the simulated continuum the `diskline` model in Xspec, which describes a relativistically broadened emission line for an accretion disk around a Schwarzschild Black Hole. We fixed R_{out} , the external radius of the accretion disk, to $1000 R_g$; we also fixed the β , the emissivity, to its default value, -2. In this hypothesis, the relativistic model adopted implies that the emissivity scales as r^{-2} :

the bulk of the line emission is concentrated in the inner disk, as 50 % of the emission is produced within $\sim 12R_g$.

We chose to leave free to vary only the inner radius, because we felt that the limited spectral quality of our average spectra did not allow to determine the full set of `diskline` parameters. For the R_{in} , the inner radius, we obtained an upper limit ($< 142 R_g$). As mentioned in Sect. 1, the inner radius of the accretion disk is expected to be lower ($6R_g$ for a non-rotating black hole and $1.23R_g$ for a maximally-rotating one). The EW is consistent with the one obtained in the fit with the Gaussian (see 4.3): $EW=152_{-70}^{+70}$ eV. The significance of adding a Fe line with `diskline` to the continuum is $> 99.99\%$, again consistent with the case of the Gaussian (4.3). The fit gives $\chi^2/dof=20.53/24$, to be compared with $\chi^2/dof=19.07/25$ for the Gaussian (with free energy and free σ): the fit does not improve introducing the more complex model represented by the `diskline`. Summarising, the `diskline` fits both the Fe K line and the Gaussian. We do not significantly detect a definite relativistic profile in the line, although it cannot be excluded.

Alternatively, the profile of the line could be characterised as the sum of both a broad and a narrow component since, in principle, we would expect a contribution from both a material away from the SMBH (narrow component) and disk (broad component) reflections. We assessed the significance of this possibility by making a final test in the low L - low z sample: we added a broad Gaussian to the narrow Gaussian (i.e. combining models in the first and second lines of 4.3). We fixed the centroid energies of the two Gaussians at 6.4 keV and the σ to zero in the narrow Gaussian and to 240 eV (the value in the second line in 4.3) in the broad Gaussian.

We calculated the EW of the narrow and broad components, obtaining < 84 eV and 158_{-78}^{+78} eV, respectively. This fit gives $\chi^2/dof=19.15/26$, to be compared with $\chi^2/dof=23.70/27$ of the fit with only narrow Gaussian (in 4.3). The significance of adding the broad component ($\Delta\chi^2=4.55$ and $\Delta\nu=1$) is $> 95.4\%$ but $< 99\%$, calculated as mentioned in Sect. 4.2. We conclude that a double Gaussian is a better fit, but only at the 2σ level.

4.3 Conclusions

We studied the average spectrum of a sample of 123 distinct AGN with more than 200 net counts each selected from the *Chandra* AEGIS, CDF-N, and CDF-S surveys, covering $0 < z < 3.5$ and totalling >70000 counts.

We repeated the averaging procedure for the subsamples defined in two intervals of column density, 2-10 keV X-ray luminosity, redshift, and in three 2D intervals in the luminosity-redshift ($L - z$) plane (see Table 4.1). We then estimated the significance of the presence of narrow and broad features around 6.4 keV in a model-independent way (4.2), finding that narrow features are significant at $\geq 98\%$, except

for the high- L , high- z subsamples, where it is lower. Broad features would be harder to detect and are most significant at low L and low z .

Analysing the spectra with Xspec using the simulated continuum and modelling the Fe line as a Gaussian, we found strong evidence of a narrow Fe line at high significance in our full sample and in most of our subsamples, in particular (Table 4.3):

- We detected a strong ($> 99.73\%$) narrow Fe line with $EW = 85 \pm 35$ eV and 73 ± 32 eV in the absorbed and unabsorbed subsamples, respectively (defined as having intrinsic column density above and below $10^{21.5}$ cm $^{-2}$, respectively), with a hint of higher central energy ~ 6.5 keV in the unabsorbed case, but still compatible with 6.4 keV at 90%.
- Segregating the sources purely on luminosity, we found that the average spectrum in the low- L ($L < 8 \times 10^{43}$ erg s $^{-1}$) subsample shows a significant and strong narrow Fe line ($EW = 89 \pm 32$ eV at $>99.99\%$). The significance and strength of the high- L are clearly smaller: $EW = 59 \pm 38$ eV at 95.4%, but the EW are compatible within 90%.
- By separating the sample instead at $z = 1.005$, the narrow Fe line is again stronger in the low- z subsample ($EW = 80 \pm 32$ eV at $>99.99\%$) than in the high- z subsample ($EW = 71 \pm 37$ eV at $>99.73\%$), but the difference is not statistically significant
- By defining distinct areas in the $L - z$ plane (the division point was $L = 14.3 \times 10^{43}$ erg s $^{-1}$, $z = 0.76$), the most significant line is found in the low L -low z subsample ($EW = 108 \pm 42$ eV at $> 99.99\%$), with a hint of a broad component ($\sigma = 240 \pm 90$ eV at $> 2\sigma$ significance). The low L -high z subsample also shows a somewhat weaker narrow line ($EW = 75 \pm 40$ eV at $\sim 99.7\%$). The Fe line detection is at $< 90\%$ significance in the high L -high z subsample ($EW < 90$ eV)

We studied the trend of the EW for the narrow Fe line with redshift and luminosity of our subsamples. We did not find a significant dependence: in Fig. 4.20 that trend is not statistically more significant than a constant. To disentangle the effects of the two parameters on the line detection, surveys of AGN covering a wider area in the $L - z$ plane are needed. Since the Fe line is detected more significantly at low- L and low- z , samples of the local Universe are particularly suited to this end.

We also investigated whether more sophisticated models for the line profile would provide a better fit, concentrating on the low L -low z subsample, since it is the only one where a broad line may have been detected. A diskline relativistic profile provides a worse fit than a broad Gaussian, with less degrees of freedom. Additionally, the inner radius of the disk would be too large to produce significant relativistic effects. Therefore, we do not find any evidence of a relativistic profile in any of our average spectra.

Allowing for both a narrow (from neutral material far away from the central source, e.g. the putative torus) and a broad Gaussian (as just discussed) component provides a better fit to the average low- z and low- L subsample than a single narrow or broad Gaussian, but with a modest significance $< 99\%$.

To explain the symmetrically broadened line detected in the low L -low z subsample of the *Chandra* survey, we should consider two possibilities. In first place, there can be a blending with narrow lines from neutral and ionised material. Evidences for the presence of an ionised line have been recently found in the stacking of COSMOS sample (Iwasawa et al. 2012). In the second hypothesis, instead, we detect a broad symmetrical gaussian because the spectral SNR in this survey is insufficient for the detection of the asymmetric relativistic line profile.

The study of more sensitive surveys with a superior spectral quality would help to assess the presence of the relativistic iron lines in more detail: to this end, we explore in the next Chapter the deepest survey by the *XMM-Newton* satellite, its observation in the *Chandra* Deep Field South.

As already stated at the beginning of this Chapter, the results of the deep *Chandra* fields are part of a paper published in A&A (Falocco et al. 2012).

TABLE 4.3: Results of fits of the average spectrum of the full sample and its subsamples. L_{43} : luminosity in units of 10^{43} erg s^{-1} . Columns: (1) sample; (2) χ^2/dof of the fit with simulated continuum model; (3) χ^2/dof of the fit with the same continuum and the Gaussian; (4) probability $P(\Delta\chi^2, \Delta\nu)s, g$ (of adding the Gaussian to the model, see text); (5) probability $P(\Delta\chi^2, \Delta\nu)g, g_0$ (of leaving the parameter of the Gaussian free, see text); (6) central energy of the Gaussian; (7) σ after subtracting resolution obtained in the simulations of the Fe line; (8) EW of the Gaussian; (9) average redshift of the sample; (10) average luminosity of the sample in (10^{43}) erg s^{-1} ; (11) average column density of the sample in 10^{22}cm^{-2} .

Sample	$\chi^2/\text{dof}(s)$	$\chi^2/\text{dof}(g)$	P_1 %	P_2 %	E keV	σ eV	EW eV	$\langle z \rangle$	$\langle L_{43} \rangle$ $10^{43} \text{erg s}^{-1}$	$\langle N_{\text{H},22} \rangle$ 10^{22}cm^{-2}
(1)	(2)	(3)	(4)	(5)	(6)	(7)	(8)	(9)	(10)	(11)
Full	47.50/28	23.74/27	> 99.99		6.4	0	74 ± 24	1.15	13.80	1.75
		21.98/26	> 99.99	< 90	6.4	< 138	94 ± 30			
		23.74/26	> 99.99	< 90	6.40 ± 0.10	0	73 ± 25			
		21.98/25	> 99.99	< 90	6.40 ± 0.10	< 123	92 ± 28			
$\log(N_{\text{H}}) > 21.5$	35.61/28	21.66/27	> 99.73		6.4	0	85 ± 35	1.15	14.11	3.93
		21.15/26	> 99.73	< 90	6.4	< 123	100 ± 45			
		21.42/26	> 99.73	< 90	6.28 ± 0.02	0	92 ± 41			
		21.22/25	> 99.73	< 90	6.40 ± 0.30	< 151	91 ± 39			
$\log(N_{\text{H}}) < 21.5$	53.03/28	39.38/27	> 99.73		6.4	0	73 ± 32	1.14	13.55	0.045
		38.18/26	> 99.73	< 90	6.4	< 189	100 ± 43			
		37.41/26	> 99.73	< 90	6.50 ± 0.10	0	85 ± 36			
		37.15/25	> 99.73	< 90	6.50 ± 0.10	< 59.6	87 ± 36			
$L_{43} < 8$	44.26/28	23.96/27	> 99.99		6.4	0	89 ± 32	0.85	2.89	1.64
		23.70/26	> 99.99	< 90	6.4	< 72	97 ± 35			
		23.96/26	> 99.99	< 90	6.4 ± 0.1	0	89 ± 32			
		23.56/25	> 99.73	< 90	6.4 ± 0.9	< 68	97 ± 34			
$L_{43} > 8$	42.59/28	36.42/27	> 95.4		6.4	0	59 ± 38	1.597	30.20	1.91
		36.41/26	~ 95.4	< 90	6.4	< 7	58 ± 39			
		36.42/26	> 90.0	< 90	6.4 ± 0.2	0	58 ± 39			
		34.86/25	> 90.0	< 90	6.30 ± 0.20	< 7	75 ± 45			
$z < 1.005$	52.34/28	35.26/27	> 99.99		6.4	0	80 ± 32	0.704	5.43	1.28
		34.21/26	> 99.73	< 90	6.4	< 100	94 ± 37			
		33.69/26	> 99.99	< 90	6.50 ± 0.10	0	92 ± 35			
		33.28/25	> 99.73	< 90	6.45 ± 0.10	< 101	99 ± 37			
$z > 1.005$	29.56/28	19.77/27	> 99.73		6.4	0	71 ± 37	1.617	22.5	2.24
		19.45/26	> 99.73	< 90	6.4	< 120	86 ± 44			
		19.77/26	> 99.73	< 90	6.40 ± 0.15	0	71 ± 37			
		18.66/25	> 99.73	< 90	6.30 ± 0.10	< 76	85 ± 43			
$L_{43} < 14.3, z < 0.76$	42.01/28	23.70/27	> 99.99		6.4	0	108 ± 42	0.566	2.	1.254
		19.23/26	> 99.99	> 95.4	6.4	240 ± 90	178 ± 63			
		23.70/26	> 99.73	< 90	6.40 ± 0.15	0	108 ± 42			
		19.07/25	> 99.99	> 90	6.42 ± 0.12	216 ± 50	172 ± 60			
$z < 0.76$	43.28/28	23.04/27	> 99.99		6.4	0	108 ± 40	0.573	3.23	1.173
		19.04/26	> 99.99	~ 95.4	6.4	157 ± 30	154 ± 50			
		23.04/26	> 99.99	< 90	6.40 ± 0.15	0	109 ± 39			
		18.72/25	> 99.99	< 90	6.43 ± 0.11	215 ± 50	170 ± 56			
$L_{43} < 14.3, z > 0.76$	25.97/28	16.99/27	~ 99.7		6.4	0	75 ± 40	1.141	5.58	1.900
		16.99/26	> 95.4	< 90	6.4	< 4	75 ± 40			
		16.99/26	> 95.4	< 90	6.40 ± 0.10	0	75 ± 40			
		16.83/25	> 95.4	< 90	6.43 ± 0.10	< 5	76 ± 42			
$L_{43} > 14.3, z > 0.76$	31.85/28	29.56/27	< 90.0		6.4	0	< 90	1.803	37.05	2.187
		29.56/26	< 90.0	< 90	6.4	< 5	< 91			
		29.09/26	< 90.0	< 90	$6.05^{+0.60}_{-0.05}$	0	50 ± 47			
		26.72/25	< 90.0	< 90	6.22 ± 0.15	< 5	73 ± 53			

Chapter 5

Stacking of the CDFS from *XMM-Newton*

In this Chapter, we explore the properties of the AGN in the Chandra deep Field South survey observed by *XMM-Newton*. This observation is realised by an international consortium to which I belong.

The higher sensitivity of *XMM-Newton* with respect to *Chandra* allows to accumulate a superior number of counts than in the previous observation in the same field. Although in the ultra-deep observation of *XMM-Newton* the background affects the spectral SNR, it is possible to study in better detail the iron line properties.

The higher stacked number of counts from these data is expected to facilitate the detection of a broad emission line if it is indeed commonly present in distant AGN.

5.1 Sample definition and properties

In order to characterize the spectra and to estimate their intrinsic luminosity, after grouping the *XMM-Newton* EPIC MOS and PN spectra at 20 counts per bin, the spectra were fitted between 1 and 12 keV rest-frame with Xspec using the χ^2 statistics. We used a simple powerlaw with Galactic (with column density $7.7 \times 10^{18} \text{ cm}^{-2}$) and intrinsic absorption. We checked the levels of the background of each spectrum and we found a strong emission feature in the spectrum coincident with the position of the Al line characterizing many background spectra at ~ 1.5 keV. To assess how this systematic feature can influence the output of our fits, we repeated the fits removing the channels corresponding to 1.5 ± 0.1 keV. The fit results show that the presence of this background feature does not really influence the output fit parameters. Comparing for example the intrinsic absorption estimated in X-rays, we found that the difference is negligible in the majority of the sample, with the exception of a handful of spectra (seven). In these spectra, we used the fit parameters obtained ignoring these channels. The luminosities were estimated from the best fit models of each spectrum, corrected for Galactic and intrinsic absorption, and calculated between 2 and 10 keV restframe.

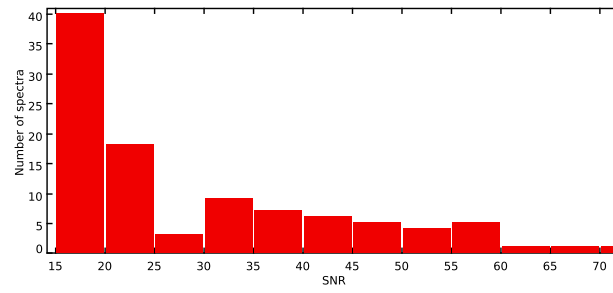


FIGURE 5.1: Spectral SNR between 2-12 keV of the full sample

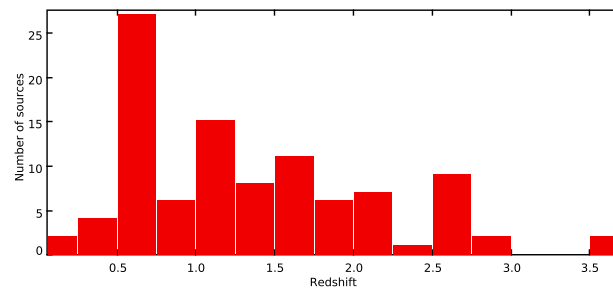


FIGURE 5.2: Redshift distribution of the full sample

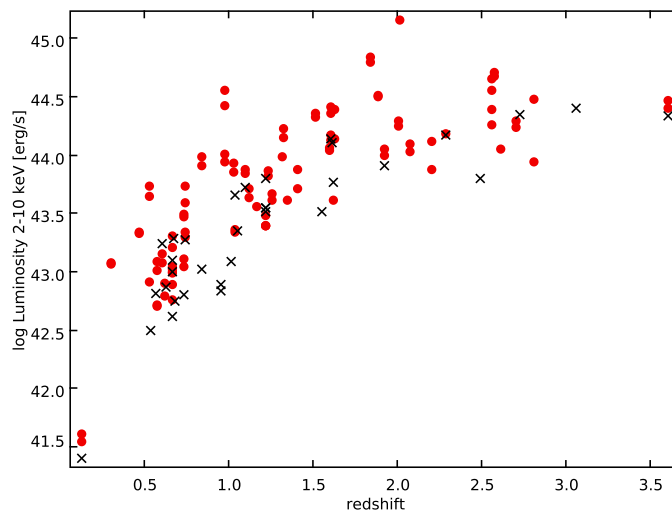
FIGURE 5.3: Distribution in Luminosity-redshift our full sample (red circles) and of the *Chandra* Deep Field South spectra (crosses) by Falocco et al. (2012)

TABLE 5.1: Properties of the full sample with $\text{SNR} > 15$ and its sub-samples. Columns: (1) (Sub)Sample; (2) Number of sources; (3) number of net counts in 2-12 keV rest-frame; (4) number of net counts in 5-8 keV rest frame; (5) average redshift; (6) Average of the logarithm of the rest-frame 2-10 keV luminosity in units of $10^{43} \text{ erg s}^{-1}$, from the fits to each spectrum (see text), corrected for Galactic and intrinsic absorption; (7) average intrinsic column density from the fits to each spectrum (see text); (8) average SNR of the (sub)sample between 2-12 keV rest-frame; (9) slope of the dependence $\sigma \propto E^{-\alpha}$ of the effective energy resolution of our method (see Chapter 3); (10) sigma at 6 keV of the effective energy resolution of our method at 6 keV (see Sect. 3.3)

Sample	N_s	N_{2-12}	N_{5-8}	$\langle z \rangle$	$\langle \log(L) \rangle$ erg s $^{-1}$	$\langle N_{\text{H},22} \rangle$ 10 22 cm $^{-2}$	$\langle \text{SNR} \rangle$	α	$\sigma(6 \text{ keV})$ eV
(1)	(2)	(3)	(4)	(5)	(6)	(7)	(8)	(9)	(10)
Full sample	100	181623	40863	1.34	43.74	1.48	29.8	0.32	110.1
$\log(N_{\text{H}}) < 21.5$	68	131383	25532	1.366	43.78	0.05	31.46	0.33	112.0
$\log(N_{\text{H}}) > 21.5$	32	50240	15331	1.30	43.64	4.51	24.63	0.31	106.1
$z <= 0.837$	35	60329	14689	0.599	43.10	1.33	28.00	0.35	93.0
$0.837 < z \leq 1.605$	33	57473	12444	1.24	43.847	1.89	28.66	0.36	111.3
$1.605 < z < 3.61$	32	63820	13730	2.26	44.32	1.20	31.29	0.38	139.1
$41.53 < \log(L) \leq 43.70$	45	59234	14121	0.78	43.167	0.81	23.24	0.34	99.0
$43.70 < \log(L) \leq 44.22$	31	59392	11930	1.54	43.98	1.82	31.40	0.35	116.7
$\log(L) > 44.22$	24	62997	14812	2.14	44.49	2.27	37.85	0.36	129.4

To maximise the average SNR of the sample, and to take in account the level of the background of the *XMM-Newton* observation, we limited our investigation to the 100 spectra (49 from the MOS camera and 51 from the PN camera) characterized with the best SNR estimated between 2 and 12 keV restframe (the band used in the analysis of the average spectra described below). In total we studied 51 unique sources. This turned out to be equivalent to discarding the spectra with $\text{SNR} < 15$. The survey accumulated a large number of sources detected with high quality spectra, as we can see in the Fig. 5.1, where the histogram of the SNR (in 2-12 keV) is shown.

We can see in Fig. 5.2 the distribution of the spectroscopic redshifts included in the sample: 40 spectra in our sample are located at redshifts $z \sim 1-2$, where the peak of AGN activity lies (Ueda et al. 2003), and a dozen at redshift $z \sim 2 - 3$ makes possible eventually to study earlier epochs.

The CDFS observation by *XMM-Newton* allows a better coverage of the parameter space than our previous work with deep Chandra fields (see Fig. 5.3). The CDFS survey is able to characterise with the highest significance reached so far the properties of distant X-ray selected AGN over 4 orders of magnitude of continuum luminosity and a broad span of redshifts, up to ~ 3.6 .

5.1.1 Subsample definition

The sample characteristics and properties are listed in Table 5.1. Given the high number of total background-subtracted counts in our sample, we have investigated the dependence of the stacked spectrum on luminosity and redshift, dividing the sample in three bins in each of those quantities, with similar number of counts in each bin.

We constructed the three luminosity sub-samples with the same number of counts in each, resulting in:

- Low-luminosity sub-sample (hereafter called 'Low-L'): composed by all the sources with $\log L[\text{erg/s}] < 43.70$
- Mid-Luminosity sub-sample (hereafter called 'Mid-L'): composed by all the sources with $43.70 < \log L[\text{erg/s}] < 44.22$
- High-Luminosity sub-sample (hereafter called 'High-L'): composed by all the sources with $43.70 < \log L[\text{erg/s}] < 44.22$

Segregating the sources in three redshift sub-samples with the same number of counts we found:

- Low-z sub-sample (hereafter called 'Low-z'): includes all the sources with $z < 0.837$
- Mid-z sub-sample (hereafter called 'Mid-z'): includes all the sources with $0.837 < z < 1.605$
- High-z sub-sample (hereafter called 'High-z'): includes all the sources with $z > 1.605$

Finally, we segregated the sources in two sub-samples of intrinsic column density estimated in X-rays (' N_{H} sub-samples') setting the threshold at $\log(N_{\text{H}}/\text{cm}^2) = 21.5$. This is often used as the threshold below which the interstellar medium of the galaxies hosting the AGN could provide the absorption without additional circum-nuclear gas. The sample with $\log(N_{\text{H}}/\text{cm}^2) < 21.5$ (hereafter called 'Un-abs') accumulates about 131000 net counts, covering $\sim 70\%$ of the total amount of X-ray counts of the full sample. The sample with $\log(N_{\text{H}}/\text{cm}^2) > 21.5$ (called hereafter 'Abs') contains just about 50000 net counts.

The N_{H} sub-samples are characterized by a similar distribution in the space formed by Luminosity and redshift, allowing to assess whether the intrinsic absorption alone can influence the detection of the X-ray spectral features of the AGN (see Fig. 5.4).

To check whether the spectral models used to unfold the spectra match correctly the underlying continuum, we checked our results against extensive simulations, as explained in Chapter 3.

We represent in Figs. 5.5, 5.7, 5.6 our average observed spectra, together with the simulated continua (solid line) and the 68% percentiles (dashed lines).

In the normalisation process applied to each spectrum before the average, we computed the continuum flux between 2 and 5 keV plus 8 and 10 keV because of the high number of absorbed sources in the survey. With such a large fraction of obscured AGN, in fact, by normalising between 2-5 keV the weight assigned to the absorbed sources would be too high. In this way, the continuum reproduced best the observed spectrum blue-wards of 7 keV. In this step, in order to minimise the effect of the Al spike at 1.5 keV in the spectra from XMM CDFS (discussed in Sect. 2.1), we ignored the bins

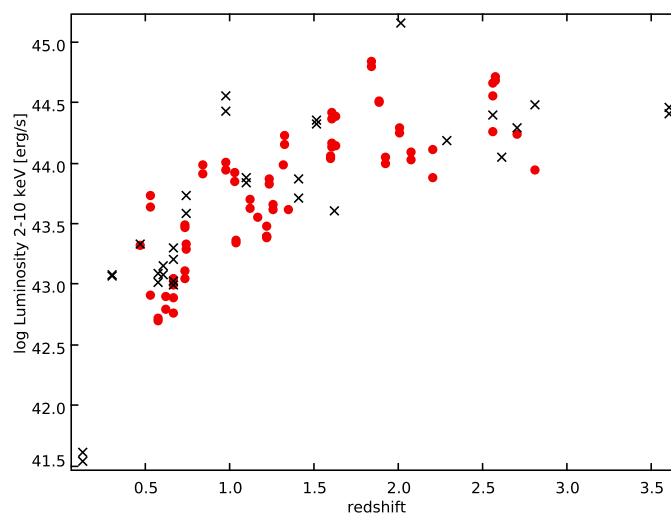


FIGURE 5.4: Distribution in Luminosity-redshift of our absorbed (crosses) and unabsorbed (full circles) sub-samples

corresponding to 1.4-1.6 keV in the observed frame in the renormalisation and in the final average both in the real and in the simulated data.

An intense iron line characterises the sample and all the sub-samples that we have constructed, furthermore the line appears to be broad in almost all cases.

In order to properly study the iron line profile, in the XMM CDFS we were interested in estimating the instrumental broadening introduced by our method in the broad energy band we were analysing. To do this, we made the simulations of unresolved lines centred at different energies, following the method described in Chapter 3. In our simulations, we recovered the input parameters of the continuum very well, reproducing a powerlaw continuum with $\Gamma \sim 1.9$, while the gaussian lines appear broadened by about 100 eV.

We can see in Fig. 5.8 the unresolved line simulated at 6.4 keV. As we can see, the effect of our method on an unresolved feature is a widening of the emission.

We studied the width of the average simulated lines as a function of their centroid energies: the results show a $\sigma \propto E^\alpha$ with $\alpha \sim 0.3$ (see Fig. 3.1). This energy-dependent instrumental response has been taken into account in the spectral fitting of the average spectra.

5.2 Results

We discuss in this section the results of our analysis of the average XMM-Newton X-ray spectra of several subsamples in the CDFS, estimating in particular the iron line significance. In Sect. 5.2.1,

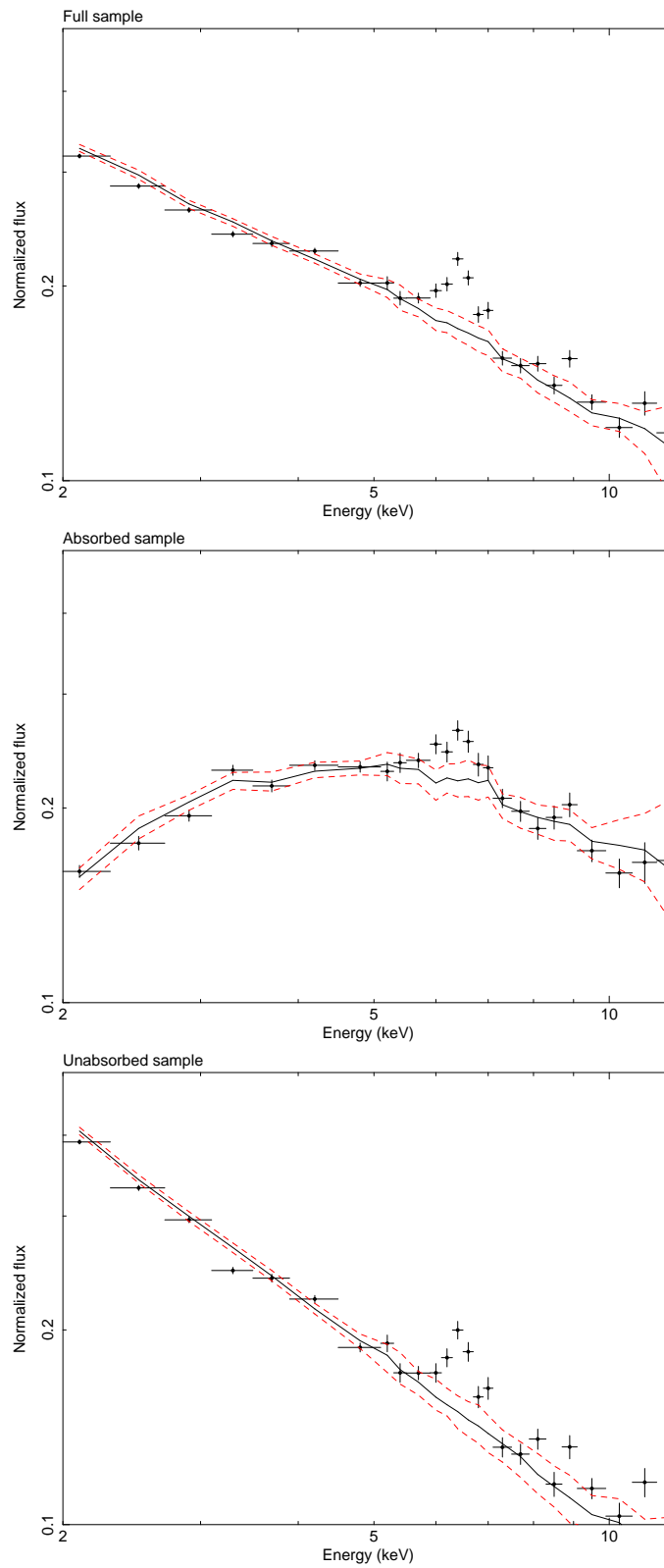


FIGURE 5.5: Average observed spectrum with its simulated continuum and the one sigma confidence line. Full sample (top panel), absorbed subsample (middle panel), unabsorbed subsample (bottom panel).

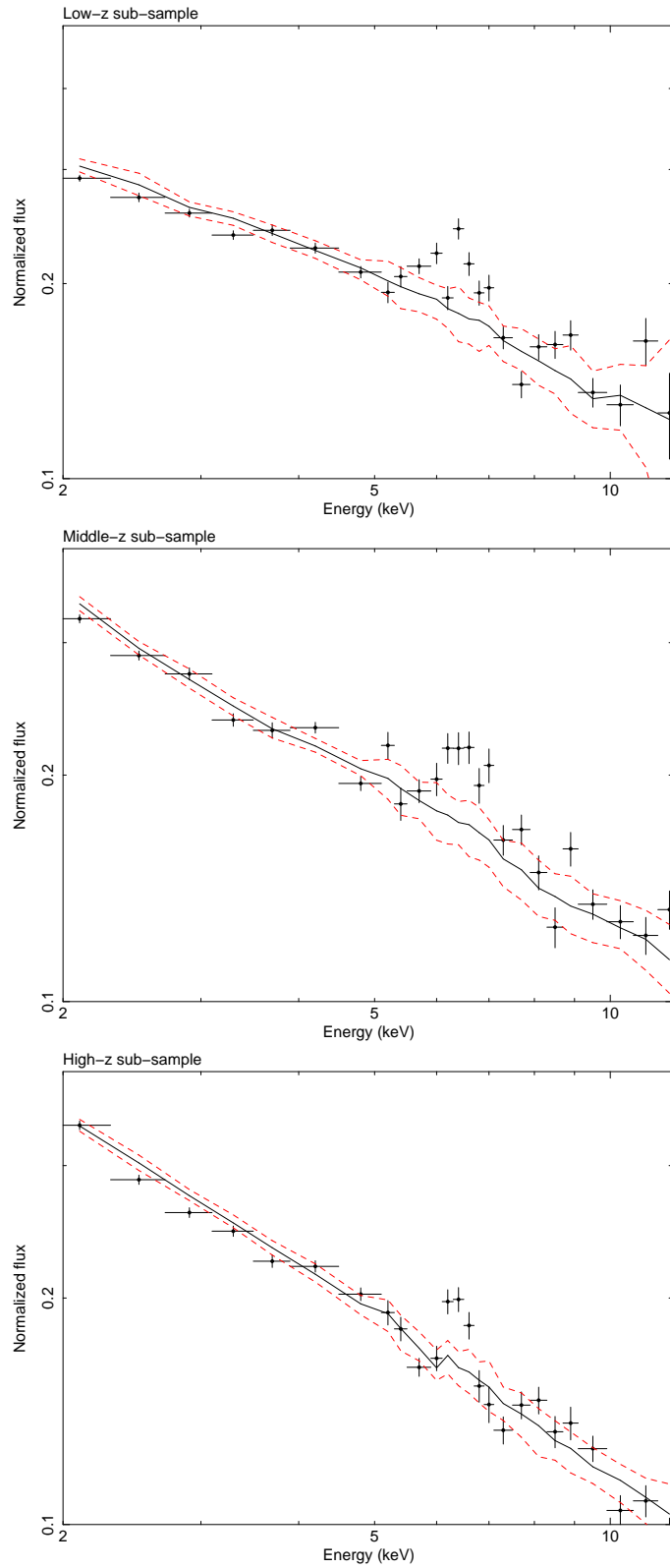


FIGURE 5.6: Average observed spectrum with its simulated continuum and the one sigma confidence line. From top to bottom: low-z subsample (top panel), middle-z subsample (middle panel), high-z subsample (bottom panel).

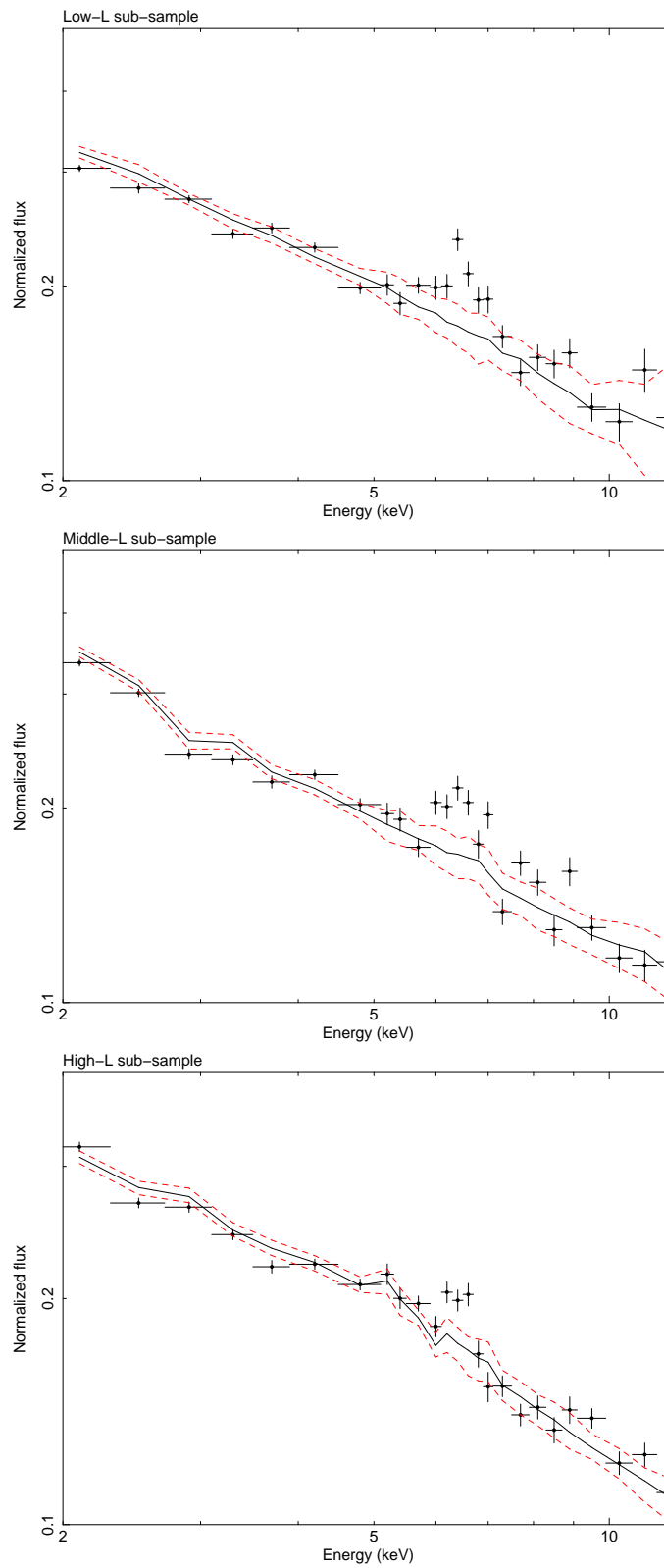


FIGURE 5.7: Average observed spectrum with its simulated continuum and the one sigma confidence line. Low-L subsample (top panel), middle-L subsample (middle panel), high-L subsample (bottom panel).

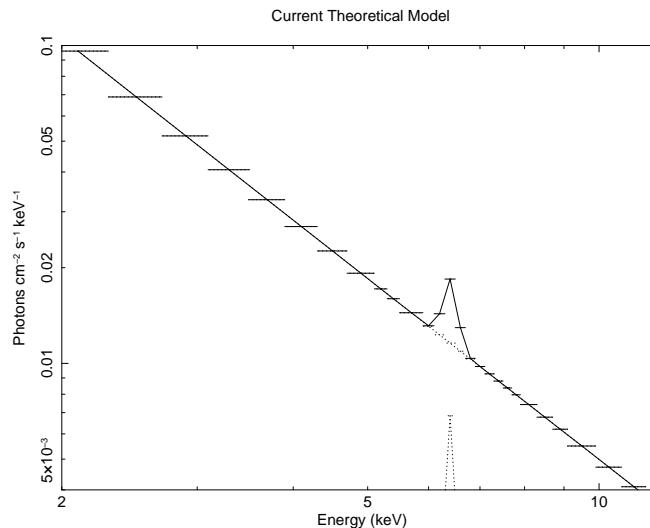


FIGURE 5.8: Unresolved line simulated at 6.4 keV for the full sample.

we use a model-independent way to estimate the statistical significance, that we developed in Falocco et al. (2012); we also employed our new method to calculate the line EW using the simulations of the continuum.

In Sect. 5.2.2, we describe the spectral fitting performed using continuum and line models available in Xspec, and the model-dependent EW.

5.2.1 Model-independent estimation of the significance and EW

We calculated the significance of the iron line excess in the observed spectrum with respect to the simulated continuum (see Table 5.1). To do this, we followed the method explained in Sect. 3.5.

An excess in the observed data between 6.2 and 6.6 keV is found with respect to our simulations, for the full sample and its subsamples, as we can see in the Table 5.2. If a broader range is considered, i.e. from 5.5 to 7.2 keV, the excess is found with respect to more than 97% of the simulations. An excess in our observed data is found also in the range 6.8-7.0 keV, in the majority of the cases. It is not significant in high-L, high-z (~30%), and Abs (~90%).

We also estimated the EW of the iron line using the 110 simulated continua and used the same energy bands considered in the calculation of its significance. The EW calculation was made following the procedure described in Sect. 3.5.

In the full sample, the EW seems to grow with increasing energy range (see Table 5.3), suggesting a significant contribution from a broad line, in agreement with the qualitative impressions expressed in the previous section.

TABLE 5.2: Model independent significance of the iron line estimated in several bandwidths using the simulations (as the fraction of simulations with a lower flux than the flux of the average observed spectrum, see text). The bandwidths are expressed in keV.

Sample	6.2-6.6	6.0-6.8	5.5-7.	6.8-7.0
Full	1	1	1	1
Unabs	1	1	1	1
Abs	1	1	0.99	0.92
Low-z	1	1	1	0.99
Middle-z	1	1	1	1
High-z	1	1	0.97	0.27
Low-L	1	1	1	1
Middle-L	1	1	1	1
High-L	1	1	1	0.26

TABLE 5.3: Median of the EW calculated in different energy ranges using the simulations. The symmetrical errors are calculated using the error propagation, the non-symmetrical errors correspond to the 1 sigma percentils of the simulations. The range is expressed in keV and the EW in eV.

sample	6.2-6.6	6.-6.8	5.5-7.	6.8-7.
Full	$129 \pm 15 \begin{pmatrix} +17 \\ -19 \end{pmatrix}$	$169 \pm 19 \begin{pmatrix} +23 \\ -24 \end{pmatrix}$	$208 \pm 24 \begin{pmatrix} +35 \\ -32 \end{pmatrix}$	$56 \pm 9 \begin{pmatrix} +11 \\ -12 \end{pmatrix}$
Unabs	$157 \pm 22 \begin{pmatrix} +29 \\ -24 \end{pmatrix}$	$200 \pm 27 \begin{pmatrix} +30 \\ -36 \end{pmatrix}$	$250 \pm 34 \begin{pmatrix} +34 \\ -37 \end{pmatrix}$	$67 \pm 13 \begin{pmatrix} +17 \\ -15 \end{pmatrix}$
Abs	$86 \pm 21 \begin{pmatrix} +31 \\ -22 \end{pmatrix}$	$132 \pm 27 \begin{pmatrix} +36 \\ -35 \end{pmatrix}$	$162 \pm 34 \begin{pmatrix} +41 \\ -51 \end{pmatrix}$	$39 \pm 12 \begin{pmatrix} +14 \\ -14 \end{pmatrix}$
Low-z	$123 \pm 26 \begin{pmatrix} +36 \\ -34 \end{pmatrix}$	$185 \pm 33 \begin{pmatrix} +41 \\ -44 \end{pmatrix}$	$258 \pm 40 \begin{pmatrix} +56 \\ -56 \end{pmatrix}$	$70 \pm 16 \begin{pmatrix} +29 \\ -25 \end{pmatrix}$
Middle-z	$157 \pm 31 \begin{pmatrix} +35 \\ -33 \end{pmatrix}$	$212 \pm 38 \begin{pmatrix} +47 \\ -47 \end{pmatrix}$	$278 \pm 47 \begin{pmatrix} +50 \\ -61 \end{pmatrix}$	$51 \pm 18 \begin{pmatrix} +18 \\ -16 \end{pmatrix}$
High-z	$116 \pm 23 \begin{pmatrix} +29 \\ -29 \end{pmatrix}$	$118 \pm 29 \begin{pmatrix} +29 \\ -35 \end{pmatrix}$	$83 \pm 35 \begin{pmatrix} +40 \\ -42 \end{pmatrix}$	$46 \pm 14 \begin{pmatrix} +14 \\ -12 \end{pmatrix}$
Low-L	$148 \pm 28 \begin{pmatrix} +26 \\ -31 \end{pmatrix}$	$202 \pm 35 \begin{pmatrix} +33 \\ -43 \end{pmatrix}$	$264 \pm 43 \begin{pmatrix} +50 \\ -56 \end{pmatrix}$	$72 \pm 17 \begin{pmatrix} +21 \\ -20 \end{pmatrix}$
Middle-L	$130 \pm 26 \begin{pmatrix} +41 \\ -30 \end{pmatrix}$	$184 \pm 33 \begin{pmatrix} +48 \\ -44 \end{pmatrix}$	$219 \pm 40 \begin{pmatrix} +59 \\ -60 \end{pmatrix}$	$53 \pm 15 \begin{pmatrix} +23 \\ -13 \end{pmatrix}$
High-L	$97 \pm 20 \begin{pmatrix} +20 \\ -19 \end{pmatrix}$	$113 \pm 25 \begin{pmatrix} +27 \\ -31 \end{pmatrix}$	$118 \pm 31 \begin{pmatrix} +30 \\ -35 \end{pmatrix}$	$28 \pm 11 \begin{pmatrix} +13 \\ -11 \end{pmatrix}$

This is also valid for the majority of the sub-samples that we constructed. The exceptions are the high-z and high-L sub-samples, where the line EW does not decrease with the width of the energy range.

There is a hint of decreasing line EW with increasing average luminosity of the sample (in agreement with the 'Iwasawa-Taniguchi effect'), but still within the mutual errors. There is no such effect with z , indicating either that there is no evolution of the iron line with redshift, or that we do not detect any evolution due to the limitations of the survey employed.

5.2.2 Spectral fits on the full sample and subsamples

In our analysis of the deep *Chandra* fields of Chapter 4 (Falocco et al. 2012) the average simulated spectrum was employed as a continuum in the spectral fits. In that approach its trend as the underlying continuum is assumed to be taken into account without any error bars. In the current work, we preferred to construct an empirical continuum with a flexible, smooth shape. To take into account the instrumental broadening at several energies between 2 and 12 keV, we convolved the model with a gaussian smoothing model (`gsmooth` in `xspec`). Our 'basic continuum' model is an absorbed power-law, fitted individually to the average spectrum of each subsample, excluding initially the 5-7.2 keV range (to avoid any contribution from a broad Fe K feature).

5.2.2.1 Partial covering absorption and Compton reflection

The observed continuum presents additional features below 4 keV and above 8 keV, which we have also tried to fit using more flexible models for the continuum. Although our primary goal was to define the iron-line properties of the sample, we also attempted to correctly characterise the broad band underlying continuum. The two main deviations from the standard absorbed powerlaw at low and high energies were considered using respectively complex absorption models and a Compton reflection component.

The band $E < 4\text{keV}$ has noise features that did not allow a correct fitting of the continuum (see Appendix B for details), but we included it anyway, for the determination of the continuum. We took into account the dispersion between the data and the basic continuum using a more flexible absorption model. This is the partial covering absorption (`pcfabs` model in `Xspec`). When we fitted the sole continuum excluding the region 5.0-7.2 keV, the fit was better, in χ^2 terms, than in the case of the `pha`. When this band is included, instead, using the simplest line models also (i.e. a simple phenomenological gaussian) the fit does not improve significantly. Moreover, the partial covering absorber has sometimes the effect to produce a hump mimicking the broad line: its significance is consequently reduced, together with its EW.

The spectra of the high- z and high- L subsamples are characterized by an excess blueward 8 keV. To take this into account, we fitted the continuum ignoring the channels in 5-7.2 keV (which exclude the sum of our basic continuum and the iron line spectral feature) with a pure reflection component (`pextrav` in `Xspec`) described in Magdziarz and Zdziarski (1995). For the latter model we fixed the slope to the same model as that of the basic continuum and the cutoff energy to 100 keV.

The reflection component does not seem to be significant, if compared with the fit with the single powerlaw. For example, the fitting does not give an improvement in the χ^2 in the high- z subsample. Moreover, in the high- L subsample, $\delta\chi^2 \sim 2.5$ with 2 degrees of freedom less. In summary, more

complex models for the continuum produced (at best) modest and low-significance improvements in the goodness-of-fit, and we have hence decided to use only the basic continuum.

5.2.2.2 Iron line fitting with a gaussian model

After having re-introduced the bins between 5 and 7.2 keV, we found a broad excess that corresponds to the iron line. The first model we used to fit it was a simple phenomenological gaussian, for simplicity.

We set the parameters of the gaussian, in analogy of what we made for the deep *Chandra* sample (see Sect 4.4.2), as follows:

- Fixed $\sigma=0$ and fixed centroid energy at 6.4 keV: this allows us to estimate the significance of the narrow component of a neutral Fe K line (hereafter 'fix-fix', in the first line of each sample in Table 5.4)
- Fixed centroid energy at 6.4 keV and free σ : it studies the significance of a possible broad component and estimates its width (hereafter 'fix-free', in the second line of each sample in Table 5.4)
- Free centroid energy and fixed $\sigma=0$: it allows for the presence of an ionized narrow Fe component and estimates its centroid energy (hereafter 'free-fix', in the third line of each sample in Table 5.4)
- Free centroid energy and free σ : considers both ionized iron emission and broad line emission (hereafter 'free-free', in the fourth line of each sample in Table 5.4)

The probability of the improvement of letting free the width, the central energy, or both, with respect to the narrow neutral iron line is calculated according to the incomplete β function and is in the fourth column of the Table 5.4 . In the first line of each sample, the probability refers to the improvements in the fit between fix-fix and the fit with the basic continuum over the full 2-12 keV range.

In the σ given in Table 5.4 , the instrumental width is already accounted for due to the use of the gaussian smoothing through the model `gsmooth`.

The sample is characterized by flat continua, in all but the unabsorbed sub-sample, where the continuum slope is ~ 1.8 as expected.

The significance of the emission line 6.4 keV is 99.99% in all cases. Leaving the width of the line free produces a significantly better fit in the full sample and in the majority of the subsamples. The exception is constituted by the high-L (>99.7%) and high-z (>90%) subsamples where the improvement introduced by a broadened gaussian is only marginal.

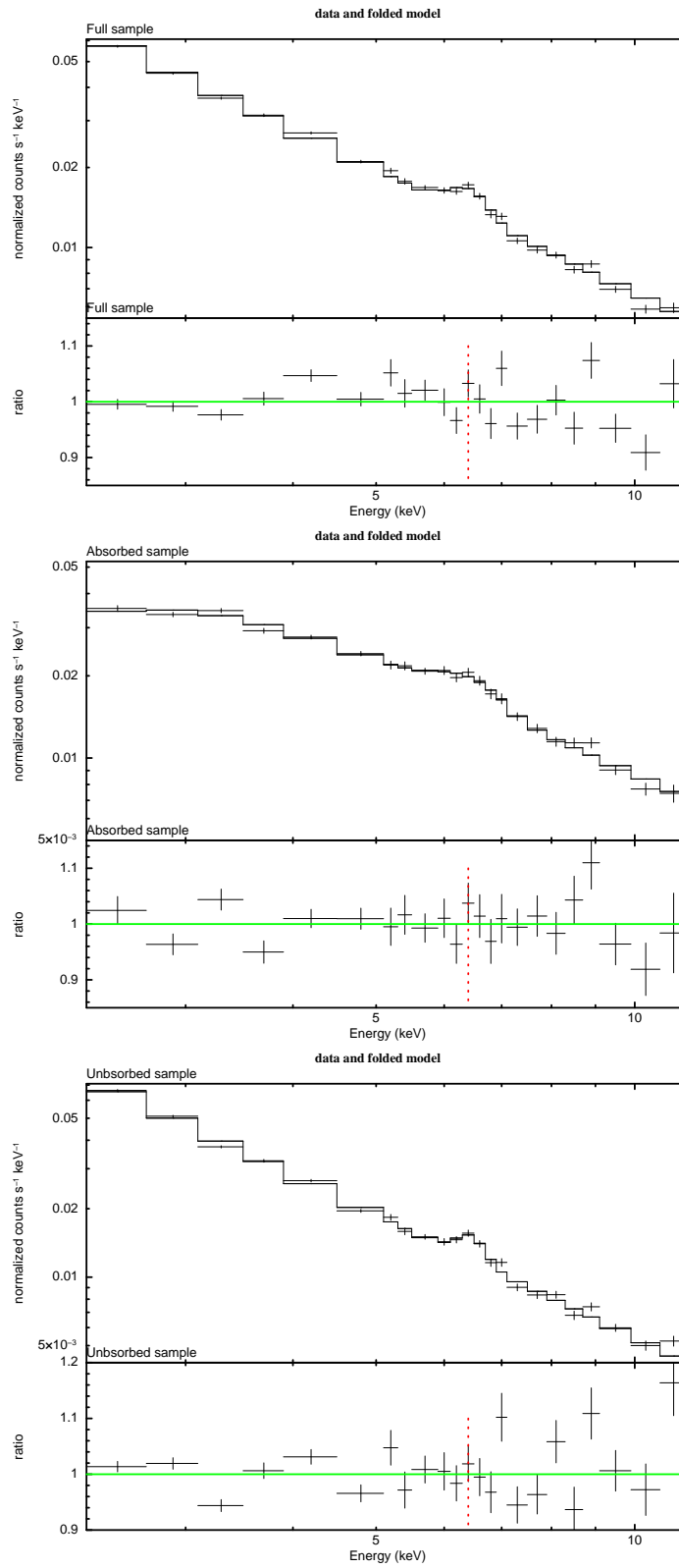


FIGURE 5.9: Fits results with the basic continuum and with 'free-free'. Full sample (top panel), absorbed (middle panel) and unabsorbed sample (bottom panel)

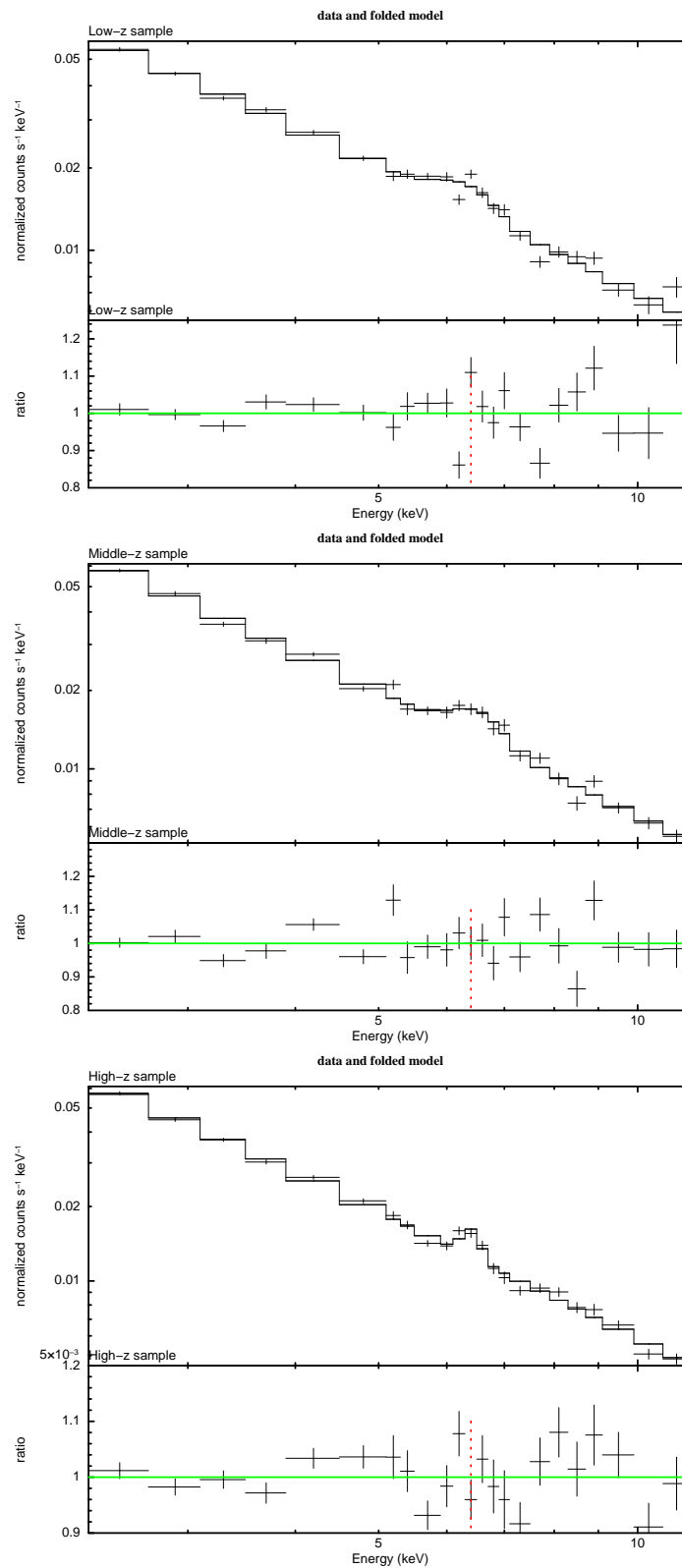


FIGURE 5.10: Fits results with the basic continuum and with 'free-free': low-z subsample (top panel), middle-z subsample (middle panel). The fit using 'fix-fix' is represented for the high-z subsample (bottom panel).

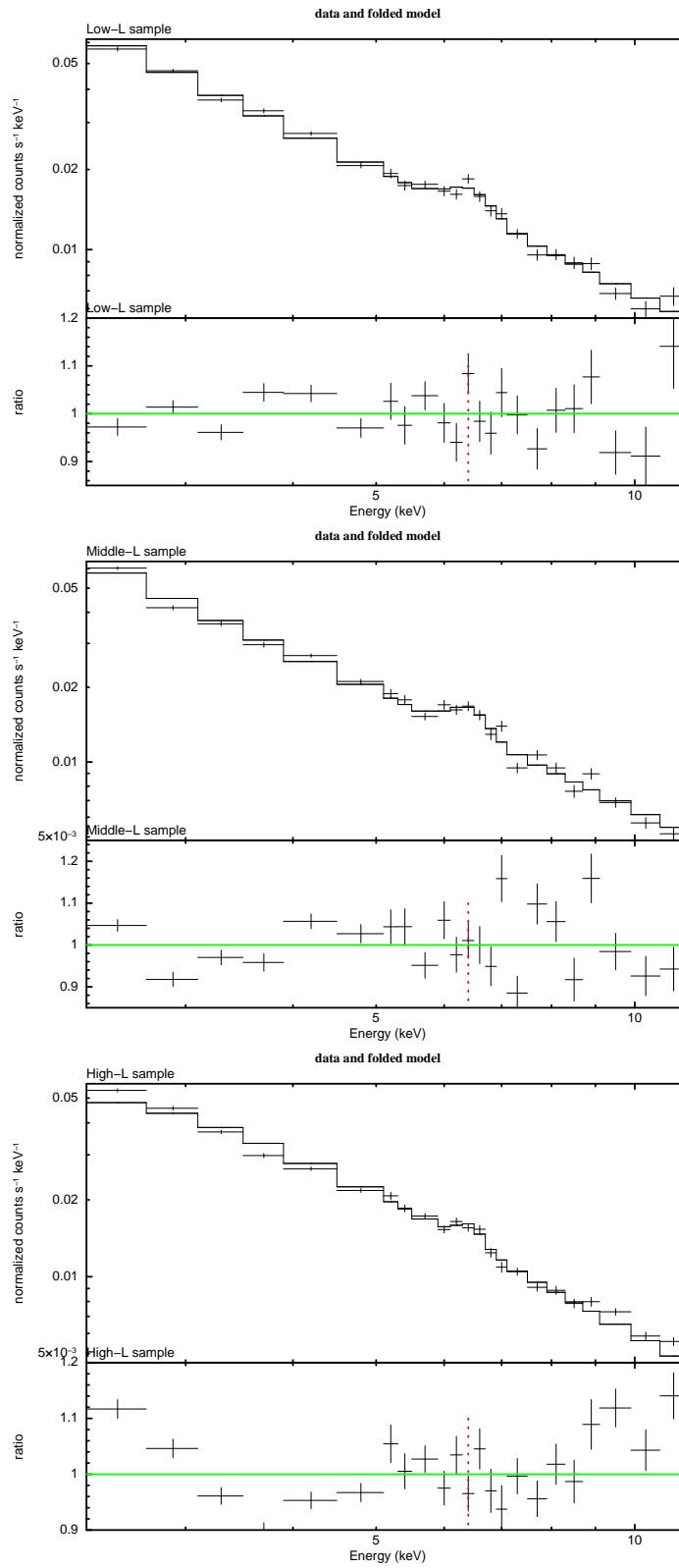


FIGURE 5.11: Fits results with the basic continuum and with 'free-free': low-L subsample (top panel), middle-L subsample (middle panel), high-L subsample (bottom panel).

TABLE 5.4: Results of fits of the average spectrum of the full sample and its subsamples with the basic continuum and the gaussian centered at 6.4 keV: $\text{gsmooth}^*(\text{pha}^*\text{pow}+\text{gauss})$. L : luminosity in erg s^{-1} . Columns: (1) sample; (2) χ^2/dof of the fit with the basic continuum model; (3) χ^2/dof of the fit with the same continuum and the Gaussian; (4) probability $P(\Delta\chi^2, \Delta\nu)$, s, g (of adding the Gaussian to the continuum model and of leaving the parameter free to vary, see text); (5) intrinsic column density estimated in the fits; (6) slope of the powerlaw; (7) central energy of the Gaussian; (8) σ of the gaussian; (9) EW of the Gaussian; (10) average redshift of the sample; (11) average of the logarithmic luminosities in erg s^{-1} from the fits of the single sources after the correction for Galactic and intrinsic absorption (see text); (12) average of the column densities from the fits to the single sources in 10^{22}cm^{-2} .

Sample	$\chi^2/\text{dof}(c)$	$\chi^2/\text{dof}(g)$	$P, \delta(\chi^2)$ %	N_{H} cm^{-2}	Γ	E keV	σ eV	EW eV	$\langle z \rangle$	$\langle \log(L) \rangle$ erg s^{-1}	$\langle N_{\text{H}} \rangle$ 10^{22}cm^{-2}
(1)	(2)	(3)	(4)	(5)	(6)	(7)	(8)	(9)	(10)	(11)	(12)
Full	216.20/20	111.08/19	>99.99	< 0.822	1.52±0.01	6.4	0	98±15	1.34	43.74	1.48
-	-	68.72/18	>99.99	< 0.822	1.54±0.01	6.4	312 ⁺⁷⁶ ₋₇₁	204±38			
-	-	106.61/18	>95.4	< 0.822	1.52±0.01	6.44 ^{+0.04} _{-0.03}	0	103±15			
-	-	68.72/17	>99.99	<0.822	1.54±0.02	6.40±0.06	311 ⁺⁸⁰ ₋₇₃	203±39			
Unabs	166.10/20	91.89/19	>99.99	< 0.822	1.78±0.02	6.4	0	106±21	1.37	43.78	0.05
-	-	77.56/18	>99.73	< 0.822	1.79±0.02	6.4	217 ⁺⁹⁴ ₋₈₃	171±44			
-	-	88.45/18	>90	<0.822	1.78±0.02	6.46 ^{+0.37} _{-0.47}	0	112±21			
-	-	76.18/17	>99.99	<0.822	1.79±0.02	6.44 ^{+0.06} _{-0.06}	212 ⁺⁹⁰ ₋₈₃	172±44			
Abs	98.32/20	64.18/19	>99.99	2.97±0.31	1.47±0.05	6.4	0	73±21	1.34	43.74	4.51
-	-	31.28/18	>99.99	2.81±0.31	1.48±0.05	6.4	541 ⁺²⁰³ ₋₁₅₀	273±90			
-	-	61.54/18	<90	2.98±0.31	1.47±0.05	6.48±0.06	0	80±22			
-	-	31.14/17	>99.99	2.79±0.33	1.48±0.06	6.37±0.13	547 ⁺²¹⁰ ₋₁₅₂	274±95			
Low-L	106.36/20	61.17/19	>99.99	<0.822	1.51±0.02	6.4	0	104±24	0.78	43.17	0.81
-	-	47.45/18	>99.73	< 0.822	1.54±0.03	6.4	382±130	244±80			
-	-	58.73/18	<90	< 0.822	1.51±0.03	6.45 ^{+0.04} _{-0.05}	0	110±26			
-	-	47.17/17	>99.7	< 0.822	1.54±0.03	6.43±0.10	371 ⁺¹³² ₋₁₄₄	241±73			
Mid-L	161.55/20	118.13/19	>99.99	< 0.822	1.56±0.02	6.4	0	111±27	1.54	43.98	1.82
-	-	96.55/18	>99.99	< 0.822	1.57±0.03	6.4	301 ⁺⁹⁴ ₋₈₂	228±59			
-	-	116.98/18	<90	< 0.822	1.56±0.02	6.44 ^{+0.06} _{-0.09}	0	114±32			
-	-	96.48/17	>99.99	< 0.822	1.58±0.03	6.41±0.09	301 ⁺⁹³ ₋₈₁	228±59			
High-L	103.38/20	64.72/19	>99.99	0.880 ^{+0.227} _{-0.228}	1.68±0.04	6.4	0	78±20	2.14	44.49	2.27
-	-	54.67/18	>99.7	0.843 ^{+0.228} _{-0.228}	1.68±0.04	6.4	193 ⁺¹⁰¹ ₋₇₇	119±37			
-	-	63.48/18	<90	0.883 ^{+0.227} _{-0.221}	1.68±0.04	6.47 ^{+0.07} _{-0.13}	0	82±21			
-	-	54.63/17	>99.7	0.840 ^{+0.231} _{-0.229}	1.68±0.04	6.38 ^{+0.11} _{-0.08}	196 ⁺¹⁴¹ ₋₈₃	120±41			
Low-z	131.62/20	83.25/19	>99.99	0.550±0.270	1.53±0.06	6.4	0	92±18	0.6	43.10	1.33
-	-	64.05/18	>99.99	0.542±0.272	1.56±0.06	6.4	450 ⁺¹⁰⁸ ₋₉₈	266±70			
-	-	76.59/18	>99.0	0.558±0.270	1.53±0.06	6.46 ^{+0.03} _{-0.04}	0	106±26			
-	-	62.35/17	>99.99	0.501±0.280	1.56±0.06	6.30±0.12	487±107	279±70			
Mid-z	118.46/20	86.23/19	>99.99	<0.435	1.56±0.05	6.4	0	104±30	1.24	43.85	1.89
-	-	54.70/18	>99.99	<0.396	1.58 ^{+0.06} _{-0.05}	6.4	446 ⁺¹⁸⁵ ₋₁₃₄	310±99			
-	-	83.37/18	>90	<0.441	1.56±0.05	6.49 ^{+0.07} _{-0.08}	0	113±30			
-	-	52.29/17	>99.99	<0.430	1.59 ^{+0.06} _{-0.05}	6.51±0.12	434 ⁺¹⁶⁹ ₋₁₂₂	316±98			
High-z	93.49/20	41.88/19	>99.99	0.432±0.242	1.71±0.05	6.4	0	114±26	2.26	44.32	1.20
-	-	39.59/18	<90	0.424±0.243	1.71±0.05	6.4	111 ⁺⁶⁹ ₋₁₀₇	130±35			
-	-	40.97/18	<90	0.43±0.24	1.71±0.05	6.37±0.06	0	144±44			
-	-	39.10/17	>90	0.420±0.240	1.71±0.05	6.38±0.06	<172	129±34			

An additional single symmetric (narrow or broad) line at $E > 6.4$ keV is not required by the data. We show the spectra with the best-fit models found with the gaussian (free-free in all cases except for high-z, where the fix-fix is shown) and the corresponding ratios in Figs. 5.9, 5.11, 5.10.

Generally, the best fit with the gaussian line is found in the 'fix-free' setting, indicating the presence of a broad line, with the exception of the high-z subsample where the detected line is instead narrow.

5.2.3 Fits of the broad iron lines

Having established that a broad profile is demanded by the data, we now discuss a physical model for the accretion disks. We considered a 'diskline' to model the iron line. The model was developed by Fabian et al. (1994) for the Xspec package to test the accretion disk hypothesis.

The relativistic model adopted here implies that the emissivity scales as r^{-2} . General and special relativistic effects in this regime can afford a most suitable explanation of the observed profile. We set the inclination angle to the average value of 45° , after having assessed that when it is left free to vary during the fits, it does not significantly deviate from the input value.

We have fixed the inner radius of the accretion disk to $6 R_g$ and the outer radius to $1000 R_g$, within the picture of standard accretion disks around a non-rotating BH. We then:

- calculated the EW with the parameters set as just mentioned (we refer to this model as 'disk-fix' and we show the results in the first line in Table 5.5)
- left the emissivity index, the inner radius, and the inclination angle free to vary: this allows to check if the parameters deviate from the input (we call this model 'disk-free', with parameters in the second line in Table 5.5)

The fits parameters are shown in the first two lines of each sample in Table 5.5. The probability of the fit improvement, calculated as usual with the inverse beta function, is shown in the third and fourth column of the Table 5.5. In the third one, it is calculated between 'disk-fix' and the simple 'fix-fix' model. In the fourth column, it is calculated between the 'disk-free' and the 'disk-fix'. The absolute χ^2 values show that our fitting of the continuum is not good in all the band considered. Moreover, the `diskline` fits the lines as well as the gaussian.

The significance of leaving the `diskline` parameters free to vary is low, as we can see from the probabilities in Column 4: these are lower than 90 % in almost all cases. We fitted the iron line of the full sample with another simple model in the literature: the `laor` model in Xspec (Laor, 1991). This model considers an accretion disk around a rotating BH: such disk can extend to a lower inner radius than in the case of the Schwarzschild BH. In fact, if the BH is maximally rotating, the expected inner radius is $1.2 R_g$. The line fitting does not improve with respect to the `diskline` fit. Probably, we would need a higher spectral quality to identify which is the best model.

We should take into account that the EW of the broad lines are higher than the ones in the literature. As a narrow core of the iron line is expected as the signature of fluorescence by material far from the central source (i.e. the torus), we added a narrow gaussian with free energy (between 6.4 keV and 7.1 keV). From now on, when the model is composed by the `disk-fix` and this narrow gaussian, it is called 'disk-fix-na'; when it has instead the `disk-free` component plus the narrow gaussian, it will be referred

to as 'disk-free-na'. The results of these two fits are in the third and fourth line of Table 5.5. Contrarily to the expectations, the addition of the narrow line does not seem to be required strongly by our data being its significance and its EW quite low in general. This result is in disagreement with the theory predicting that a narrow fluorescent feature, emitted from material far away from the central source, should be found in all or most AGN spectra.

TABLE 5.5: Results of fits of the average spectrum of the full sample and its subsamples using $\text{gsmo}*(\text{pha}*\text{pow}+\text{diskline})$ and $\text{gsmo}*(\text{pha}*\text{pow}+\text{diskline}+\text{gauss})$. Columns: (1) sample; (2) χ^2/dof of the fit with disk-fix in the first line of each sample, disk-free in the second one, disk-fix-na in the third one, disk-free-na in the fourth one. (3) Probability of each fit with respect to the fit with the basic continuum. (4) Probability between disk-free and disk-fix (second line), between disk-fix-na and disk-fix (third line), between disk-free-na and disk-free (fourth line). (5) intrinsic column density given by the fits to the average spectra. (6) powerlaw slope. (7) inner radius. (8) emissivity index. (9) inclination angle. (10) diskline EW. (11) central energy of the narrow component. (12) EW of the narrow component

Sample	χ^2/dof	$P_1\delta\chi^2$ %	$P_2\delta\chi^2$ %	N_{H} 10^{22}cm^{-2}	Γ	R_i R_g	β -	θ °	EW _{disk} eV	E keV	EW _{na} eV
(1)	(2)	(3)	(4)	(5)	(6)	(7)	(8)	(9)	(10)	(11)	(12)
Full	55.61/19	> 99.99	-	0.254±0.155	1.59±0.01	≡ 6	≡ -2	≡ 45	244±31	-	-
	55.0/16	> 99.99	< 90	0.258±0.150	1.59±0.02	6 ⁺¹⁴ ₋₀	-1.95±0.25	44 ⁺⁴ ₋₈	233±38	-	-
	51.55/17	> 99.99	< 90	0.26±0.15	1.59±0.03	≡ 6	≡ -2	≡ 45	193±44	6.43 ^{+0.09} _{-0.01}	28±21
	47.87/14	> 99.99	>95.4	0.25 ^{+0.10} _{-0.20}	1.59 ^{+0.03} _{-0.04}	6 ⁺¹⁶ ₋₀	-2.2 ^{+0.3} _{-0.5}	29 ⁺³ ₋₄	224±46	6.95 ^{+0.09} _{-0.08}	43±17
Unabs	81.26/19	> 99.99	-	<0.82	1.8±0.02	≡ 6	≡ -2	≡ 45	239±43	-	-
	77.17/16	> 99.99	< 90	<0.82	1.79±0.02	6 ⁺¹⁹⁸ ₋₀	-1.55 ^{+1.6} _{-0.6}	43 ⁺²⁴ ₋₁₃	191±51	-	-
	74.03/17	> 99.99	> 95.4	<0.82	1.79±0.02	≡ 6	≡ -2	≡ 45	150±67	6.50 ^{+0.01} _{-0.10}	52±35
	72.0/14	> 99.99	<95.4	<0.82	1.79±0.02	14 ⁺⁷⁸⁶ ₋₈	-1.6 ^{+9.0} _{-0.9}	21 ⁺¹⁰ ₋₂₁	168±42	6.95 ^{+0.10} _{-0.10}	39±19
Abs	35.36/19	> 99.99	-	2.8 ± 0.3	1.47±0.05	≡ 6	≡ -2	≡ 45	223±43	-	-
	32.73/16	> 99.99	< 90	2.8 ^{+0.2} _{-0.3}	1.47 ^{+0.06} _{-0.05}	8 ⁺⁴³ ₋₈	-2.2±0.5	40 ⁺⁹ ₋₄₀	271±52	-	-
	33.93/17	> 99.99	< 90	2.8 ± 0.3	1.47±0.05	≡ 6	≡ -2	≡ 45	202±36	7.1 ^{+0.0} _{-0.5}	20±20
	30.03/14	> 99.99	< 90	2.7±0.4	1.46±0.06	6.8 ^{+39.6} _{-6.8}	-2.8 ^{+0.4} _{-1.6}	32 ⁺⁵ ₋₉	248±58	7.0 ^{+0.1} _{-0.2}	47±17
Low-L	43.99/19	> 99.99	-	0.29±0.28	1.59±0.06	≡ 6	≡ -2	≡ 45	259±53	-	-
	43.93/16	> 99.99	< 90	0.29±0.28	1.59±0.06	6 ⁺⁴² ₋₀	-1.98 ± 0.55	46 ⁺¹⁷ ₋₆	260±41	-	-
	42.98/17	> 99.99	< 90	<0.82	1.53±0.03	≡ 6	≡ -2	≡ 45	188±72	6.41 ^{+0.09} _{-0.01}	43±36
	33.52/14	> 99.99	> 99	0.34±0.27	1.60±0.06	64 ⁺⁵³ ₋₄₈	-4.8 ^{+2.4} _{-0.6}	89 ⁺¹ ₋₄₉	166±29	6.44 ^{+0.05} _{-0.04}	72±22
Mid-L	94.97/19	> 99.99	-	< 0.82	1.58 ± 0.03	≡ 6	≡ -2	≡ 45	282±55	-	-
	94.68/16	> 99.99	< 90	< 0.82	1.58±0.03	6 ⁺⁶⁵ ₋₆	-2.0±0.4	43 ⁺¹¹ ₋₅	278±69	-	-
	93.80/17	> 99.99	<90	< 0.82	1.58±0.03	≡ 6	≡ -2	≡ 45	261±54	6.97 ^{+0.1} _{-0.53}	21±18
	82.16/14	> 99.99	> 95.4	< 0.82	1.60±0.03	6.9±0.7	-6.9 ^{+6.9} _{-3.1}	35.0±1.8	396±79	6.96 ^{+0.2} _{-0.1}	81±36
High-L	56.62/19	> 99.99	-	0.79±0.23	1.68±0.04	≡ 6	≡ -2	≡ 45	173±38	-	-
	31.14/16	> 99.99	> 99.99	0.45±0.25	1.63±0.04	7.7 ^{+6.2} _{-1.5}	-3.9 ^{+3.9} ₋₀	33.9 ^{+2.2} _{-4.5}	334±75	-	-
	54.87/17	> 99.99	< 90	0.81±0.23	1.68±0.04	≡ 6	≡ -2	≡ 45	126±67	6.44 ^{+0.01} _{-0.05}	30±29
	31.14/14	> 99.99	< 90	0.45±0.26	1.63±0.0	7.7 ^{+6.2} _{-1.5}	-9.9 ^{+6.0} _{-0.1}	34 ⁺² ₋₁₁	320±76	6.6 ^{+0.4} _{-0.2}	<72
Low-z	66.15/19	> 99.99	-	0.50±0.27	1.55±0.06	≡ 6	≡ -2	≡ 45	251±52	-	-
	60.23/16	> 99.99	< 90	0.44±0.27	1.53±0.06	25 ⁺²⁷ ₋₁₉	-3.2 ^{+3.2} ₀	25 ⁺⁶ ₋₃	243±51	-	-
	61.16/17	> 99.99	< 95.4	0.52±0.27	1.55±0.06	≡ 6	≡ -2	≡ 45	186±93	6.45 ^{+0.05} _{-0.05}	47±39
	46.54/14	> 99.99	>99.79	0.53±0.27	1.56±0.06	38 ⁺⁶⁹ ₋₁₆	-3.1 ^{+3.1} _{-2.5}	52±5	188±91	6.44±0.04	78±30
Mid-z	54.10/19	> 99.99	-	0.11 ^{+0.26} _{-0.11}	1.57±0.05	≡ 6	≡ -2	≡ 45	304±59	-	-
	51.44/16	> 99.99	< 90	0.12±0.12	1.59±0.06	6 ⁺⁶⁶ ₋₆	-2.05±0.37	44 ⁺¹¹ ₋₅	390±78	-	-
	49.12/17	> 99.99	< 95.4	0.13±0.13	1.58±0.05	≡ 6	≡ -2	≡ 45	283±57	7.02 ^{+0.08} _{-0.12}	48±28
	48.32/14	> 99.99	< 90	<0.42	1.59±0.02	6 ⁺⁷⁴³ ₋₀	-1.7 ^{+5.4} _{-2.0}	63 ⁺⁰ ₋₆₃	278±52	7.0 ± 0.1	52±20
High-z	67.91/19	> 99.99	-	< 0.82	1.64±0.02	≡ 6	≡ -2	≡ 45	177±51	-	-
	46.79/16	> 99.99	> 99.99	< 0.82	1.64±0.02	272 ⁺⁹²⁰ ₋₂₆₆	>-10	25 ⁺¹ ₋₂₅	137±30	-	-
	50.57/17	> 99.99	> 99.79	< 0.82	1.63±0.02	≡ 6	≡ -2	≡ 45	<1000	6.4 ^{+0.03} _{-0.0}	111±55
	36.1/14	> 99.99	< 90	< 0.82	1.64±0.02	6 ^{+0.3} ₋₀	-7 ⁺⁷ ₋₃	11 ⁺⁴ ₋₇	129±49	6.4 ^{+0.04} ₋₀	120±42

5.2.4 Complex continuum models with a complete set of fluorescent lines

We considered a more proper model to represent both the primary continuum, absorption from a warm absorber, absorption from a cold absorber, and fluorescence from a material far away from the primary continuum source (i.e. the torus). We followed the lines of de la Calle Pérez et al. (2010) and Nandra et al. (2007). The spectrum $f(E)$ is represented by the model:

$$f(E) = W(\Gamma, N_H^i, \psi) \cdot [e^{-\sigma N_H} \cdot AE^{-\Gamma} + \sum G_i]$$

Hereafter, we call the model including the primary emission and the reprocessing from material far away from the central BH the 'complex' model. The results are in the first line of the Table 5.6.

After, we modified the model adding a relativistic iron line represented by a `diskline`:

$$f(E) = W(\Gamma, N_H^i, \psi) \cdot [e^{-\sigma N_H} \cdot [AE^{-\Gamma} + D(\theta, \beta, R_i)] + \sum G_i]$$

The main components taken into account with this model are:

- $W(\Gamma, N_H^i, \psi)$: warm absorber represented by the Xspec model `Absori`. N_H^i is the intrinsic column density and is left free; ψ =ionization parameter, left free; Γ = slope, it was set to the same value as the photon index of the primary powerlaw; T is the temperature of the absorber, that we fixed to the default value of 2×10^5 K.
- $\sum G_i$ is the sum of gaussian lines emitted by fluorescence from material far away from the central BH (e.g. the torus), considering the prescriptions of Matt (2002):
 - Fe K_α line at 6.4 keV from neutral iron (EW in the 11th column of Table 5.6)
 - Fe K_β line centered at 7.06 keV with flux 11 percent of the flux of the Fe K_α ,
 - Ni K_α line centered at 7.47 keV with flux 5 percent of the flux of the Fe K_α
 - Compton Shoulder line centered at 6.3 keV with $\sigma=30$ eV and flux 20 percent of Fe K_α)
- $D(\theta, \beta, R_i)$ is the `diskline` model with inner radius of $6 R_g$, outer radius of $1000 R_g$, emissivity (β) fixed to -2. Being our sample dominated by unabsorbed sources that constitute 68 % of the full sample, we expect that the accretion disks are seen preferentially face-on, under the hypothesis that the accretion disk and the torus axes are aligned. For this reason we set the θ to 30 degrees. The parameters θ, β, R_i are frozen in the second line of Table 5.6 and free in the third line.

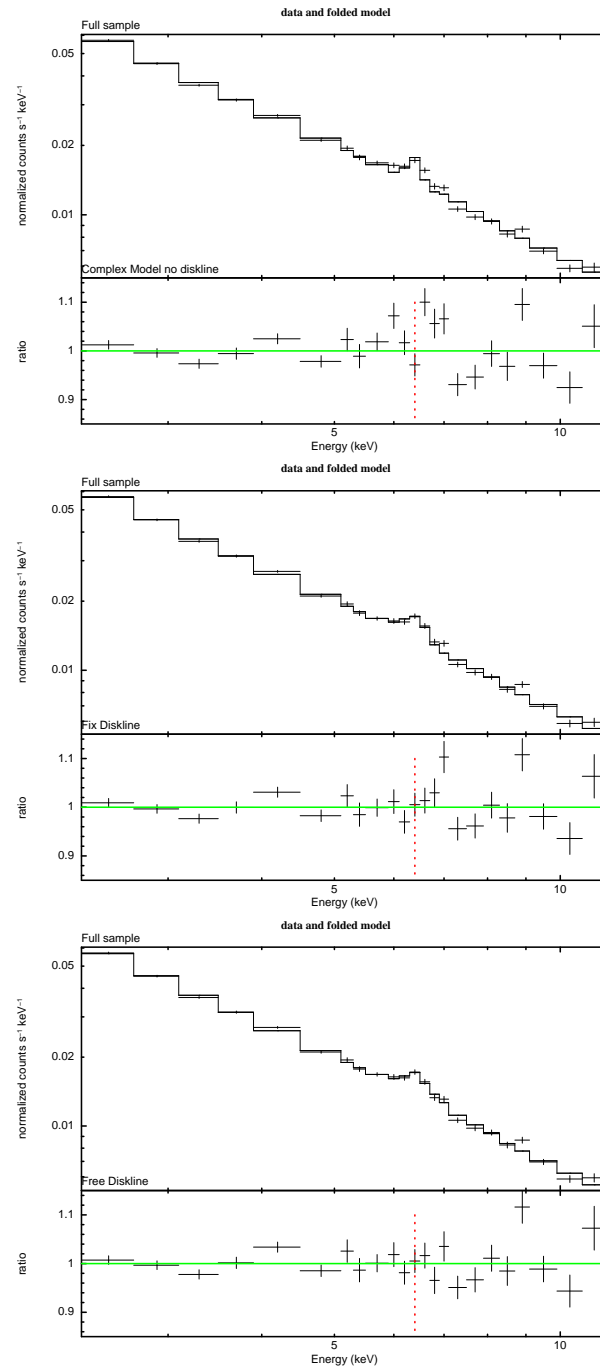


FIGURE 5.12: Fits results with the complex model (top panel), with the diskline (fixed in the middle panel, free in the bottom panel). Full sample

TABLE 5.6: Results of fits of the average spectrum of the full sample and its subsamples using the complex model: $\text{gsmo*absori}[\text{pha*pow}+\sum\text{gauss}]$ in the first line of each sample; the complex model plus the diskline with fixed parameters: $\text{gsmo*absori}[\text{pha}*(\text{pow}+\text{diskline})+\sum\text{gaus}]$ in the second line; the complex model plus the diskline with free parameters in the third line. Columns: (1) sample; (2) χ^2/dof of the fit with the complex model with narrow lines only in the first line of each sample; with the addition of fix diskline in the second one, addition of both fix diskline and ionised line in the third one, with free diskline in the fourth one. (3) Significance of the addition of the diskline, in the first line, and significance of leaving its parameters free to vary in the second line. (4)intrinsic column density given by the fits. (5) powerlaw slope. (6) inner radius. (7) emissivity index. (8) inclination angle. (9) diskline EW. (10) EW of the narrow gaussian line at 6.4 keV

Sample	χ^2/dof	$P_{\text{disk}}\delta\chi^2$ %	N_{H} 10^{22}cm^{-2}	$N_{\text{H,ion}}$ 10^{22}cm^{-2}	Γ	R_i R_g	β	θ °	EW_{disk} eV	EW_{na} eV
(1)	(2)	(3)	(4)	(5)	(6)	(7)	(8)	(9)	(10)	(11)
Full	83.86/17	-	< 0.82	$4.1^{+2.43}_{-1.96}$	1.62 ± 0.04	-	-	-	-	78^{+16}_{-15}
Full	57.47/16	>99.99	< 0.82	$2.45^{+2.29}_{-1.78}$	1.61 ± 0.04	$\equiv 6$	$\equiv -2$	$\equiv 30$	167^{+51}_{-51}	< 33
Full	45.80/13	>99.00	< 0.82	$0.43^{+2.53}_{-0.27}$	$1.56^{+0.04}_{-0.02}$	$6.5^{+1.0}_{-0.5}$	$-9.99^{+9.99}_{-0}$	$38.2^{+2.4}_{-2.1}$	261^{+75}_{-75}	44^{+22}_{-22}
Unabs	91.41/17	-	< 0.82	< 1.64	1.78 ± 0.02	-	-	-	-	92^{+17}_{-17}
Unabs	80.30/16	>99.7	< 0.82	< 0.82	1.79 ± 0.02	$\equiv 6$	$\equiv -2$	$\equiv 30$	143^{+67}_{-67}	27^{+24}_{-24}
Unabs	75.31/13	<90	< 0.82	< 0.82	1.80 ± 0.02	19^{+189}_{-13}	$-2.08^{+1.80}_{-1.68}$	33^{+13}_{-33}	146^{+75}_{-75}	43^{+42}_{-42}
Abs	50.04/17	-	$2.60^{+0.29}_{-0.36}$	14^{+7}_{-7}	1.42 ± 0.05	-	-	-	-	53^{+16}_{-16}
Abs	39.31/16	>99.7	< 1.6	4^{+3}_{-1}	1.48 ± 0.05	$\equiv 6$	$\equiv -2$	$\equiv 30$	134^{+33}_{-33}	< 1000
Abs	31.52/13	>95.4	< 1.64	$3.48^{+1.78}_{-0.93}$	$1.48^{+0.06}_{-0.03}$	$8.73^{+57.73}_{-2.73}$	$-2.2^{+0.62}_{-0.49}$	39^{+7}_{-39}	232^{+38}_{-58}	< 1000
Low-L	53.63/17	-	< 0.82	$1.16^{+4.37}_{-0.98}$	$1.60^{+0.07}_{-0.06}$	-	-	-	-	90^{+21}_{-21}
Low-L	46.49/16	<99.7	< 0.82	$0.86^{+2.84}_{-0.76}$	1.59 ± 0.06	$\equiv 6$	$\equiv -2$	$\equiv 30$	131^{+71}_{-71}	36^{+35}_{-35}
Low-L	35.22/13	>95.4	< 0.82	$0.72^{+1.82}_{-0.61}$	1.61 ± 0.06	55^{+83}_{-42}	$-2.1^{+2.1}_{-2.2}$	35.3^{+27}_{-35}	159^{+73}_{-73}	66^{+29}_{-29}
Mid-L	109.67/17	-	< 0.82	$9.1^{+6.6}_{-7.7}$	$1.58^{+0.10}_{-0.03}$	-	-	-	-	86^{+22}_{-22}
Mid-L	98.95/16	>99.7	< 0.82	6^{+6}_{-6}	$1.58^{+0.08}_{-0.03}$	$\equiv 6$	$\equiv -2$	$\equiv 30$	197^{+53}_{-53}	< 25
Mid-L	93.69/13	<90	< 0.82	$3.72^{+7.82}_{-3.72}$	$1.60^{+0.07}_{-0.05}$	$105.8^{+172.5}_{-54.9}$	18^{+0}_{-18}	90^{+0}_{-90}	163^{+82}_{-82}	< 64
High-L	63.60/17	-	< 0.82	$2.44^{+2.15}_{-1.20}$	1.70 ± 0.05	-	-	-	-	60^{+15}_{-15}
High-L	46.21/16	>99.99	< 0.82	$1.80^{+1.53}_{-1.16}$	1.68 ± 0.05	$\equiv 6$	$\equiv -2$	$\equiv 30$	145^{+36}_{-36}	< 1000
High-L	31.15/13	>99.7	< 0.822	$0.45^{+1.29}_{-0.25}$	1.63 ± 0.04	$7.7^{+6.4}_{-1.5}$	-10^{+10}_{-0}	34^{+2}_{-4}	323^{+60}_{-60}	< 1000
low-z	81.94/17	-	< 0.82	$1.64^{+4.8}_{-1.0}$	$1.56^{+0.07}_{-0.06}$	-	-	-	-	77^{+21}_{-21}
low-z	69.74/16	>99.7	< 0.82	$1.23^{+2.48}_{-0.85}$	1.55 ± 0.06	$\equiv 6$	$\equiv -2$	$\equiv 30$	154^{+69}_{-68}	16^{+16}_{-16}
low-z	51.69/13	>99.7	< 0.82	$1.03^{+1.27}_{-0.73}$	1.57 ± 0.06	33^{+23}_{-14}	$-2.86^{+2.86}_{-0}$	27^{+0}_{-27}	190^{+56}_{-56}	56^{+21}_{-21}
Mid-z	73.79/17	-	< 0.82	$4.56^{+3.8}_{-3.2}$	$1.62^{+0.06}_{-0.04}$	-	-	-	-	88^{+26}_{-26}
Mid-z	64.08/16	>99.7	< 0.82	$2.94^{+3.17}_{-2.63}$	$1.60^{+0.06}_{-0.07}$	$\equiv 6$	$\equiv -2$	$\equiv 30$	200^{+50}_{-50}	< 1000
Mid-z	50.33/13	<99.7	< 0.82	$1.09^{+3.62}_{-1.09}$	$1.61^{+0.05}_{-0.06}$	$7.0^{+114}_{-1.1}$	$-1.52^{+1.52}_{-0}$	42^{+0}_{-42}	334^{+149}_{-149}	< 67
High-z	44.52/17	-	$0.44^{+0.24}_{-0.24}$	< 3.29	1.72 ± 0.05	-	-	-	-	95^{+24}_{-24}
High-z	44.15/16	<90	$0.42^{+0.25}_{-0.25}$	< 3.29	1.72 ± 0.05	$\equiv 6$	$\equiv -2$	$\equiv 30$	37^{+3}_{-3}	77^{+42}_{-42}
High-z	38.64/13	<90	$0.42^{+0.24}_{-0.24}$	< 3.29	$1.71^{+0.02}_{-0.05}$	289^{+700}_{-230}	-10^{+10}_{-0}	26^{+0}_{-26}	133^{+32}_{-32}	< 1000

The spectrum of the full sample fitted with the complex model is in the top panel of Fig. 5.12; its fit with the diskline with fixed parameters added to the complex model is in the middle panel of the same figure; the fit with the diskline with free parameters is instead in the bottom panel. The vertical line marks the position of the energy 6.4 keV. The two models obtained for the full sample using a complex model plus a diskline with fixed and free parameters are shown in Fig. 5.13 in the left panel and right panel respectively. In that figure, the vertical line is located at 6.4 keV and the blue profile represents the diskline model component.

For each subsample, from Fig. 5.14 to Fig. 5.21, we show: in the first panel the fits with the complex model plus the fixed diskline, in the middle panel the fits with the same model with free diskline; in

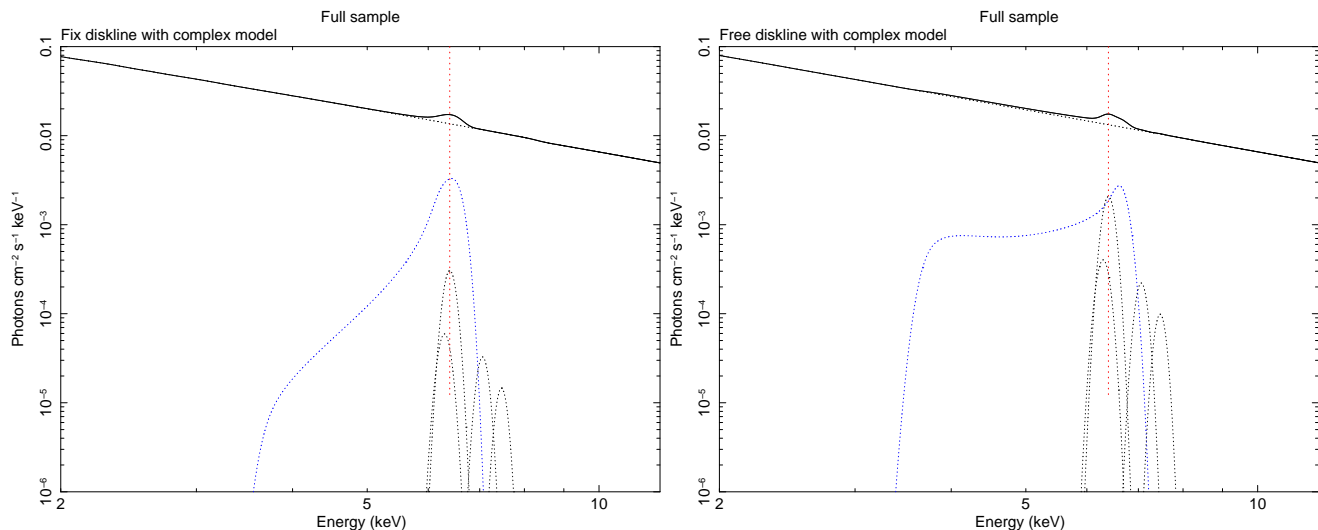


FIGURE 5.13: Complex models with diskline: model with fixed diskline parameters (left panel); model obtained with free diskline parameters (right panel). Full sample

the bottom panel the model obtained in this last fit. The vertical line is always located at 6.4 keV and the blue profile indicates the `diskline` component.

5.3 Discussion

A significant iron line characterizes the X-ray spectra of our full sample and all our subsamples in luminosity, redshift and N_{H} . Employing our new, model-independent analysis, and modelling the line profile with a gaussian, we have shown that the line is significantly broadened (~ 310 eV in the full sample) in all the subsamples with the exception of high-L and high-z.

We investigated subsamples in luminosity and redshift to check a possible trend of the EW of the narrow iron line. The results of such subsample division did not highlight any dependence of the line EW on these two parameters. While a non-dependence with the redshift has been found the previous analysis of Brusa et al. (2005), a non-variable EW for different luminosities would be instead harder to understand, given that the Iwasawa-Taniguchi effect has been well assessed in many recent works (Bianchi et al. 2007). Given the uncertainties to the EW, it is probable that we did not accumulate a sufficient number of counts in each subsample to detect such dependence.

The fits with the `diskline` are in general as good as the fits with the broad gaussian and, adding the narrow core, we found that its significance is generally lower than expected. Probably, to disentangle the two components, a better spectral quality is required.

We used a more realistic model to fit the primary continuum and the reprocessing from material far away from the central engine, along the lines of de la Calle Pérez et al. (2010) and Nandra et al. (2007). The fits to the spectra improve with the addition of the `diskline` at $>99.7\%$ of significance in almost

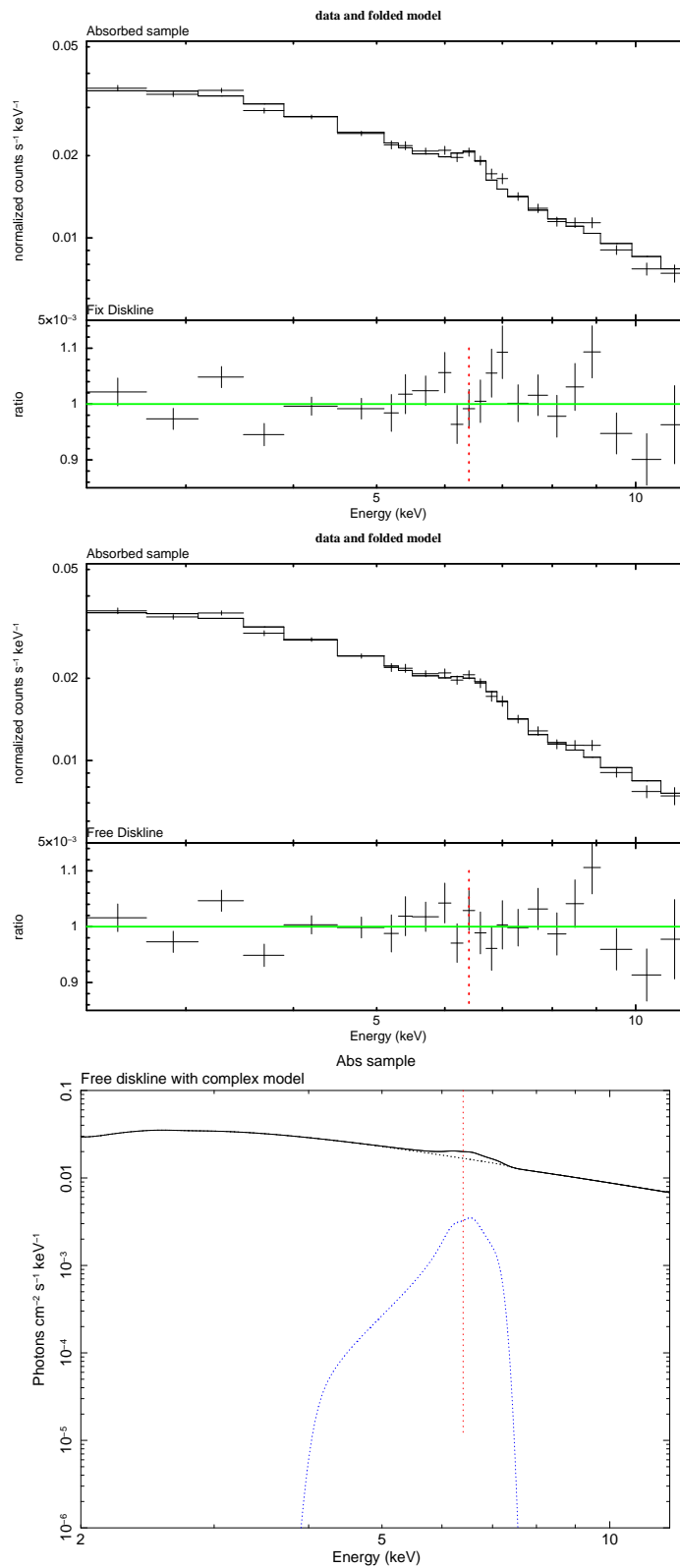


FIGURE 5.14: Fits with the complex model plus diskline with fixed parameters (top panel), with the complex model plus diskline with free parameters (middle-panel) and model found in this second case (bottom panel). Abs sample

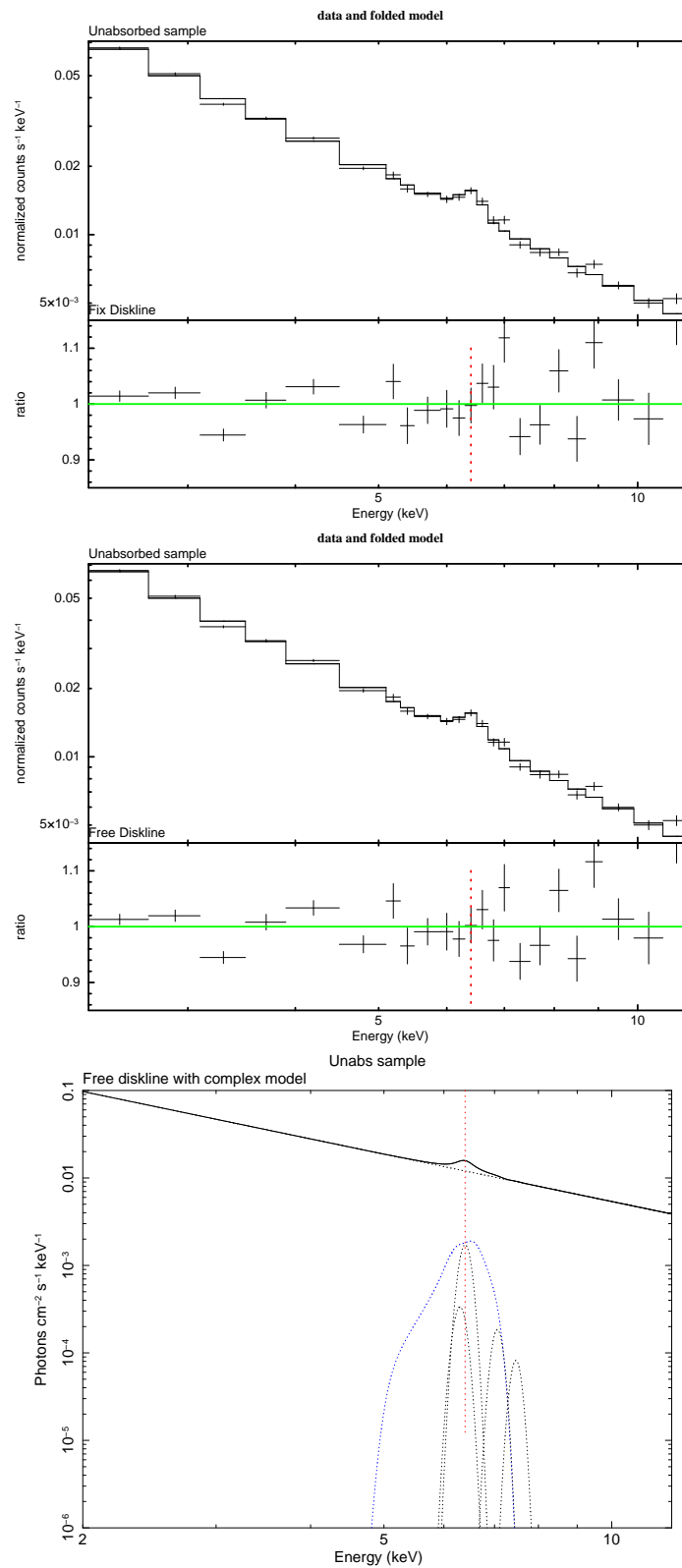


FIGURE 5.15: Fits with the complex model plus diskline with fixed parameters (top panel), with the complex model plus diskline with free parameters (middle-panel) and model found in this second case (bottom panel). Unabs sample

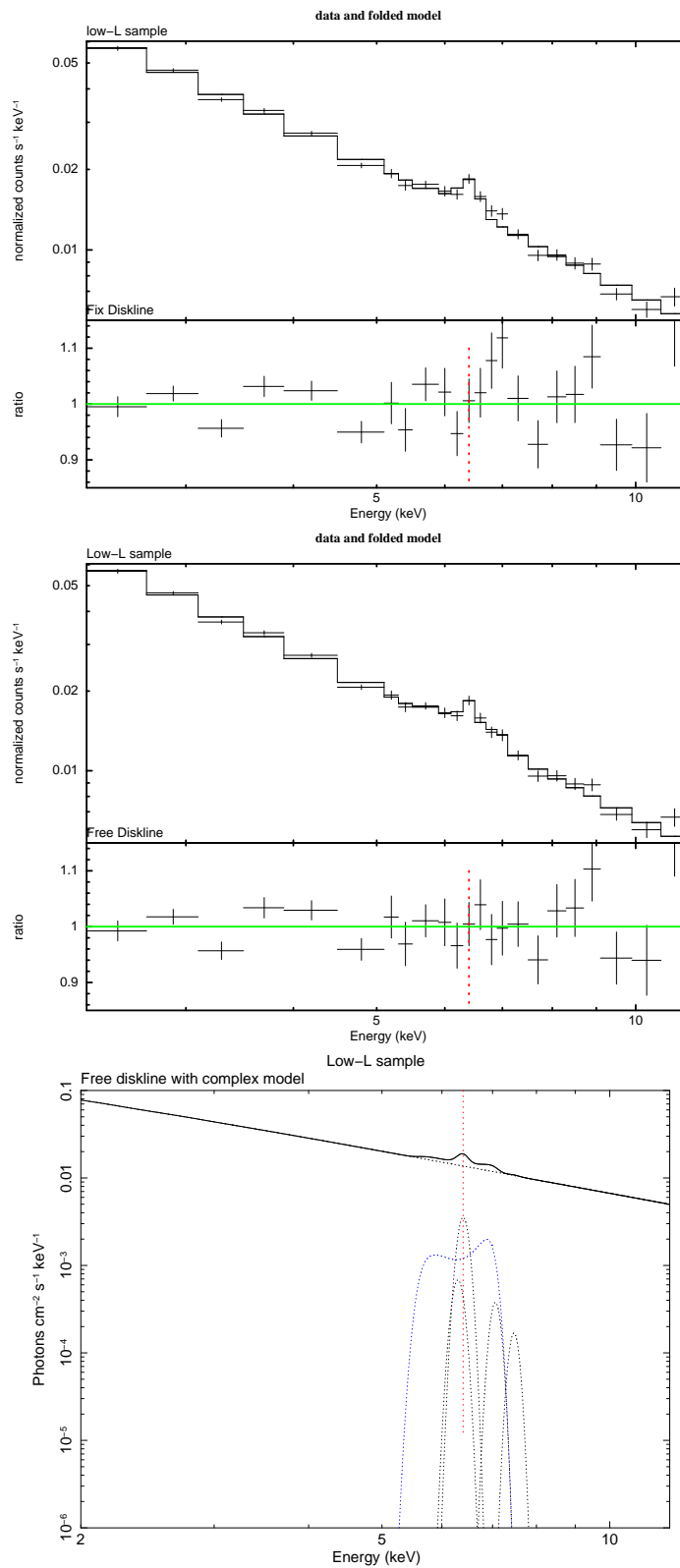


FIGURE 5.16: Fits with the complex model plus diskline with fixed parameters (top panel), with the complex model plus diskline with free parameters (middle-panel) and model found in this second case (bottom panel). Low-L sample

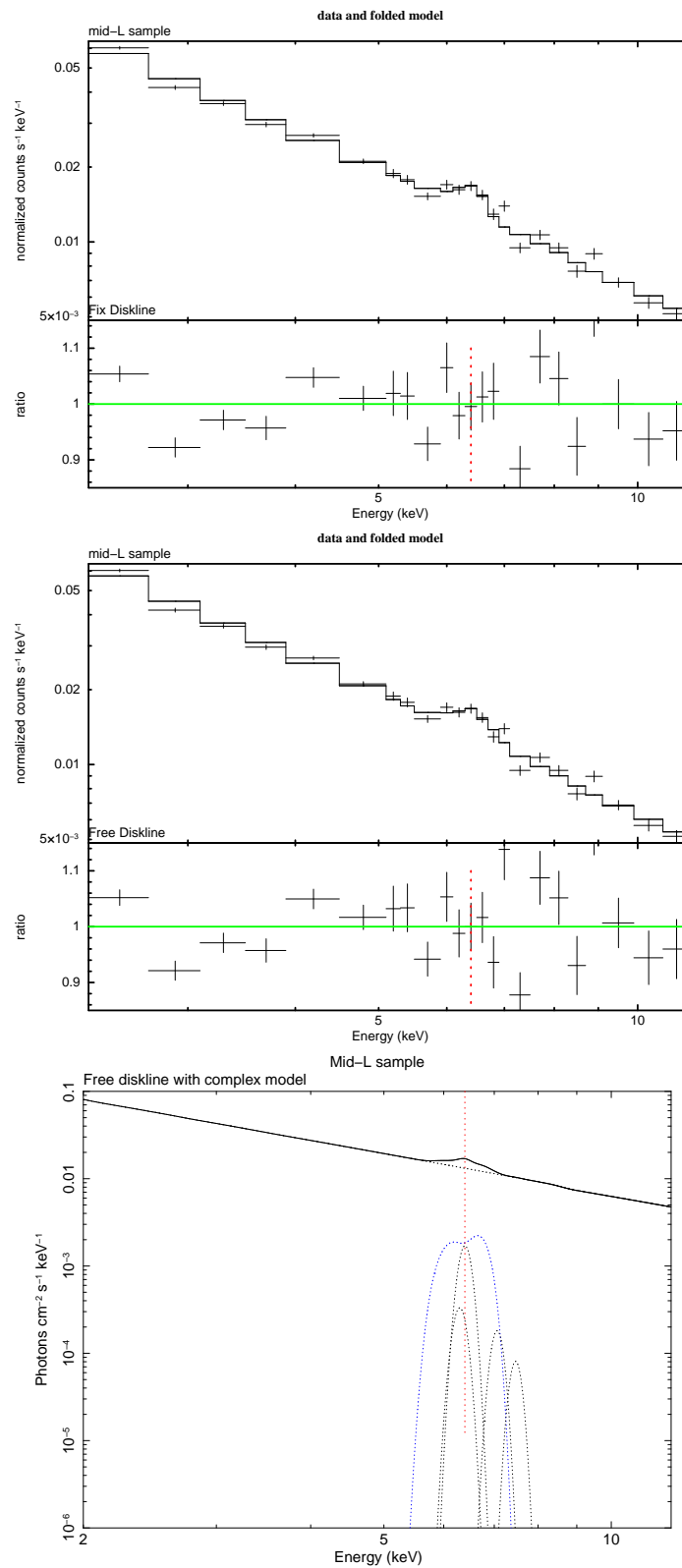


FIGURE 5.17: Fits with the complex model plus diskline with fixed parameters (top panel), with the complex model plus diskline with free parameters (middle-panel) and model found in this second case (bottom panel). Mid-L sample

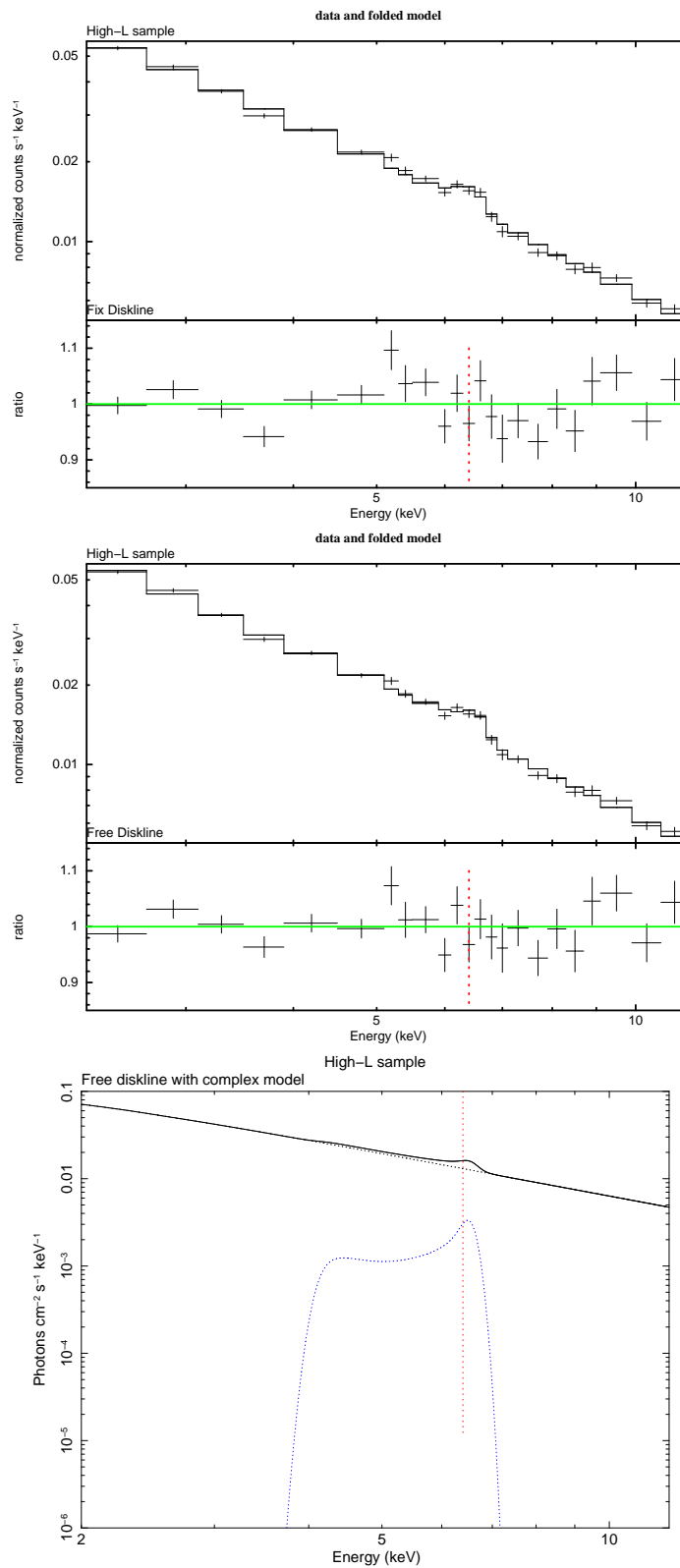


FIGURE 5.18: Fits with the complex model plus diskline with fixed parameters (top panel), with the complex model plus diskline with free parameters (middle-panel) and model found in this second case (bottom panel). High-L sample

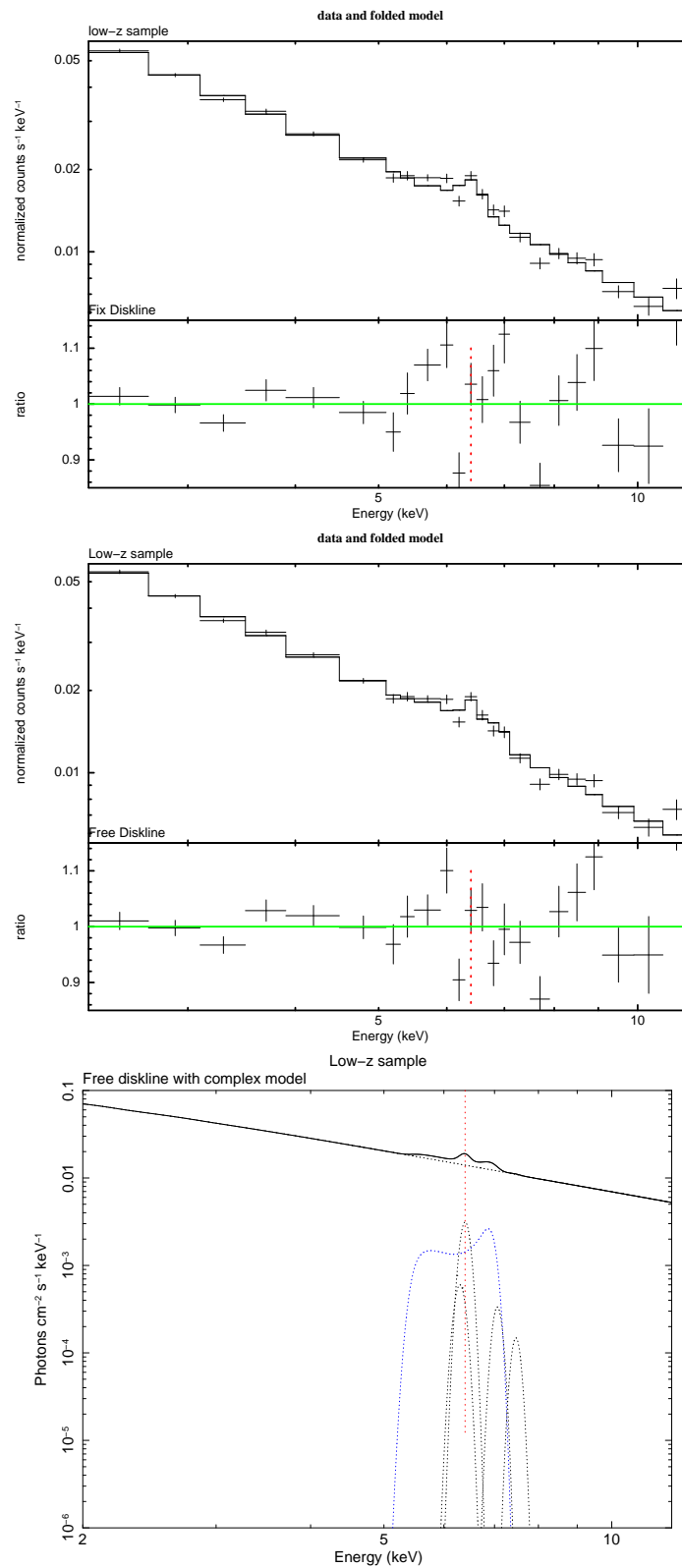


FIGURE 5.19: Fits with the complex model plus diskline with fixed parameters (top panel), with the complex model plus diskline with free parameters (middle-panel) and model found in this second case (bottom panel). Low-z sample

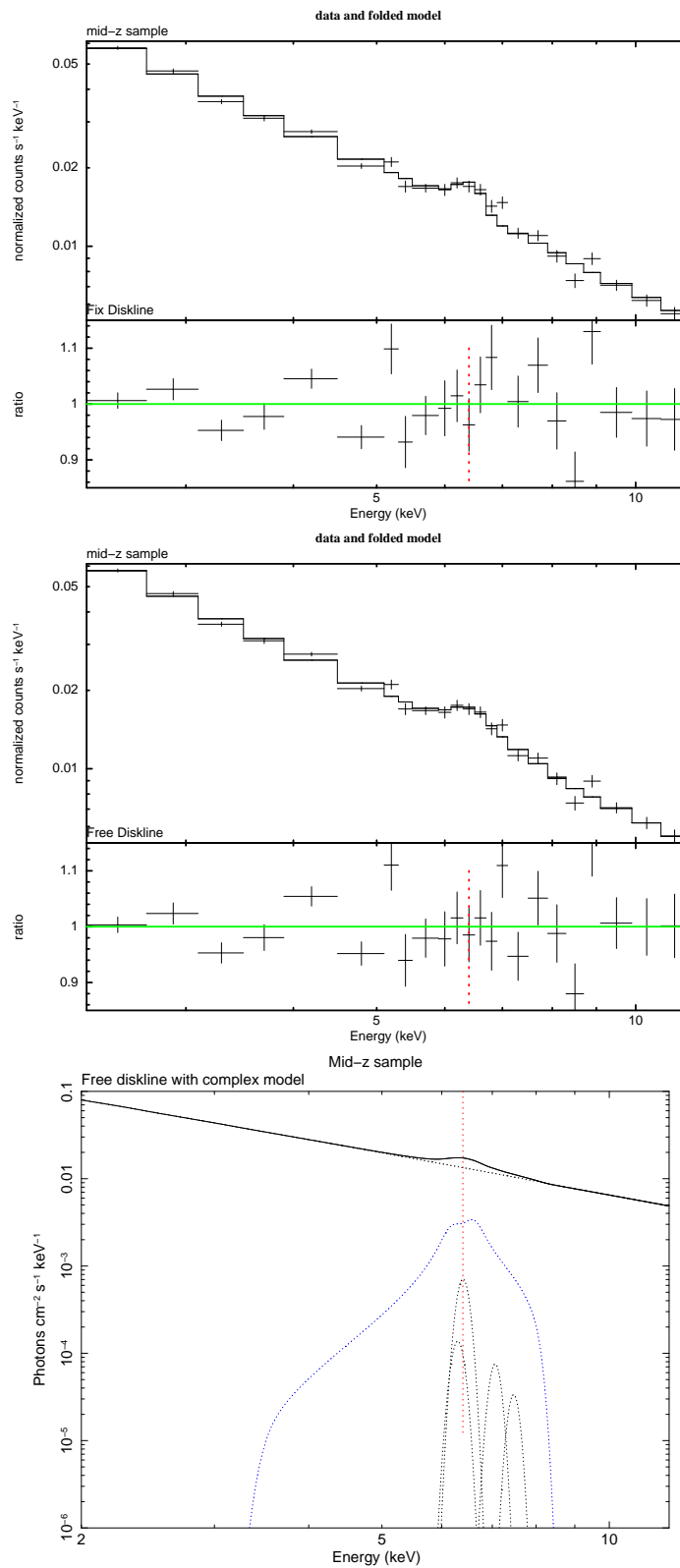


FIGURE 5.20: Fits with the complex model plus diskline with fixed parameters (top panel), with the complex model plus diskline with free parameters (middle-panel) and model found in this second case (bottom panel). Mid-z sample

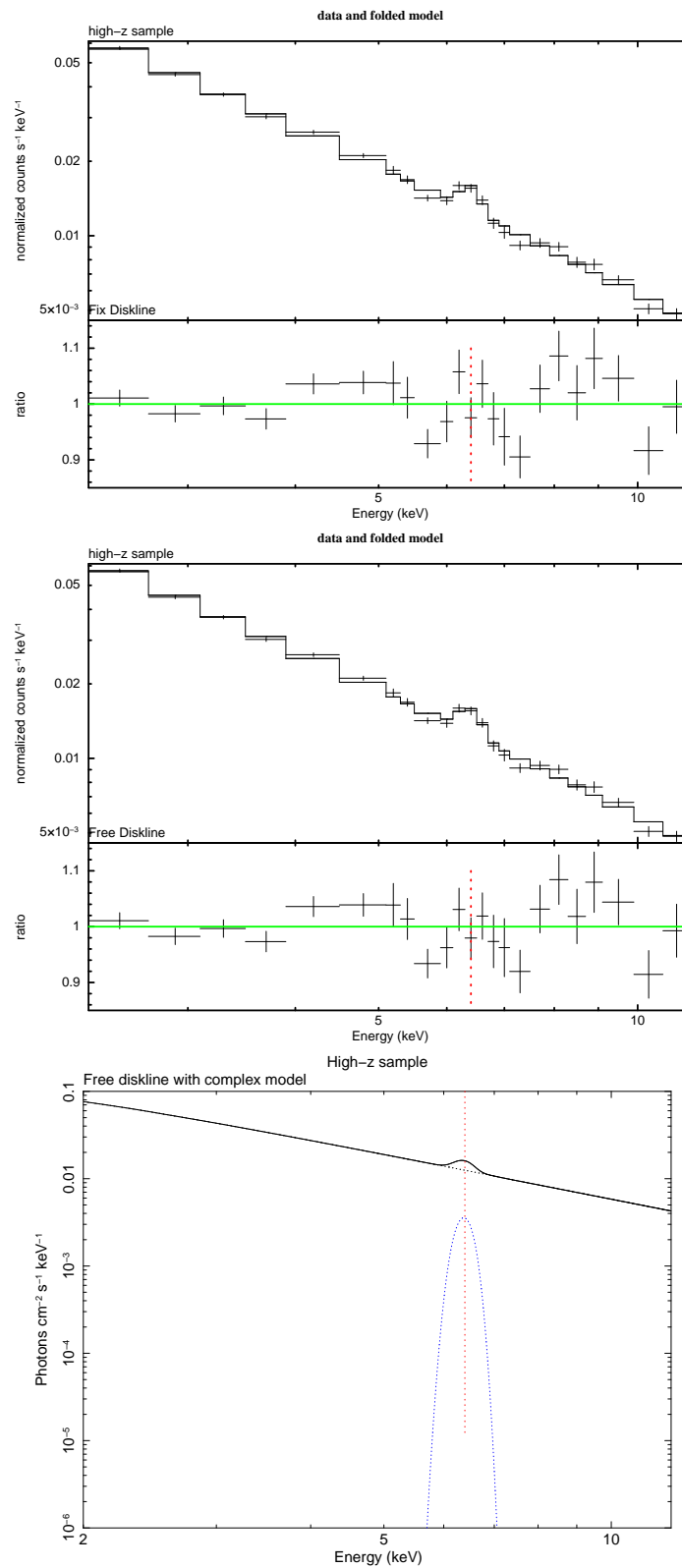


FIGURE 5.21: Fits with the complex model plus diskline with fixed parameters (top panel), with the complex model plus diskline with free parameters (middle-panel) and model found in this second case (bottom panel). High-z sample

all cases. In general, our data do not require to change the input disk parameters significantly. In most cases, the `diskline` parameters θ , R_i , β , are strongly degenerate or cannot be constrained with precision. Anyway, taking the results at face value, they tend to be consistent with the input.

The estimation of the EW of the relativistic line and its comparison with individual values in the literature, give an information about the fraction of the sources contributing to such feature. In the fits with a `diskline` component and a narrow gaussian, for the relativistic component we obtained EW of 193 eV in the full sample. A probable overestimation of this component is accompanied by the low significance and EW of the narrow core, and its EW of just 28 eV.

Using a complete model that represents fluorescent emission from material far away from the central sources, like in de la Calle Pérez et al. (2010) and Nandra et al. (2007), we obtained a lower value of the EW. An EW of 164 eV was found in the full sample. The EW of the narrow core at 6.4 keV has been constrained to be lower than 36 eV.

The EW of the relativistic lines are consistent with those of Nandra et al. (2007) and de la Calle Pérez et al. (2010). In particular, de la Calle Pérez et al. (2010) found in their flux-limited sample an EW distribution extended up to about 250 eV, with an average value of about 170 eV.

5.4 Conclusions

We studied a complete sample of 100 spectra (51 AGN) with the best spectral SNR in the CDFS *XMM-Newton* observation. The ultra-deep exposure of 3.3 Ms allowed to collect a good number of high quality spectra, with $\text{SNR} > 15$, totalling more than 180000 counts between 2 and 12 keV rest-frame.

We averaged the spectra of the full sample and several subsamples developing further our own method previously used in Corral et al. (2008) and Falocco et al. (2012) and we characterised the instrumental and averaging effects using extensive simulations.

With our new methodologies, we could explore for the first time in X-ray stacking the relativistic contribution to the average iron line of a deep AGN survey with high confidence, taking full account of the instrumental and methodological effects.

We estimated the EW and the line significance in a model-independent way, finding that an iron line is significant $>99.99\%$ in the full sample and in all its subsamples. The model-independent estimation of the EW is 129 eV in the full sample, and ranges from 86 eV to 157 eV in the subsamples.

Investigating subsamples in luminosity and redshift, we did not detect a significant dependence of the line EW on these parameters: our uncertainties on the EW do not allow to study such trends. This is probably due to the fact that we have accumulated an insufficient number of counts in each subsample.

Fitting the line with a relativistic line profile and a narrow gaussian core, we probably overestimated the EW of the broad line component. Given that we expect to detect a primary continuum reprocessed from material far away from the central engine (i.e. the torus), we decided to employ a more realistic model taking this into account: we used a complex physically-motivated model to represent it along the lines of de la Calle Pérez et al. (2010) and Nandra et al. (2007). From the fits with such models, we found that our data require, besides the expected set of fluorescent lines from material far away from the central source, a broad line in the full sample and in almost all the subsamples that we constructed. For its correct physical interpretation we used a relativistic line: `diskline` in `Xspec`. Given the limited spectra resolution of the average spectra in analysis, we chose to not employ more complicated models such as, for example, `laor` (Laor 1991), because we felt that the data do not allow to distinguish between them. For this reason we used the simplest model in the literature.

The input disk parameters were broadly consistent with: the average angle between the perpendicular to the disks and the observer to be of 30 degrees; the accretion disks to be extended from $6 R_g$ to $1000 R_g$; the emissivity function to scale as r^{-2} . Under this last hypothesis, the bulk of the fluorescence production occurs in the innermost annuli of the accretion disk, and this means that the continuum source is located in the inner edge of the accretion disk.

Leaving the parameters of the *diskline* model free does not allow in general to determine whether deviations from the input model should be considered to fit our data. Although the limited spectral resolution and the average over many sources would not allow to detect with high accuracy significant deviations from the model, it affords a satisfying interpretation of the broad line profile.

Concluding, our main result is that the relativistic lines are significant at >99.7% in the majority of our subsamples: for the first time in X-ray stacking, a broad iron line has been detected with high confidence and its presence has been well assessed with a large amount of simulations.

The EW of the relativistic iron lines are generally consistent with the average values found in de la Calle Pérez et al. (2010) and Nandra et al. (2007), being 167 eV in the full sample. This highlights that the broad iron line is emitted by a large fraction of AGN in this survey.

Summarising, we found that a broad iron line is strongly detected, emitted through fluorescence at 6.4 keV in material both far away from the primary emission source and relatively close to the SMBH since the relativistic effects are also detected.

Increasing the total number of counts available for these studies would help to constrain better the parameters of the line and hence, the general properties of the emitting region. This is investigated in the next Chapter with the VCV sample.

The results discussed in this Chapter are part of a paper close to submission to *Astronomy & Astrophysics*.

Chapter 6

Stacking of the VCV survey

We employ the VCV survey for the study of the AGN X-ray spectra with a high SNR. It is a superficial survey that, thanks to the high sensitivity of the instruments of *XMM-Newton*, allows to compile many spectra with good spectral quality.

With its high counts statistics, the average spectra of this wide survey allow the detection and the characterization of the relativistic iron lines.

We show in this chapter the preliminary results of this analysis.

6.1 Properties of the VCV sample

In this analysis, we focussed on the spectra with spectral SNR > 15 in the rest-frame band between 2 and 12 keV rest-frame.

TABLE 6.1: Properties of the VCV full sample and the subsamples. Columns: (1) (Sub)Sample; (2) Number of sources; (3) number of net counts in 2-12 keV rest-frame; (4) number of net counts in 5-8 keV rest frame; (5) average redshift; (6) average rest-frame 2-10 keV luminosity; (7) average intrinsic column density in 10^{22} cm^{-2} *

Sample	N	N_{2-12}	N_{5-8}	$\langle z \rangle$	$\langle \log(L) \rangle$ erg/s	$\langle N_{\text{H},22} \rangle$ 10^{22} cm^{-2}
Full	672	706870	160242	1.03	44.46	0.454
Unabs	544	510818	100605	0.950	44.20	0.04
Abs	128	196052	59636	1.399	44.46	2.22

The resulting VCV sample contains a total of 672 spectra (340 individual sources) observed with the EPIC camera. The high number of counts accumulated in good quality spectra is 706870, promising for the detection and an accurate study of the iron line properties. The spectra, after being grouped with a minimum number of 20 counts per bin, were fitted between 1 and 12 keV restframe using an

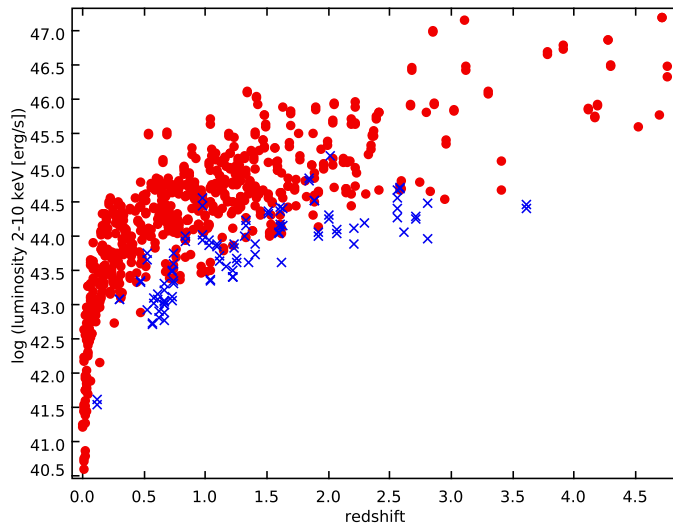


FIGURE 6.1: Distribution of VCV sample (blue crosses) and XMM CDFS sample (red circles) in the parameter space

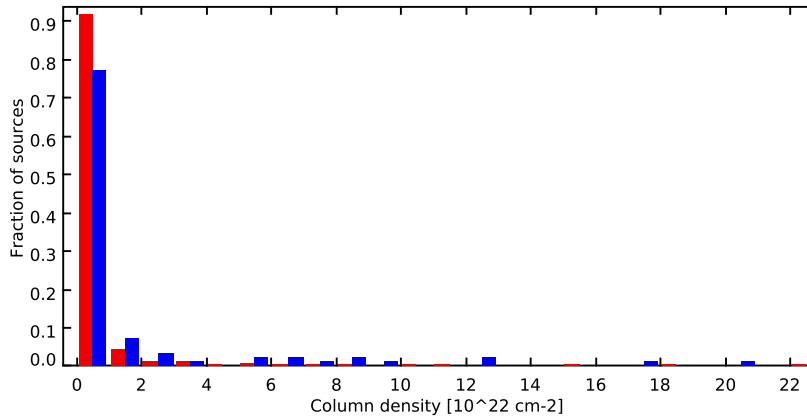


FIGURE 6.2: Fraction of sources with a given intrinsic N_{H} in 10^{22}cm^{-2} in the VCV catalogue (red histogram) and in the CDFS catalogue (blue histogram)

absorbed powerlaw ($\text{pha} * z^{\text{zpha}} * \text{pow}$) by Galactic and local absorption. We calculated the luminosities between 2 and 10 keV rest-frame with the best fit model corrected for intrinsic and Galactic absorption, as usual.

The distribution of the sample in the parameter space (see Fig. 6.1) shows that the VCV covers a larger area than the XMM CDFS explored in the previous chapter. Moreover, it fills up the low redshift zone of $z < 0.5$ with a large quantity of sources distributed over a broad span of luminosities. In general, VCV sources have higher luminosities than XMM CDFS ones, because it is a shallower survey.

We have estimated the N_{H} of the intrinsic absorption using the best fit models, too. Their distribution shows a large amount of unabsorbed sources (see Fig. 6.2). Comparing the VCV and the XMM CDFS

N_{H} distributions, the first one has a dominant population of Unabsorbed sources, while the second one has a larger fraction of Absorbed AGN (though the majority of the sources is unabsorbed).

We divided the sample in Absorbed and Unabsorbed subsamples setting the threshold, as always, at $\log(N_{\text{H}}/\text{cm}^2) = 21.5$ as explained in Sect. 4.0.5.

The characteristics of the samples so defined are in the Table 6.1. This survey is strongly dominated by unabsorbed sources, being the obscured ones only one fifth of the full selected sample. For this reason, in the normalisation process of each spectrum, the integral of the continuum flux per each source is performed in the band between 2 and 5 keV rest-frame (considering also the band between 8-10 keV rest-frame as we made in Chap. 5 is not necessary in this case because the majority of the sample is made by Unabsorbed sources).

6.2 Results

After applying our procedure for the spectral stacking, we obtained the average spectra in Fig. 6.3. An intense iron line is detected in this survey, and it is visually broadened on both its red and blue side.

Before making the spectral fitting, we measured the resolution of our method. To estimate it, we considered that the narrow core of the line is broadened by this effect. Fitting its profile, we obtained that it was 132 eV in the full sample and 123 eV in the unabsorbed sample. We assumed that the trend of the resolution $\sigma(E)$ is approximately constant in the band that we analyse. To do that, we set the value α of the `gsmooth` convolution model to 0.

Taking into account the complexity of the line profile in the absorbed sample (which should also be present in the full sample), we have only attempted a preliminary characterisation of the unabsorbed sample apparently and (as expected) free of such complexities.

We fitted the average spectrum of the Unabsorbed sample using the 'complex model' employed for the XMM CDFS sample (see Chap. 5.1). An excess leftward and rightward of the energy 6.4 keV is found (see Fig. 6.4), indicating that there must be a contribution of iron line also from material close to the central BH.

We added a `diskline` with fixed parameters as we made in the analysis of the XMM CDFS (set as we have made in Sect. 6.4): in these fits, the angle θ is 30 degrees, the emissivity β is -2, the inner radius R_i is $6 R_g$.

The spectral fitting is more appropriate to recover the line profile found, at least red-ward the narrow line emission (see Fig. 6.4). No improvement of the ratios is instead reached blue-ward the narrow core.

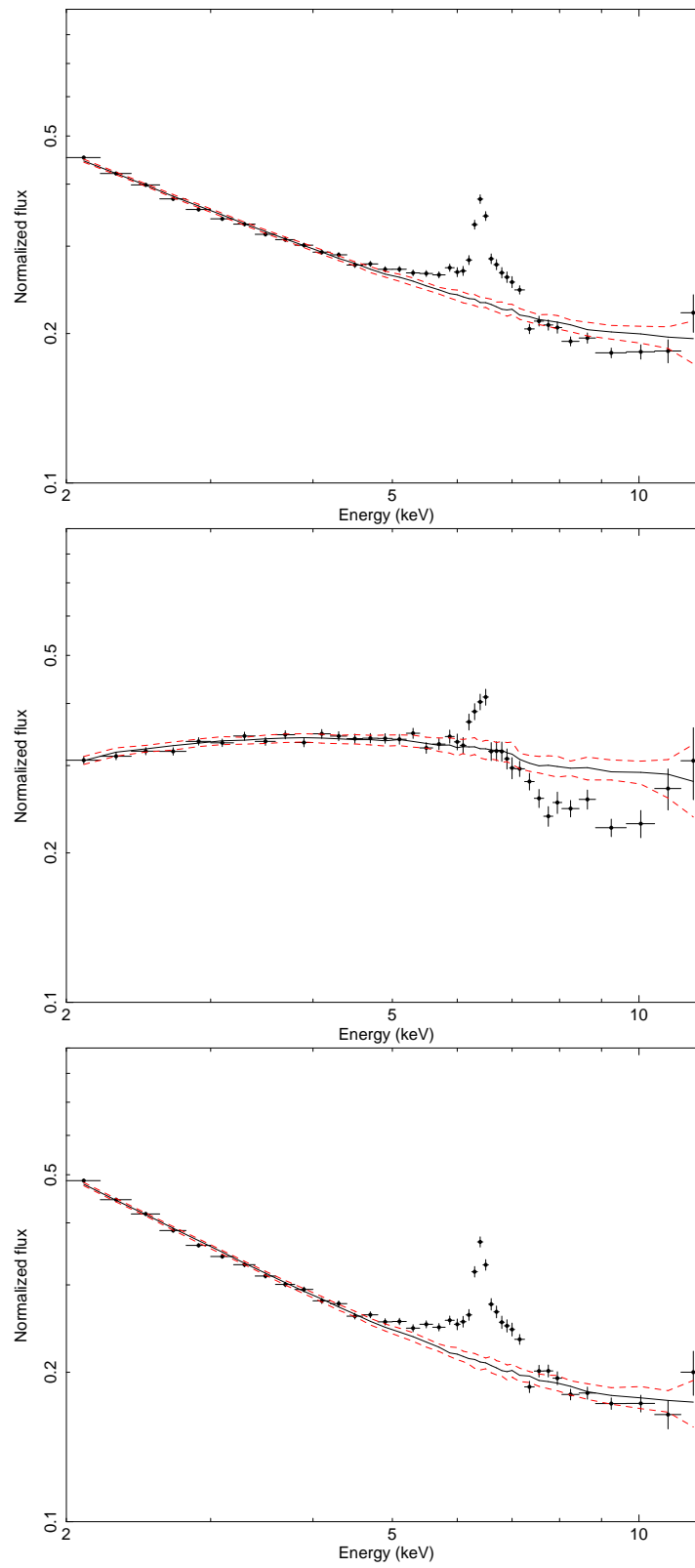


FIGURE 6.3: Average spectrum of the VCV full (top panel), absorbed (middle panel), unabsorbed sample (bottom panel) with their simulated continua

Then, we left the `diskline` parameters (θ , β , R_i) free and the adjustment corrects the residuals blueward the line, while slight improvements are introduced for $E < 6.4$ keV (see the bottom panel of Fig. 6.4)

6.3 Conclusions

Although we still need to progress in the quantitative analysis of the spectral features of the average spectrum of VCV, we can already draw some preliminary conclusions from our analysis. We performed the spectral fitting of the sample taking into account the full set of fluorescent lines that are expected to be emitted far away from the central BH.

From the fitting, a strong excess is still left, displaying large ratios between data and model both blueward and leftward the energy 6.4 keV.

Adding the `diskline` model to represent such feature, we recovered the red wing: the model considering the emission from an accretion disk affords a more suitable fitting of the line. The fixed `diskline`, while taking into account the red wing of the relativistic component, leaves instead unrepresented the excess detected blueward the line (see Fig. 6.4, middle panel).

When we leave the parameters of the `diskline` free to vary, the inner radius increases from 6 to $\sim 18R_g$ (that is still an annulus close enough to the central BH to detect the relativistic effects) which would argue against very strongly rotating BH. The inclination angle of the fit is about 48° , indicating a preference for higher inclination angles, even for these unabsorbed objects. The emissivity law is slightly steeper, indicating that the location of the continuum source is preferentially in the inner edge of the disk. Perhaps, leaving the parameters free, we might have overestimated its EW because some contribution from an ionized line, as found by Iwasawa et al. (2012), might be present and unaccounted for in the current state of our analysis.

There are some systematic residuals in the continuum at low and high energies that we still need to model. The former might be accounted for by a partial covering with mild absorption, while the latter might correspond to a reflection component, which is expected to accompany the narrow reflection lines.

Concluding, we strongly (>99.99% significance) detect the presence of a broad, relativistic component of the iron line, with an EW of 219 eV. This value is within the range of the EW found in the flux-limited sample of de la Calle Pérez et al. (2010). It indicates with high significance that an intense relativistic line is a common feature in the unabsorbed AGN. The narrow component is also detected, indicating the presence of fluorescent emission from neutral material far away from the central engine (i.e. the torus), even in unabsorbed objects.

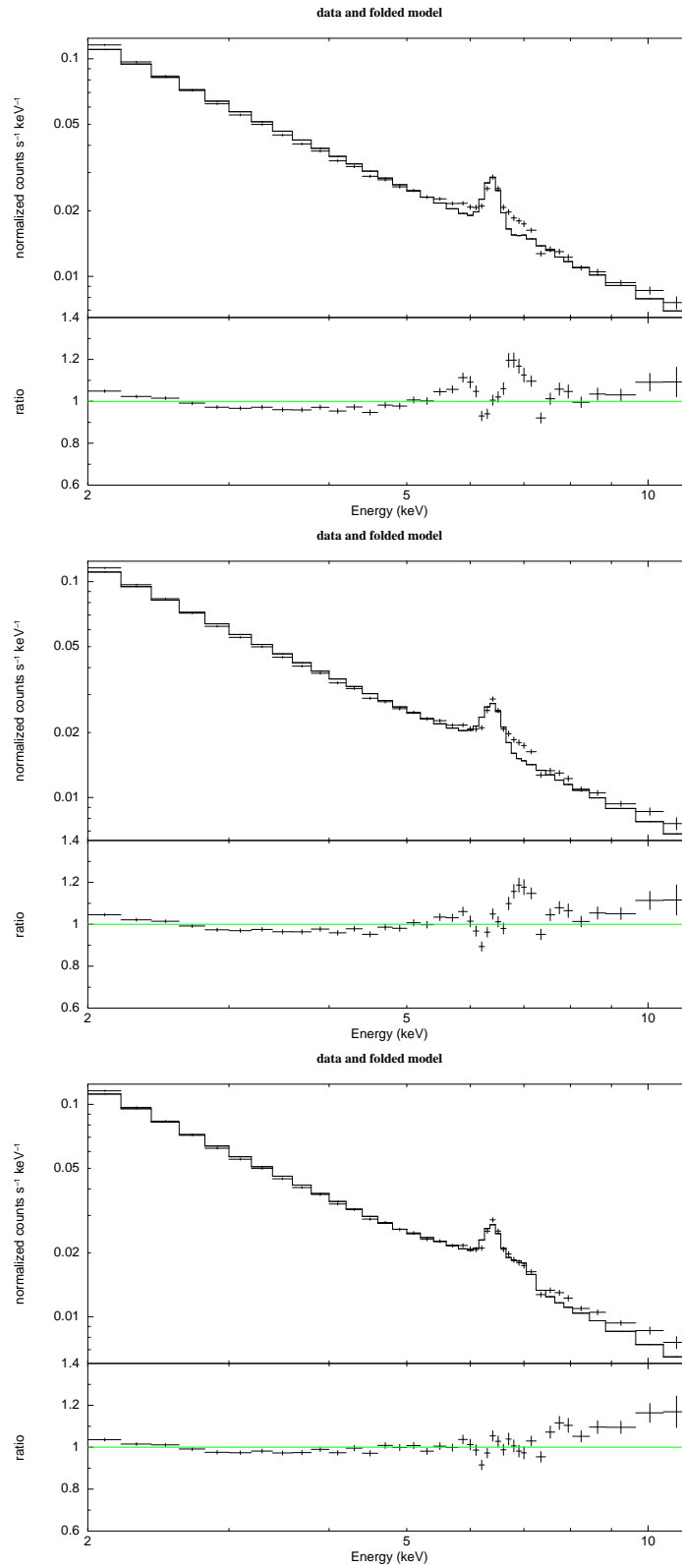


FIGURE 6.4: Average spectrum of the VCV unabsorbed sample fitted with the complex model (top panel), the complex model with the fixed diskline (middle panel), the complex model with the free diskline (bottom panel)

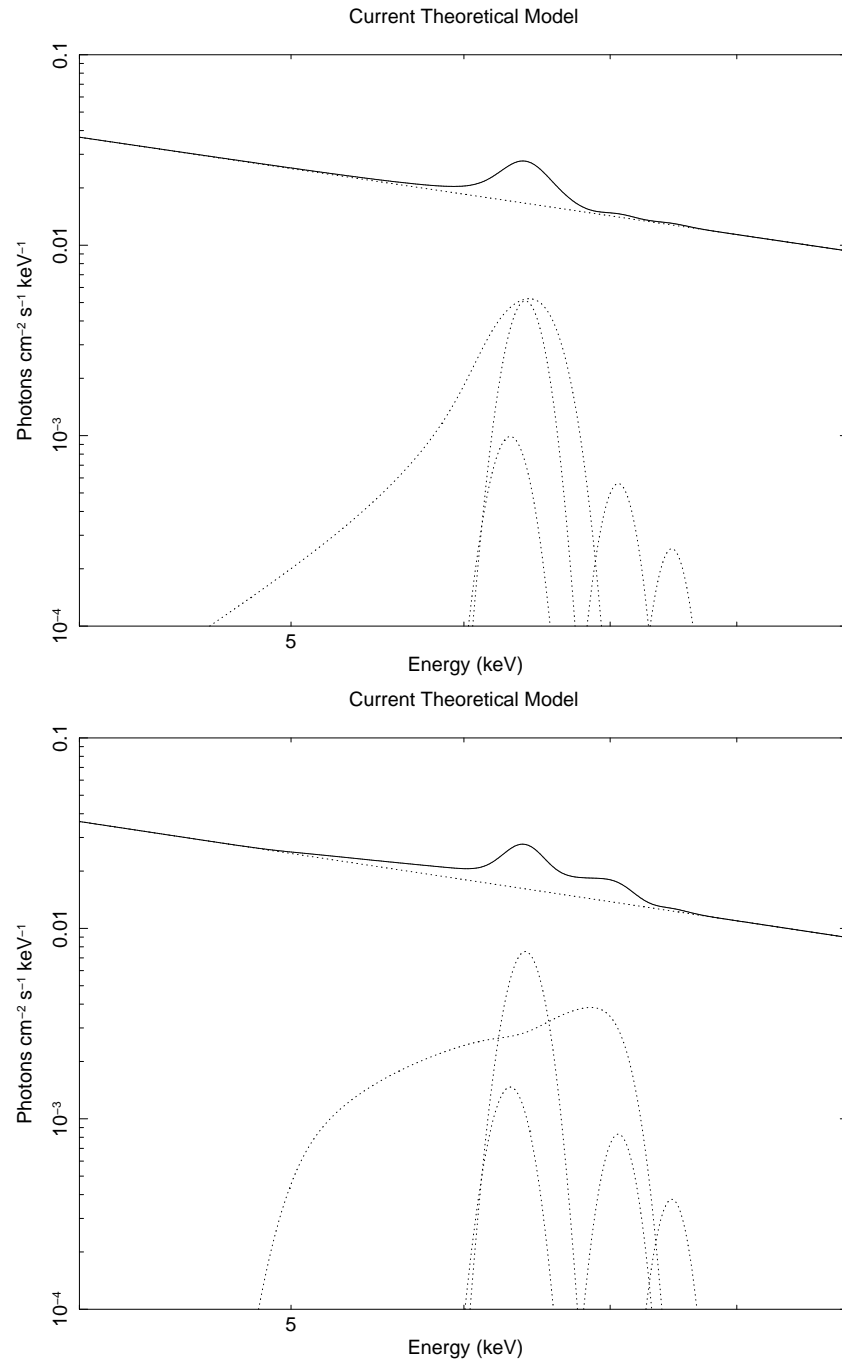


FIGURE 6.5: Complex model with the fixed diskline (top panel), complex model with the free diskline (bottom panel)

TABLE 6.2: Results of fits of the average spectrum of the full sample and its subsamples using the complex model ($\text{gsmo}*\text{absori}(\text{pha}*\text{pow}+\sum\text{gaus})$) in the first line of each sample; the complex model plus the `diskline` with fix parameters $\text{gsmo}*\text{absori}[\text{pha}*(\text{pow}+\text{diskline})+\sum\text{gaus}]$ in the second line; the complex model plus the `diskline` with free parameters in the third line. Columns: (1) sample; (2) χ^2/dof of the fit with the complex model with narrow lines only in the first line of each sample; with the addition of fix `diskline` in the second one, addition of both fix `diskline` and ionized line in the third one, with free `diskline` in the fourth one. (3) Significance of the addition of the `diskline`, in the first line, and significance of leaving its parameters free to vary in the second line. (4)intrinsic column density given by the fits. (5) powerlaw slope. (6) inner radius. (7) emissivity index. (8) inclination angle. (9) `diskline` EW. (10) Narrow gaussian line at 6.4 keV EW.(11) central energy of the ionized component. (12) EW of the ionized component

Sample	χ^2/dof	$P_{\text{disk}}\delta\chi^2$ %	N_{H} 10^{22}cm^{-2}	$N_{\text{H,ion}}$ 10^{22}cm^{-2}	Γ	R_i R_G	β	θ °	EW_{disk} eV	EW_{na} eV
(1)	(2)	(3)	(4)	(5)	(6)	(7)	(8)	(9)	(10)	(11)
Unabs	428.74/35	>99.99	< 0.822	< 1.645	$1.68^{+0.01}_{-0.01}$	-	-	-	-	192^{+11}_{-11}
Unabs	356.51/34	>99.99	< 0.822	< 0.822	$1.69^{+0.01}_{-0.01}$	$\equiv 6$	$\equiv -2$	$\equiv 30$	219^{+42}_{-42}	95^{+24}_{-24}
Unabs	189.32/31	>99.99	< 0.82	< 0.82	$1.73^{+0.01}_{-0.01}$	$17.8^{+12.6}_{-5.8}$	$-3.17^{+0.5}_{-0.9}$	$47.9^{+7.0}_{-3.5}$	333^{+43}_{-43}	146^{+19}_{-19}

Chapter 7

Conclusions

Most astronomers nowadays accept that Active Galactic Nuclei are powered by accretion onto a SMBH. Such a model represents the most reasonable explanation for the observed phenomena. However, as a BH is not directly observable, it is possible to infer its existence only through the influence to its close environment. Detection of the characteristic relativistic effects of the black holes requires data that probe such small scales, close to the event horizon. The velocities involved begin to approach to the velocity of light and furthermore the gravitational field of the black hole will cause time-dilation effects resulting in gravitational redshift. These characteristics represent the most compelling test of the black hole paradigm. Modern X-ray spectroscopy is an excellent tool with which we can peer into the exotic world of accretion onto black holes.

7.1 Conclusions of this thesis

In this thesis we have presented a uniform analysis of AGN surveys employing our averaging method. Having been the results of the X-ray spectral analysis of AGN quite controversial during the last years, confirming the presence of relativistic lines in some works (Streblyanska et al. 2005) or rejecting it in others (Corral et al. 2008), our work proposes to apply a uniform approach of analysis for substantially different samples.

The strategy adopted was to compile as many spectra as possible for AGN, to construct an average spectrum and to obtain the mean properties of the iron line from it.

We have used the deepest surveys observed by *Chandra* and *XMM-Newton* (CDFN, AEGIS, CDFS) to understand the iron line emission of the AGN in the distant Universe and to explore the accretion properties in different cosmic epochs.

With the purpose to accumulate a large number of counts using spectra that possess good SNR, we have also explored the iron lines in the Universe using the VCV sample. The body of data accumulated in this survey allows a detailed study of the iron line properties of AGN.

7.1.1 Average Fe line emission from *Chandra* deep fields

In our study of the *Chandra* deep fields, we focused on the spectra in the surveys of CDFS, CDFN and AEGIS. This is one of the most relevant surveys of AGN made so far in today's X-ray observatories, totalling 123 unique sources with spectroscopic redshifts and good quality spectra. The total amount of counts is ~ 70000 in the 2-12 keV rest-frame band. After having checked our results with the use of extensive simulations, we found that a narrow line characterises our sample with an EW of 74 eV. Investigating the subsamples in luminosity of the continuum and in redshift, we found that the EW of the narrow line is somewhat lower for higher luminosities in agreement with the Iwasawa-Taniguchi effect, but considering the error bars on the EW the correlation cannot be considered as significant. Given the distribution of the sample in the parameter space formed by luminosity and redshift, we could not check whether the decrease is due to the increase of the luminosity or of the redshift. To disentangle the two effects, we will need wider samples that cover better the low redshift zone of the parameter space.

We investigated the presence of the broad component of the iron line by fitting the spectra with a gaussian, the simplest phenomenological model that allows to check if the line required by our data is broadened. We found that the line is broad only in the low-L low-z subsample being its σ 240 eV. The line is symmetrical: the asymmetries due to the relativistic contribution should be very prominent to be significantly detected in stacked spectra. In fact, we should consider two effects. First, in such spectra not only the relativistic lines contribute to the average, but also neutral iron and ionised iron lines emitted by material far away from the central source. A contribution from ionised iron, for example, has been recently found in Iwasawa et al. (2012). In a second hypothesis, a superior SNR is required for the detection of relativistic lines.

7.1.2 Average Fe line emission from the XMM CDFS deep field

The *XMM-Newton* observation of the CDFS allows to accumulate a higher number of counts than the previous 2 Ms observation of *Chandra*. This survey is the deepest one available today from *XMM-Newton* observatory and it affords a more significant detection of the iron line thanks to the highest sensitivity of the instruments. Studying this sample, we were allowed to focus on a total 100 spectra (51 distinct sources) with a good quality, totalling about 180000 counts in the band between 2 and 12 keV rest-frame.

To study in better detail the iron line profile, we applied for the first time our new methodology checking the effects of broadening introduced by our averaging method over the full 1-12 keV rest-frame range.

To avoid being affected by errors in the EW estimations due to an incorrect determination of the continuum underlying the iron line, in this study we estimated the line EW and significance in a model-independent way. Using our innovative method, we found that the iron line is a fundamental spectral characteristic (significant at 4 sigma) of AGN and its EW is 129 eV in the full sample.

From this model-independent analysis and from the fits to the spectra, we found that the line is broadened at more than 3 sigma. Fitting the spectra with a proper model taking into account the primary continuum and its reprocessing from cold material, we understood that our data require, besides a set of fluorescent lines emitted from material far away from the central source, a relativistic line emitted from the accretion disk. This component affords a better physical interpretation of the excess around 6.4 keV, being significant at more than 3 sigma in the majority of the subsamples.

The EW estimated from the fits is of 167 eV, consistent with the values of single spectra in the literature. In particular, it this value is consistent with the average value found in the sample studied by de la Calle Pérez et al. (2010). If emitted by a low fraction of sources, the AGN contributing to the line should have EWs higher than individual observed values. For this reason, we can conclude that the sources contributing to the average relativistic line are an important fraction of the full XMM CDFS sample.

7.1.3 Average Fe line emission from XMM VCV wide field

This sample, being a wide, *XMM-Newton* survey, allows to collect many spectra with good quality: using the ~ 700000 counts we can afford a more detailed study of the iron line profile. The iron line appears evidently broadened. We have checked this result making the spectral fits to the average data of the Unabsorbed subsample, the one that lacks the complexities due to the X-ray absorption features. From the fits with `diskline`, the inclination angle of the average spectrum is $\sim 48^\circ$. The inner radius is $\sim 18 R_g$: we did not find any evidence for the presence of a rapidly spinning BH. We found that a narrow core of the iron line has $EW=95$ eV and the broad component, significant at more than 4σ , has EW of 215 eV. This component is well reproduced by the relativistic model. The EW value of the relativistic component is within the range of EW found in the sample of de la Calle Pérez et al. (2010). This means that the relativistic sources should represent here an important fraction of this survey.

7.1.4 Overall conclusions

We studied multi-comprehensive samples of AGN belonging to the most relevant fields presently available, obtaining information on the iron line properties over several orders of magnitudes of luminosities and a broad span of redshift. From our analysis, we can conclude that the iron lines are a common

characteristic the AGN.

We checked whether the EW of the narrow line depends on luminosities and redshifts: our results did not show any significant dependence of the line on these parameters. We cannot tell whether this is an effect of the limited SNR in spectra of the subsamples that we constructed, or whether the line characteristics do not really depend on the luminosity or on cosmic time.

The broad iron lines are detected with high significance in samples with a very good spectral quality (such as our sample of VCV). In samples with less spectral counts, it is possible to unveil the broad component, but it is difficult to detect its difference from a simple phenomenological broad gaussian for the effect of the lower SNR (as we have seen in the XMM CDFS). To explain such symmetrical broadening, we also considered a probable ionised line contribution, but its only marginal detection in our best quality survey (VCV), compared with its highly significant relativistic line, seems to favour instead the first hypothesis, an effect of the SNR.

To disentangle the broad line component and the narrow core, good quality spectra are needed, such as the ones from the VCV catalogue.

Finally, we obtained a strong indication that the broad component is common in AGN: its EW is compatible with the ones found in individual spectra. Consequently, the relativistic line is emitted by the majority of the sources in our surveys.

7.2 Pending issues

In our work, with the three substantially different classes of surveys, the ultra-deep fields from *Chandra* and from *XMM-Newton* observatory, and shallower fields from *XMM-Newton*, we have characterised successfully the iron line properties from the nearby Seyferts to far AGN. We could also explore the relativistic profile of the iron line thanks to the high sensitivity of the *XMM-Newton* detector. Nevertheless, we could not make a detailed study of the dependence of the iron line on the physical properties of the central engine. First of all, we could not detect any trend of the EW with the continuum luminosity: although we found some indication of an anti-correlation between the two, we could not understand if this effect is due to a luminosity dependence or a redshift dependence. In our deep surveys, in fact, we could not disentangle the effects of the two parameters on the iron line detection due to the strong correlation existing between luminosity and redshift.

Another interesting issue we need to address is that we found, in our works, a broad line in the absorbed sample (in CDFS) even though its contribution for such class of sources is not expected according with the theory.

We plan to address these pending issues in these ways:

- finalising the analysis of the VCV sample studying the absorbed sample and the full sample applying our model-independent technique
- EW trend with luminosity and redshift: we plan to take advantage of our large amount of data already reduced and analysed, the VCV catalogue together with the XMM CDFS, selecting the sources with $z < 1$ and dividing them in several luminosity subsamples with the same number of counts. In this way it will be possible to check the Iwasawa-Taniguchi effect in the local Universe. We will also select the sources with luminosities between 10^{44} erg/s and 10^{45} erg/s and construct several bins of redshift with the same number of spectral counts in each one. This will help to check any possible trend of the iron line EW with cosmic time
- Iron lines in absorbed sources can be successfully studied in different samples selected in $E > 5$ keV. Such band is not strongly affected by even moderate amounts of obscuration, so it allows to survey more absorbed AGN
- On a larger time scale we are going to check any dependence of the iron line on the physical properties of the central engines such as the BH masses. To do that, it is necessary to make use of multi-wavelength information in the catalogues, to get the accretion rate or the BH masses

Before the launch of the first X-ray satellites, the physics of the relativistic accretion disks and the astrophysics of BH was only pure theory. Modern X-ray spectroscopy has offered the opportunity to explore these complex systems, although many open questions still remain, the black hole formation and evolution, the physics determining the accretion disk properties, the demography of spinning BH, the BH accretion in relation with galaxy formation and evolution, etc.

It is hoped that in the next decades, increasingly capable instruments will allow to address the most fascinating open questions of X-ray Astronomy. While waiting for these new facilities, our work offers a statistical preview of the results that will be obtained in the future for individual sources.

Appendix A

Different selections of the Chandra sample

We assessed the robustness of our results from the *Chandra* sample by changing the SNR that characterizes our sample selection. To do that, we repeated the analysis for all the sources with more than 50 and more than 100 counts in 2 - 12 keV. We excluded from these samples the spectra with the lowest continuum flux between 2 - 5 keV (otherwise a bias during the normalization process can be introduced, see Sect.3.1 for the details for method): CDFS_227 (CDF-S RA: 53.082, DEC: -27.690), CDFN_405 (CDF-N RA: 189.431, DEC: 62.177), EGS1_003 (AEGIS RA: 215.76, DEC: 53.45). After having defined the samples, we redefined the subsamples of intrinsic column density, luminosity, and redshift, as described in Sect. 4.0.5.

The results are in Tables A.1 and A.3. We can see from the last column in the tables A.2 and A.4 that the Fe line significance, estimated from our model-independent analysis (and confirmed by the spectral fitting) grows with the SNR of the sample, as found in previous results (Guainazzi et al. 2006).

We made the simulations of an unresolved 6.4 keV line for the > 50 cts sample, obtaining results compatible for the spectral resolution of our method with the default > 200 cts sample.

After having applied the same analysis method used for the default > 200 cts sample, we repeated the analysis in XSPEC for the > 50 cts and > 100 cts sample, finding consistent results, although the line significance clearly decreases with the decreasing cut in counts of the sample selection. We can conclude from this analysis that making a more conservative selection of the sample (i.e. including higher quality spectra), despite reducing the total number of spectra and of counts, actually improves the quality of the results.

TABLE A.1: Properties of the sample composed of all the sources with more than 50 counts. L_{43} : luminosity in units of 10^{43} erg s^{-1} . Columns: (1) (Sub)Sample; (2) Number of sources; (3) Number of counts in 2-12 keV; (4) Number of counts in 5-8 keV; (5) average redshift; (6) average luminosity in 10^{43} erg s^{-1} ; (7) average column density of the local absorber in 10^{22} cm^{-2} ; (8) model-independent significance of the Fe line (calculation made between between 6.2 and 6.6 keV).

Sample	N	N_{2-12}	N_{5-8}	$\langle z \rangle$	$\langle L_{43} \rangle$ 10^{43} erg s^{-1}	$\langle N_{H,22} \rangle$ $10^{22} \times cm^{-2}$	Significance
(1)	(2)	(3)	(4)	(5)	(6)	(7)	(8)
Full	347	93385	21730	1.20	8.60	3.08	85
$\log(N_H) > 21.5$	177	40174	10944	1.14	8.00	6.04	85
$\log(N_H) < 21.5$	170	53211	10786	1.28	9.50	0.04	72
$L_{43} < 6$	234	46546	11021	0.90	1.60	3.09	89
$L_{43} > 6$	113	46840	10709	1.80	23.40	3.07	74
$z < 1$	184	46672	10530	0.65	2.60	3.08	83
$z > 1$	163	46713	11199	1.83	15.60	3.08	85
$z < 0.76$	120	31537	7511	0.53	1.80	3.75	81
$L_{43} < 8.4, z < 0.76$	116	26743	6614	0.52	1.20	3.35	82
$L_{43} < 8.4, z > 0.76$	157	31862	6866	1.34	1.70	2.47	94
$L_{43} > 8.4, z > 0.76$	70	29985	7353	2.08	32.10	3.32	77

TABLE A.2: Comparison between fluxes of real and simulated spectra in the total sample with more than 50 counts in each spectrum. F_{simu} : flux of the average simulated spectrum (units of normalized flux per keV); F_{real} : flux of the average observed spectrum; $\frac{N_{<real}}{N_{simu}}$ is the percentage of simulations having lower flux than the observed spectrum. Calculation is performed between 6.3 and 6.5 (1); 6.2 and 6.6 keV (2); between 6.0 and 6.8 keV (3)

Sample	$\frac{N_{<r,1}}{N_{s,1}}$	$\frac{N_{<r,2}}{N_{s,2}}$	$\frac{N_{<r,3}}{N_{s,3}}$
Total	89	85	80
$\log(N_H/cm^2) < 21.5$	75	72	55
$\log(N_H/cm^2) > 21.5$	86	85	80
$L_{43} > 6$	76	74	66
$L_{43} < 6$	91	89	86
$z > 1$	90	85	81
$z < 1$	87	83	76
$z < 0.76$	82	81	67
$z < 0.76$ and $L_{43} < 8.4$	85	82	69
$z > 0.76$ and $L_{43} < 8.4$	94	94	94
$z > 0.76$ and $L_{43} > 8.4$	82	77	68

TABLE A.3: Properties of the sample composed of all the sources with more than 100 counts. L_{43} : luminosity in units of 10^{43} erg s^{-1} . Columns: (1) (Sub)Sample; (2) Number of sources; (3) Number of counts in 2 -12 keV; (4) Number of counts in 5-8 keV; (5) average redshift; (6) average luminosity in 10^{43} erg s^{-1} ; (7) average column density of the local absorber in 10^{22} cm^{-2} ; (8) significance of the Fe line calculated as the number of average simulated spectra with a lower flux than the flux of the average observed spectrum (calculation between 6.2 and 6.6 keV).

Sample	N	N_{2-12}	N_{5-8}	$\langle z \rangle$	$\langle L_{43} \rangle$ 10^{43} erg s^{-1}	$\langle N_{h,22} \rangle$ $10^{22} cm^{-2}$	Significance
(1)	(2)	(3)	(4)	(5)	(6)	(7)	(8)
Full	219	84275	19312	1.24	11.83	2.63	92
$\log(N_H) > 21.5$	104	34893	9422	1.15	10.80	5.50	91
$\log(N_H) < 21.5$	115	49382	9890	1.32	12.69	0.04	100
$L_{43} < 6.65$	134	42061	9718	0.91	2.25	3.03	91
$L_{43} > 6.65$	85	42214	9594	1.76	26.82	1.99	94
$z < 1.01$	109	41477	9216	0.68	3.80	2.74	90
$z > 1.01$	110	42798	10096	1.80	19.71	2.52	99
$L_{43} < 21.0, z < 0.78$	71	28349	6587	0.55	2.40	3.58	90
$L_{43} < 21.0, z > 0.78$	93	29478	6273	1.30	4.80	2.16	100
$L_{43} > 21.0, z > 0.78$	55	26448	6452	2.02	35.80	2.20	90

TABLE A.4: Comparison between fluxes of real and simulated spectra in the total sample with more than 100 counts in each spectrum

Sample	$\frac{N_{<r,1}}{N_{s,1}}$	$\frac{N_{<r,2}}{N_{s,2}}$	$\frac{N_{<r,3}}{N_{s,3}}$
Tot	0.92	0.92	0.89
$\log(N_H) > 21.5$	0.91	0.91	0.87
$\log(N_H) < 21.5$	1.	1.	1.
$L_{43} < 6.65$	0.91	0.91	0.87
$L_{43} > 6.65$	0.88	0.94	0.94
$z < 1.01$	0.91	0.90	0.85
$z > 1.01$	0.98	0.99	0.99
$z > 0.78, L_{44} > 2.1$	0.89	0.90	0.89
$z < 0.78, L_{44} < 2.1$	0.90	0.90	0.83
$z > 0.78, L_{44} < 2.1$	1.	1.0	1.0

TABLE A.5: Sample composed by all the sources with more than **50** net counts in 2 - 12 keV. (1) sample; (2) photon index of the powerlaw ; (3) χ^2 of the fitting with the powerlaw ; (4) χ^2 of the fitting with table model; (5) χ^2 of the fitting with table model plus gaussian; (6) significance of adding the gaussian to the table model; (7) gaussian centroid; (8) gaussian width; (9) EW of the gaussian; (10) average redshift; (11) average luminosity; (12) average column density of the absorber; *: indicates that it was not possible to calculate errors because Xspec gives un-physical values and steppar gives a constant $\Delta\chi^2 < 2.71$ for high sigma ($> 1keV$)

Sample (1)	Γ (2)	χ_p^2/dof (3)	χ_s^2/dof (4)	χ_g^2/dof (5)	$P(\Delta\chi^2, \nu)$ (6)	E(keV) (7)	σ (eV) (8)	EW(eV) (9)	$\langle z \rangle$ (10)	$\langle L_{43} \rangle$ (11)	$\langle N_{H,22} \rangle$ (12)
Full	1.11 ^{+0.07} _{-0.07}	13.34/13	40.70/28	23.77/27	> 99.99	6.4	0	96 ⁺³⁸ ₋₃₈	1.2	8.6	3.08
Full				23.75/26	> 99.7	6.4	< 207	100 ⁺⁵⁰ ₋₄₀			
Full				22.97/26	> 99.7	6.5 ^{+0.5} _{-0.15}	0	107 ⁺⁴⁰ ₋₄₀			
Full				22.68/25	> 99.7	6.49 ^{+0.13} _{-0.04}	< 199	105 ⁺⁴⁰ ₋₄₀			
$\log(N_H) > 21.5$	0.47 ^{+0.09} _{-0.09}	18.15/13	46.90/28	30.31/27	> 99.99	6.4	0	129 ⁺⁵² ₋₅₂	1.14	8.0	6.04
$\log(N_H) > 21.5$				29.93/26	> 99.7	6.4	< 333	145 ⁺⁶⁵ ₋₆₅	-	-	-
$\log(N_H) > 21.5$				30.31/26	> 99.7	6.4 ^{+0.13} _{-0.09}	0	129 ⁺⁵² ₋₅₂	-	-	-
$\log(N_H) > 21.5$				29.88/25	> 99.7	6.40 ^{+0.13} _{-0.08}	< 344	145 ⁺⁷⁰ ₋₆₀	-	-	-
$\log(N_H) < 21.5$	1.71 ^{+0.09} _{-0.09}	20.65/13	34.66/28	33.66/27	< 90	6.4	0	< 29	1.28	9.5	0.04
$\log(N_H) < 21.5$				33.62/26	< 90	6.4	< 2000	< 130	-	-	-
$\log(N_H) < 21.5$				33.43/26	< 90	6.5 ^{+*} _{-*}	0	< 81	-	-	-
$\log(N_H) < 21.5$				33.36/25	< 90	6.48 ^{+*} _{-*}	< *	< 137	-	-	-
$L_{43} > 6$	1.26 ^{+0.09} _{-0.09}	12.45/13	32.11/28	29.81/27	< 90	6.4	0	< 125	1.8	23.4	3.07
$L_{43} > 6$				29.74/26	< 90	6.4	< 945	< 124	-	-	-
$L_{43} > 6$				29.81/26	< 90	6.4 ^{+*} _{-*}	0	< 125	-	-	-
$L_{43} > 6$				28.64/25	< 90	6.50 ^{+*} _{-0.17}	< 268	80 ⁺⁷⁰ ₋₇₀	-	-	-
$L_{43} < 6$	1.05 ^{+0.08} _{-0.08}	16.73/13	45.74/28	31.13/27	> 99.7	6.4	0	110 ⁺⁴⁷ ₋₄₇	0.90	1.6	3.09
$L_{43} < 6$				30.59/26	> 99.7	6.4	< 636	130 ⁺¹³⁰ ₋₆₀	-	-	-
$L_{43} < 6$				31.13/26	> 99.7	6.4 ^{+0.13} _{-0.11}	0	110 ⁺⁴⁷ ₋₄₇	-	-	-
$L_{43} < 6$				30.53/25	> 99.99	6.43 ^{+0.26} _{-0.12}	< 678	130 ⁺⁵⁵ ₋₆₀	-	-	-
$z > 1$	1.13 ^{+0.10} _{-0.10}	16.12/13	35.83/28	26.95/27	> 99.0	6.4	0	98 ⁺⁵⁵ ₋₅₅	1.83	15.6	3.08
$z > 1$				26.61/26	> 95.4	6.4	< 526	115 ⁺⁹⁰ ₋₆₅	-	-	-
$z > 1$				26.95/26	> 95.4	6.4 ^{+0.17} _{-0.11}	0	98 ⁺⁵⁵ ₋₅₅	-	-	-
$z > 1$				26.61/25	> 95.4	6.40 ^{+0.23} _{-0.18}	< 520	115 ⁺⁶⁰ ₋₆₀	-	-	-
$z < 1$	1.13 ^{+0.08} _{-0.08}	26.07/13	43.00/28	35.87/27	> 99.0	6.4	0	86 ⁺⁵² ₋₅₂	0.65	2.6	3.08
$z < 1$				35.81/26	> 95.45	6.4	< 216	85 ⁺⁵⁵ ₋₅₀	-	-	-
$z < 1$				35.87/26	> 95.45	6.4 ^{+0.15} _{-0.10}	0	86 ⁺⁵² ₋₅₂	-	-	-
$z < 1$				35.59/25	> 90	6.44 ^{+0.11} _{-0.13}	< 217	85 ⁺⁶⁰ ₋₅₀	-	-	-
$z < 0.76$	1.06 ^{+0.10} _{-0.10}	24.69/13	40.01/28	35.81/27	> 95.45	6.4	0	78 ⁺⁶³ ₋₆₃	0.53	1.8	3.75
$z < 0.76$				35.73/26	< 90	6.4	< 238	80 ⁺⁶³ ₋₆₀	-	-	-
$z < 0.76$				35.81/26	< 90	6.4 ^{+0.15} _{-0.14}	0	78 ⁺⁶³ ₋₆₃	-	-	-
$z < 0.76$				35.73/25	< 90	6.40 ^{+0.51} _{-0.14}	< 233	80 ⁺⁶⁰ ₋₆₀	-	-	-
$z < 0.76, L_{43} < 8.4$	1.07 ^{+0.10} _{-0.10}	25.76/13	42.49/28	37.56/27	> 95.45	6.4	0	90 ⁺⁶⁷ ₋₆₇	0.52	1.2	3.35
$z < 0.76, L_{43} < 8.4$				37.42/26	< 90	6.4	< 157	90 ⁺⁶⁵ ₋₆₅	-	-	-
$z < 0.76, L_{43} < 8.4$				37.56/26	> 90	6.4 ^{+0.12} _{-0.11}	0	90 ⁺⁶⁷ ₋₆₇	-	-	-
$z < 0.76, L_{43} < 8.4$				37.41/25	< 90	6.4 ^{+0.1} _{-0.1}	< 154	90 ⁺⁶⁵ ₋₆₅	-	-	-
$z > 0.76, L_{43} < 8.4$	1.19 ^{+0.10} _{-0.10}	12.34/13	35.27/28	26.98/27	> 95.45	6.4	0	95 ⁺⁵⁴ ₋₅₄	1.34	1.7	2.47
$z > 0.76, L_{43} < 8.4$				19.97/26	> 99.73	6.4	450 ⁺²⁶⁰ ₋₁₉₅	235 ⁺¹¹⁵ ₋₁₀₅	-	-	-
$z > 0.76, L_{43} < 8.4$				26.62/26	> 95.45	6.5 ^{+0.09} _{-0.30}	0	104 ⁺⁵⁸ ₋₅₈	-	-	-
$z > 0.76, L_{43} < 8.4$				19.93/25	> 99.73	6.36 ^{+0.27} _{-0.06}	445 ⁺²⁵⁰ ₋₁₄₅	235 ⁺¹¹⁵ ₋₁₀₅	-	-	-
$z > 0.76, L_{43} > 8.4$	1.14 ^{+0.12} _{-0.12}	9.39/13	34.80/28	33.32/27	< 90	6.4	0	< 158	2.08	32.1	3.32
$z > 0.76, L_{43} > 8.4$				33.06/26	< 90	6.4	< 724	< 162	-	-	-
$z > 0.76, L_{43} > 8.4$				32.84/26	< 90	6.66 ^{+0.34} _{-0.46}	0	< 169	-	-	-
$z > 0.76, L_{43} > 8.4$				29.47/25	< 90	6.50 ^{+0.12} _{-0.09}	< 316	125 ⁺¹³⁰ ₋₈₀	-	-	-

TABLE A.6: Sample composed by all the sources with more than **100** net counts in 2-12 keV. (1) sample; (2) photon index of the powerlaw ; (3) χ^2 of the fitting with the powerlaw ; (4) χ^2 of the fitting with table model; (5) χ^2 of the fitting with table model plus gaussian; (6) significance of adding the gaussian to the table model; (7) gaussian centroid; (8) gaussian width; (9) EW of the gaussian; (10) average redshift; (11) average luminosity; (12) average column density of the absorber; * impossible to calculate the error; with steppar we get a $\Delta\chi^2$ lower than 2.7

Sample (1)	Γ (2)	$\chi^2/\text{dof(p)}$ (3)	$\chi^2/\text{dof(s)}$ (4)	$\chi^2/\text{dof(g)}$ (5)	$P(\Delta\chi^2, \nu)$ (6)	E(keV) (7)	σ (eV) (8)	EW(eV) (9)	$\langle z \rangle$ (10)	$\langle L_{43} \rangle$ (11)	$\langle N_{H,22} \rangle$ (12)
Full	1.11 ^{+0.06} _{-0.06}	9.68/13	48.08/28	28.35/27	> 99.99	6.4	0	113 ⁺⁴² ₋₄₂	1.24	11.81	2.63
Full				27.96/26	> 99.99	6.4	< 83	124 ⁺⁴⁵ ₋₄₆	-	-	-
Full				28.18/26	> 99.99	6.32 ^{+0.02} _{-0.04}	0	118 ⁺⁴¹ ₋₄₅	-	-	-
Full				27.99/25	> 99.73	6.4 ^{+0.06} _{-0.2}	< 69.7	121 ⁺⁴⁵ ₋₄₄	-	-	-
$\log(N_H) > 21.5$	0.30 ^{+0.09} _{-0.09}	11.42/13	39.52/28	27.14/27	> 99.73	6.4	0	128 ⁺⁶¹ ₋₆₀	1.15	10.8	5.50
$\log(N_H) > 21.5$				27.13/26	> 99.73	6.4	< 45	132 ⁺⁶² ₋₆₂	-	-	-
$\log(N_H) > 21.5$				27.14/26	> 99.73	6.4 ^{+0.02} _{-0.14}	0	128 ⁺⁶¹ ₋₆₀	-	-	-
$\log(N_H) > 21.5$				27.13/25	> 99.0	6.4 ^{+0.6} _{-0.12}	< 38	131 ⁺⁶¹ ₋₆₁	-	-	-
$\log(N_H) < 21.5$	1.74 ^{+0.07} _{-0.07}	12.34/13	44.44/28	28.61/27	> 99.99	6.4	0	80 ⁺³³ ₋₃₃	1.32	12.72	4.28
$\log(N_H) < 21.5$				26.77/26	> 99.73	6.4	< 215	120 ⁺⁴⁷ ₋₄₇	-	-	-
$\log(N_H) < 21.5$				28.61/26	> 99.73	6.4 ^{+0.13} _{-0.15}	0	80 ⁺³³ ₋₃₃	-	-	-
$\log(N_H) < 21.5$				28.82/25	> 99.73	6.5 ^{+0.60} _{-0.12}	< 719	134 ⁺⁵⁶ ₋₅₆	-	-	-
$L_{43} < 6.65$	1.03 ^{+0.07} _{-0.07}	16.39/13	57.38/28	41.46/27	> 99.99	6.4	0	145 ⁺⁶⁰ ₋₆₀	0.91	2.25	3.04
$L_{43} < 6.65$				41.37/26	> 99.73	6.4	< 68	154 ⁺⁶⁴ ₋₆₄	-	-	-
$L_{43} < 6.65$				41.46/26	> 99.73	6.4 ^{+0.04} _{-0.10}	0	145 ⁺⁶⁰ ₋₆₀	-	-	-
$L_{43} < 6.65$				44.85/25	> 99.0	6.5 ^{+0.3} _{-0.3}	< 926	184 ⁺⁸⁸ ₋₈₈	-	-	-
$L_{43} > 6.65$	1.23 ^{+0.08} _{-0.08}	14.64/13	33.30/28	29.95/27	> 90.0	6.4	0	40 ⁺³³ ₋₃₆	1.76	26.88	1.99
$L_{43} > 6.65$				28.46/26	> 90.0	6.4	< 643	66 ⁺⁴⁷ ₋₅₀	-	-	-
$L_{43} > 6.65$				29.81/26	< 90.0	6.1 ^{+0.5} _{-0.1}	0	40 ⁺³² ₋₃₆	-	-	-
$L_{43} > 6.65$				28.48/25	< 90.0	6.4 ^{+0.2} _{-0.4}	< 646	62 ⁺⁷⁵ ₋₄₆	-	-	-
$z < 1.01$	1.15 ^{+0.07} _{-0.07}	16.74/13	48.08/28	36.74/27	> 99.73	6.4	0	151 ⁺⁷⁴ ₋₇₄	0.68	3.8	2.74
$z < 1.01$				36.72/26	> 99.0	6.4	< 38.4	154 ⁺⁷⁶ ₋₇₆	-	-	-
$z < 1.01$				36.74/26	> 99.0	6.4 ^{+0.1} _{-0.1}	0	151 ⁺⁷⁴ ₋₇₄	-	-	-
$z < 1.01$				38.84/25	> 95.45	6.4 ^{+0.1} _{-0.1}	< 485	152 ⁺⁷⁴ ₋₇₄	-	-	-
$z > 1.01$	1.07 ^{+0.08} _{-0.08}	12.20/13	34.20/28	25.92/27	> 99.0	6.4	0	66 ⁺³⁸ ₋₃₈	1.80	19.71	2.52
$z > 1.01$				25.17/26	> 95.45	6.4	*	89 ⁺⁴⁹ ₋₄₉	-	-	-
$z > 1.01$				25.92/26	> 95.45	6.4 ^{+0.7} _{-0.4}	0	66 ⁺³⁸ ₋₃₈	-	-	-
$z > 1.01$				22.58/25	> 99.0	6.19 ^{+0.17} _{-0.16}	< 374	111 ⁺¹³⁷ ₋₅₄	-	-	-
$z > 0.78, L_{44} > 2.1$	1.26 ^{+0.11} _{-0.11}	8.15/13	23.21/28	20.59/27	< 90.0	6.4	0	45 ⁺⁴⁴ ₋₄₃	2.02	35.8	2.20
$z > 0.78, L_{44} > 2.1$				20.17/26	> 90.0	6.4	< 797	60 ⁺⁶² ₋₅₇	-	-	-
$z > 0.78, L_{44} > 2.1$				18.96/26	> 90.0	6.25 ^{+0.25} _{-0.25}	0	61 ⁺⁵⁴ ₋₄₉	-	-	-
$z > 0.78, L_{44} > 2.1$				19.02/25	< 90.0	6.27 ^{+0.27} _{-0.26}	< 66	64 ⁺¹⁰⁹ ₋₅₁	-	-	-
$z > 0.78, L_{44} < 2.1$	1.03 ^{+0.09} _{-0.09}	12.85/13	40.73/28	31.50/27	> 99.73	6.4	0	81 ⁺⁴⁴ ₋₄₄	1.3	4.8	2.16
$z > 0.78, L_{44} < 2.1$				29.69/26	> 99.0	6.4	328 ⁺ _{-*}	147 ⁺⁷³ ₋₇₃	-	-	-
$z > 0.78, L_{44} < 2.1$				31.50/26	> 99.0	6.4 ^{+0.1} _{-0.3}	0	81 ⁺⁴⁴ ₋₄₄	-	-	-
$z > 0.78, L_{44} < 2.1$				28.04/25	> 99.0	6.22 ^{+0.23} _{-0.12}	< 804	155 ⁺⁷² ₋₇₂	-	-	-
$z < 0.78, L_{44} < 2.1$	1.08 ^{+0.09} _{-0.09}	17.22/13	49.14/28	38.89/27	> 99.73	6.4	0	194 ⁺¹⁰⁰ ₋₁₀₀	0.55	2.4	3.58
$z < 0.78, L_{44} < 2.1$				38.89/26	> 99.0	6.4	< 219	194 ⁺⁹⁹ ₋₉₉	-	-	-
$z < 0.78, L_{44} < 2.1$				38.89/26	> 99.0	6.4 ^{+0.1} _{-0.1}	0	194 ⁺¹⁰⁰ ₋₁₀₀	-	-	-
$z < 0.78, L_{44} < 2.1$				38.89/25	> 95.45	6.4 ^{+0.1} _{-0.1}	< 219	194 ⁺¹⁰⁰ ₋₁₀₀	-	-	-

Appendix B

The XMM CDFS background

Given the long exposure of the observation of XMM-Newton in the CDFS, we expect that the background level is also relatively high. For this reason, we performed two checks: first, we checked the average spectrum of the background in rest-frame; secondly, we looked for the presence of background features at particular observed energies computing the average spectra in observed-frame.

To compute the average spectra of the background, we used the same treatment applied to the observed spectra (as explained in Chap. 3). The region around the expected position of the Fe K_α line is relatively smooth for the total, unabsorbed and low and middle redshift and luminosity samples, while that for the absorbed, high-L and high-z subsamples (see Figs. B.1, B.2 and B.3) is more complex, making any observed features at those energies in the average observed spectra difficult to model and interpret. In particular we found features in the background for energies lower than 5 keV. The iron line region is affected by background irregularities in the high-L subsample, where the background displays features for all the energies lower than 8 keV.

We investigated the possible presence of any instrumental emission in our spectra, by computing the average spectra in the observed frame. Applying our averaging procedure (see Chap. 3), we skipped the shift to a common frame only. We included the Al line channels in the computation of the average observed-frame spectra, in order to check the effect of this background peak also.

As mentioned in Sect. 5.1, there does not seem to be a strong residual contribution from the background Al line. In addition, no strong, well defined, structure is clearly seen in these average spectra. This is reassuring for our method, specially taking into account that any such features would be diluted in the observed average spectrum by shifting all spectra to rest-frame. (see Figs. B.4, B.5, B.6).

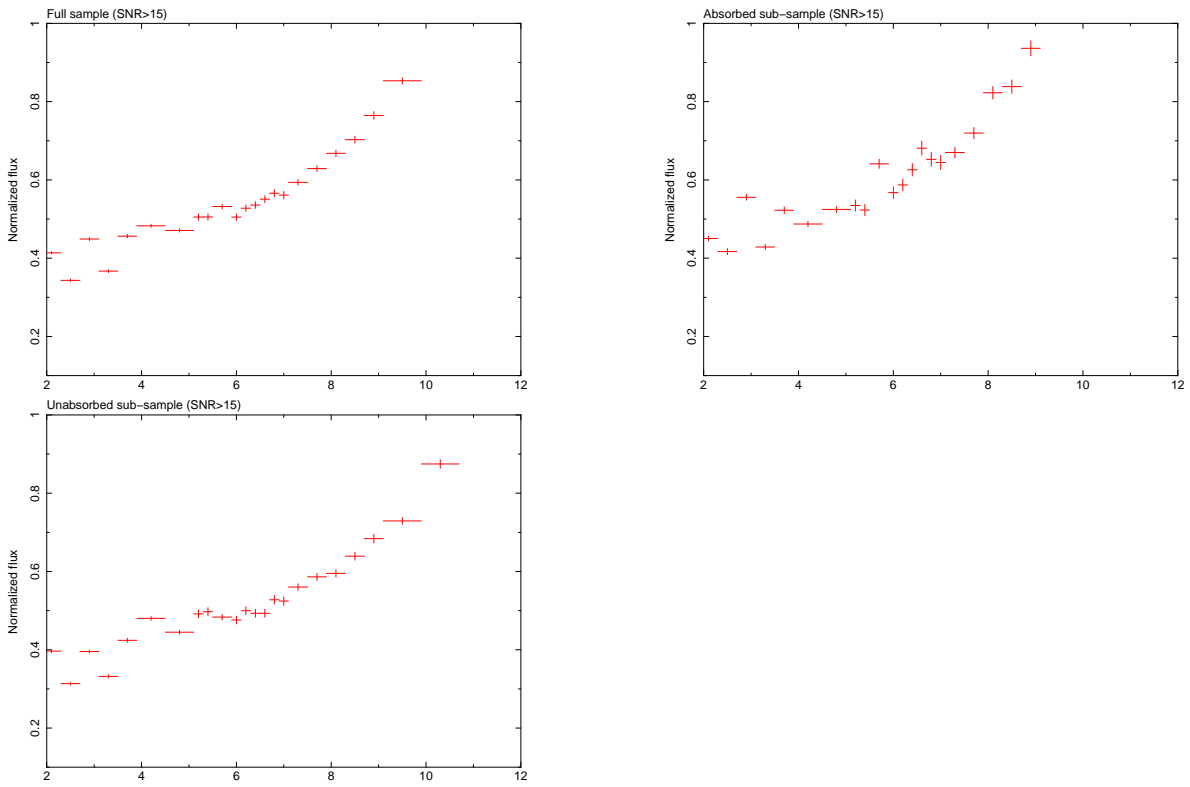


FIGURE B.1: Average observed spectra of the background in rest-frame

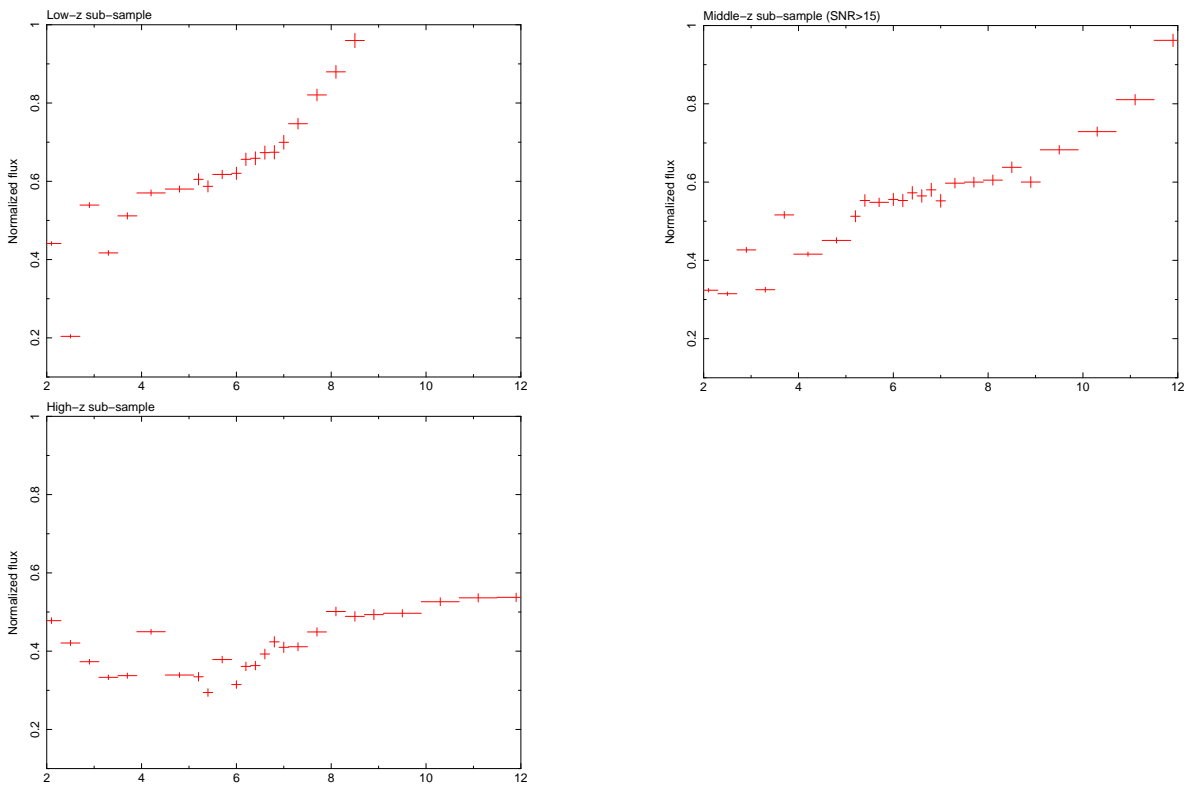


FIGURE B.2: Average observed spectra of the background in rest-frame

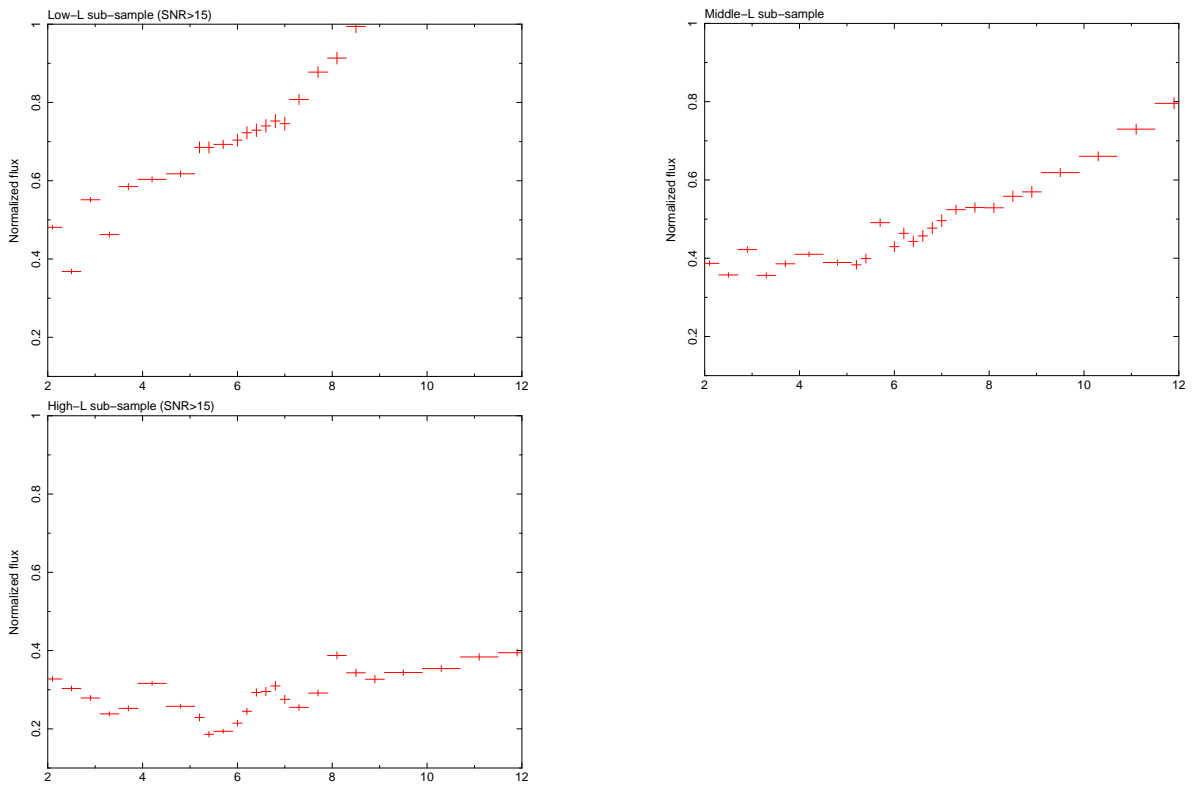


FIGURE B.3: Average observed spectra of the background in rest-frame

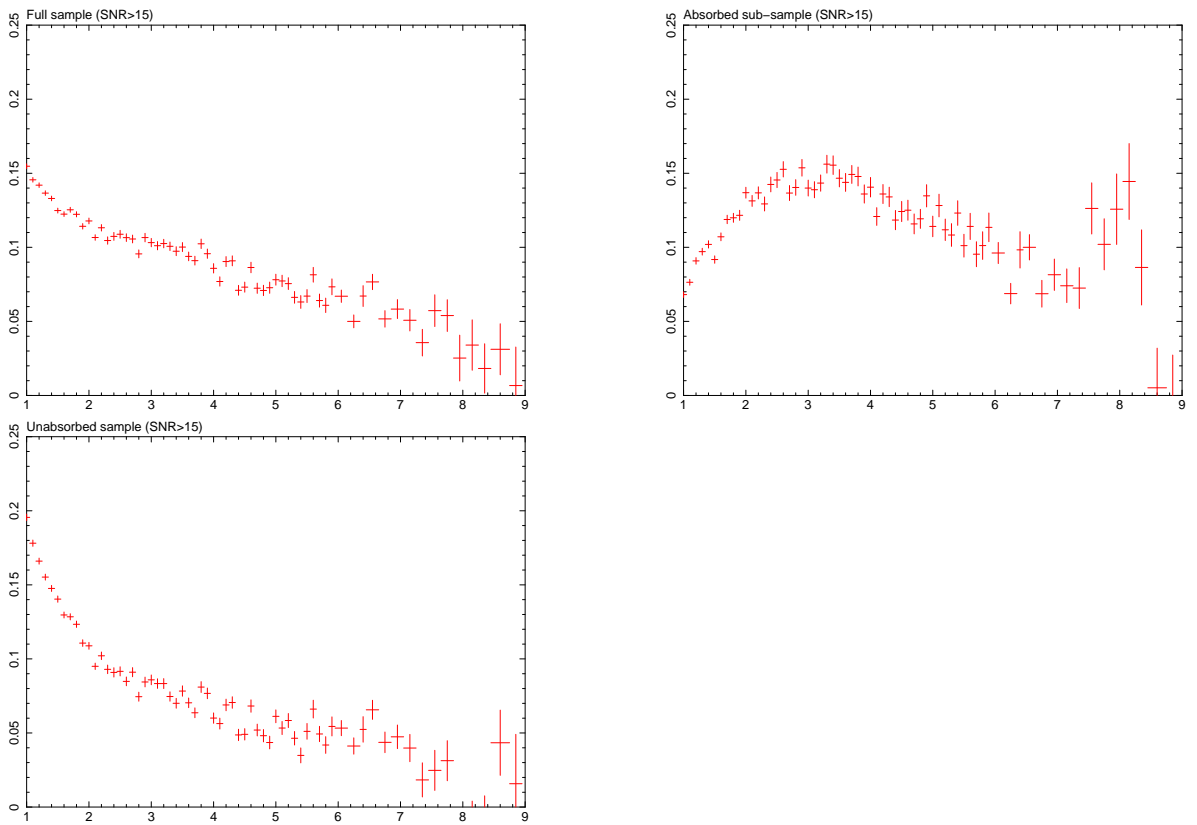


FIGURE B.4: Average observed spectra of in observed-frame

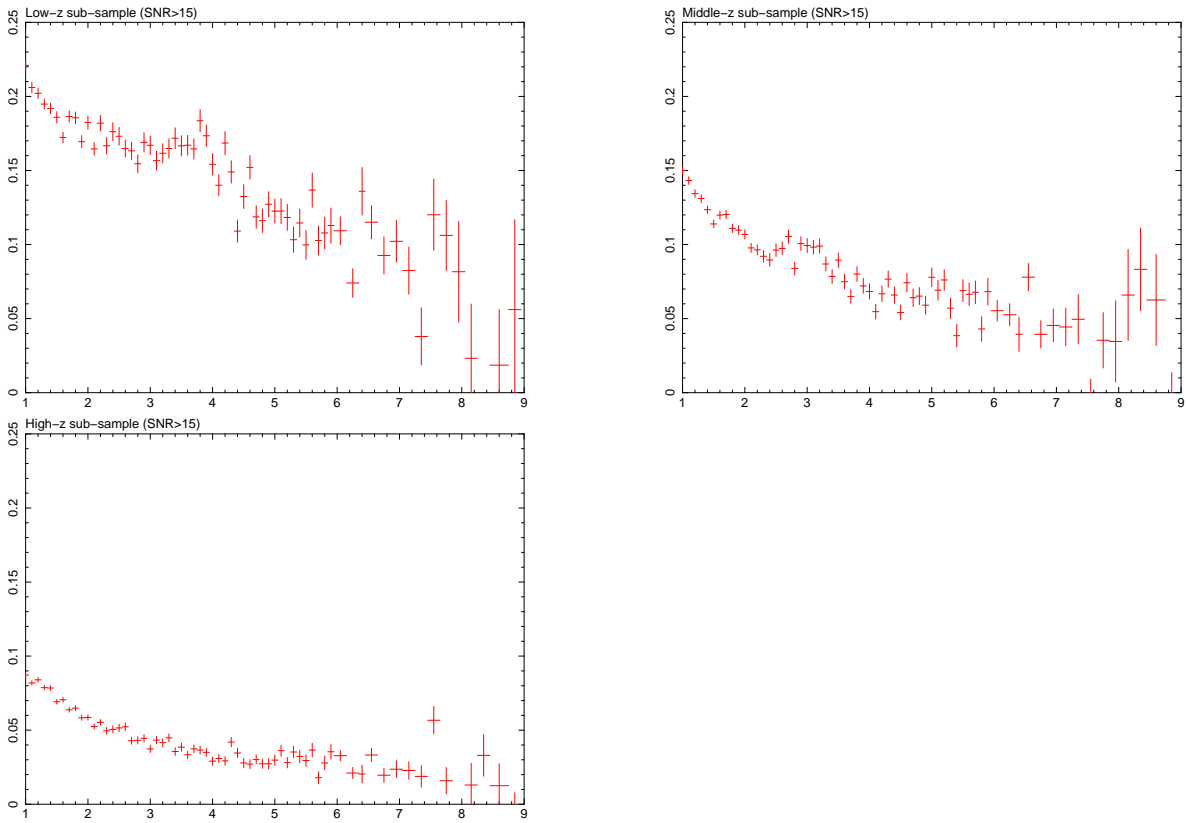


FIGURE B.5: Average observed spectra in observed-frame

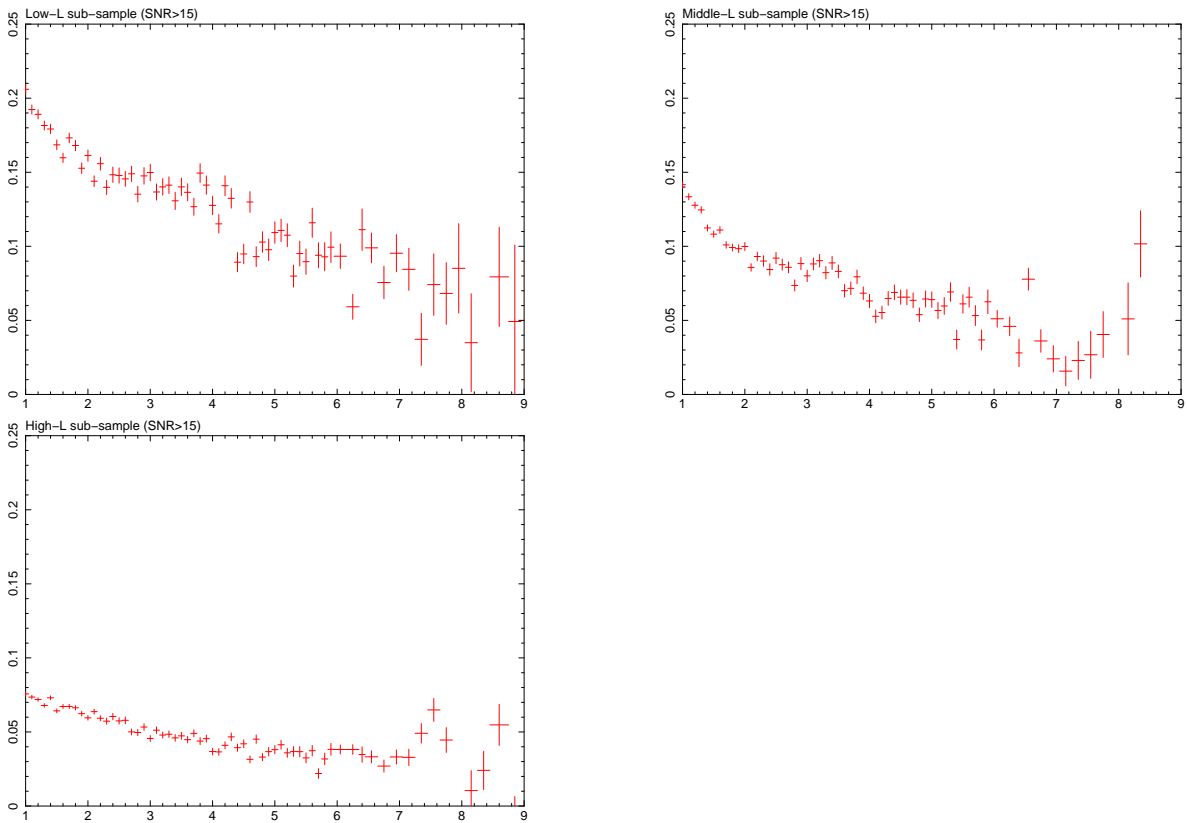


FIGURE B.6: Average observed spectra in observed-frame

Appendix C

Tests of the method

We checked whether the correction for the response matrices (made using the command `eufspec`) depends strongly on the model used to do it. To make this check, we ran `Xspec` simulations. We used Chandra data to make this check, and did not repeat it for the XMM data assuming that this effect is basically the same independently from the instrument.

We start with an “average” source with high SNR modeled with an intrinsically absorbed powerlaw and an unresolved Gaussian line at 6.4 keV, with the average values of the full sample (see Table 4.1): $z = 1.15$, $\Gamma = 1.24$, $N_{\text{H}} = 1.75 \times 10^{22} \text{ cm}^{-2}$, $\text{EW}=100 \text{ eV}$. We compared the input model with the response-matrix-corrected spectra (“unfolded” spectra in `Xspec`) assuming three different models:

1. the input model without the Gaussian
2. a powerlaw with $\Gamma = 0$
3. a powerlaw with $\Gamma = 2$.

We can see the results in Fig. C.1 in the observed frame. The best approximation is obtained using the input parameters, as expected. However, in a wide range around the line, the result does not depend noticeably on the model used for the response matrix correction, even for clearly different models from the input one. The significant discrepancies start only below about 2 keV rest-frame.

We ran another simulation for an absorbed source, using the continuum parameters of one source in the absorbed subsample, ($z = 1.15$, $\Gamma = 1.64$; $N_{\text{H}} = 43.22 \times 10^{22} \text{ cm}^{-2}$,) and a Gaussian at 6.4 keV with $\sigma = 0$, $\text{EW} = 100 \text{ eV}$, again with high SNR. We show in Fig. C.2 the input model and the “unfolded” spectra using the three models above. In this case we also see that there is no important difference in the continuum close to the Fe line between the various models. The differences below $\sim 3 \text{ keV}$ rest-frame are much stronger in this case than in the “average” source, but again the result of the input model follows the input spectrum very closely.

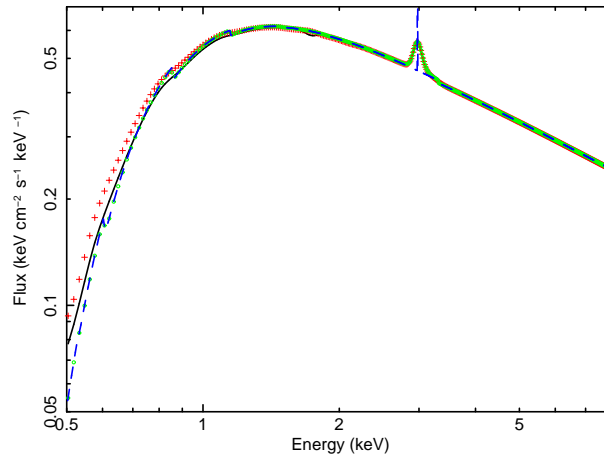


FIGURE C.1: Comparison, for a simulated “average” source, between the input model (dashed blue line) and the unfolded spectra using the best fit (green circles), using $\Gamma = 2$ (red plus), using $\Gamma = 0$ (continuous black line).

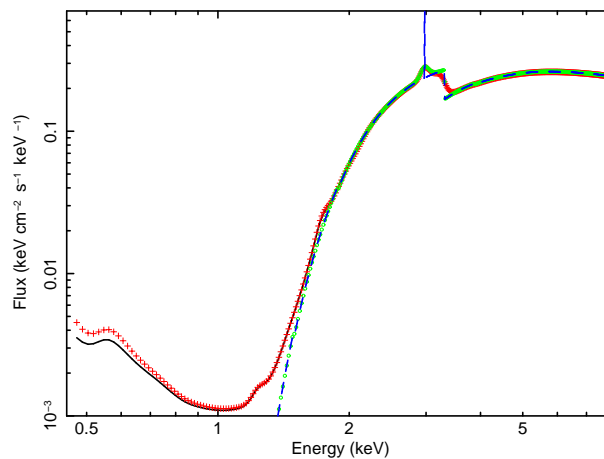


FIGURE C.2: Comparison, for a simulated absorbed source, between: the input model (dashed blue line) and the spectra using the best fit (green circles), using $\Gamma = 2$ (red plus), using $\Gamma = 0$ (continuous black line)

Therefore, we chose to correct the spectra for the response matrices using their own best-fit continuum models and we did not simply divide the spectra for the effective area of the detector. This simple method actually assumes a flat continuum and does not account for the limited spectral resolution of X-ray detectors.

It is important to notice that, in any case, there is an energy blending that widens the Fe line. We have quantified this effect using simulations, as explained in the Sect. 3.5.3.

To check the effect of the correction for detector response on the actual average spectrum, we corrected the spectra for the detector responses using a powerlaw with $\Gamma = 2$. We then took the average of the observed and simulated spectra, using the procedure as explained in Sect. 3. We can see in Fig. C.3 that the differences are again small and, in any case, within the mutual error bars. If anything, using the best-fit model for the “unfolding” appears to produce a more conservative estimate of the Fe line flux.

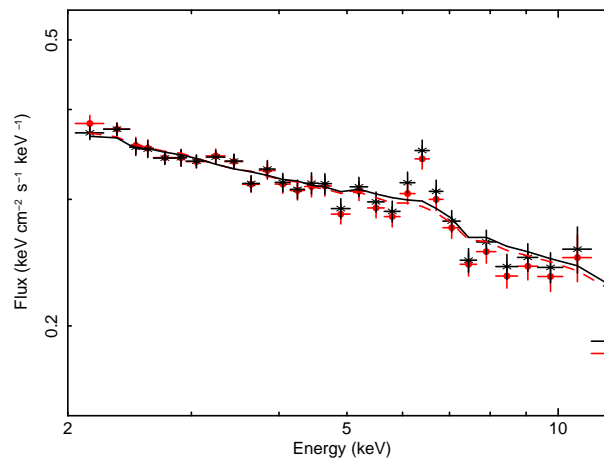


FIGURE C.3: Comparison between the average spectra after having corrected for the detector response using: the best fit (average observed spectrum represented by red full circles, simulated continuum by a dashed line) and with the powerlaw with $\Gamma = 2$ (average observed spectrum represented by black stars, simulated continuum by a black continuous line). Sample with the sources with more than 200 net counts.

References

- Alexander, D. M., Bauer, F. E., Brandt, W. N., Schneider, D. P., Hornschemeier, A. E., Vignali, C., Barger, A. J., Broos, P. S., Cowie, L. L., Garmire, G. P., Townsley, L. K., Bautz, M. W., Chartas, G., and Sargent, W. L. W.: 2003, *AJ* **126**, 539
- Antonucci, R. R. J. and Miller, J. S.: 1985, *ApJ* **297**, 621
- Arnaud, K. A.: 1996, in G. H. Jacoby and J. Barnes (eds.), *Astronomical Data Analysis Software and Systems V*, Vol. 101 of *Astronomical Society of the Pacific Conference Series*, p. 17
- Balestra, I., Mainieri, V., Popesso, P., Dickinson, M., Nonino, M., Rosati, P., Teimoorinia, H., Vanzella, E., Cristiani, S., Cesarsky, C., Fosbury, R. A. E., Kuntschner, H., and Rettura, A.: 2010, *VizieR Online Data Catalog* **351**, 29012
- Ballantyne, D. R., Ross, R. R., and Fabian, A. C.: 2001, *MNRAS* **327**, 10
- Bardeen, J. M., Press, W. H., and Teukolsky, S. A.: 1972, *ApJ* **178**, 347
- Bhayani, S. and Nandra, K.: 2011, *MNRAS* **416**, 629
- Bianchi, S., Corral, A., Panessa, F., Barcons, X., Matt, G., Bassani, L., Carrera, F. J., and Jiménez-Bailón, E.: 2008, *MNRAS* **385**, 195
- Bianchi, S., Guainazzi, M., Matt, G., and Fonseca Bonilla, N.: 2007, *A&A* **467**, L19
- Blandford, R. D. and McKee, C. F.: 1982, *ApJ* **255**, 419
- Braitto, V., Reeves, J. N., Dewangan, G. C., George, I., Griffiths, R. E., Markowitz, A., Nandra, K., Porquet, D., Ptak, A., Turner, T. J., Yaqoob, T., and Weaver, K.: 2007, *ApJ* **670**, 978
- Broos, P. S., Townsley, L. K., Feigelson, E. D., Getman, K. V., Bauer, F. E., and Garmire, G. P.: 2010, *The Astrophysical Journal*, 714:1582–1605
- Brusa, M., Gilli, R., and Comastri, A.: 2005, *ApJ* **621**, L5
- Casey, C. M., Chapman, S. C., Smail, I., Alaghband-Zadeh, S., Bothwell, M. S., and Swinbank, A. M.: 2011, *MNRAS* **411**, 2739
- Cash, W.: 1979, *ApJ* **228**, 939
- Chaudhary, P., Brusa, M., Hasinger, G., Merloni, A., and Comastri, A.: 2010, *A&A* **518**, A58

- Chiang, J., Reynolds, C., Blaes, O., Nowak, M., Murray, N., Madejski, G., Marshall, H., and Magdziarz, P.: 2001, *X-ray Astronomy: Stellar Endpoints, AGN, and the Diffuse X-ray Background* **599**, 578
- Civano, F., Comastri, A., and Brusa, M.: 2005, *MNRAS* **358**, 693
- Comastri, A., Ranalli, P., Iwasawa, K., Vignali, C., Gilli, R., Georgantopoulos, I., Barcons, X., Brandt, W. N., Brunner, H., Brusa, M., Cappelluti, N., Carrera, F. J., Civano, F., Fiore, F., Hasinger, G., Mainieri, V., Merloni, A., Nicastro, F., Paolillo, M., Puccetti, S., Rosati, P., Silverman, J. D., Tozzi, P., Zamorani, G., Balestra, I., Bauer, F. E., Luo, B., and Xue, Y. Q.: 2011, *A&A* **526**, L9
- Cooper, M. C., Aird, J. A., Coil, A. L., Davis, M., Faber, S. M., Juneau, S., Lotz, J. M., Nandra, K., Newman, J. A., Willmer, C. N. A., and Yan, R.: 2011, *ApJS* **193**, 14
- Corral, A., Barcons, X., Carrera, F. J., Ceballos, M. T., and Mateos, S.: 2005, *A&A* **431**, 97
- Corral, A., Della Ceca, R., Caccianiga, A., Severgnini, P., Brunner, H., Carrera, F. J., Page, M. J., and Schwobe, A. D.: 2011, *A&A* **530**, A42
- Corral, A., Page, M. J., Carrera, F. J., Barcons, X., Mateos, S., Ebrero, J., Krumpe, M., Schwobe, A., Tedds, J. A., and Watson, M. G.: 2008, *A&A* **492**, 71
- de la Calle Pérez, I., Longinotti, A. L., Guainazzi, M., Bianchi, S., Dovčiak, M., Cappi, M., Matt, G., Miniutti, G., Petrucci, P. O., Piconcelli, E., Ponti, G., Porquet, D., and Santos-Lleó, M.: 2010, *A&A* **524**, A50
- Digby-North, J.: 2011, *Thesis (PhD), Imperial College London*
- Done, C., Mulchaey, J. S., Mushotzky, R. F., and Arnaud, K. A.: 1992, *ApJ* **395**, 275
- Fabian, A. C., Iwasawa, K., Reynolds, C. S., and Young, A. J.: 2000, *PASP* **112**, 1145
- Fabian, A. C., Kunieda, H., Inoue, S., Matsuoka, M., Mihara, T., Miyamoto, S., Otani, C., Ricker, G., Tanaka, Y., Yamauchi, M., and Yaqoob, T.: 1994, *PASJ* **46**, L59
- Fabian, A. C., Rees, M. J., Stella, L., and White, N. E.: 1989, *MNRAS* **238**, 729
- Fabian, A. C., Vaughan, S., Nandra, K., Iwasawa, K., Ballantyne, D. R., Lee, J. C., De Rosa, A., Turner, A., and Young, A. J.: 2002, *MNRAS* **335**, L1
- Falocco, S., Carrera, F. J., Corral, A., Laird, E., Nandra, K., Barcons, X., Page, M. J., and Digby-North, J.: 2012, *A&A* **538**, A83
- Fruscione, A., McDowell, J. C., Allen, G. E., Brickhouse, N. S., Burke, D. J., Davis, J. E., Durham, N., Elvis, M., Galle, E. C., Harris, D. E., Huenemoerder, D. P., Houck, J. C., Ishibashi, B., Karovska, M., Nicastro, F., Noble, M. S., Nowak, M. A., Primini, F. A., Siemiginowska, A., Smith, R. K., and Wise, M.: 2006, in *Society of Photo-Optical Instrumentation Engineers (SPIE) Conference Series*, Vol. 6270 of *Society of Photo-Optical Instrumentation Engineers (SPIE) Conference Series*
- Ghisellini, G., Haardt, F., and Matt, G.: 1994, *MNRAS* **267**, 743
- Gilli, R., Comastri, A., and Hasinger, G.: 2007, *A&A* **463**, 79
- Gilli, R., Risaliti, G., and Salvati, M.: 1999, *A&A* **347**, 424

- Guainazzi, M., Bianchi, S., de La Calle Pérez, I., Dovčiak, M., and Longinotti, A. L.: 2011, *A&A* **531**, A131
- Guainazzi, M., Bianchi, S., and Dovčiak, M.: 2006, *Astronomische Nachrichten* **327**, 1032
- Haardt, F. and Maraschi, L.: 1991, *ApJ* **380**, L51
- Ho, L. C., Filippenko, A. V., and Sargent, W. L.: 1995, *ApJS* **98**, 477
- Iwasawa, K., Fabian, A. C., Mushotzky, R. F., Brandt, W. N., Awaki, H., and Kunieda, H.: 1996, *MNRAS* **279**, 837
- Iwasawa, K., Fabian, A. C., Young, A. J., Inoue, H., and Matsumoto, C.: 1999, *MNRAS* **306**, L19
- Iwasawa, K., Mainieri, V., Brusa, M., Comastri, A., Gilli, R., Vignali, C., Hasinger, G., Sanders, D. B., Cappelluti, N., Impey, C. D., Koekemoer, A., Lanzuisi, G., Lusso, E., Merloni, A., Salvato, M., Taniguchi, Y., and Trump, J. R.: 2012, *A&A* **537**, A86
- Iwasawa, K. and Taniguchi, Y.: 1993, *ApJ* **413**, L15
- Jiménez-Bailón, E., Piconcelli, E., Guainazzi, M., Schartel, N., Rodríguez-Pascual, P. M., and Santos-Lleó, M.: 2005, *A&A* **435**, 449
- Kaspi, S., Brandt, W. N., Netzer, H., Sambruna, R., Chartas, G., Garmire, G. P., and Nousek, J. A.: 2000, *ApJ* **535**, L17
- Kriek, M., van Dokkum, P. G., Franx, M., Illingworth, G. D., Marchesini, D., Quadri, R., Rudnick, G., Taylor, E. N., Förster Schreiber, N. M., Gawiser, E., Labbé, I., Lira, P., and Wuyts, S.: 2008, *ApJ* **677**, 219
- Laird, E. S., Nandra, K., Georgakakis, A., Aird, J. A., Barmby, P., Conselice, C. J., Coil, A. L., Davis, M., Faber, S. M., Fazio, G. G., Guhathakurta, P., Koo, D. C., Sarajedini, V., and Willmer, C. N. A.: 2009, *ApJS* **180**, 102
- Laor, A.: 1991, *ApJ* **376**, 90
- Le Fèvre, O., Guzzo, L., Meneux, B., Pollo, A., Cappi, A., Colombi, S., Iovino, A., Marinoni, C., McCracken, H. J., Scaramella, R., Bottini, D., Garilli, B., Le Brun, V., Maccagni, D., Picat, J. P., Scodreggio, M., Tresse, L., Vettolani, G., Zanichelli, A., Adami, C., Arnaboldi, M., Arnouts, S., Bardelli, S., Blaizot, J., Bolzonella, M., Charlot, S., Ciliegi, P., Contini, T., Foucaud, S., Franzetti, P., Gavignaud, I., Ilbert, O., Marano, B., Mathez, G., Mazure, A., Merighi, R., Paltani, S., Pellò, R., Pozzetti, L., Radovich, M., Zamorani, G., Zucca, E., Bondi, M., Bongiorno, A., Busarello, G., Lamareille, F., Mellier, Y., Merluzzi, P., Ripepi, V., and Rizzo, D.: 2005, *A&A* **439**, 877
- Le Fèvre, O., Vettolani, G., Paltani, S., Tresse, L., Zamorani, G., Le Brun, V., Moreau, C., Bottini, D., Maccagni, D., Picat, J. P., Scaramella, R., Scodreggio, M., Zanichelli, A., Adami, C., Arnouts, S., Bardelli, S., Bolzonella, M., Cappi, A., Charlot, S., Contini, T., Foucaud, S., Franzetti, P., Garilli, B., Gavignaud, I., Guzzo, L., Ilbert, O., Iovino, A., McCracken, H. J., Mancini, D., Marano, B., Marinoni, C., Mathez, G., Mazure, A., Meneux, B., Merighi, R., Pellò, R., Pollo, A., Pozzetti, L., Radovich, M., Zucca, E., Arnaboldi, M., Bondi, M., Bongiorno, A., Busarello, G., Ciliegi, P., Gregorini, L., Mellier, Y., Merluzzi, P., Ripepi, V., and Rizzo, D.: 2004, *A&A* **428**, 1043

- Luo, B., Bauer, F. E., Brandt, W. N., Alexander, D. M., Lehmer, B. D., Schneider, D. P., Brusa, M., Comastri, A., Fabian, A. C., Finoguenov, A., Gilli, R., Hasinger, G., Hornschemeier, A. E., Koekemoer, A., Mainieri, V., Paolillo, M., Rosati, P., Shemmer, O., Silverman, J. D., Smail, I., Steffen, A. T., and Vignali, C.: 2008, *ApJS* **179**, 19
- Magdziarz, P. and Zdziarski, A. A.: 1995, *MNRAS* **273**, 837
- Mateos, S., Barcons, X., Carrera, F. J., Ceballos, M. T., Hasinger, G., Lehmann, I., Fabian, A. C., and Streblyanska, A.: 2005, *A&A* **444**, 79
- Mateos, S., Warwick, R. S., Carrera, F. J., Stewart, G. C., Ebrero, J., Della Ceca, R., Caccianiga, A., Gilli, R., Page, M. J., Treister, E., Tedds, J. A., Watson, M. G., Lamer, G., Saxton, R. D., Brunner, H., and Page, C. G.: 2008, *A&A* **492**, 51
- Matt, G.: 2002, *MNRAS* **337**, 147
- Matt, G., Bianchi, S., Guainazzi, M., and Molendi, S.: 2004, *A&A* **414**, 155
- Matt, G., Fabian, A. C., and Reynolds, C. S.: 1997, *MNRAS* **289**, 175
- Matt, G., Fabian, A. C., and Ross, R. R.: 1996, *MNRAS* **278**, 1111
- Matt, G., Perola, G. C., Piro, L., and Stella, L.: 1992, *A&A* **257**, 63
- Matt, G., Porquet, D., Bianchi, S., Falocco, S., Maiolino, R., Reeves, J. N., and Zappacosta, L.: 2005, *A&A* **435**, 857
- Mignoli, M., Cimatti, A., Zamorani, G., Pozzetti, L., Daddi, E., Renzini, A., Broadhurst, T., Cristiani, S., D'Odorico, S., Fontana, A., Giallongo, E., Gilmozzi, R., Menci, N., and Saracco, P.: 2005, *A&A* **437**, 883
- Mushotzky, R. F., Fabian, A. C., Iwasawa, K., Kunieda, H., Matsuoka, M., Nandra, K., and Tanaka, Y.: 1995, *MNRAS* **272**, L9
- N. I. Shakura and R. A. Sunyaev: 1974, *Astronomy and Astrophysics* **24**, 337
- Nandra, K., George, I. M., Mushotzky, R. F., Turner, T. J., and Yaqoob, T.: 1997, *ApJ* **488**, L91
- Nandra, K., George, I. M., Mushotzky, R. F., Turner, T. J., and Yaqoob, T.: 1999, *ApJ* **523**, L17
- Nandra, K., O'Neill, P. M., George, I. M., and Reeves, J. N.: 2007, *MNRAS* **382**, 194
- Nandra, K., O'Neill, P. M., George, I. M., Reeves, J. N., and Turner, T. J.: 2006, *Astronomische Nachrichten* **327**, 1039
- Nandra, K., Pounds, K. A., Stewart, G. C., Fabian, A. C., and Rees, M. J.: 1989, *MNRAS* **236**, 39P
- Osterbrock, D. E.: 1978, *Phys. Scr* **17**, 285
- Panessa, F., Carrera, F. J., Bianchi, S., Corral, A., Gastaldello, F., Barcons, X., Bassani, L., Matt, G., and Monaco, L.: 2009, *MNRAS* **398**, 1951
- Peterson, B. M. and Horne, K.: 2004, *Astronomische Nachrichten* **325**, 248

- Pounds, K., Reeves, J., O'Brien, P., Page, K., Turner, M., and Nayakshin, S.: 2001, *ApJ* **559**, 181
- Pounds, K. A., Reeves, J. N., Page, K. L., Edelson, R., Matt, G., and Perola, G. C.: 2003, *MNRAS* **341**, 953
- Press, W., Teukolsky, S., Vetterling, V., and Flannery, B.: 2007, *Numerical Recipes*, Cambridge University Press
- Ravikumar, C. D., Puech, M., Flores, H., Proust, D., Hammer, F., Lehnert, M., Rawat, A., Amram, P., Balkowski, C., Burgarella, D., Cassata, P., Cesarsky, C., Cimatti, A., Combes, F., Daddi, E., Dannerbauer, H., di Serego Alighieri, S., Elbaz, D., Guiderdoni, B., Kembhavi, A., Liang, Y. C., Pozzetti, L., Vergani, D., Vernet, J., Wozniak, H., and Zheng, X. Z.: 2007, *A&A* **465**, 1099
- Reynolds, C. S., Fabian, A. C., Nandra, K., Inoue, H., Kunieda, H., and Iwasawa, K.: 1995, *MNRAS* **277**, 901
- Risaliti, G. and Elvis, M.: 2004, in A. J. Barger (ed.), *Supermassive Black Holes in the Distant Universe*, Vol. 308 of *Astrophysics and Space Science Library*, p. 187
- Ruszkowski, M. and Fabian, A. C.: 2000, *MNRAS* **315**, 223
- Silverman, J. D., Mainieri, V., Salvato, M., Hasinger, G., Bergeron, J., Capak, P., Szokoly, G., Finoguenov, A., Gilli, R., Rosati, P., Tozzi, P., Vignali, C., Alexander, D. M., Brandt, W. N., Lehmer, B. D., Luo, B., Rafferty, D., Xue, Y. Q., Balestra, I., Bauer, F. E., Brusa, M., Comastri, A., Kartaltepe, J., Koekemoer, A. M., Miyaji, T., Schneider, D. P., Treister, E., Wisotski, L., and Schramm, M.: 2010, *ApJS* **191**, 124
- Streblyanska, A., Hasinger, G., Finoguenov, A., Barcons, X., Mateos, S., and Fabian, A. C.: 2005, *A&A* **432**, 395
- Szokoly, G. P., Bergeron, J., Hasinger, G., Lehmann, I., Kewley, L., Mainieri, V., Nonino, M., Rosati, P., Giacconi, R., Gilli, R., Gilmozzi, R., Norman, C., Romaniello, M., Schreier, E., Tozzi, P., Wang, J. X., Zheng, W., and Zirm, A.: 2004, *ApJS* **155**, 271
- Tanaka, Y., Nandra, K., Fabian, A. C., Inoue, H., Otani, C., Dotani, T., Hayashida, K., Iwasawa, K., Kii, T., Kunieda, H., Makino, F., and Matsuoka, M.: 1995, *Nature* **375**, 659
- Taylor, E. N., Franx, M., van Dokkum, P. G., Quadri, R. F., Gawiser, E., Bell, E. F., Barrientos, L. F., Blanc, G. A., Castander, F. J., Damen, M., Gonzalez-Perez, V., Hall, P. B., Herrera, D., Hildebrandt, H., Kriek, M., Labbé, I., Lira, P., Maza, J., Rudnick, G., Treister, E., Urry, C. M., Willis, J. P., and Wuyts, S.: 2009, *ApJS* **183**, 295
- Treister, E., Virani, S., Gawiser, E., Urry, C. M., Lira, P., Francke, H., Blanc, G. A., Cardamone, C. N., Damen, M., Taylor, E. N., and Schawinski, K.: 2009, *ApJ* **693**, 1713
- Ueda, Y., Akiyama, M., Ohta, K., and Miyaji, T.: 2003, *ApJ* **598**, 886
- van der Wel, A., Franx, M., van Dokkum, P. G., Rix, H.-W., Illingworth, G. D., and Rosati, P.: 2005, *ApJ* **631**, 145
- Vanzella, E., Cristiani, S., Dickinson, M., Giavalisco, M., Kuntschner, H., Haase, J., Nonino, M., Rosati, P., Cesarsky, C., Ferguson, H. C., Fosbury, R. A. E., Grazian, A., Moustakas, L. A., Rettura, A., Popesso, P., Renzini, A., Stern, D., and GOODS Team: 2008, *A&A* **478**, 83

- Véron-Cetty, M.-P. and Véron, P.: 2006, *A&A* **455**, 773
- Véron-Cetty, M.-P. and Véron, P.: 2010, *A&A* **518**, A10
- Wang, J.-X., Zhou, Y.-Y., and Wang, T.-G.: 1999, *ApJ* **523**, L129
- Watson, M. G., Schroder, A. C., Fyfe, D., Page, C. G., Lamer, G., Mateos, S., Pye, J., Sakano, M., Rosen, S., Ballet, J., Barcons, X., Barret, D., Boller, T., Brunner, H., Brusa, M., Caccianiga, A., Carrera, F. J., Ceballos, M., Della Ceca, R., Denby, M., Denkinson, G., Dupuy, S., Farrell, S., Frascchetti, F., Freyberg, M. J., Guillout, P., Hambaryan, V., Maccacaro, T., Mathiesen, B., McMahon, R., Michel, L., Motch, C., Osborne, J. P., Page, M., Pakull, M. W., Pietsch, W., Saxton, R., Schwobe, A., Severgnini, P., Simpson, M., Sironi, G., Stewart, G., Stewart, I. M., Stobbart, A.-M., Tedds, J., Warwick, R., Webb, N., West, R., Worrall, D., and Yuan, W.: 2008, *VizieR Online Data Catalog* **349**, 30339
- Wilms, J., Reynolds, C. S., Begelman, M. C., Reeves, J., Molendi, S., Staubert, R., and Kendziorra, E.: 2001, *MNRAS* **328**, L27
- Xue, Y. Q., Luo, B., Brandt, W. N., Bauer, F. E., Lehmer, B. D., Broos, P. S., Schneider, D. P., Alexander, D. M., Brusa, M., Comastri, A., Fabian, A. C., Gilli, R., Hasinger, G., Hornschemeier, A. E., Koekemoer, A., Liu, T., Mainieri, V., Paolillo, M., Rafferty, D. A., Rosati, P., Shemmer, O., Silverman, J. D., Smail, I., Tozzi, P., and Vignali, C.: 2011, *ApJS* **195**, 10
- Yaqoob, T., Edelson, R., Weaver, K. A., Warwick, R. S., Mushotzky, R. F., Serlemitsos, P. J., and Holt, S. S.: 1995, *ApJ* **453**, L81
- Yaqoob, T., George, I. M., Nandra, K., Turner, T. J., Serlemitsos, P. J., and Mushotzky, R. F.: 2001, *ApJ* **546**, 759
- Yaqoob, T., Reeves, J. N., Markowitz, A., Serlemitsos, P. J., and Padmanabhan, U.: 2005, *ApJ* **627**, 156
- Zdziarski, A. A., Johnson, W. N., Done, C., Smith, D., and McNaron-Brown, K.: 1995, *ApJ* **438**, L63
- Zdziarski, A. A., Lubiński, P., and Smith, D. A.: 1999, *MNRAS* **303**, L11